A Search for Matter Enhanced Neutrino Oscillations through
Measurements of Day and Night Solar Neutrino Fluxes at the
Sudbury Neutrino Observatory

Kathryn Kelly Schaffer Miknaitis

A dissertation submitted in partial fulfillment
of the requirements for the degree of

Doctor of Philosophy

University of Washington

2005

Program Authorized to Offer Degree:  Physics

University of Washington
Graduate School


This is to certify that I have examined this copy of a doctoral dissertation by


Kathryn Kelly Schaffer Miknaitis


and have found that it is complete and satisfactory in all respects,
and that any and all revisions required by the final
examining committee have been made.


Chair of Supervisory Committee:


_____
John F. Wilkerson


Reading Committee:


_____
John F. Wilkerson


_____
R. G. Hamish Robertson


_____
Joseph A. Formaggio


Date: _____

University of Washington

Abstract

A Search for Matter Enhanced Neutrino Oscillations through Measurements of Day and Night Solar Neutrino Fluxes at the Sudbury Neutrino Observatory

Kathryn Kelly Schaffer Miknaitis

Chair of Supervisory Committee:

Professor John F. Wilkerson
Department of Physics

The Sudbury Neutrino Observatory (SNO) is a heavy-water Cherenkov detector designed to study $^8$B neutrinos from the sun. Through the charged-current (CC) and neutral-current (NC) reactions of neutrinos on deuterium, SNO separately determines the flux of electron neutrinos and the flux of all active flavors of solar $^8$B neutrinos. SNO is also sensitive to the elastic scattering (ES) of neutrinos on electrons in the heavy water. Measurements of the CC and NC rates in SNO have conclusively demonstrated solar neutrino flavor change. This flavor change is believed to be caused by matter-enhanced oscillations in the sun, through the Mikheyev-Smirnov-Wolfenstein (MSW) effect. Matter effects could also change the flavor composition of neutrinos that traverse the earth. A comparison of the day and night measured CC flux at SNO directly tests for the MSW effect and contributes to constraints on neutrino oscillation parameters in the MSW model.

We perform measurements of the day and night neutrino fluxes using data from the second phase of SNO, in which salt (NaCl) was added to the heavy water to enhance sensitivity to the NC reaction. Better discrimination between CC and NC events in the salt phase allows the fluxes to be determined without constraining the neutrino energy spectrum. The day-night asymmetry in the CC flux measured in this model-independent analysis is $A_{CC} = [-5.6 \pm 7.4(\text{stat.}) \pm 5.3(\text{syst.})]\%$ , where the asymmetry is defined as

the difference between the night and day values divided by their average. The asymmetries in the NC and ES fluxes are $A_{NC} = [4.2 \pm 8.6(\text{stat.}) \pm 7.2(\text{syst.})]\%$, and $A_{ES} = [14.6 \pm 19.8(\text{stat.}) \pm 3.3(\text{syst.})]\%$. The neutral current asymmetry is expected to be zero assuming standard neutrino oscillations. When we constrain it to be zero, we obtain $A_{CC} = [-3.7 \pm 6.3(\text{stat.}) \pm 3.2(\text{syst.})]\%$ and $A_{ES} = [15.3 \pm 19.8(\text{stat.}) \pm 3.0(\text{syst.})]\%$. The day and night energy spectra from the CC reaction have been measured and show no evidence for day-night variations as a function of energy.

# TABLE OF CONTENTS

# LIST OF FIGURES

# LIST OF TABLES

# ACRONYMS

SNO: The Sudbury Neutrino Observatory experiment.

AV: The Acrylic Vessel that holds the heavy water in SNO.

PMT: Photomultiplier Tube.

PSUP: The PMT Support Structure.

CC: The Charged Current reaction of neutrinos on deuterium.

NC: The Neutral Current reaction of neutrinos on deuterium.

ES: The Elastic Scattering of neutrinos on electrons.

EXTN: The External Neutron background source.

PGT: The Pulsed Global Trigger, a diagnostic trigger issued at 5 Hz.

LSP: The Livetime Summary Processor in SNOMAN.

PDF: Probability Density Function.

MC: Monte Carlo.

NHIT: The number of PMT hits in an event.

SNOMAN: The SNO Monte Carlo and Analysis package.

MSW EFFECT: Mikheyev-Wolfenstein-Smirnov effect; matter enhanced neutrino oscillations.

CKM MATRIX: Cabibbo-Kobayashi-Maskawa matrix; gives mixings of quark flavors.

PMNS MATRIX: Pontecorvo-Maki-Nakagawa-Sakagata matrix; gives mixings of neutrino flavors.

GWS THEORY: Glashow-Weinberg-Salam theory; theory unifying the weak and electromagnetic forces.

PREM: Preliminary Reference Earth Model.

SSM: Standard Solar Model.

SK: Super-Kamiokande experiment.

LMA: Large Mixing Angle region of the MSW parameter space.

NCD: Neutral Current Detector.

FEC: Front-End Card in the SNO electronics system.

MTC: Master Trigger Card in the SNO electronics system.

GTID: Global Trigger ID; identification number for each triggered event.

# ACKNOWLEDGMENTS

In the process of obtaining this degree and writing this thesis, I have drawn on guidance, support, instruction, and inspiration from so many people that, without a doubt, this is the hardest part of my dissertation to write.

First and foremost, I have to express my gratitude to the entire Sudbury Neutrino Observatory Collaboration for the opportunity to work with all of you and to contribute to this amazing experiment. I'm in awe at what this collaboration has achieved, from the day-to-day maintenance of the world's cleanest underground laboratory to the production of beautiful physics results. I have learned so much from working on this project.

I am also extremely fortunate to have had Professor John Wilkerson as my advisor. John responded to my graduate student frustrations and insecurities by giving me as much freedom as I needed, yet challenging me with opportunities to prove my mettle. His confidence in me and his willingness to take any idea or concern seriously were essential prerequisites to gaining a sense of confidence in myself as a physicist. It has been a pleasure to witness the growth of John's own Electroweak Interactions Group empire, and I have learned many things from him about the managerial, political, and interpersonal aspects of physics as well as about how to do research.

Thanks are due to Hamish Robertson, for knowing absolutely everything, and for all those last-minute reviews of my talks, abstracts, and articles. And to Scott Oser, who has overseen much of the analysis in this thesis, and taught me a lot (starting with how to handle error matrices). There are many other people in SNO to whom I owe thanks, but I would specifically like to acknowledge Aksel Hallin, for what I have learned from his hands-on approach to analysis, and Kevin Graham, for herculean efforts in the analysis of the salt phase data, as well as for all of his help. Thanks also to the salt phase day-night group, including Neil McCauley, who has answered countless technical questions over the years.

I learned at least as much in the process of proposing, designing, teaching, and reflecting on that course as I have in all of the rest of graduate school, and I am deeply indebted to everyone who made the experience possible. I thank my energetic students, the faculty members who took time out of their schedules to talk with me about my ideas, and the instructors associated with the Huckabay program, who expanded my ideas about teaching and scholarship. I also thank my advisor, for encouraging me to pursue the project even though it meant a hiatus in my research.

I am very grateful for having had the opportunity to work with the incomparable Stamatis Vokos as one of my mentors on the Huckabay project. Stamatis was and will continue to be an inspiration to me, in his generosity, his passion, and his thoughtful approach to learning and teaching. I also thank Derek Storm, my second mentor for the project, for always having the time to review my course materials, to argue with me, to answer my questions about nuclear physics, and to support me in whatever ways I needed. I have fond memories of all of our conversations in the kitchen at the lab, often as everyone else was heading home, and I was still lingering around obsessing about some aspect of the course.

Thanks to the extended family of housemates, former housemates, and friends of 5635 Keystone Place, for throwing great parties and making Seattle feel like home. Likewise, thanks to all of the students and postdocs at CENPA, for "ice cream time" at the lab, movie outings in Sudbury, and lots of laughs around the table in John's office. Thanks to Sean McGee for being a great officemate. And, for keeping me company from afar, thanks to my friend David Gondek.

My parents deserve the deepest gratitude for all of their support and love (and help getting me out of difficult situations in airports). Mostly, I thank them for supporting the choice that I have made to do something that is so demanding. I hope that they know that in spending all of this time with my head tied up in physics, I have not forgotten what I learned from them about life.

Finally, thanks to my husband Gajus, for his friendship, love, support, and all those cups of coffee.

# DEDICATION

*To my parents.*

Chapter 1

## INTRODUCTION

Ubiquitous yet elusive, neutrinos participate in physical processes from the mundane through the exotic. They are produced copiously in ordinary matter, with the typical human body releasing 340 million of them each day.[1] In the history of the universe, they have influenced the physics of the big bang, the formation of structure on the largest scales, and the explosive deaths of stars. Yet once created, neutrinos stream through matter leaving virtually no trace of their passage. Detecting these "ghost particles" and discerning their properties is a formidable endeavor, but one with the potential to tell us a great deal about the cosmos as well as about its smallest constituents.

Wolfgang Pauli invented the idea of the neutrino in 1930. Despite the early successes of quantum mechanics in explaining atomic and nuclear phenomena, the picture of the atom that emerged in the 1920s was problematic. Beta decay seemed to require the presence of electrons along with protons in the nucleus, but this model predicted incorrect spin statistics for some nuclei. Pauli's 1930 proposal was to add a third particle to the nucleus. A neutral spin-1/2 particle could resolve the spin difficulties, and could also settle a vexing problem in the interpretation of beta decay data. Electrons emitted in beta decay were expected to carry away all of the energy released in the decay, but instead they were observed to carry a range of energies up to the total decay energy. The continuous beta decay spectrum was an apparent violation of energy conservation, which could be avoided if a light neutral particle shared the energy released in the decay. Pauli's invented particle was therefore a "desperate way out" that would restore energy conservation in beta decay.

Pauli cautiously suggested his hypothesis in a now-famous letter to his colleagues, who

---

[1]These come from the beta decay of $^{40}$K.

were assembled for a meeting at Tubingen [1][2]. One of his first concerns was reconciling his proposal with observations, which had not yet seen the particle. The new radiation must therefore be more penetrating than any known variety. The "Radioactive Ladies and Gentlemen" to whom Pauli addressed his letter were the world's leading experts on radioactive decay, and Pauli implored them to consider whether there was any hope of detecting the new particle.

In 1934, two years after the discovery of the neutron reshaped the model of the atom, Enrico Fermi formulated a theory of beta decay that became the foundation for our modern theory of the weak interaction [3]. Naming Pauli's invented particle the neutrino, or "little neutral one", Fermi proposed that beta decay occurred when a neutron disintegrated into a proton, electron, and a neutrino (what we now call an electron anti-neutrino):

$$n \longrightarrow p + e^- + \overline{\nu_e} \tag{1.1}$$

Fermi's neutrino was no longer considered a component of the nucleus, as Pauli had originally intended, but was instead spontaneously produced along with the electron. In analogy to Dirac's theory of the electromagnetic interaction, Fermi treated beta decay as an interaction of two currents, carrying a new kind of charge associated with the weak force. His theory also suggested a method for detecting neutrinos, through so-called "inverse" beta decay:

$$\overline{\nu_e} + p \longrightarrow n + e^+. \tag{1.2}$$

Theorists Hans Bethe and Rudolf Peierls were the first to calculate the cross section for inverse beta decay using Fermi's theory [4]. In 1936 they estimated the cross section to be only $10^{-44}$ cm$^2$, implying that a neutrino could travel through light-years of material before being absorbed by a nucleus. Bethe and Peierls concluded from their calculation that the neutrino would be impossible to detect.

Given the tiny cross sections for neutrino interactions, detection of neutrinos from ordinary radioactive sources certainly was impossible. Only with the advent of the atomic bomb program did neutrino detection become realizable, since fission chain reactions provide an extremely intense neutrino source. In 1951, Los Alamos physicist Fred Reines

recognized that neutrinos from atomic explosions might be observable in a large enough detector. Joined by Clyde Cowan, he undertook "Project Poltergeist", which led to the eventual discovery of the neutrino in 1956 [6](and a Nobel Prize for Reines in 1995).

Reines and Cowan's final experiment used a nuclear reactor instead of a bomb as the neutrino source. The experimenters relied on a coincidence measurement – detecting both the positron and the neutron produced in inverse beta decay reactions – to discriminate between neutrinos and background radiation. Correlating their signal to the reactor operating schedule and varying the shielding that blocked other radiation, they were able to make a robust detection of what we now know as the electron anti-neutrino [7].

These early neutrino experiments presaged the development of large-scale particle detectors and pioneered techniques that are in use today. The basic requirements for direct neutrino detection remain the same: an intense source of neutrinos, and a large detector volume. Neutrino interaction "events" in a detector are still typically so rare that extreme care must be taken to mitigate backgrounds and distinguish the neutrino signal. An understanding of current neutrino experiments begins with a recognition of these basic constraints, which continue to make neutrino physics uniquely challenging.

Experimental neutrino physics in the five decades since Project Poltergeist has emphasized two broad sets of questions. The first continues our inquiries into the fundamental properties of neutrinos in the context of particle physics. The second, launched in the early 1960s when John Bahcall and Ray Davis first discussed using neutrinos to "see" into the interior of the sun, concerns the study of distant physics using neutrinos as probes. Neutrinos can carry information from environments that are opaque to other radiation. Experiments that detect neutrinos from extraterrestrial sources can therefore provide insights into astrophysical phenomena as well into the properties of neutrinos themselves.

The Sudbury Neutrino Observatory (SNO) is a large-volume, ultra-low-background neutrino detector designed to study neutrinos from the sun. Since SNO began taking data in 1999, it has made important contributions to our understanding of the fundamental properties of neutrinos as well as to models of solar fusion. The measurements presented in this thesis are part of SNO's ongoing progress in both of these research directions.

Chapter 2

# NEUTRINO PROPERTIES

## 2.1 Experimental Foundations

Early beta decay experiments established that neutrinos must be light neutral fermions whose interactions with matter were almost unimaginably feeble. The Standard Model of particle physics, which solidified in the latter half of the 20th century, gives a much more detailed description of neutrinos and their interactions. Current experimental neutrino physics extends beyond the Standard Model, but continues a long tradition of extremely challenging experiments to uncover neutrino properties.

### 2.1.1 Neutrinos and Antineutrinos

When Project Poltergeist was proposed, it was not known whether the neutrino had a distinct antiparticle. In 1937, theorist Ettore Majorana proposed that the neutrino, lacking any charge, could conceivably be its own antiparticle [8]. A 1955 experiment at the Savannah River nuclear reactor, performed by Ray Davis [9], demonstrated that the type of neutrino emitted in fission fragment decays (what we now call the electron antineutrino) was apparently not capable of initiating the reaction

$$\nu + {}^{37}\mathrm{Cl} \longrightarrow {}^{37}\mathrm{Ar} + e^-. \tag{2.1}$$

Davis's experiment established that neutrinos come in at least two states, although the interpretation of these states as distinct antiparticles remained ambiguous as the nature of the neutrino was further revealed. For practical purposes, we distinguish the neutrino from the antineutrino based on its ability to initiate reactions like Equation 2.1, rather than reactions like Equation 1.2.

### 2.1.2   Parity Violation and the V-A Structure of the Weak Interaction

Muons, pions, and "strange mesons" were discovered and studied in the 1930s and 1940s. The long lifetimes and weak couplings involved in some of the newly observed processes suggested a "Universal Fermi Interaction", governing these interactions as well as beta decay. In the mid-1950s, two essentially identical strange mesons (then called the $\tau$ and $\theta$) were observed to decay with long lifetimes into states of opposite parity. Identifying the $\tau$ and $\theta$ as the same particle would require that the decay processes could violate parity conservation; that is, that the behavior of the initial and final particle states under an inversion of the coordinate system could differ. Until this point, parity invariance had been assumed for all interactions.

Reviewing experimental results in 1956, theorists T.D. Lee and C.N. Yang explored the radical possibility that the interaction responsible for $\tau$ and $\theta$ decays might actually violate parity [10]. After their suggestion, parity violation in the weak interaction was immediately demonstrated in the landmark 1956 experiment by C.S. Wu, E. Ambler, and collaborators, using the angular distribution of beta decay electrons from polarized $^{60}$Co nuclei [11]. Beta decay electrons from the polarized nuclei preferentially emerged in the direction antiparallel to the nuclear spins, demonstrating the "handedness" of the weak interaction. Meson decay experiments soon verified that, indeed, the weak interaction appeared to violate parity maximally (as well as intuition!).

Ensuing beta decay and particle physics experiments uncovered the space-time structure of the universal weak interaction [12]. A "V-A" form, involving a vector minus an axial vector coupling, explained the data and ensured maximal parity violation. In the Lagrangian density describing weak interactions in the Standard Model, this is represented by an interaction term that looks like:

$$\overline{\psi}\gamma^{\mu}(1-\gamma^{5})\psi \tag{2.2}$$

where $\psi$ is a fermion field operator and $\gamma^{\mu}$ and $\gamma^{5}$ are the standard Dirac gamma matrices. The relative sign on the vector and axial vector components changes under an inversion of coordinates, giving the parity violating behavior.

*2.1.3  The Handedness of Neutrinos*

Lee and Yang explained parity violation in weak interactions by postulating that neutrinos only exist in left-handed helicity states [13]. Helicity is defined as the projection of spin along the direction of motion, and a "left-handed" particle has its spin antiparallel to its direction of motion. For any particle going less than the speed of light, the helicity one would observe would depend on the frame of reference. Therefore, the only way to guarantee that neutrinos always have left-handed helicity would be to make them massless.

In the fall of 1957, Maurice Goldhaber, along with Lee Grodzins and Andrew Sunyar, undertook an exceptionally challenging experiment to test the handedness of neutrinos. They looked at an electron capture reaction from a spin-0 state, in which the spin states of the neutrino and the recoiling nucleus would have to "cancel out". They then measured the polarization of the de-excitation gamma from the nucleus, and used this to infer the helicity of the neutrino. The results definitively showed that neutrinos are left handed [14].

To relate the handedness of the neutrino to the V-A structure of the weak interaction, note that helicity states are eigenstates of the $\gamma^5$ operator for massless particles. Right-handed states have eigenvalue $+1$, so the term $1 - \gamma^5$ vanishes for massless particles with right-handed helicity. In other words, the V-A structure of the weak interaction means it only operates on left-handed states.

Generalizing to the case of massive particles, the states that participate in the weak interaction don't have a straightforward interpretation as left-handed *helicity* states, because the helicity of a massive particle depends on the frame of reference. Nevertheless, a "chirality" or "handedness" can still be specified for massive particles, depending on the behavior of the particle under the $\gamma^5$ operator. We define the chiral particle states $\psi_L$ and $\psi_R$ using the "chirality projection operators":

$$P_L = \frac{1 - \gamma^5}{2}, \qquad P_L\psi_L = \psi_L, \ P_L\psi_R = 0;$$
$$P_R = \frac{1 + \gamma^5}{2}, \qquad P_R\psi_R = \psi_R, \ P_R\psi_L = 0. \tag{2.3}$$

If the particle represented by $\psi$ is massless, then the states $\psi_L$ and $\psi_R$ as defined in Equation 2.3 will be states of definite left or right helicity. If the particle is massive, they will be states

that have the specified helicity when viewed in a frame in which the particle is relativistic. Using the above definitions, the weak interaction term in the Lagrangian (Equation 2.2) can be written $\overline{\psi}_L \gamma^\mu \psi_L$. In other words, the weak interaction only acts on particles with left-handed chirality (or on antiparticles with right-handed chirality).

### 2.1.4  Neutral Currents

As early as the 1940's, weak interactions were explained in terms of the exchange of an intermediate vector boson, the $W$. The $W$ must be very heavy to explain the short range of the weak interaction, and it must exist in two charge states ($W^+$ and $W^-$) to explain the charged weak currents. Theoretical and experimental explorations of speculative *neutral* weak currents in the 1960s encountered a number of stumbling blocks [15]. However, the notion of weak neutral currents gained fortitude in 1971, when G. t' Hooft proved that the Glashow-Weinberg-Salam (GWS) theory of electroweak interactions was renormalizable.

The GWS theory explained both the electromagnetic and weak interactions through an underlying local gauge symmetry with an SU(2)xU(1) group structure. The symmetry is spontaneously broken, explaining the large masses of the weak gauge bosons and leading to fermion masses through the Higgs mechanism. The theory predicted the existence of a neutral heavy gauge boson, the $Z^0$, in addition to the charged $W^\pm$ bosons and the photon. Once renormalizability was demonstrated, the GWS theory became a viable description of electroweak physics with testable predictions, including the existence of weak neutral currents.

Neutral currents were first discovered in the Gargamelle bubble chamber at CERN in 1973, through the reaction:

$$\overline{\nu_\mu} + e^- \longrightarrow \overline{\nu_\mu} + e^-, \tag{2.4}$$

with evidence also coming from neutrino-nucleon scattering reactions [16] [17] . Later, in 1983, the $W$ and $Z^0$ were both produced at CERN, and their masses were found to match those predicted by the GWS theory [20] [21] [22] [23]. These discoveries were fantastic confirmations of the GWS electroweak theory, which was incorporated into the Standard Model. Representative neutrino interaction vertices involving the $Z$ and the $W$ are shown

in Figure 2.1.
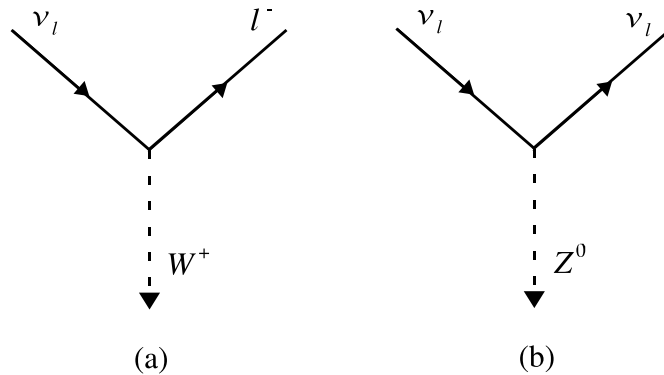


Figure 2.1: Examples of vertices for charged (a) and neutral (b) weak currents. $l^-$ represents a charged lepton $e, \mu$, or $\tau$ and $\nu_l$ represents the corresponding neutrino.

### 2.1.5   The Number of Neutrinos

Early studies of muon decay suggested that a separate kind of neutrino might be associated with muons, distinct from the neutrino associated with beta decays. In 1961, Melvin Schwartz, Jack Steinberger, and Leon Lederman performed an experiment at Brookhaven that proved that the neutrinos associated with muon production in meson decays were incapable of initiating reactions that produce electrons [24]. In 1975 Martin Perl and his collaborators announced evidence for the tau lepton in $e^+ - e^-$ collisions at the SPEAR collider, rounding out the three known types of charged lepton [25]. Although an associated tau neutrino was also built into the Standard Model, it was not actually observed until the year 2000, when it was detected by the DONUT collaboration at Fermi National Accelerator Laboratory [26].

In the 1980s, there had already been limits on the total number of distinct neutrino flavors, derived from increasingly precise measurements of light element abundances in the universe [27]. Primordial nucleosynthesis depends on the neutron to proton ratio when the weak interaction "freezes out", which in turn depends on the number of light neutrino species. Measurements of light element abundances are consistent with the conventional

three flavors, and limit the number of light neutrino species ($m_\nu < 1\text{MeV}$) to be less than four [28].

Stronger constraints on the number of "active" neutrino species (those that participate in standard model interactions) come from measurements of the $Z^0$ boson decay width, which became possible at SLAC and at CERN toward the end of the 1980s. $Z^0$ particles produced in colliders can decay into neutrino-antineutrino pairs, and a measurement of the partial decay width for such "invisible" modes gives a limit on the number of possible neutrino types (with masses up to half the mass of the $Z^0$). The best measurements were done at the LEP $e^+ - e^-$ collider at CERN, and a recent analysis [29] gives

$$N_\nu = 2.9841 \pm 0.0083 \qquad (2.5)$$

for the number of active neutrino species $N_\nu$.

## 2.2  Neutrinos in the Standard Model

In the Standard Model, all of these properties of the neutrino are included, and can be relatively simply represented. The standard model combines the spontaneously broken SU(2)xU(1) symmetry of electroweak theory with the color SU(3) of QCD, but for the purposes of neutrino physics we can continue to neglect the latter. The particle content of the theory can be summarized below,

$$\begin{pmatrix} u' \\ d' \end{pmatrix}_L \begin{pmatrix} c' \\ s' \end{pmatrix}_L \begin{pmatrix} t' \\ b' \end{pmatrix}_L , \qquad u'_R, d'_R, c'_R, s'_R, t'_R, b'_R$$

$$\begin{pmatrix} \nu_e \\ e \end{pmatrix}_L \begin{pmatrix} \nu_\mu \\ \mu \end{pmatrix}_L \begin{pmatrix} \nu_\tau \\ \tau \end{pmatrix}_L , \qquad e_R, \mu_R, \tau_R. \qquad (2.6)$$

The left-handed quark and lepton states come in "isodoublets", with $W^\pm$-exchange connecting the upper and lower components in vertices similar to the one shown in Figure 2.1(a). The right-handed particle states are "singlets" and experience no weak interactions. The particles are characterized by two quantum numbers, the weak isospin and the weak hypercharge. Particle interactions are described in the electroweak portion of the full standard

model Lagrangian [30]:

$$
\begin{aligned}
\mathcal{L} = {} & \sum_i \overline{\psi_i}\left(i\slashed{\partial} - m_i - \frac{gm_iH}{2M_W}\right)\psi_i \\
& - \frac{g}{2\sqrt{2}}\sum_i \overline{\psi_i}\gamma^\mu(1-\gamma^5)(T^+W_\mu^+ + T^-W_\mu^-)\psi_i \\
& - e\sum_i q_i\overline{\psi_i}\gamma^\mu\psi_i A_\mu \\
& - \frac{g}{2\cos\theta_W}\sum_i \overline{\psi_i}\gamma^\mu(c_V^i - c_A^i\gamma^5)\psi_i Z_\mu.
\end{aligned} \tag{2.7}
$$

In this expression, $\psi$ represents the fermion fields, and the $T^\pm$ operators are the weak isospin raising and lowering operators, which select the upper or lower partner in a weak isospin doublet. The first term in the Lagrangian includes the masses and the couplings to the Higgs. The second term gives the charged current couplings to the $W^\pm$, where the $1-\gamma^5$ form selects only the left-handed states. The third term describes electromagnetic interactions, and the final term describes couplings to the $Z^0$ boson. The vector and axial vector coupling constants $c_v$ and $c_a$ are related to the electromagnetic and weak charges of the particles and the value of the "weak mixing angle" $\theta_W$, which is a fundamental parameter of the electroweak theory. For neutrinos, $c_a$ and $c_v$ are both 1.

As we can see from Equation 2.7, the "mass term" in the Lagrangian is of the form

$$
\mathcal{L}_{\text{mass}} = -m\overline{\psi}\psi \tag{2.8}
$$

Using Equation 2.3, we can write the fermion field $\psi$ as a sum of left- and right-handed components: $\psi = \psi_L + \psi_R$. Then,

$$
\mathcal{L}_{\text{mass}} = m(\overline{\psi_L} + \overline{\psi_R})(\psi_L + \psi_R) = m(\overline{\psi_L}\psi_R + \overline{\psi_R}\psi_L) \tag{2.9}
$$

In the Standard Model, a right handed neutrino does not exist, so this mass term is automatically zero.

## 2.3   Evidence for Neutrino Mass

In the quark sector of the Standard Model, the quark states that participate in the weak interaction are not the same as the quark states that participate in the strong interaction.

This "mixing" suggests an analogous possibility for neutrinos. However, neutrino mixing requires neutrino mass – otherwise, the weak interaction eigenstates are sufficient to describe all neutrino behavior. If neutrinos have mass, mixing could lead to observable effects through the phenomenon of oscillations.

Consider a simple case involving just two neutrino states. We can relate the states of definite mass to the "flavor" states through a unitary rotation matrix,

$$\begin{pmatrix} \nu_\alpha \\ \nu_\beta \end{pmatrix} = \begin{pmatrix} \cos\theta & \sin\theta \\ -\sin\theta & \cos\theta \end{pmatrix} \begin{pmatrix} \nu_1 \\ \nu_2 \end{pmatrix} \tag{2.10}$$

where $\nu_\alpha$ and $\nu_\beta$ are weak interaction eigenstates (states of definite flavor), and $\nu_1$ and $\nu_2$ are states of definite mass with masses $m_1$ and $m_2$. The matrix is parameterized by the mixing angle $\theta$.

Suppose a neutrino is created in state $\nu_\alpha$. Over time, the neutrino will propagate according to[1]

$$|\nu_\alpha(t)\rangle = e^{-iE_1 t}\sin\theta\, |\nu_1\rangle + e^{-iE_2 t}\cos\theta\, |\nu_2\rangle . \tag{2.11}$$

If the neutrino is absorbed in a detector after a time $t$, there will be some probability that it will be detected as a neutrino of flavor $\beta$, given by

$$P(\nu_\alpha \longrightarrow \nu_\beta) = |\langle\nu_\beta|\nu_\alpha(t)\rangle|^2 = \sin^2 2\theta \sin^2(1.27\Delta m^2{}_{21}\frac{L}{E}), \tag{2.12}$$

where $\Delta m^2{}_{21} = m_2^2 - m_1^2$, $L$ is the distance traveled in meters, $E$ is the neutrino energy in GeV, and the constant 1.27 accounts for factors of $\hbar$ and $c$. The flavor of the neutrino state effectively "oscillates" as it propagates, with an amplitude determined by the mixing angle $\theta$ and a frequency determined by the ratio of the mass splitting $\Delta m^2$ to the neutrino energy (assuming a fixed $L$).

Sources of neutrinos that can be studied for oscillations include the sun (from solar fusion), the atmosphere (from the interactions of cosmic rays), nuclear reactors, and accelerators. Experiments studying these neutrinos will have sensitivities to different values of the fundamental physical parameters, $\Delta m^2$ and $\sin^2 2\theta$, with longer baselines allowing

---

[1]This derivation assumes that the neutrinos are produced in a state of definite momentum. Using stationary states instead leads to the same result.

Table 2.1: Some typical energies and propagation distances for neutrinos from several sources, with the mass splittings that can be reached by studying each source.

| Neutrinos | L(m) | E(GeV) | $\Delta m^2$ sensitivity (eV$^2$) |
|---|---|---|---|
| Accelerator | $10^3$ | 1 | 1 |
| Reactor | $10^2$ | 0.001 | $10^{-2}$ |
| Atmosphere | $10^7$ | 10 | $10^{-3}$ |
| Solar | $10^{11}$ | 0.001 | $10^{-11}$ |

sensitivity to smaller mass splittings. The typical ranges of mass splittings that experiments can explore are given in Table 2.1. In most cases, a simple two neutrino description such as that given here is a reasonable approximation to the physics involved.

If a source is known to produce neutrinos of a given flavor, then a detector placed some distance away may observe a deficit of the original flavor of neutrinos, and this may be interpreted as evidence for oscillations. Such a "disappearance" measurement may be strengthened if it is possible to analyze the neutrino interactions as a function of $L$, $E$, or $L/E$, in order to reveal the oscillatory behavior indicated by Equation 2.10. "Appearance" measurements can also search for the presence of neutrinos with flavor different from that produced by the source. A strong case for neutrino oscillations can be made if an experiment has sensitivity to multiple flavors, so that neutrino flavor change can be demonstrated conclusively.

The first hints of neutrino oscillations came in 1968 when Ray Davis announced detection of electron neutrinos from the sun [31], using a detector technique similar to the one described in Section 2.1.1. The total flux that he measured was around a third of the flux that was theoretically predicted. Decades of improving solar theory and making independent measurements did not eliminate the discrepancy, which came to be known as the "Solar Neutrino Problem". In the early 1980s, the IMB and Kamiokande experiments observed a similar "atmospheric neutrino anomaly": the ratio of observed atmospheric muon neutrinos to electron neutrinos was smaller than expected. The missing solar and atmospheric neutri-

nos could both be explained if the neutrinos were oscillating into other flavors and thereby evading detection.

In 1998, the Super-Kamiokande experiment released an analysis of atmospheric neutrinos that demonstrated the dependence of the muon neutrino rate on the distance the neutrinos traveled, giving clear evidence that oscillation was in fact responsible for the atmospheric anomaly [32]. Recent data from the K2K accelerator neutrino experiment has added to the case for the oscillations observed by Super-Kamiokande, which are well explained by $\nu_\mu \longrightarrow \nu_\tau$ with a "maximal" mixing angle ($\theta_{atm} \approx 45°$) and a mass splitting $\Delta m^2{}_{atm} \approx 10^{-3}\text{eV}^2$ [33].

In 2001 and 2002, the Sudbury Neutrino Observatory conclusively solved the solar neutrino problem with an appearance measurement [34] [35]. Using reactions of neutrinos on heavy water, SNO measured the total flux of all flavors of solar neutrino as well as the flux of electron neutrinos. Only a third of the solar neutrinos detected at SNO were electron neutrinos, with the remaining two thirds arriving as other flavors. Interpretation of solar neutrino flavor change as oscillations was strengthened in 2003 and 2004, when evidence for reactor antineutrino oscillation was released by the KamLAND experiment [36] [37]. Assuming CPT invariance (so that we can relate the results for solar electron neutrinos to those for reactor anti-electron neutrinos), both experiments can be well described by oscillations with a mass splitting of around $\Delta m^2 \approx 8 \times 10^{-5}$ and a mixing angle of 34° [38].

The results of atmospheric, solar, reactor, and accelerator neutrino experiments can be consistently interpreted in a model with three massive neutrinos, characterized by the mass splitting seen in the solar and KamLAND experiments (looking at oscillations between the electron and mu families) and that seen in the atmospheric and K2K experiments (looking at oscillations between the mu and tau families). With only three massive neutrino states, two mass splittings characterize the mass spectrum (up to an overall scale). However, in the late 1990s the LSND accelerator neutrino experiment at Los Alamos reported detection of oscillations in an appearance measurement, $\overline{\nu_\mu} \longrightarrow \overline{\nu_e}$, with an implied mass splitting $\Delta m^2{}_{LSND} > 0.2$ eV [39]. One way to accommodate the LSND signal is to introduce a

fourth neutrino.[2] This fourth neutrino must be "sterile" (non-interacting) with respect to Standard Model interactions, in order to agree with limits on the number of neutrino species. The LSND result is unconfirmed, and will be checked in the near future by the MiniBooNE experiment at Fermilab [42].

On the basis of oscillation experiments, we now know that neutrinos have mass, and do indeed mix. Even though the idea of neutrino mixing arises naturally out of the analogy to quarks, experimental tests of neutrino oscillation have led to surprises. In addition to hinting at sterile neutrinos, experiments have shown that the mixing angles involved in solar and atmospheric oscillations are very large, in contrast to the small mixings in the quark mixing matrix. The consequences of neutrino mass and the implications for physics beyond the Standard Model are far from being understood.

### 2.3.1   Adding Neutrino Mass to the Standard Model

The mass term described in Equation 2.9 is called a Dirac mass. To introduce neutrino mass to the model, we might simply include a right handed neutrino state $\nu_R$, in order to construct a Dirac mass term. $\nu_R$, like $\nu_L$, carries no hypercharge. But unlike $\nu_L$ it is an isospin singlet, so it truly carries no Standard Model charges. There is therefore nothing in the Standard Model that prevents the occurrence of an additional "Majorana" mass term $m(\overline{\nu_R}^c\nu_R + \overline{\nu_R}\nu_R^c)$.[3]. Such a mass term couples a right handed particle to its conjugate under the particle-antiparticle conjugation operator $C$, rather than coupling the left and right handed components. The Majorana mass term changes the charges of a particle by two units, so it is forbidden for the rest of the fundamental fermions.

In the Majorana formalism, separate mass terms for the left and right particle states can be defined as described above. The notation for including these in the Lagrangian simplifies if we define particle states $\chi_L = \nu_L + \nu_L^c$ and $\chi_R = \nu_R + \nu_R^c$. The states $\chi_L$ and $\chi_R$ are self-conjugate, meaning $\chi_L^c = \chi_L$ and $\chi_R^c = \chi_R$. In terms of these states, the Majorana

---

[2]Alternative methods of accommodating the LSND results include recent work on "mass-varying neutrinos", see [40] and [41].

[3]This argument is based on arguments by Boris Kayser. See, for example, [43].

mass terms for the left and right handed states can be written,

$$
\begin{aligned}
m_L \overline{\chi_L} \chi_L &= m_L(\overline{\nu_L}\nu_L^c + \overline{\nu_L}^c \nu_L) \\
m_R \overline{\chi_R} \chi_R &= m_R(\overline{\nu_R}\nu_R^c + \overline{\nu_R}^c \nu_R).
\end{aligned}
\tag{2.13}
$$

The masses associated with these mass terms are given by $m_L$ and $m_R$. The most general case of Dirac plus Majorana mass terms for the neutrino can then be written in terms of $\chi_R$ and $\chi_L$, as

$$
\begin{aligned}
-\mathcal{L}_{\text{mass}} &= m_D(\overline{\chi_R}\chi_L + \overline{\chi_L}\chi_R) + m_L \overline{\chi_L}\chi_L + m_R \overline{\chi_R}\chi_R \\
&= \begin{pmatrix} \overline{\chi_L}, & \overline{\chi_R} \end{pmatrix} \begin{pmatrix} m_L & m_D \\ m_D & m_R \end{pmatrix} \begin{pmatrix} \chi_L \\ \chi_R \end{pmatrix}
\end{aligned}
\tag{2.14}
$$

Suppose that $m_L = 0$ and $m_R \gg m_D$. Then

$$
\begin{aligned}
-\mathcal{L} &= m_D(\overline{\chi_R}\chi_L + \overline{\chi_L}\chi_R) + m_R \overline{\chi_R}\chi_R \\
&= m_1 \overline{\chi_1}\chi_1 + m_2 \overline{\chi_2}\chi_2,
\end{aligned}
\tag{2.15}
$$

where

$$
\begin{aligned}
m_1 &\simeq -m_D \frac{m_D}{m_R} \approx 0 \\
m_2 &\simeq m_R,
\end{aligned}
\tag{2.16}
$$

and

$$
\begin{aligned}
\chi_1 &= \chi_L - \frac{m_D}{m_R}\chi_R \\
\chi_2 &= \chi_R + \frac{m_D}{m_R}\chi_L.
\end{aligned}
\tag{2.17}
$$

This is the so-called "See-saw mechanism" for generating light neutrino masses [44]. In the most general case where Dirac and Majorana mass terms are included, there are two mass eigenstates for each neutrino flavor, which behave as Majorana particles. In the special case of the See-saw mechanism, there is one light state which is primarily left-handed, and one heavy state that is primarily right handed. The see-saw mechanism provides a natural explanation for extremely light neutrino masses, which are otherwise glaringly incongruous in light of the other fermion masses.

### 2.3.2 Neutrino Oscillations in the General Case

Extending the simple two-flavor oscillation derivation from Section 2.3 to the more general case reveals some important features of neutrino oscillation physics.[4] In the mass eigenstate basis, the standard model interaction describing the coupling of neutrinos to the $W$ boson is

$$-\mathcal{L}_W = \frac{-g}{\sqrt{2}} \sum_{\substack{\alpha=e,\mu,\tau \\ i=1,2,3}} \overline{l_{L\alpha}} \gamma^\mu (V_L^\dagger U_L)_{\alpha i} \nu_{Li} W_\mu^- + \text{h.c.} \tag{2.18}$$

where $l_{L\alpha}$ represents the charged lepton field (in the mass eigenstate basis), $\nu_{Li}$ represents a neutrino mass eigenstate, and we are assuming three neutrino states. The matrices $V_L$ and $U_L$ (and their right-handed counterparts) diagonalize the mass matrices for the charged leptons and neutrinos, respectively.

$$V_L^\dagger m_l V_R = (m_l)_{\text{diag}} \quad U_L^\dagger m_D U_R = (m_D)_{\text{diag}}, \tag{2.19}$$

where $m_l$ is the mass matrix for the charged leptons, and $m_D$ is the mass matrix for the neutrinos, assuming the Dirac case for the moment.

The matrix $U = V_L^\dagger U_L$ is the leptonic analogue of the CKM matrix, and is often called the PMNS matrix for the work of Pontecorvo [48] [49], and Maki, Nakagawa, and Sakata [50]. A charged current reaction producing a charged lepton $l_\alpha^+$ of definite mass and flavor $\alpha$ will produce a neutrino that is a superposition of the neutrino mass states $\nu_j$, given in terms of the matrix $U$ as:

$$|\nu_\alpha\rangle = \sum_j U_{\alpha j}^* |\nu_j\rangle . \tag{2.20}$$

If a neutrino is produced at time $t = 0$ in a state $|\nu(0)\rangle = |\nu_\alpha\rangle = \sum_j U_{\alpha j}^* |\nu_j\rangle$, then as it evolves over time, each mass eigenstate component will pick up a phase, $|\nu_\alpha(t)\rangle = \sum_j U_{\alpha j}^* e^{-iE_j t} |\nu_j\rangle$. The oscillation probability is given by

$$
\begin{aligned}
P(\nu_\alpha \to \nu_\beta) &= |\langle \nu_\beta | \nu(t) \rangle|^2 \\
&= |\sum_j U_{\beta j} U_{\alpha j}^* e^{iE_j t}|^2 \\
&= \delta_{\alpha\beta} - 4 \sum_{i>j} Re(U_{\alpha i}^* U_{\beta i} U_{\alpha j} U_{\beta j}^*) \sin^2 \left( \Delta m^2{}_{ij} \frac{L}{4E} \right)
\end{aligned}
$$

---

[4]The discussion in the next few sections draws on material from [45], [46], and [47]

$$+2\sum_{i>j} Im(U_{\alpha i}^* U_{\beta i} U_{\alpha j} U_{\beta j}^*)\sin\left(\Delta m^2{}_{ij}\frac{L}{2E}\right), \tag{2.21}$$

where we have used the fact that neutrinos are very relativistic, $E_i = \sqrt{p^2 + m_i^2} \simeq p + m_i^2/2p$, and the fact that U is unitary, $\sum_i U_{\alpha i}^* U_{\beta i} = \delta_{\alpha\beta}$. As in the two-neutrino derivation, $\Delta m^2{}_{ij} = m_i^2 - m_j^2$, and we have used $E \approx p$ and $t \approx L$. This formula can be used to describe neutrino oscillations in the more general, three-neutrino case.

Let's take a look at the matrix $U$ in more detail. In the $3\times3$, Dirac neutrino case, we can express the leptonic mixing matrix as a product of three rotations, $U_{PMNS} = U_{23}U_{13}U_{12}$, or

$$U_{PMNS} = \begin{pmatrix} 1 & 0 & 0 \\ 0 & c_{23} & s_{23} \\ 0 & -s_{23} & c_{23} \end{pmatrix} \times \begin{pmatrix} c_{13} & 0 & s_{13}e^{-i\delta} \\ 0 & 1 & 0 \\ -s_{13}e^{i\delta} & 0 & c_{13} \end{pmatrix} \times \begin{pmatrix} c_{12} & s_{12} & 0 \\ -s_{12} & c_{12} & 0 \\ 0 & 0 & 1 \end{pmatrix}. \tag{2.22}$$

Here, $c_{12} = \cos\theta_{12}$ and $s_{12} = \sin\theta_{12}$, etc. The mixing angles $\theta_{12}$ and $\theta_{23}$ correspond approximately to the effective two-neutrino mixing angles governing solar and atmospheric neutrino oscillations. The third mixing angle, $\theta_{13}$, has not been measured directly but is constrained to be considerably smaller than the other two.

In the Dirac neutrino case, the matrix $U_{PMNS}$ exhibits a single complex phase $\delta$. If $\delta \neq 0$, then the imaginary term in Equation 2.21 can lead to CP-violating effects in neutrino oscillations. In general, a unitary complex $3 \times 3$ matrix will have four independent phases. However, three of these can be absorbed into the definitions of the charged lepton states without affecting any terms in the Lagrangian. The existence of a remaining "essential" phase $\delta$ requires three non-zero mixing angles. If one of the mixing angles is zero, then all complex phases can be absorbed into the definitions of the states, and no CP violation is observable. For this reason, the parameterization in Equation 2.22 is chosen such that the phase term is associated with the smallest mixing angle, $\theta_{13}$. The potential for observing CP-violation in neutrino oscillations depends on just how small $\theta_{13}$ turns out to be.

*Other Cases*

Equation 2.21 was explicitly derived for the case of three Dirac neutrinos. In the Majorana case, the diagonalization of the neutrino mass matrix (previously given by Equation 2.19),

will now look like $U_L^T m_M U_L = (m_M)_{\text{diag}}$. Assuming that there are three Majorana neutrinos, the charged current interaction Lagrangian will have exactly the same structure, and the oscillation derivation will proceed in the same way. Taking a closer look at the mixing matrix $U_{PMNS}$, however, we note that it is no longer possible to absorb the extra complex phases into the definitions of the neutrino states, if the mass terms are to remain real. So to describe neutrino mixing in the Majorana case, the matrix $U_{PMNS}$ retains an extra set of "Majorana phases",

$$U_{PMNS}(\text{Majorana}) = U_{PMNS}(\text{Dirac}) \times \begin{pmatrix} 1 & 0 & 0 \\ 0 & e^{-i\alpha_1/2} & 0 \\ 0 & 0 & e^{-i\alpha_2/2} \end{pmatrix} \quad (2.23)$$

Inspection of 2.21 indicates that phases appearing on the diagonal will not affect neutrino oscillations. Oscillation experiments cannot discriminate between Majorana and Dirac neutrinos.

In the most general, Dirac + Majorana case, we arrived at $2N$ massive Majorana neutrinos for $N$ generations. In this case (or for the general case in which there are additional, "sterile" neutrinos), the size of the neutrino mass matrix will be $N_\nu \times N_\nu$ where $N_\nu$ is the total number of neutrino states of definite mass ($2N$ in the Dirac + Majorana case). The matrix $U$ will then have $N_\nu$ columns. If there are more than three neutrino states of definite mass, oscillations into sterile neutrinos can occur. Depending on the strength of the mixing and the masses of the sterile states, these oscillations may be observable.

### 2.3.3   Special Case: Solar Neutrinos

For three-neutrino oscillations, a particularly relevant special case occurs when

$$|\Delta m^2{}_{21}| << |\Delta m^2{}_{31}| \approx |\Delta m^2{}_{32}| \quad (2.24)$$

and

$$\Delta m^2{}_{31} \frac{L}{2E} \approx \Delta m^2{}_{32} \frac{L}{2E} >> 1. \quad (2.25)$$

The first condition is motivated by the relative sizes of the solar and atmospheric mass splittings. The second condition is specifically appropriate for describing solar neutrino

oscillations. It implies that the oscillations due to the mass squared differences $\Delta m^2_{31}$ and $\Delta m^2_{32}$ will be very fast and "average out", making these mass splittings irrelevant for describing solar neutrino oscillations. In this case, we can derive from 2.21 the expression for the electron neutrino survival probability:

$$P(\nu_e \longrightarrow \nu_e) \approx \cos^4\theta_{13}P_{2\nu} + \sin^4\theta_{13}, \tag{2.26}$$

where $P_{2\nu}$ is the expression derived for the survival probability using the two-neutrino formalism (using $\Delta m^2_{12}$ and $\theta_{12}$)), as in Section 2.3. Oscillation measurements directly sensitive to $\theta_{13}$ have only set upper bounds on this parameter, but from those bounds it is known to be small enough that neglecting it is a reasonable approximation for the solar neutrino case [51]. For $\theta_{13} = 0$, Equation 2.26 reduces to the two-neutrino formula, Equation 2.12. Alternatively, experimental results from solar neutrino oscillations can be added to other experimental results to derive tighter constraints on $\theta_{13}$, using the dependence on $\theta_{13}$ in the full three-neutrino formalism. Global fits give roughly $\sin^2\theta_{13} < 0.05$.[5]

### 2.4   The New Experimental Questions

Decades of experimental work established the properties of the Standard Model neutrino. Now that we know that neutrinos have mass, exploration of neutrino properties takes us outside the realm of the Standard Model, and decades of future research will undoubtedly be required before the properties of the *massive* neutrino are well understood. Several of the major questions for current and future neutrino research are:

- *Is the neutrino its own antiparticle?* The only currently feasible technique for answering this question involves searching for neutrinoless double beta decay ($0\nu\beta\beta$-decay) in which a nucleus undergoes a transition N(A,Z)$\longrightarrow$N(A,Z+2) + $e^-$ + $e^-$. Lepton number is clearly violated in this process, which can be envisioned as an ordinary beta decay in which the antineutrino is then immediately reabsorbed *as a neutrino* to initiate the second beta emission. $0\nu\beta\beta$-decay is only possible if neutrinos are massive Majorana particles. The signature would be a line in the summed energy spectrum

---

[5]See, for example, [52], [53], [54], and [55].

for the two electrons, since none of the energy in the decay is carried off by neutrinos. If neutrinoless double beta decay exists, it is very very rare – not only is it a second order weak process, but the process is helicity suppressed as well, since the intermediate neutrino is emitted in a right-handed state but must be left-handed when it is absorbed. Sensitive experiments to search for this process are underway [56], and a controversial claim exists that it has already been discovered [57].

- *What is the neutrino mass spectrum?* In the three-neutrino scenario, the mass splittings are determined by the results of solar, atmospheric, and reactor experiments. Solar and reactor experiments give $\Delta m^2_{\text{SUN}} = \Delta m^2_{21} \approx 8.0 \times 10^{-5}$ eV$^2$. The mass splitting in the atmospheric case is considerably larger, with $\Delta m^2_{\text{ATM}} = |\Delta m^2_{31}| \approx |\Delta m^2_{32}| \approx 2.4 \times 10^{-3}$ eV$^2$. The sign of the larger mass splitting is not known.[6] Depending on the sign of the atmospheric mass splitting, the hierarchy of neutrino masses $m_1, m_2, m_3$ may be "normal" (with $m_1$ being the lightest), or "inverted" (with $m_3$ being the lightest).

The second open question related to the neutrino mass spectrum is the absolute mass scale, since oscillation experiments only provide mass differences. We do not know, for example, whether neutrino masses are relatively large compared to the atmospheric mass splitting (the "quasi-degenerate" case), or if the lightest neutrino has a mass much smaller than the atmospheric mass splitting (the "non-degenerate" case). A variety of experimental techniques can address the question of the absolute neutrino mass scale. Sensitive tests of kinematics in beta decay provide the best direct limits, giving $m_\beta < 2.2$ eV (at 95% C.L.) [58]. Next-generation experiments should improve that limit by an order of magnitude [59]. Because of neutrino mixing, beta decay is sensitive to an effective neutrino mass defined by

$$m_\beta = (c_{12}^2 c_{13}^2 m_1^2 + c_{13}^2 s_{12}^2 m_2^2 + s_{13}^2 m_3^2)^{1/2}. \tag{2.27}$$

If neutrinos are Majorana particles, then neutrinoless double beta decay may also

---

[6]The presence of matter effects in solar neutrino oscillations, which will be described in the next chapter, determines the sign of the mass splitting in the solar case.

reveal the absolute mass scale. The probability of neutrinoless double beta decay depends on neutrino mass, which determines the mixing of helicity states characterizing the intermediate neutrino. A measurement of or limit on the $0\nu\beta\beta$-decay lifetime can be translated into a statement about neutrino mass, but the translation also depends on calculations of the nuclear matrix elements, which are currently rather uncertain. The effective neutrino mass tested in $0\nu\beta\beta$-decay is

$$m_{\beta\beta} = \sum_k U_{ek} m_k = c_{12}^2 c_{13}^2 m_1 + s_{12}^2 c_{13}^2 e^{i\alpha_1} m_2 + s_{13}^2 e^{i\alpha_2} m_3. \qquad (2.28)$$

The current best limit is $m_{\beta\beta} < 0.32-1.0$eV at 90% confidence level, where the range of possible upper limits reflects the uncertainties in nuclear matrix elements [60] [61] [62]. The claimed detection of $0\nu\beta\beta$-decay implies a neutrino mass between 0.2 and 0.6 eV at 99.73% confidence level [63]. Future experiments expect to reach sensitivities below $10^{-2}$ eV [56].

Although there are other ways of measuring or limiting neutrino mass, a third technique that is potentially very sensitive uses indirect evidence from cosmology and large scale structure. Light neutrinos tend to erase structure on small scales in the early universe by streaming away from dense regions. Measurements of density fluctuations in cosmic microwave background can be combined with large scale structure data to place constraints on the overall sum of neutrino masses. Cosmological neutrino mass limits vary depending on which sets of data are used, and range from around $\sum_k m_k < 0.5eV$ to $\sum_k m_k < 1eV$ [61]. These limits may not yet be robust, but they are a valuable complement to direct methods.

- *Do neutrinos violate CP?* CP violation in neutrino oscillations is impossible in the limit that $\theta_{13}$ is zero. Hence, the first step towards tests of CP symmetry is to determine the size of this parameter. Future reactor and long-baseline experiments will address the size of $\theta_{13}$, but current best limits on this parameter use inputs from all oscillation experiments in a global three-neutrino analysis. If $\theta_{13}$ is not zero, then tests of CP violation may be possible using accelerator neutrino and antineutrino

beams [64]. A non-zero CP-violating phase $\delta$ in the mixing matrix could mean that $P(\overline{\nu_\alpha} \to \overline{\nu_\beta}; t) \neq P(\nu_\alpha \to \nu_\beta; t)$, as can be seen from Equation 2.21.

- *Are there sterile neutrinos?* The LSND result, in combination with other oscillation results, suggests the existence of at least one relatively light sterile neutrino. Many theories that reach beyond the standard model include such additional neutrino states. Testing for sterile neutrinos can be done with increasingly precise measurements of neutrino oscillations. The MiniBooNE experiment will directly test the LSND claim, but experiments like SNO also have an impact in limiting sterile neutrino models. For example, SNO's measurements of the active neutrino flux from the sun can be combined with solar luminosity constraints or predictions from solar models to limit oscillations into sterile neutrino states. Precision tests of neutrino oscillation in the future should limit or measure subdominant contributions from sterile neutrino oscillations or other exotic physics [65].

The measurements described in this thesis concern oscillations of solar neutrinos detected at SNO. Oscillation measurements cannot distinguish whether neutrinos are Dirac or Majorana particles, but they are essential as part of the process of unraveling the rest of the neutrino mysteries listed above. Most importantly, neutrino measurements at SNO contribute to measurements of the fundamental neutrino mass and mixing parameters. From Equation 2.26, we can see that solar neutrino oscillation measurements are primarily sensitive to $\Delta m_{12}^2$ and $\theta_{12}$, and can contribute to global constraints on $\theta_{13}$.

Chapter 3

# SOLAR NEUTRINOS AND THE DAY-NIGHT EFFECT

## 3.1 Astrophysical Neutrinos

The same property that makes neutrinos so challenging to detect – that their interactions with matter are so weak – also makes neutrinos informative messengers from distant environments. Photons and charged particles from astrophysical sources typically undergo absorption, scattering, and deflection before they reach terrestrial detectors. Neutrinos, on the other hand, can stream through dense stellar interiors, interstellar dust clouds, regions with high magnetic fields, and finally the earth itself, without suffering deflection or absorption.

In the early 1960s, Ray Davis and John Bahcall recognized the potential for using neutrinos to test the hypothesis of solar fusion. Theorist Hans Bethe had previously detailed several mechanisms for solar energy generation through fusion reaction chains [66]. But because photons in the sun have a mean free path of less than a centimeter, standard optical techniques were useless for testing physics in the solar core. In 1968, Davis announced the first detection of neutrinos from the sun, launching an era of experimental tests of solar theory, and earning him a Nobel Prize in 2002.

## 3.2 Solar Fusion

The sun is fueled by the fusion of hydrogen into helium, with more than 98% of the sun's energy produced by the "pp chain" of nuclear reactions and decays. Light element fusion tends to produce proton-rich nuclei, so progressive fusion reactions will favor conversions of protons into neutrons. Each such conversion produces an electron neutrino as a by-product, consuming an electron or creating a positron at the same time. The total thermal energy released in a typical pp chain process (including the energy from the annihilation of the

positrons) is approximately 26.7 MeV per transformation:

$$4p \longrightarrow 2\alpha + 2e^+ + 2\nu_e. \tag{3.1}$$

The creation of helium from hydrogen can take place via several chains of reactions, as illustrated in Figure 3.1. The amount of energy carried away by a particular neutrino produced in the process can vary considerably depending on which reaction produced it. Neutrinos produced in the two electron-capture reactions in the pp chain ("pep" and $^7$Be) have line-spectra; neutrinos from the other reactions have typical beta-decay spectral shapes. The full spectrum of solar neutrinos is shown in Figure 3.2. The figure also includes neutrinos from the CNO (carbon-nitrogen-oxygen) reaction chain, which is an additional stellar fusion chain that contributes less than 2% of the total solar energy. The spectrum is dominated by low-energy neutrinos from the pp reaction, with a flux of $\sim 6 \times 10^{10}$ neutrinos per square centimeter per second at the surface of the earth.

## 3.3   Solar Models

The starting point for modeling the sun is the requirement of hydrostatic equilibrium: the radiative and mechanical pressures inside the sun must exactly balance gravity to prevent stellar collapse. Energy released in nuclear reactions is assumed to propagate outward through radiative and convective processes, and the composition of the sun is assumed to have been homogeneous before hydrogen burning began. With these assumptions, and with the constraint that the model must reproduce present-day solar features, a few important physical inputs are sufficient to produce a detailed model of the sun as it evolves.

First, a detailed equation of state relating the pressure and density in the sun must be specified, which takes into account radiation pressure, electron degeneracy, and screening effects. Second, the surface abundances of various elements in the sun must be measured. These are then taken as representative of the initial conditions in the solar interior. Third, nuclear physics reaction parameters must be known to describe the evolution of the solar composition and energy generation. The transport of radiation from the core to the surface must then be described. In the interior regions of the sun, energy transport is dominated by photon radiation, so a fourth important input is an understanding of the opacity of the

$$p+p\rightarrow{}^{2}H+\mathrm{e}^{+}+\nu_{e} \qquad\qquad p+p+e^{-}\rightarrow{}^{2}H+\nu_{e}$$

99.75%  0.25%

$${}^{2}H+p\rightarrow{}^{3}He+\gamma$$

86%  14%

$${}^{3}He+{}^{3}He\rightarrow{}^{4}He+2\,p \qquad\qquad {}^{3}He+{}^{4}He\rightarrow{}^{7}Be+\gamma$$

99.89%  0.11%

$${}^{7}Be+e^{-}\rightarrow{}^{7}Li+\nu_{e} \qquad\qquad {}^{7}Be+p\rightarrow{}^{8}B+\gamma$$

$${}^{7}Li+p\rightarrow{}^{4}He+{}^{4}He \qquad\qquad {}^{8}B\rightarrow{}^{8}Be^{*}+e^{+}+\nu_{e}$$

$${}^{4}He+{}^{4}He$$
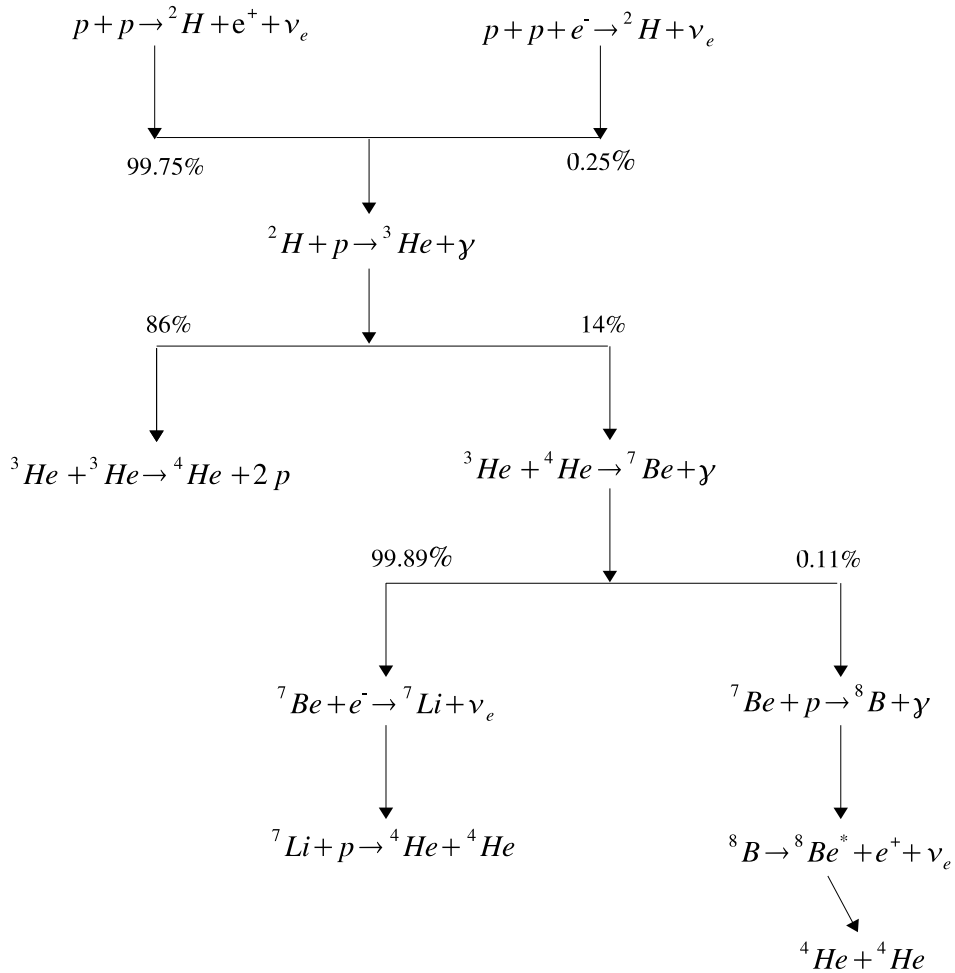
Figure 3.1: Reactions in the solar pp chain.

solar plasma to photons. Atomic physics must be combined with composition information to model the opacity.

The set of inputs described above is sufficient to model the evolution of the sun over time, and to characterize the density, temperature, and composition profiles at the present epoch. Testable predictions of the model include the solar neutrino fluxes and spectra, and the sound speed in the convective zone near the solar surface. This latter prediction can be compared with helioseismology, which measures the frequency spectrum of pressure oscillations in the outermost layers of the sun. In 1996, solar model predictions were com-
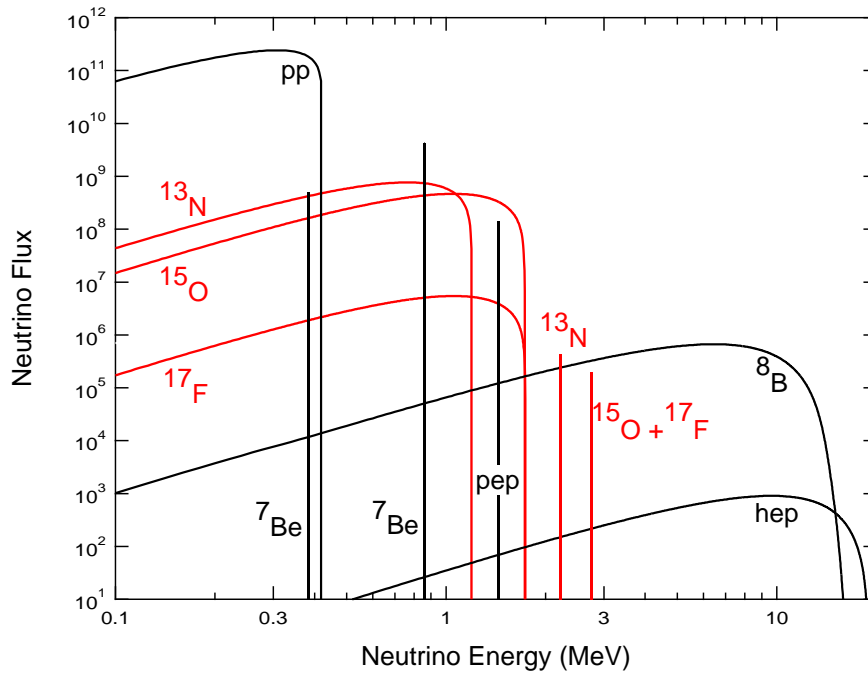
Figure 3.2: Spectrum of neutrinos produced by fusion reactions in the Sun, from [67]. Line fluxes are in units of $\text{cm}^{-2}\text{ s}^{-1}$ and spectra are in units of $\text{cm}^{-2}\text{ s}^{-1}\text{ MeV}^{-1}$.Neutrinos from the CNO reaction chain are shown as well as those from the pp chain.

pared to improved helioseismology data, and the agreement was a strong confirmation of solar theory [68]. More recently, conflicts have arisen between helioseismology results and solar models incorporating new measurements of solar abundances [69]. The standard solar model continues to be refined, and solar neutrino measurements are an important test of solar model predictions.

## 3.4  Solving the Solar Neutrino Problem

When Ray Davis made his first detection of neutrinos from the sun, the inferred flux was only around a third of what John Bahcall predicted. Davis's experiment was primarily sensitive to neutrinos from the decay of $^8$B, which were detected through the reaction $\nu_e + {}^{37}\text{Cl} \longrightarrow {}^{37}\text{Ar} + e^-$ . The production rate for $^8$B neutrinos in the sun is extremely sensitive to the temperature in the solar core, with the flux varying as $\phi_{{}^8\text{B}} \propto T^{25}$. This

temperature dependence was one reason that many physicists suspected that uncertainties in the solar model were the cause of the discrepancy, which came to be known as the "Solar Neutrino Problem". However, as solar models and experimental results improved in their precision, the discrepancy persisted.

Davis's Homestake experiment ran for 30 years, with a final measurement of $2.56 \pm 0.23$ SNU [70][1]. For comparison, Standard Solar Model (SSM) calculations predict that the Homestake experiment should measure $8.5 \pm 1.8$ SNU [71]. In the early 1990s, data from a second radiochemical neutrino detection technique added to the mystery. The SAGE experiment in Russia and the Gallex/GNO experiments in Italy were based on the reaction

$$\nu_e + {}^{71}Ga \longrightarrow {}^{71}Ge + e^-, \tag{3.2}$$

which has a threshold of 233 keV. This technique is sensitive to lower energy neutrinos from the pp and pep reactions as well as higher energy $^7$Be and $^8$B neutrinos. Combined SAGE and Gallex/GNO results give $68.1 \pm 3.75$ SNU [72] [73] [74], while the SSM predicted value is around 131 SNU [71].

Between 1983 and 1996, the Kamiokande experiment in Japan detected $^8$B solar neutrinos through elastic scattering on electrons, using a vessel filled with a kiloton of water. Unlike the radiochemical techniques (which relied on periodic extraction of the neutrino reaction products from the detector medium), the Kamiokande experiment could detect neutrinos in real time using the Cherenkov light emitted by scattered electrons. The measured neutrino interaction rate at the Kamiokande experiment translates to a $^8$B neutrino flux of $2.8 \pm 0.38 \times 10^6$ cm$^{-2}$s$^{-1}$ [75], which should be compared to solar model predictions of $5.79 \pm 1.33 \times 10^6$ cm$^{-2}$s$^{-1}$ [71]. In 1996, the Super-Kamiokande experiment began operating in the same location, using a much larger volume of water (50 ktons). Super-Kamiokande measured a $^8$B flux of $2.35 \pm 0.08 \times 10^6$ cm$^{-2}$s$^{-1}$ [76]. The results of the radiochemical and $H_2O$ experiments with comparisons to the SSM predictions are shown in Figure 3.3.

---

[1]The "SNU", or Solar Neutrino Unit, is equal to $10^{-36}$ neutrino capture reactions per second per absorber nucleus
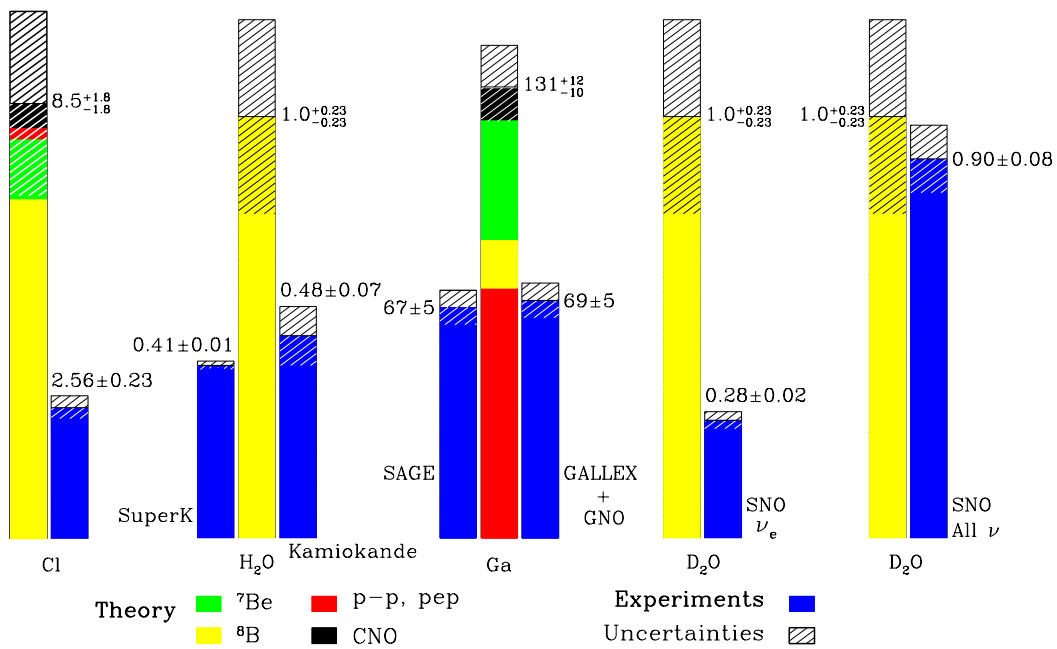
Figure 3.3: Comparison of Standard Solar Model predictions for neutrino fluxes to experimental results, from [71]. For Cl and Ga experiments, the rates are given in SNU, where 1 SNU = $10^{-36}$ neutrino capture reactions per second per absorber nucleus. For $H_2O$ and $D_2O$ experiments, rates are given relative to the SSM prediction. One-sigma uncertainties are quoted for the model predictions and experimental results (including systematics). The different energy thresholds for each method provide sensitivity to neutrinos from different reactions in the pp chain.

All solar neutrino experiments through the end of the 20th century showed a deficit relative to the predicted numbers of neutrinos. Radiochemical detection techniques rely on charged current neutrino interactions, so they are only sensitive to electron neutrinos. Water Cherenkov detectors have some sensitivity to other flavors of neutrinos (through neutral current scattering with electrons), but are primarily sensitive to the charged current scattering of electron neutrinos on electrons. So one way that solar neutrinos could evade detection was to change flavors through oscillation (or other mechanisms).

The Sudbury Neutrino Observatory was designed to test whether flavor change was responsible for the observed solar neutrino deficit. SNO uses a heavy water neutrino target, and has a unique ability to measure the flux of all active flavors as well as the flux of electron neutrinos. In 2002, SNO released the first direct measurement of the $^8$B neutrino flux that included all flavors of neutrino. The measured value was

$$\phi_{\text{tot}} = 5.09^{+0.44}_{-0.43}(\text{stat.})^{+0.46}_{-0.43}(\text{syst.}) \times 10^6 \text{cm}^{-2}\text{s}^{-1}, \tag{3.3}$$

in excellent agreement with solar model predictions (see Figure 3.3) . The flux of *electron* neutrinos was found to be only around a third of the total number of $^8$B neutrinos arriving at SNO,

$$\phi_{\text{e}} = 1.76^{+0.05}_{-0.05}(\text{stat.})^{+0.09}_{-0.09}(\text{syst.}) \times 10^6 \text{cm}^{-2}\text{s}^{-1}, \tag{3.4}$$

proving that flavor change is the solution to the long-standing solar neutrino problem.

Continued measurements at SNO (including those in this thesis) provide even more precise tests of solar physics, and experimental uncertainties on the measured $^8$B flux are now smaller than the theoretical uncertainties in the calculated SSM flux. The dominant contribution to uncertainty in the calculated $^8$B flux is related to solar composition, which affects the opacity of the solar plasma. Recent measurements of the surface abundance of heavy elements in the sun have resulted in lower values than those incorporated in previous solar models, and the new abundances lead to some disagreements between solar models and helioseismology [69]. Although these controversies in solar modeling do not have a large effect on predictions of solar neutrino fluxes, they underscore the importance of direct experimental tests of solar physics for helping us to understand the inner workings of the sun.

## 3.5 The MSW Effect

SNO has conclusively demonstrated solar neutrino flavor change by demonstrating the appearance of non-electron neutrinos in the solar neutrino flux. Following the discussion from the previous chapter, this flavor change is interpreted as evidence for neutrino oscillations, and therefore neutrino mass. However, "vacuum oscillations" as described by Equation 2.21 are not believed to be the explanation for the flavor change for solar neutrinos. The favored model for explaining all of the observations represented in Figure 3.3 incorporates matter interactions as the neutrinos pass through the dense material of the solar interior.

In 1978, Lincoln Wolfenstein pointed out that neutrinos traveling through matter would experience an "effective potential" due to forward scattering [77]. In 1985, S.P. Mikheyev and A. Yu. Smirnov extended this idea to the case of matter with varying density, showing that forward scattering could enhance neutrino oscillations [78]. The so-called "MSW" effect invented by these authors takes into account the contribution of coherent forward scattering to the energy of a neutrino in matter, which will be different for electron neutrinos and neutrinos of other flavors.

Neutrinos passing through matter can scatter on the particles in the material through $W^{\pm}$ exchange or $Z$ exchange. Contributions to the effective matter potential from $Z$ exchange will be the same for all active neutrino flavors, and will have no effect on the relative phases of the flavor components of a propagating neutrino state. However, the electron neutrino can participate in charged-current scattering with electrons. The additional effective potential felt by electron neutrinos in matter is

$$V_e = \sqrt{2}G_F N_e \tag{3.5}$$

where $G_F$ is Fermi's constant and $N_e$ is the electron density. $V_e$ is extremely small, even in dense material. However, because the mass splittings between neutrino states are also potentially extremely tiny, matter effects can substantially affect oscillations.

Including $V_e$ in the Hamiltonian means that the propagating neutrino eigenstates in matter will be different from those in a vacuum. The matter interactions are diagonal in the flavor basis, so we can summarize the propagation equation in matter (for the two-

neutrino case) as:

$$i\frac{d}{dt}\begin{pmatrix} \psi_{ee} \\ \psi_{e\mu} \end{pmatrix} = H \begin{pmatrix} \psi_{ee} \\ \psi_{e\mu} \end{pmatrix}, \tag{3.6}$$

with

$$H = \begin{pmatrix} -\frac{\Delta m^2}{4E_\nu}\cos 2\theta + \sqrt{2}G_F N_e & \frac{\Delta m^2}{4E_\nu}\sin 2\theta \\ \frac{\Delta m^2}{4E_\nu}\sin 2\theta & \frac{\Delta m^2}{4E_\nu}\cos 2\theta \end{pmatrix}, \tag{3.7}$$

where all terms that lead to a common phase for both $\nu_e$ and $\nu_\mu$ have been dropped. Here, $\psi_{\alpha\beta}(p,t) \equiv \langle\nu_\beta(p)|\nu_\alpha(p,t)\rangle$ is the time-dependent amplitude for transformation from flavor $\alpha$ to $\beta$. If the density $N_e$ is taken to be constant, then the diagonalization of the Hamiltonian in Equation 3.7 gives the eigenstates in matter:

$$|\nu_{1m}\rangle = \cos\theta_m |\nu_e\rangle + \sin\theta_m |\nu_\mu\rangle \tag{3.8}$$

$$|\nu_{2m}\rangle = -\sin\theta_m |\nu_e\rangle + \cos\theta_m |\nu_\mu\rangle. \tag{3.9}$$

The "matter mixing angle" $\theta_m$ is defined by

$$\tan 2\theta_m = \frac{\frac{\Delta m^2}{2E}\sin 2\theta}{\frac{\Delta m^2}{2E}\cos 2\theta - \sqrt{2}G_F N_e}. \tag{3.10}$$

For the constant-density case, the oscillation equations describing the transformation probability from one neutrino flavor into another have exactly the same form, just with the mixing angle and oscillation length changed to effective matter versions that are defined in terms of the vacuum mass splitting and mixing angle, $\Delta m^2$ and $\theta$. The oscillation amplitude for electron neutrinos in the two-flavor case is given by,

$$\sin^2 2\theta_m = \frac{\left(\frac{\Delta m^2}{2E}\right)^2 \sin^2 2\theta}{\left(\frac{\Delta m^2}{2E}\cos 2\theta - \sqrt{2}G_F N_e\right)^2 + \left(\frac{\Delta m^2}{2E}\right)^2 \sin^2 2\theta}. \tag{3.11}$$

When the density is such that $\sqrt{2}G_F N_e = \frac{\Delta m^2}{2E}\cos 2\theta$, the mixing is maximal ($\theta_m = 45°$) in matter, even if the value of $\theta$ itself is small. This is the "resonance condition", which will be satisfied at a particular "resonance density" for neutrinos of a particular energy $E$. For a wide range of values of $\Delta m^2$ and $\theta$, the resonance densities appropriate for solar neutrino energies can be found somewhere in the sun. To model neutrino oscillations in the sun, we need to take into account the solar density gradient.

In the case of matter of varying density, the mixing angle $\theta_m$ becomes a function of time as the neutrinos propagate through the medium. The instantaneous eigenstates $\nu_{1m}$ and $\nu_{2m}$ are no longer eigenstates of the Hamiltonian, and transitions between the two states can occur. In general, it is not possible to find a solution to the propagation equation analytically. However, a relatively simple solution is possible in the special case of adiabatic variation, when the characteristic scale of density variations is large compared to the oscillation length for the neutrinos. In this case, the survival probability for electron neutrinos is given by

$$P_{ee} = |\langle \nu_e | \nu_e(t) \rangle|^2 = \frac{1}{2} \left[ 1 + (1 - P_c) \cos 2\theta_M^0 \cos 2\theta \right], \qquad (3.12)$$

where $\theta_M^0$ is the instantaneous matter mixing angle at the point of origin for the propagating neutrino state. The term $P_c$ quantifies the probability for transitions between the $\nu_{1m}$ and $\nu_{2m}$ states, which will be negligible if the adiabaticity condition is truly respected.

Originally, the MSW effect was hailed as a way to make small mixing angles translate into large suppressions of solar electron neutrino fluxes. Small mixing angles were theoretically favored because of the obvious analogy to the parameters of the quark sector. However, *experiments* favor a vacuum mixing angle of 34° for solar neutrinos, along with a mass splitting of around $\Delta m^2 \approx 8.0 \times 10^{-5} \text{eV}^2$. Given these parameters, the adiabatic condition is satisfied for the high-energy solar neutrinos that SNO can detect. The "jump probability" $P_c$ is negligible, and densities at the center of the sun are much larger than the relevant resonant densities.

At very high densities, the instantaneous matter mixing angle approaches $\theta_M = \pi/2$. When the initial matter density $\theta_M^0 \approx \pi/2$ and the adiabaticity condition is also satisfied, the electron neutrino survival probability simplifies to

$$P_{ee} = \sin^2 \theta. \qquad (3.13)$$

Electron neutrinos produced at high densities begin in a $\nu_{2m}$ state, as can be determined by inverting equation 3.9. The effective potential experienced by the electron neutrinos is greater than the mass splitting between the neutrino states, so in the center of the sun the electron neutrino is effectively heavier than the muon neutrino. The neutrino will remain in the $\nu_{2m}$ state if propagation is adiabatic, but the flavor composition of this state will

change. At low densities, of course, the $\nu_{2m}$ state approaches the $\nu_2$ mass eigenstate, which contains a greater fraction of muon flavor. So the neutrinos emerge having adiabatically transformed from electron into muon neutrinos. [2]

In the more general three-neutrino case, the survival probability can be taken from 2.26, where we replace $P_{2\nu}$ with the appropriate MSW survival probability, and replace the effective potential $V$ with $\cos^2 \theta_{13} V$ [79].

In addition to predicting the overall survival probability for solar electron neutrinos, the MSW effect has several specific signatures that can be tested experimentally. Adiabatic conversion characterized by a survival probability $P_{ee} = \sin^2 \theta$ will only take place for a specific range of neutrino energies, such that the density at the solar core is large compared to the resonance density. For lower energy neutrinos, the density at the solar core will be below the resonance density, and matter-enhanced transitions will not take place. The MSW effect for large neutrino mixing angles therefore predicts a distortion in the solar electron neutrino spectrum. Higher energy neutrinos experience substantial flavor conversion, so the spectrum will be suppressed at higher energies. Lower energy neutrinos essentially undergo vacuum oscillations, and their average survival probabilities will be larger. This distortion may be visible in the spectrum of $^8$B neutrinos measured at SNO. Previous radiochemical experiments have explored lower energy solar neutrinos, and are consistent with vacuum-dominated oscillations. Future experiments sensitive to $^7$Be and pp neutrinos may be able to give strong evidence for the transition between vacuum-dominated and matter-dominated neutrino flavor conversion that is predicted by the MSW model.

### 3.6   Day-Night Effect for Solar Neutrinos

An additional signature of the MSW effect is regeneration of electron neutrinos in the matter of the earth. Assuming that adiabaticity holds and that the matter effect at the center of the sun is large compared to the mass splitting, the neutrinos that emerge from the sun

---

[2]These statements assume that the muon neutrino is mostly made up of the heavier fundamental mass eigenstate, $\nu_2$. If it were mostly made up of the lighter state, and the electron neutrino had a larger effective mass in a vacuum, then matter effects would suppress oscillations rather than enhancing them. Matter effects can therefore discriminate between mass hierarchies.

are essentially in a $\nu_2$ state. The probability of detecting electron neutrinos is therefore given by the transition probability $P(\nu_2 \longrightarrow \nu_e)$. For neutrinos detected during the day, this probability is simply $\sin^2 \theta$.

When neutrinos pass through the earth, matter effects may alter the probability that the neutrinos will be detected as electron flavor. In matter, $P(\nu_2 \longrightarrow \nu_e)$ will be larger than it is in a vacuum, due to the extra effective mass that the electron neutrino acquires. The earth matter effects can be characterized through an additional electron neutrino regeneration factor $f_{reg}$ in the survival probability,

$$P(\nu_2 \longrightarrow \nu_e) = \sin^2 \theta + f_{reg}. \tag{3.14}$$

For neutrinos traveling through a single layer of earth material with constant density, the regeneration factor is approximately given by [80]

$$f_{reg} = \frac{2EV}{\Delta m^2} \sin^2 2\theta \sin^2 \frac{\pi L}{l_m}, \tag{3.15}$$

where $V = \sqrt{2} G_F N_e$ is the potential due to the electron density $N_e$, $l_m$ is the neutrino oscillation length in matter, $L$ is the distance traveled by the neutrino, and $E$ is its energy. Given that the neutrino state that emerges from the sun is dominantly made up of the $\nu_2$ mass eigenstate, the earth matter effects can only increase the number of electron neutrinos detected at night relative to what is detected during the day.

The density profile of the earth is not smooth, but is characterized by a series of layers, as shown in Figure 3.4. The actual regeneration factor $f_{reg}$ must be computed either numerically or analytically, accounting for the actual density profile and the effects of discrete jumps in the matter potential. Although neutrinos passing through the dense core are more likely to experience matter effects, even neutrinos crossing boundaries in the outermost layers of the earth may exhibit significant regeneration due to interference effects. The regeneration will depend on the path that the neutrino takes through the earth, as well as on the energy of the neutrino and the underlying oscillation parameters $\Delta m^2$ and $\theta$.[3] The average effect of electron neutrino regeneration over the range of energies and neutrino

---

[3]The details of earth matter effects have been explored by many authors. See [80], [82], [83], [84], [85], [79] and references therein.

**Electron Density in the Earth:  PREM Model**
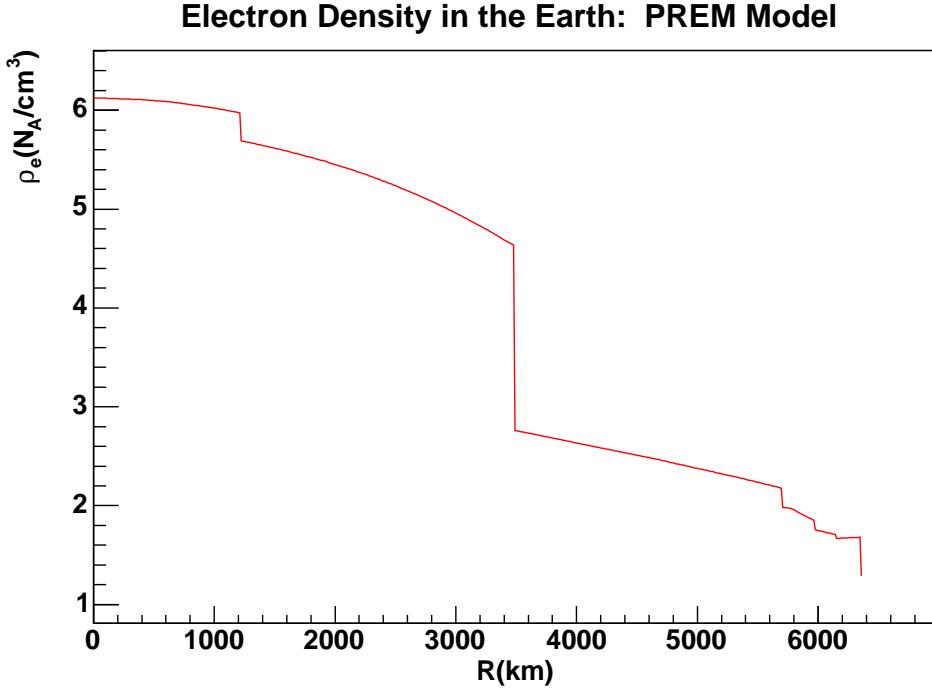


Figure 3.4: The electron density profile as a function of radius in the earth, based on the "Preliminary Reference Earth Model" [81].

paths sampled by SNO can be tested by comparing the night and day electron neutrino fluxes. We define an asymmetry parameter,

$$A_e = 2\frac{\Phi_e^N - \Phi_e^D}{\Phi_e^N + \Phi_e^D}, \tag{3.16}$$

where $\Phi_e^N$ and $\Phi_e^D$ are the measured night and day fluxes of electron neutrinos. $A_e > 0$ would be a sign of matter effects. More detailed analyses studying the flux of electron neutrinos as a function of energy and/or path through the earth are possible, but are more difficult than doing a simple test for a day-night asymmetry and require sufficient statistics.

Even if the day-night asymmetry is too small to be a powerful signature of the MSW effect, the measured value of $A_e$ can be used in a global analysis constraining allowed values of the fundamental oscillation parameters. In Figure 3.5, predicted values of $A_e$ are compared to the best fit values of $\Delta m^2 - \tan^2\theta$. The best-fit neutrino oscillation parameters are in the so-called Large Mixing Angle (LMA) region of the parameter space.
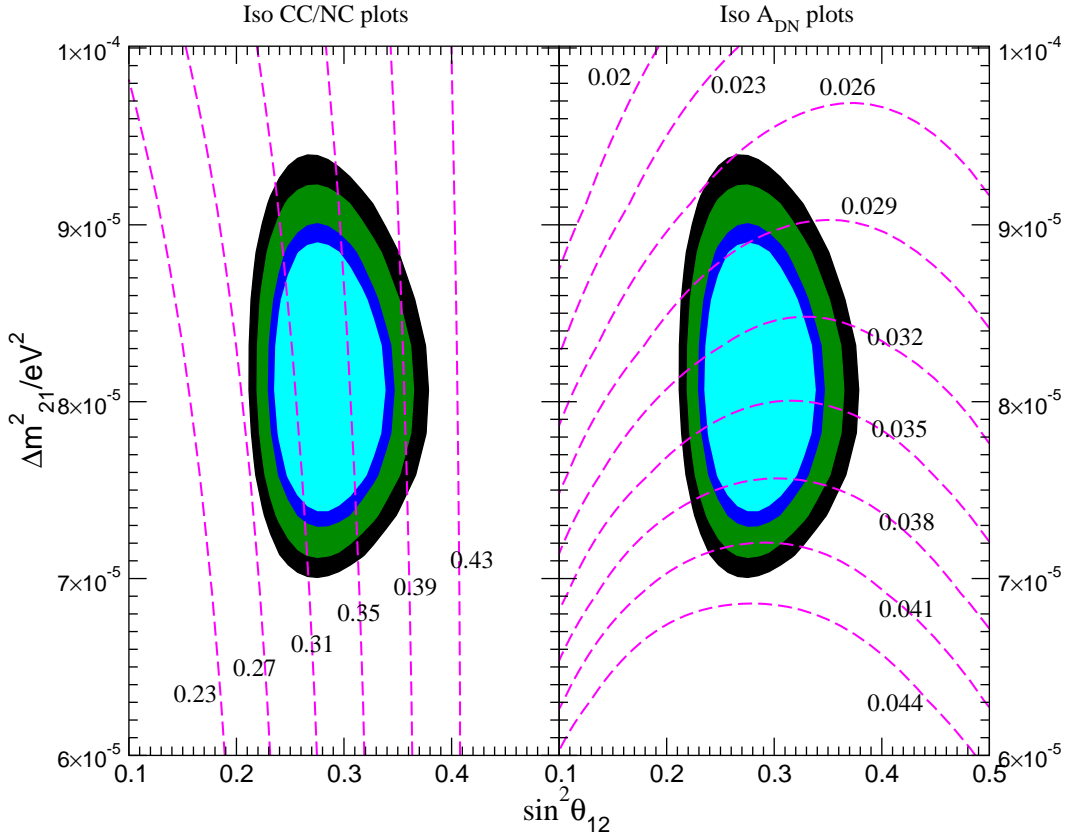
Figure 3.5: Contours of constant CC/NC ratio (left panel) and contours of constant day-night asymmetry (right panel) in SNO. The allowed region of the MSW parameter space is shown for a global MSW analysis including solar neutrino and KamLAND results available in 2004. Figure reproduced from [53].

The predicted day-night asymmetries for the LMA MSW model are very small, less than 4% for the best-fit parameters. In the LMA region of the parameter space, the day-night asymmetry is primarily sensitive to the value of $\Delta m^2$. This complements the sensitivity to $\sin^2\theta$ that is obtained through SNO's measurement of the electron and total active neutrino fluxes through the charged-current (CC) and neutral-current (NC) reactions of neutrinos on deuterium.

### 3.6.1 Day-Night Asymmetries and Sterile Neutrinos

Beyond the MSW model for solar neutrino oscillations, a non-zero asymmetry in the *total* flux of neutrinos measured at SNO could be evidence for oscillations into sterile neutrinos. Large day-night asymmetries in the total active solar neutrino flux are not a typical prediction of models involving an extra sterile neutrino, however. Motivated by the mass splitting $\Delta m^2{}_{LSND} \sim 1$ eV$^2$ implied by the LSND result, most models presume that the frequency of oscillations to sterile neutrinos would be large enough that these oscillations would average out over the distance scales that are relevant for solar neutrino experiments. In typical models, solar $^8$B electron neutrinos are taken to oscillate into a fixed fraction of sterile neutrinos,

$$|\nu_e\rangle = \sin\eta \, |\nu_s\rangle + \cos\eta \, |\nu_{\mu\tau}\rangle, \tag{3.17}$$

where $\eta$ parameterizes the mixing into the sterile neutrino state $\nu_s$ (see [55], [86], [87] and references therein). The total flux of $^8$B neutrinos $\Phi_B$ is then made up of fluxes of electron, mu-tau, and sterile neutrino fluxes when it arrives at the earth. The fluxes are related through conservation of probability,

$$
\begin{aligned}
\Phi_e &= \Phi_B P_{ee} \\
\Phi_{\mu\tau} &= \Phi_B \cos^2\eta (1 - P_{ee}) \\
\Phi_s &= \Phi_B \sin^2\eta (1 - P_{ee}).
\end{aligned}
\tag{3.18}
$$

$P_{ee}$ is the electron neutrino survival probability, which varies as a function of energy or time due to matter effects. The total active neutrino flux $\Phi_{tot}$ is the sum of the electron and mu-tau components. The above expressions can be used to derive a simple relationship between the day-night asymmetry observed for all active neutrino flavors and the asymmetry in the electron neutrino flux,

$$A_{tot} = A_e < P_{ee} > \frac{\sin^2\eta}{\sin^2\eta < P_{ee} > + \cos^2\eta}, \tag{3.19}$$

where $< P_{ee} >$ is the day-night averaged survival probability. If the $^8$B neutrinos in the sun are oscillating partially into sterile neutrinos according to this simple model, the resulting day-night asymmetry in the total active neutrino flux measured at SNO will be smaller than

the asymmetry measured for electron neutrinos. Considering that predicted asymmetries for electron neutrinos are small (less than 10% for the LMA region of the parameter space), the day-night asymmetries for active neutrinos are not likely to be large enough for SNO to observe. However, there are many more subtle models that incorporate sterile neutrino oscillations into solar neutrino phenomenology. Depending on the underlying physics, day-night effects due to sterile oscillations may be observable, if not by SNO, then perhaps by other experiments [88].

Chapter 4

# THE SUDBURY NEUTRINO OBSERVATORY

## 4.1    Detecting Neutrinos with Heavy Water

The SNO detector is located 2092 meters underground, in a nickel mine near Sudbury, Ontario. A large volume of heavy water serves as a target for solar neutrinos. Neutrino interactions in the heavy water are detected when energetic reaction products produce Cherenkov light in the detector.[1]

A schematic of the SNO detector is shown in Figure 4.1. The 1000-tonne $D_2O$ target resides in a spherical acrylic vessel with a diameter of 12 meters. Roughly 9500 photomultiplier tubes (PMTs) are mounted on an external support structure 17.8 m in diameter. The region between the acrylic vessel (AV) and the PMT support structure (PSUP) is filled with ultra-pure $H_2O$, which also fills the remainder of the cavity. The $H_2O$ provides physical support and radiation shielding for the principal detector components.

SNO detects the highest-energy neutrinos from the pp chain, primarily those from the decay of $^8$B. The use of heavy water as a target enables a rich description of the physics of $^8$B neutrinos, using three distinct neutrino interactions with heavy water. Like Super-Kamiokande and Kamiokande, SNO can detect solar neutrinos when they elastically scatter electrons in the target volume. In addition, charged-current and neutral-current neutrino-deuteron reactions yield observable signatures that are unique to SNO. The characteristics of the elastic scattering, charged current, and neutral current reactions define the basic design constraints and physics potential of the SNO experiment.

---

[1]In the final phase of the experiment, an additional detection technique is used that does not rely on Cherenkov light. See Section 4.1.3.
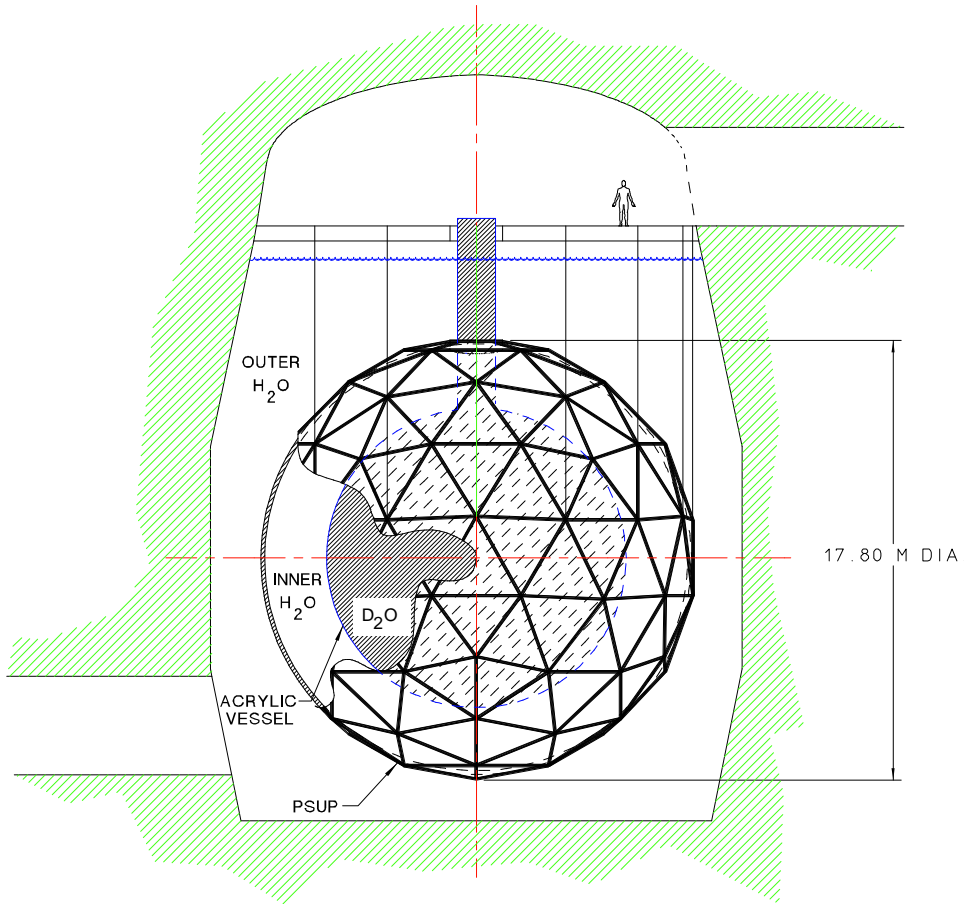
Figure 4.1: The SNO detector. Figurefrom [89].

### 4.1.1  Elastic Scattering

Neutrino-electron elastic scattering (ES)

$$\nu_x + e^- \longrightarrow \nu_x + e^-, \tag{4.1}$$

can take place through exchange of a $Z$ boson or exchange of a $W$ boson. Neutrinos of any flavor $\nu_x$, $x = e, \mu, \tau$ can scatter electrons through $Z$ exchange, but only electron neutrinos can scatter electrons through $W$ exchange. The elastic scattering cross section for electron neutrinos is enhanced relative to the cross sections for mu and tau neutrinos, due to the extra reaction channel. The two types of elastic scattering are indistinguishable in the SNO experiment: both are detected when energetic scattered electrons radiate Cherenkov light in

the detector. When the ES rate is measured in a detector like SNO or Super-Kamiokande, independent information about the neutrino flavor composition is required to disentangle the contributions due to charged current or neutral current scattering.

The energy-dependent cross sections for the two elastic scattering reactions are shown in Figure 4.2(a) For typical analysis thresholds of around 5-6 MeV, the total cross section for mu and tau neutrino scattering reactions is roughly one-sixth the cross section for electron neutrino scattering reactions. For neutrinos of a given energy, the scattered electrons will display a characteristic distribution of energies. The observed electron energy distribution therefore depends on the original neutrino spectrum, but does not directly trace that spectrum. The differential cross sections for 8 MeV neutrinos are shown in Figure 4.2(b), indicating the relative frequency with which electrons of given energies will be produced for neutrinos of that energy.

The most striking feature of the elastic scattering reaction is its directional dependence: scattered electrons are strongly forward-peaked, along the direction of motion of the incoming neutrino. If the direction of the electron can be reconstructed, this directional dependence can be used to distinguish ES reactions from other signals in the detector. The ES reaction can also give convincing evidence that the neutrinos observed are actually coming from the sun, since the direction of the scattered electrons should track the location of the sun as a function of time.

### 4.1.2  Charged Current

Solar neutrinos can also interact with the *nuclei* in matter through $W$ and $Z$ exchange. Neutrino-nucleus interactions involving the exchange of a $W$ will change the identity of a nucleon. For $^8$B neutrinos interacting with deuterium, the only such exchange that is energetically allowed is the absorption of an electron-flavor neutrino by a deuteron, which changes the neutron to a proton and produces an electron.

$$\nu_e + \mathrm{d} \longrightarrow \mathrm{p} + \mathrm{p} + e^- \tag{4.2}$$
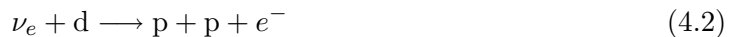
The electron from this charged-current (CC) interaction is detected through its Cherenkov radiation. The cross section for the CC interaction as a function of neutrino energy is shown
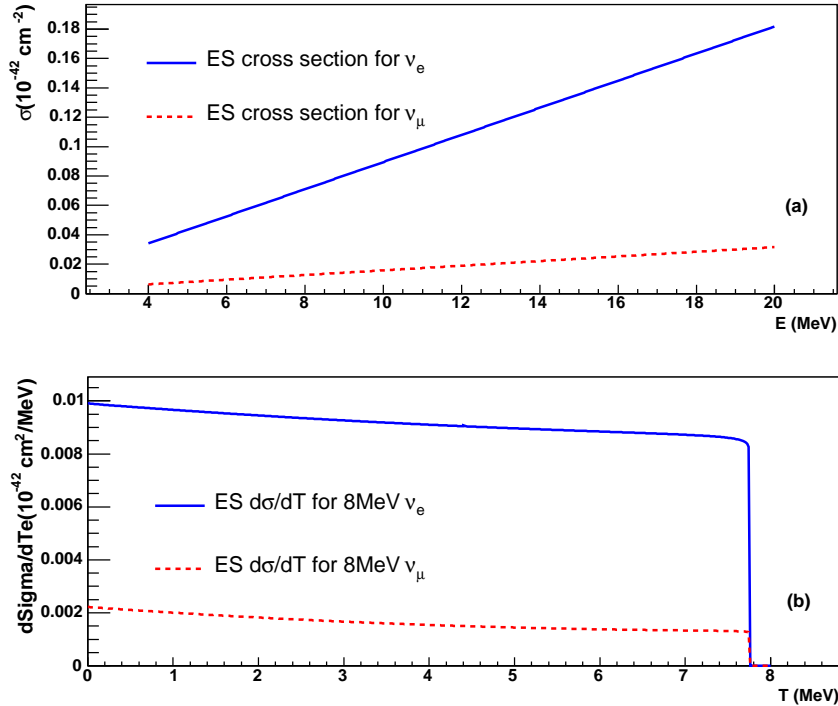
Figure 4.2: (a) Cross section as a function of neutrino energy for the elastic scattering of electron neutrinos and muon neutrinos on electrons, as a function of neutrino energy. (b) Differential cross section for the elastic scattering of 8 MeV electron and muon neutrinos on electrons. Figure produced using the QPhysics package [90], based on scattering formulae in [91].

in Figure 4.3(a).

The electron in the CC reaction carries away most of the energy of the incoming neutrino, less the 1.44 MeV threshold energy required for the reaction to take place, and the recoil energy of the two protons. The measured energy distribution for electrons from CC reactions will therefore directly reflect the neutrino spectrum. Since oscillations or exotic physics can produce distortions in the $^8$B solar neutrino spectrum, the CC spectrum measurement is an extremely valuable tool for testing oscillation physics. The CC differential cross section is illustrated in Figure 4.3(b).

The signal from the CC reaction in SNO is a Cherenkov-radiating electron, similar to the signal detected from the ES reaction. In addition to having different energy distributions,
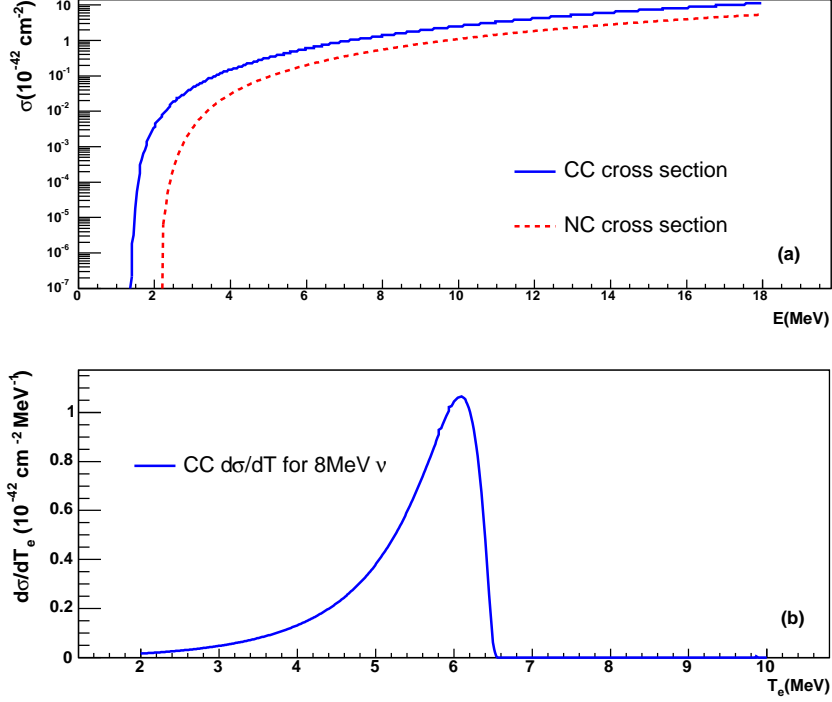
Figure 4.3: (a) Cross section as a function of neutrino energy for the CC and NC reactions. (b) Differential CC cross section for 8 MeV electron neutrinos. Figure produced using the QPhysics package [90], based on theoretical cross sections from [92].

the electrons from the two reactions have very different angular distributions. In contrast to the forward-peaked ES electrons, CC electrons are preferentially emitted backwards relative to the incoming neutrino direction. The direction distribution is approximately described by $1 - 1/3 \cos \theta$, where $\theta$ is the angle between the recoil electron direction and the direction of the incoming neutrino.

### 4.1.3 Neutral Current

A neutrino of any active flavor $e, \mu, \tau$ can exchange a $Z$ with a deuterium nucleus. If the energy of the neutrino is greater than 2.2 MeV, it may impart enough energy to dissociate the deuteron into a proton and a neutron.

$$\nu_x + \mathrm{d} \longrightarrow \nu_x + \mathrm{p} + \mathrm{n} \tag{4.3}$$

The neutron will thermalize in the surrounding medium, and its subsequent capture on a nucleus may provide an observable signal. Because the neutron thermalizes before it is detected, any information about the neutrino direction or energy is erased.

Sensitivity to the NC reaction is a unique feature of the SNO experiment that allows tests of solar physics as well as unambiguous demonstration of solar neutrino flavor change. One of the greatest challenges to performing a measurement of the NC reaction rate in deuterium is the unfortunate resemblance of the NC reaction to ordinary photodisintegration of the deuteron into a proton and neutron. Any gamma ray with an energy above 2.2 MeV can photodisintegrate deuterium, and the neutron produced is indistinguishable from the NC signal. The uranium and thorium decay chains include two radioisotopes with sufficiently energetic gamma decays, $^{214}$Bi (2.445 MeV $\gamma$), and $^{208}$Tl (2.615 MeV $\gamma$). Radioactive impurities in the detector materials must be strictly controlled and carefully characterized in order to make the NC measurement possible.

SNO was designed to run in three phases, each employing a distinct capture reaction to detect free neutrons in the detector. In each phase, the systematic uncertainties, background characteristics, and analysis techniques differ, leading to robust measurements of the NC rate as well as opportunities to optimize different physics measurements.

- *Pure $D_2O$ phase, November 1999 to May 2001:* In the first phase of SNO, neutrons were detected through capture on deuterium, which releases a 6.25 MeV capture gamma. The gamma typically Compton-scatters a single electron, which then produces Cherenkov light. The neutrons thermalize before capturing, and the distribution of observed energies from NC events is determined by the energy released in the neutron capture reaction. If neutrons wander beyond the heavy water region of the detector, they will quickly capture on the acrylic or $H_2O$ and be lost to detection. Capture on materials surrounding the $D_2O$ leads to a characteristic radial distribution of the neutron capture "events" in the $D_2O$ phase. If the position of events can be resolved, the radial fall-off of NC reactions is a useful tool for telling them apart from CC and ES events.

- *Salt phase, July 2001 to September 2003:* The work in this dissertation primarily

concerns the second phase of the experiment, in which purified NaCl was dissolved in the $D_2O$ to a concentration of $(0.196 \pm 0.002)\%$ by weight. Neutron capture on $^{35}$Cl has a higher cross section than capture on deuterium, (44 barns compared to 0.0005 barns). The de-excitation of the chlorine nucleus releases 8.6 MeV in a cascade of gammas. The higher cross section and higher energy improve SNO's efficiency for detecting NC neutrons above a given energy threshold, allowing a more statistically precise measurement. The higher capture cross section also means that fewer neutrons are captured outside the heavy water region, making the radial profile a weak discriminator of neutral current events in the salt phase. To distinguish NC events from CC and ES events, we rely on the differences in the spatial characteristics of light produced by cascades of gammas relative to single electrons. The multiple gammas scatter multiple electrons, resulting in light that is less spatially concentrated than that produced by single electrons. A parameterization characterizing the light isotropy in each event allows statistical separation of the NC signal in the salt phase.

- *NCD phase, November 2004 to December 2006:* The third phase of the experiment began in late 2004, after the salt had been removed from the $D_2O$. An array of discrete detectors, made up of 36 vertical strings of $^3$He proportional counters and 4 strings of $^4$He proportional counters, was deployed inside the acrylic vessel. The $^3$He "neutral current detectors" (NCDs) decouple neutron detection from detection of the CC and ES signals. Neutrons produced in the $D_2O$ thermalize, scatter into one of the NCDs, and capture on $^3$He. The proton and $^3$H nucleus produced in the reaction recoil back-to-back, producing ionization that is collected along a central anode wire. The capture cross section for neutrons on $^3$He is much larger than that on $D_2O$, so the NCDs effectively remove neutron capture reactions from the set of events detected through Cherenkov light. The NCDs allow an event-by-event determination of the NC reaction rate, eliminating statistical correlations inherent in the process of extracting the NC signal in the previous phases.

### 4.1.4 Basic SNO Design Considerations

With its unique suite of neutrino reactions, SNO can measure the total flux of $^8$B solar neutrinos, disentangle the flavor composition, and test the predicted $^8$B neutrino spectrum. Since SNO is a real-time experiment, it can also profile temporal variations in the flavor or flux of the $^8$B neutrinos on a variety of time scales. Beyond solar neutrino physics, SNO may provide invaluable data on the flavor, spectrum, and arrival times of supernova neutrinos in the event of a galactic supernova. These are the major physics goals behind the design of the detector.

Neutrino detection takes place primarily by detecting the Cherenkov radiation produced by electrons (either the electrons produced in the neutrino interaction or those scattered by neutron capture gammas). Cherenkov light is emitted at an angle $\theta_c$ from the electron track, which is determined by the index of refraction of the medium and the velocity of the particle. For relativistic electrons in water, the Cherenkov angle is around $42°$. Electrons of MeV energies will lose energy rapidly through ionization, dropping below the threshold for emitting Cherenkov light in a matter of picoseconds. The signature of a single electron in SNO will be prompt detection of Cherenkov photons in a ring-like geometry in the PMT array. The number of photons produced by a radiating electron is proportional to its energy, so the number of "hits" collected for a given event gives a rough energy measure, although the efficiency for detecting the photons varies as a function of location in the detector. The Cherenkov photons detected in the heavy water will have frequencies in the blue and ultraviolet.

With the exception of neutron detection in the NCD phase, the three neutrino signals in SNO cannot be distinguished on an event-by-event basis. The rates of CC, NC, and ES reactions and the energy spectra for the CC and ES events must be statistically separated, using the differences in the event characteristics. Extracting neutrino physics from SNO therefore requires accurate reconstruction of event energies, positions, directions, and times, as well as characterizations of the light isotropy in an event (particularly for the salt phase data). A variety of calibration techniques and careful Monte Carlo modeling are required to estimate systematic uncertainties in detector energy, radial, direction, and isotropy response,

as well as any temporal variations.

Radioactive contaminants that can produce gamma rays above 2.2 MeV must be carefully controlled and monitored, because they can produce neutron backgrounds that are indistinguishable from the NC signal. This places severe constraints on the materials that can be used in SNO. For the construction of the experiment, a number of custom low-background components had to be specially developed. Radioactive backgrounds with energies below 2.2 MeV also need to be controlled and characterized, since they can "leak" into the signal region due to the moderate energy resolution of the detector. The analysis energy threshold that can be used for studying solar neutrino reactions ultimately depends on how well these backgrounds have been controlled and understood.

The depth of the experiment (6010 meters water equivalent) screens out most cosmic rays, keeping related backgrounds to a minimum. While locating the experiment deep underground is essential for attaining the desired sensitivity, operating conditions in an active mine also place constraints on the detector design, including requirements of seismic stability and remote detector operation capabilities.

## 4.2    The $D_2O$, the $H_2O$, and the AV

The neutrino target consists of 1000 tonnes of 99.92% isotopically-pure $D_2O$. There are two volumes of "light water" ($H_2O$): an inner volume of $\sim$1700 tonnes and an outer volume of $\sim$5700 tonnes. The inner volume fills the region between the acrylic vessel and the array of PMTs, and the outer volume fills the rest of the detector cavity (see Figure 4.1). The light water acts to shield the heavy water region from external radioactivity, as well as to provide physical support for the detector components. Restrictions on contaminants in the $D_2O$ are the most stringent, but the inner $H_2O$ volume also must be kept extremely clean. Cherenkov light produced in this region is visible to the PMTs, and neutron backgrounds from the $H_2O$ may migrate into the $D_2O$ region. The outer volume of $H_2O$ is also highly purified, but is in contact with a larger number of materials and has higher levels of contaminants.

The $H_2O$ from both the inner and outer volumes is continuously circulated for purification and monitoring. The $H_2O$ circulation system filters particulates, removes oxygen and

radon through a degassing unit, regasses the water with ultra-pure $N_2$, and exposes the water to UV radiation to eliminate biological contaminants.[2] The water is cooled to 10° C before it is returned to the detector cavity. Regular assays monitor physical characteristics of the water (pH, conductivity, etc.) as well as levels of uranium- and thorium-chain radioisotopes.

The $D_2O$ is circulated through an independent system including reverse osmosis and ultrafiltration units. The $D_2O$ processing systems were designed to manage the introduction and removal of salt for the second phase of the experiment as well as to provide purification and monitoring. Three assay techniques were developed to monitor precursor isotopes to $^{208}$Tl and $^{214}$Bi in the heavy water, and these techniques are described in detail in references [93], [94], and [95]. The target activity levels were originally set by requiring the number of photodisintegration neutrons to be less than 10% of the expected neutron rate from NC events, assuming Standard Solar Model neutrino fluxes [89]. The target values are $3 \times 10^{-15}$ g Th/g $D_2O$ and $4.5 \times 10^{-14}$ g U/g $D_2O$. Assays are combined with in-situ analysis of background events in the detector to determine the actual amounts of radioactive contaminants in both the $D_2O$ and the $H_2O$. Measured radioactivity levels have been below the target values for the data-taking periods used for neutrino physics analysis.

The acrylic vessel (AV) that houses the $D_2O$ is made from 122 panels of ultraviolet-transmitting acrylic, which were bonded together in the cavity during construction of the detector. The AV is nominally 5.6 cm thick, except around the equator, where ten "belly plates" are thicker to anchor a rope suspension system that supports the vessel. At the top of the AV is a "chimney" 1.46 meters in diameter, made of ultraviolet-absorbing acrylic. The chimney is the only means of access into the $D_2O$ volume, and is used for deployment of calibration sources as well as for the deployment of the NCDs in the third phase of the experiment.

---

[2]The water must be regassed to prevent potentially serious high-voltage breakdown of the PMT connectors, which depends on internal gas pressures within the connectors themselves.

### 4.3   The PMTs and the PSUP

With care, low levels of radioactivity can be achieved in acrylic, and water can be purified. However, the components required to build photomultiplier tubes typically have higher levels of radioactivity. A new highly pure borosilicate glass was developed for SNO's ultra-low-background application, and all other PMT components were carefully selected and assayed to ensure minimum levels of radioactive contaminants. Radioactivity in the PMTs (particularly U, Th, and K in the PMT glass) ultimately limits the energy threshold that can be used for studying neutrino reactions in SNO, which is 6 MeV for the analysis in this thesis.

The energy resolution of the detector as a whole will depend on the efficiency and noise properties of the PMTs. The Hamamatsu R1408 PMT model used in SNO was chosen for its intrinsically low dark current noise rate, high photoelectron collection efficiency, and low sensitivity to external magnetic fields, as well as its stability under the expected physical conditions of the mine. The PMTs are operated at a temperature of $10°$ C, which helps to suppress the noise rate to around 500 Hz (including noise from residual radioactivity as well as dark current noise). To improve the PMT efficiency, 14 horizontal field-compensation coils were mounted in the SNO cavity walls, to cancel the vertical component of the earth's magnetic field.

The arrival times of photons from a single physics event can be used to reconstruct the location of that event. Event vertex position resolution will therefore depend on the PMT timing resolution, as well as on noise rates. SNO's PMTs have a single photoelectron timing resolution width of around 1.7 ns, reflecting a relatively small spread in the transit times for photoelectrons in the PMTs.

9438 PMTs are oriented to face the acrylic vessel, attached to a PMT support structure (PSUP) that also serves as a barrier between the two $H_2O$ regions. Each PMT is mounted inside a light-concentrator assembly that increases the photocathode coverage of the spherical volume from 31% to 54%, and limits the wide-angle photon acceptance of each PMT. Ninety-one PMTs without light concentrators are anchored outside the PSUP. These outward-looking tubes, or "OWLs", are used to veto signals from cosmic ray muons.

A small failure rate of PMT components requires that some PMTs be permanently disconnected (at the "dry" end), at a rate of around two per week. The effective number of PMTs being used for data taking is therefore smaller than the total number, and decreases with time. For the salt phase, the number of PMTs in use was between around 8600 and 8800.

## 4.4 Electronics and Data Acquisition

### 4.4.1 Electronics and Triggering Overview

A single neutrino interaction event will generate pulses in several dozen PMTs within a narrow time window. The SNO electronics system [89][96] is responsible for collecting and characterizing those PMT pulses, deciding whether a set of pulses looks like a possible physics event, and digitizing and saving the information when trigger conditions are met. In addition, the electronics system must maintain synchronized absolute timing and accurate relative, inter-event timing. It provides calibration and diagnostic capabilities as well as interfaces for triggering the detector on signals from external calibration devices. The electronics must be able to handle background and calibration source event rates of $\sim$1 kHz, and be able to buffer up to a million events (at 1 MHz) in the event of a galactic supernova.

The PMT electronics are housed in 19 crates on the light-sealed "deck" above the detector itself. A single $\sim$32 m long 75 $\Omega$ cable transmits HV to each PMT and carries its signal output. HV-decoupled signals from 32 PMTs are sent to one of 16 front-end cards (FECs) per crate for processing. Each PMT signal is passed to a fast discriminator. If the pulse exceeds the discriminator threshold, it is split and sent to low-gain and high-gain integrators. The high-gain integrator is sampled twice and the low-gain integrator once to provide three charge measurements for the PMT pulse. A single-channel timing cycle begins when the discriminator fires, beginning a time-to-amplitude conversion (TAC) ramp. If a global detector trigger signal is received within 400 ns, the charge and TAC voltages are saved and later digitized for readout by the data acquisition system. Otherwise, the channel resets.

The digitized "PMT data bundle" that is stored by the FEC when a valid trigger has

been received contains the charge and TAC voltages and the identification number for the particular channel. It also stores the current value of a local counter that is synchronized with the rest of the system, and is incremented on every global trigger. The count value is used as a "global trigger identification" number (GTID), allowing all of the PMT data bundles associated with a given trigger to later be collected and assembled into events by the data acquisition system.

A global trigger is issued when one of several trigger conditions is met. Each time a discriminator fires, a fixed-width (nominally 100 ns) analog pulse is generated, and these pulses are then summed in one of several analog master trigger cards (MTC/As). A coincidence of 16 of these pulses initiates the primary physics trigger, which essentially requires that 16 PMTs have detected incident light within 100 ns. The timing allows for the ∼80 nanoseconds it takes for Cherenkov light that is reflected by the AV to traverse the detector and be detected as part of the total light in the event. Additional triggers include one based on a 20 ns coincidence and one that is based on an analog sum of the individual PMT pulses, which is useful for identifying instrumentation-generated background events. Separate trigger conditions are based on coincidences of several OWL tubes in order to veto cosmic ray muons.[97]

The trigger logic is handled by a digital master trigger card (MTC/D), which receives candidate trigger signals from the MTC/As and decides whether or not to issue a global trigger based on which trigger types are currently set to be valid (trigger conditions can be customized for special calibration needs or other purposes). The MTC/D collects all of the trigger signals associated with a particular event, records the current global trigger ID number, and sets the event time based on two separate clocks. The "trigger data bundle" stored by the MTC/D for each triggered event therefore includes information about which trigger conditions were satisfied, when the event occurred, and what the count was on the global trigger counter. The MTC/D also handles calibration of the electronics signals and interfacing with external calibration devices.

In addition to the physics triggers and the triggers associated with particular calibration sources, a pulsed global trigger (PGT) is issued at a frequency of 5 Hz. The PGT events allow an unbiased measure of the background noise rate in the detector, and have been

useful for a number of different studies of detector conditions over time.

### 4.4.2  Clocks

Two independent clocks are used to provide timing information in SNO [98] [89]. The first is a commercial GPS system, which provides a 10 MHz oscillator signal and allows for synchronization of SNO event times with Universal Coordinated Time (UTC). Accurate absolute timing information is important for correlating events in SNO to external phenomena, such as the current relative position of the sun or, potentially, a supernova explosion detected in other experiments. The 10 MHz clock can maintain absolute timing accuracy to within around 100 ns over long periods of time.

The GPS receiver is located on the surface, and the 10 MHz signal is transmitted to the underground electronics via a fiberoptic cable four kilometers long. Communication delays are monitored by measuring the round-trip propagation time hourly, as part of the regular synchronization process. The 10 MHz clock provides the primary event times used for analysis.

Accurate relative timing is provided by a 50 MHz clock that is driven by a quartz oscillator located underground. The oscillator increments a 43-bit counter, which rolls over approximately every two days. The 50 MHz clock is not synchronized to absolute time, but it provides accurate inter-event timing as well as verification of the 10 MHz clock times. Problems with the GPS receiver or damage to the fiber optic cable can corrupt or interrupt the 10 MHz clock, in which case the 50 MHz clock can be used to rebuild event times offline. Comparison of the two clock times shows that the 50 MHz clock actually runs at 49.9995 MHz [99], although this difference is so small that it is essentially unimportant. The independence of the two clocks is very useful for verification of event timing and detector livetime.

### 4.4.3  Data Acquisition and Event Building

The data acquisition (DAQ) system for SNO needs to perform continuous readout of all of the PMT channels, manage calibration functions, control the configuration of the detector,

record the data to tape, and provide tools to monitor and log hardware status. For the third phase of the experiment, it also needs to incorporate the NCDs and handle the coordination between the NCD and PMT systems. Configuration control and monitoring is handled by a program called "SHARC" (SNO Hardware Acquisition and Readout Control) that runs on a Macintosh G4 underground. Other functions are handled by additional hardware components as well as software to perform readout and assemble and write the data stream.

When a global trigger has been issued by the MTC and received by all of the PMT crates, the "PMT data bundles" associated with that trigger are stored on the front end cards, while the master trigger card stores the trigger and timing information. A VME-mounted single-board computer (the embedded CPU or eCPU) reads out the FEC data and transfers it to a VME-based dual port memory, or DPM. The eCPU also reads out the MTC information and sends it to a separate memory buffer on the DPM. The DPM is simultaneously read by a Sun Ultra-1 workstation running a program called the PMT Builder, which assembles associated FEC and MTC data into events.

The MTC and FEC data that is read in by the PMT Builder is built into events by collecting MTC words and PMT bundles with the same GTID. The PMT Builder maintains a table of events based on the lower 17 bits of the GTID. A PMT bundle or MTC word with a new GTID is given a new entry; if an entry already exists for its GTID, then the new data is added to the existing data for that event. Events are required to remain in the table until a specified time has elapsed, to ensure that all of the data associated with the event is collected. After the conditions for output have been met, the event is written locally to tape, sent above ground to be written to a back-up tape, and broadcast through a dispatcher for near-line monitoring.

## 4.5 Calibration Systems

The raw data that is stored for each event includes the 10 MHz and 50 MHz clock times associated with the event, the triggers satisfied by the event, and the charges and TAC values for each PMT pulse that registered as part of that event (along with the channel ID numbers for the PMTs). Interpreting the PMT times and charges requires regular calibration of the

electronics using injected pulses, as well as calibration of the channel-by-channel timing and charge response to light produced in the detector. A "laserball" source is used for channel timing and general optical response calibration. It consists of a pulsed nitrogen laser that feeds light through optical fibers to a diffuser ball. The laserball is lowered into the vessel and positioned at various locations using a "manipulator" system of ropes and pulleys, which is shown in Figure 4.4. A selection of dye cells yields wavelengths between 337 nm and 620 nm, and neutral-density filters can be used to adjust the intensity of light from single photo-electron intensities to intensities of hundreds of photoelectrons per PMT. In addition to calibrating channel characteristics, laserball data taken with the source at a variety of locations in the detector can be used to measure the attenuation, scattering, and reflection characteristics of detector components.
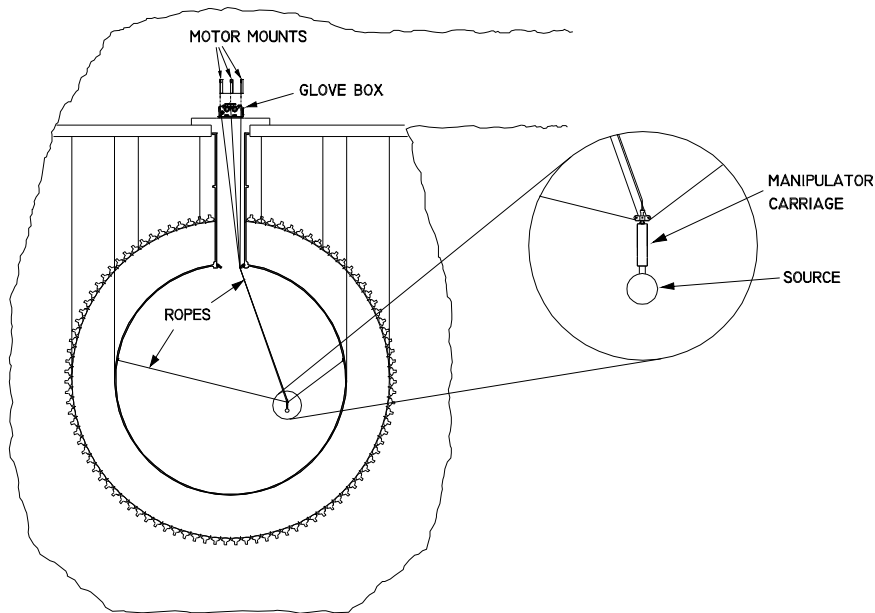


Figure 4.4: The "manipulator" system for deploying calibration sources in the SNO detector at a variety of locations. The laserball calibration source is shown. Figure from [89].

Calibrated charges and times for the PMT hits in a particular event are used along with a Monte Carlo (MC) model of the detector optical response to reconstruct the position, direction, and energy of the event. Comparison to additional calibration data fixes the

overall energy scale. A number of different radioactive sources are then used to study uncertainties in energy scale and resolution, reconstruction performance, and other aspects of detector response. The major calibration sources used in the salt phase are briefly described below.

- $^{16}$N: A commercial D-T neutron generator located 30 m from the detector volume is used to bombard a $CO_2$ target with neutrons, producing $^{16}$N through the $(n, p)$ reaction on $^{16}$O. Gas capillaries convey the $^{16}$N through an "umbilical" cable to a decay chamber that is lowered into the detector on the manipulator carriage. The cylindrical decay chamber is 41.9 cm long and 5.7 cm in radius, and is made of 5 mm-thick stainless steel. $^{16}$N beta decays with a 7.13 s half-life, releasing a 6.13 MeV gamma 66% of the time and a 7.12 MeV gamma 4.8% of the time. The gammas pass through the walls of the chamber and scatter electrons that produce Cherenkov light. The betas (which have an endpoint energy around 10 MeV) are stopped by the stainless steel. A sleeve of scintillator on the inside of the decay chamber is used along with a 5 cm PMT to trigger the SNO detector when betas from within the decay chamber are observed. The associated gammas coming from the decay chamber are therefore distinguished from backgrounds or gammas coming from decays taking place in the umbilical. The $^{16}$N source is deployed at a range of locations in the detector. It is used to set the absolute energy scale of the detector and to evaluate energy systematics. The average reconstructed position of the $^{16}$N events is used to study the accuracy of the reconstruction algorithm. Additionally, since the gammas from the source travel typical distances of ∼15 cm before scattering an electron, the vector between the source center and the reconstructed vertex position gives an indication of the direction of the gamma. Comparisons of the reconstructed direction to the calculated direction can be used to study angular response. A detailed description of the $^{16}$N source can be found in reference [100].

- $^{252}$Cf: To measure the neutron capture efficiency and study neutron response, the primarily calibration source is a $^{252}$Cf fission neutron source. A small amount of $^{252}$Cf is encapsulated in multiple layers of acrylic, and the acrylic is lowered into the vessel

using the manipulator system. $^{252}$Cf decays with a half-life of 2.645 years, with a 3.09% spontaneous fission branch. A fission decay produces prompt betas and gammas, and an average of 3.77 neutrons that thermalize and capture in the detector. Deploying the source at various locations allows the variations in neutron capture efficiency, energy, and light isotropy to be measured. In the D$_2$O phase, the $^{252}$Cf neutron events could be separated from the backgrounds caused by fission betas and gammas by applying a spatial cut to reject events reconstructing close to the source. In the salt phase, the neutrons typically capture much closer to the source itself, so the spectrum of fission betas and gammas has to be measured and taken into account. To determine the neutron capture efficiency, the source absolute strength is measured through multiple ex-situ and in-situ techniques.

- **U and Th Encapsulated Sources:** Uranium and thorium sources (multiply encapsulated in acrylic) are used to study the response of the detector to low energy backgrounds. These sources are deployed in the light water region to construct a model of the radial profile of low energy background events.

- **Radon spike:** To further understand the response to low-energy backgrounds, a known quantity of $^{222}$Rn was injected into the detector at one point during the salt phase and allowed to decay.

- **Sources for Studying Differential Energy Response:** To study energy response at the high-energy end of the neutrino spectrum, high intensity laserball data is used to probe cross-talk and multi-photon effects at high energies. A $^8$Li beta decay source (with an endpoint energy of 13.5 MeV) is used as a check on energy response [101]. A $^3$H(p,$\gamma$)$^4$He ("pT") source producing 19.8 MeV gammas is used to study energy nonlinearities [102]. The pT source was not deployed in the salt phase because it produces too many neutrons. Calibrations taken before the salt phase were used instead.

- **Sources for Studying Differential Temporal Response:** Long term variations

in detector response are evaluated with regular deployment of the $^{16}$N, laserball, and $^{252}$Cf sources. Calibrations are not typically performed during the night, so day-night variations in detector response must be constrained using in-situ techniques based on radioactive backgrounds or secondaries from cosmic ray interactions.

## *4.6   Monte Carlo*

A detailed model of the detector and its response to physics events is central to nearly all analysis of SNO data. Data processing, analysis, and simulation tools are provided by the SNO Monte Carlo and ANalysis (SNOMAN) package. SNOMAN includes processors to calibrate the raw data, to reconstruct event positions and directions, and to estimate the energy of events. Calibration constants associated with each individual channel are input to the SNOMAN detector model, as well as calibrated values for the optical properties of detector components and the measured absolute energy scale from $^{16}$N.

SNOMAN can generate and propagate particles through the detector, modeling the detection of the particles or their secondary products. Some physics simulations are custom built, but the existing packages EGS4[103], MCNP[104], and FLUKA[105] are used for electromagnetic showers, neutrons, and hadrons, respectively. SNOMAN simulations of signals and backgrounds are used to build probability density functions (PDFs) describing distributions in the observables (energy, radius, etc.) for different classes of physics events. Simulations of calibration sources are also compared with calibration data to estimate systematic uncertainties in detector response.

Chapter 5

# DATA SELECTION AND LIVETIME

## 5.1 Overview

The raw data that is written to tape during neutrino running must go through many steps of selection, processing, and study to produce a final data set for analysis. Raw data consists of recorded events with calibrated PMT time and charge values, trigger information, and clock times. During ordinary running in the salt phase, the trigger rate was around 20 Hz, with the pulsed global trigger (PGT) contributing 5 Hz. Most of the events making up the remaining 15 Hz were instrumental events and radioactive backgrounds, with only about 10 candidate neutrino events per day.

The first step to produce a final data set is to select individual "runs" that are expected to have high-quality neutrino data. Typical run durations in the salt phase range from half an hour to a day, and many thousands of runs make up the entire salt phase. Runs dedicated to calibration activities or maintenance are automatically removed from consideration for neutrino analysis. Careful inspection of hardware status logs and comments by the detector operators is necessary to select a final data set. The analysis presented in this thesis includes data from runs recorded between July 26, 2001 and August 28, 2003. Between these dates, 20.2% of the total running time was allocated to calibration activities, 22.6% of the total time was taken up by maintenance activities, periods with elevated background rates, or runs that failed data quality checks, and 6.2% of the total time was spent with the detector turned off. 1212 data runs were selected for solar neutrino analysis, representing 51% of the total time between the start of the salt phase in July, 2001 and its completion in August, 2003.

The runs in the selected runlist must be processed to remove as many backgrounds as possible from the final data set. Many of the instrumental backgrounds (and some non-

instrumental backgrounds) are directly removed based on their "low-level" characteristics: the recorded PMT charges, times, and locations, and the event times. Muon interactions in the detector can also be tagged using PMT information and the presence of PMT "hits" in the outward looking muon-veto PMTs (the OWLS). Using the muon tag, time following muons can be cut in order to avoid backgrounds from potential long-lived spallation products. Twenty seconds following each tagged muon is removed from the data set, as part of a suite of cuts that removes about 2% of the total "livetime". Careful calculations are performed to determine the amount of time that is sampled by the reduced data set, so that the number of neutrino events extracted in the final analysis can be interpreted in terms of solar neutrino fluxes.

## 5.2 Instrumental Backgrounds

A wide range of instrumental effects can generate SNO event triggers, ranging from high-voltage breakdown in the PMT components to static discharges at the gas-$D_2O$ interface in the neck of the detector. Each class of instrumental event was characterized extensively in the first phase of the experiment, and a set of data selection cuts was developed to remove them from the data set. These cuts rely on the the PMT times and charges, the geometry of the set of PMT hits recorded in the event, the total number of PMT hits ("Nhit") in the event, and the presence of hits in specific PMTs used to veto special event classes.

- *Flashers and Related Events:* A common type of instrumental event that can resemble neutrino events is the "flasher", in which a PMT spontaneously emits light. Flashers are believed to be caused by static discharges in the dynode stack of the PMT. The PMT that flashes typically registers a large charge, as do the channels that are adjacent to it in the electronics. Light from the PMT travels across the detector and produces an oval-shaped pattern of hits in the PMTs on the other side. Although the light distribution can mimic a Cherenkov ring, the distinct charge, spatial, and timing features of flashers can be used to cut these events from the neutrino sample. Flashers happen at a rate of around 50 events per hour. They can also happen in "bursts", often when seismic activity triggers discharges in a large number of PMTs at the same

time. Similar phenomena can occur without the production of light in the detector. These events are characterized by a single high-charge PMT hit surrounded by a cluster of adjacent channels that register electrical pickup. Discharge events with no light output occur with rates on the order of 3000 per hour, but they can be efficiently cut based on their charge characteristics.

- *Neck Events:* A second common instrumental event is apparently caused by static discharge in the neck region of the acrylic vessel. Light produced near the air-water interface travels into the AV and produces a distribution of PMT hits at the bottom of the detector. A set of four PMTs was installed in the neck region to veto events associated with light in the neck region. Neck events can also happen in large bursts, especially when calibration sources traverse the neck region. Similar processes produce light in the system of pipes into the AV during the recirculation of the $D_2O$.

- *Pickup:* Electrical pickup can generate detector triggers, often due to personnel activity or equipment operation near the electronics crates. Electrical pickup is typically oscillatory in nature and integration of the charge over a long time window yields a value consistent with zero. The charge features can be used to reject these events, and care is taken to prevent them by avoiding unnecessary activity around the electronics during neutrino runs. Pickup events also tend to occur in bursts, with the duration depending on the cause.

- *Breakdown:* High voltage breakdown in the PMT base or connectors can cause very high Nhit events, characterized by high charge and pickup localized around one electronics crate. Light produced by these events often saturates the rest of the detector as well. Breakdown taking place in the base of the PMT sometimes produces light with a flat, continuous time spectrum. These sorts of breakdown events tend to occur in bursts, signaling the death of a PMT. Major bursts of breakdown events are diagnosed and the offending channel is permanently disconnected from the high voltage.

- *Retriggers:* After high Nhit events or events with a large deposited charge, the detector may "retrigger" on residual light, PMT after-pulsing, or electrical pickup signals that persist after the initial event. Retrigger events are primarily identified by their proximity in time to the original event, rather than their specific characteristics, although they do have common features.

- *AV Events:* A final known variety of instrumental events cannot be eliminated using cuts based on low-level event characteristics. These are the so-called "AV events". They are characterized by Nhit values in the solar neutrino range (or higher), an isotropic distribution of light around the detector, and reconstructed event positions at the AV. They are believed to be light emission from stress releases in the acrylic itself, although the exact cause is not known. AV events must be addressed through "high level" cuts on the reconstructed data.

The standard set of cuts used to remove instrumental events is discussed extensively in [106], and summarized more recently in [107] and [108]. For the purposes of describing livetime calculations, the important thing to note is the fact that instrumental events often occur in bursts. Instrumental event bursts signal periods of time when the detector is potentially unstable, and a neutrino event would be less likely to be recorded properly. These periods of time are tagged through a set of "burst cuts", and removed from the data set.

## 5.3    The Burst Cuts

In addition to the event-by-event cuts to remove events based on their PMT, charge, and veto-tube information, an additional set of cuts address bursts of instrumental events. We define "burst" loosely, as a coincidence of multiple events within some small time window, or a period of high trigger rates relative to normal running conditions. Retrigger events occur within a time window of microseconds, while bursts of flashers or breakdown events can involve elevated event rates over many seconds or minutes. The cuts that remove clusters of instrumental events from the data address periods of time when the detector is potentially

unstable, or when conditions are otherwise suspect for recording good neutrino events.

A more general motivation for removing events that appear to be correlated in time is that solar neutrino events, occurring at a rate of only around 10 a day, have an extremely small probability of occurring in coincidence with other neutrino events. Any events that appear to cluster in time are due to backgrounds, instrumental or otherwise.[1] The burst cuts not only remove time periods that are abnormal, but also prevent any time-correlated backgrounds from contributing to the final data set.

Cosmic ray muon interactions are the most common source of time-correlated physics backgrounds. Energetic muons interacting in the detector can produce high energy secondary particles, which are unlikely to resemble solar neutrino events. However, muons can also generate neutrons through photodisintegration of deuterium or spallation of oxygen. Spallation and muon capture can produce radioisotopes whose subsequent decay products generate signals some time after the original muon event takes place. High-energy atmospheric neutrino interactions can also produce neutrons or excite nuclei that later decay. The strategy for removing muon or atmospheric neutrino "followers" from the data set is to define simple tags to identify the original events, and then to cut periods of time after these events. These cuts are part of a set of burst cuts that remove time from the data set.

Various algorithms are applied during data processing to identify periods of time that should be cut, and then all events that fall within those time windows are tagged and removed from later analysis. Corrections are made to the calculated livetime to subtract the "dead" time due to the burst cuts. The cuts are summarized below.

- *The Retrigger Cut:* When 2 events occur within 5 $\mu$s, the second event is cut.

- *The Nhit Burst Cut:* The Nhit burst cut removes periods of time in which 6 events with Nhit $> 40$ occur within four seconds, excluding retriggers. This cut primarily removes bursts of instrumental events.[2]

---

[1]This statement is not true for all physics analysis in SNO. For example, anti-neutrino interactions in heavy water will produce multiple physics events in coincidence. In this case, the coincident events may *be* the signal.

[2]A similar cut, called simply the Burst Cut, was also used in the $D_2O$ phase. It removed periods of time

- *Muon Follower Cut:* To avoid contamination of the neutrino sample with muon-related backgrounds, 20 seconds of time is cut from the data set after each tagged muon interaction in the detector. An event is tagged as a muon based on simple event characteristics such as a high Nhit and at least 5 hits in the OWL PMTs. The duration of the cut allows for two lifetimes of $^{16}$N, which can be produced by $(n, p)$ reactions or muon capture on $^{16}$O. Other radioactive spallation products are typically shorter-lived or very rare, so the 20 second cut limits contamination of the neutrino data set. An extensive discussion of secondary products of muon interactions can be found in [107].

- *"Missed Muon" Follower Cut:* Some muon interactions may escape the muon identification tag, due to their particular geometry. To eliminate secondary products from these interactions, as well as similar backgrounds due to atmospheric neutrino interactions, 250 ms of time is cut following every event in the detector that contains more than 150 PMT hits.

- *"Multiples" removed by hand:* Some atmospheric neutrino interactions may not be tagged by the presence of a high-Nhit event. In addition, anti-neutrino interactions, spontaneous fission processes, and $^{2}$H$(n, 2n)^{1}$H reactions can produce events that resemble solar neutrino interactions, but occur in coincidence with other events. In the salt phase, 11 "multiples" were observed, defined as two or more events that occur within a coincidence of 50 ms, where all events satisfy the data selection, fiducial volume, and energy cuts. The 28 events making up these 11 multiples were removed by hand, rather than by an automated burst cut in the data processing. The effect on livetime and on signal acceptance due to this cut is negligibly small. The cause of these time-coincident events is not entirely understood [109].

---

in which three events occurred within 3 ms, regardless of their Nhit values. It was found to be largely redundant with the Nhit burst cut. It is only mentioned here because of a related correction to the livetime calculations described in Section 5.5.

### 5.4 The "Junk Cut" and a Note on Orphans

The data selection cuts efficiently reject instrumental events, and the burst cuts cut periods of time affected by instrumental instability or time-correlated physics backgrounds. An additional cut that is applied to the raw data removes events that have been obviously mis-built in the data acquisition process. When PMT and MTC data is read in by the PMT Builder program, it is collected into events based on the GTID associated with each bundle of data. Hardware read errors and stuck bits on the GTID counters can lead to incorrect GTIDs being associated with individual PMT or MTC data bundles. In addition, a known hardware problem results in common GTID errors for PMT hits in events with GTIDs ending in 00 (hex).[3] GTID problems lead to mis-built data.

When the builder receives PMT bundles with GTIDs that do not match any MTC data currently in the Builder queue, these PMT hits are recorded as "orphans". Orphaned PMT hits are written to the data stream every two seconds or every time 80 orphan hits have been collected, in orphan "events" that lack valid trigger and timing information. Orphan events can also occur if MTC data has a corrupt GTID, because the associated PMT data can not be matched to any valid trigger data. If a PMT bundle has an incorrect GTID that happens to match another valid GTID that is currently in the Builder queue, that PMT hit will be mis-assigned to the valid event. This can occasionally result in a single PMT having multiple records in an event. Orphan events and any event with more than one record for a PMT are removed by the "junk cut".

A second problem involving event building is potentially more serious. Large bursts of instrumental events or HV breakdown problems can result in a spike in the data rate that can overwhelm the Builder or cause overflows of the hardware data-storage buffers before all information can be properly read out. In very high rate conditions, the Builder does not have enough memory to store the data long enough to collect all of the matching GTIDs, and events are sent to the data stream that are potentially incomplete. In extreme cases,

---

[3]This problem arises due to the time that it takes for the local GTID counters to roll over to increment a GTID that ends in 00. For PMT hits that take place early in the event (typically due to random noise), the individual channel timing cycle can end before the counter has completely rolled over. The upper bits of the GTID for these hits will be incorrect.

there is not enough time to assemble *any* of the PMT data with the MTC data, and all of the PMT hits are orphaned. In less extreme cases, events may be flushed to the data stream before the data from particular crates has been read out. The signature of such situations is a period with elevated orphan rates, while the number of PMT hits that are recorded in triggered events (events with valid MTC data) is suppressed. It can take tens of minutes for the readout and event building to catch up, before regular data taking can resume. Typically the detector operator ends the data run during this time in response to the problem, so these periods of "orphan bursts" are most common at the ends of runs.

An example of such an "orphan burst" at the end of a run is illustrated in Figure 5.1. During regular data taking, the rate of orphan events in the data stream is low, and orphan events usually consist of just a few orphaned PMT hits. After a major spike in the event rate, the Builder is incapable of properly assembling the large number of PMT data bundles with their trigger information. Triggered events saved to the data stream have few or no PMT hits associated with them, and these PMT hits are instead orphaned. Major orphan burst periods like the one in Figure 5.1 can affect the efficiency for detecting neutrinos if they are a frequent occurrence. Existing data selection cuts do not necessarily cut the affected events, since the events are often corrupted so much that they do not match any of the patterns used for identifying instrumental problems. The orphans will be cut by the junk cut, but the data will still contain a large number of empty or incomplete triggered event records. Inspection of the Builder log files for neutrino runs can identify any runs with extended problems involving event building, so that these runs are not used in analysis. Isolated occurrences of orphan bursts are treated with small corrections to the calculation of the time that the detector is live to neutrinos.

## 5.5   Livetime

Measurements of solar neutrino interaction rates in SNO require an accurate determination of the amount of time over which data has been taken. Any error in measurements of detector "livetime" will translate directly into an error in the measured neutrino fluxes. Livetime must also be calculated separately day and night and as a function of solar zenith

66

**Last 1000 Seconds of Run 24521**
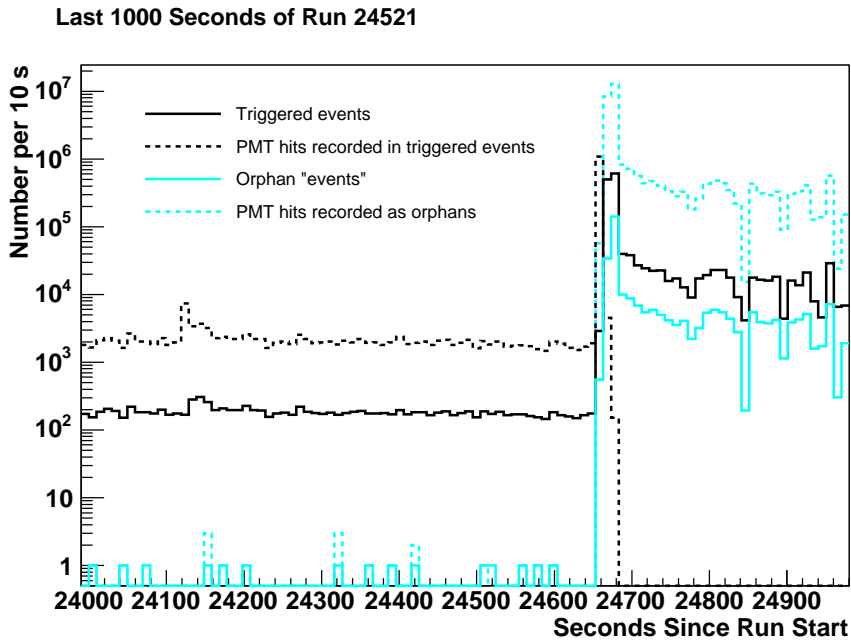


Figure 5.1: An example of a major "orphan burst" at the end of a run. After a spike in the trigger rate, the data acquisition system is overwhelmed and the PMT hits associated with events are "orphaned" instead of being correctly built. The event rate after the burst appears to still be high, but the events are mostly empty. Neutrino events occuring during this time period would likely be lost.

angle, for use in the day-night analyses and calculations of MSW parameter constraints. Livetime measurements must take into account data selection cuts that remove periods of time from the data. Small corrections are also applied to account for time affected by large bursts of orphan events.

### 5.5.1 Raw Livetimes

The raw livetime for a run is based on the 10 MHz clock. It is defined as the time between the earliest event and the latest event in a run. Because events are sometimes written to the data stream out of order, the earliest and latest events are not necessarily the first and last events recorded. There is a small amount of bias inherent in the use of the earliest and latest triggered events as the start and end of a run, since there will be some time in

each run before the first event and after the last. However, the maximum amount of time between two events is 0.2 seconds, because of the 5 Hz pulsed global trigger. The maximum amount of bias due to this method is therefore 0.4 s per run, which for the 1212 runs in the salt data set amounts to 485 seconds. In practice, the trigger rate of the detector is usually around 20 Hz, so the actual bias is much smaller.

The same method is used to construct raw livetimes based on the 50 MHz clock. Because the 50 MHz clock rolls over every two days, care is taken to account for rollovers in the calculation. The 50 MHz clock gives an independent verification of the 10 MHz clock livetimes, as long as both clocks are working properly. During the salt phase, damage to the fiberoptic cable carrying the 10 MHz signal corrupted the 10 MHz clock times for a number of runs. Event times in these runs were rebuilt in software using the 50 MHz clock, with a loss of an independent timing verification for those runs. For some runs near the end of the runlist, a local 10 MHz oscillator was used to replace the GPS-synchronized 10 MHz clock times until the fiberoptic cable to surface could be repaired.

The differences between the run-by-run livetimes measured with the two clocks are shown in Figure 5.2. For most runs, the agreement is better than two seconds, although most of the runs with exact agreement between the clock times are ones in which the 10 MHz times were rebuilt. The 50 MHz clock runs slightly slow (at 49.9995 MHz). When both clocks are running, typically the 10 MHz times are slightly longer, so the differences between the 10 MHz and 50 MHz times in Figure 5.2 are expected to be positive. The local 10 MHz oscillator that was used when the fiberoptic cable was broken was slightly slower than the 50 MHz clock, accounting for the negative values for the clock differences in Figure 5.2. These small systematic differences in clock times are essentially negligible for the overall livetime calculations.

A handful of runs exhibit discrepancies of tens or hundreds of seconds between the 10 MHz and 50 MHz clock times. The exact causes of these discrepancies are not understood. One possible cause is hardware read errors that affect the timing information recorded for particular events. The total amount of time represented by these discrepancies is so small that it is irrelevant for analysis.

An additional verification of the raw livetimes makes use of the pulsed global trigger
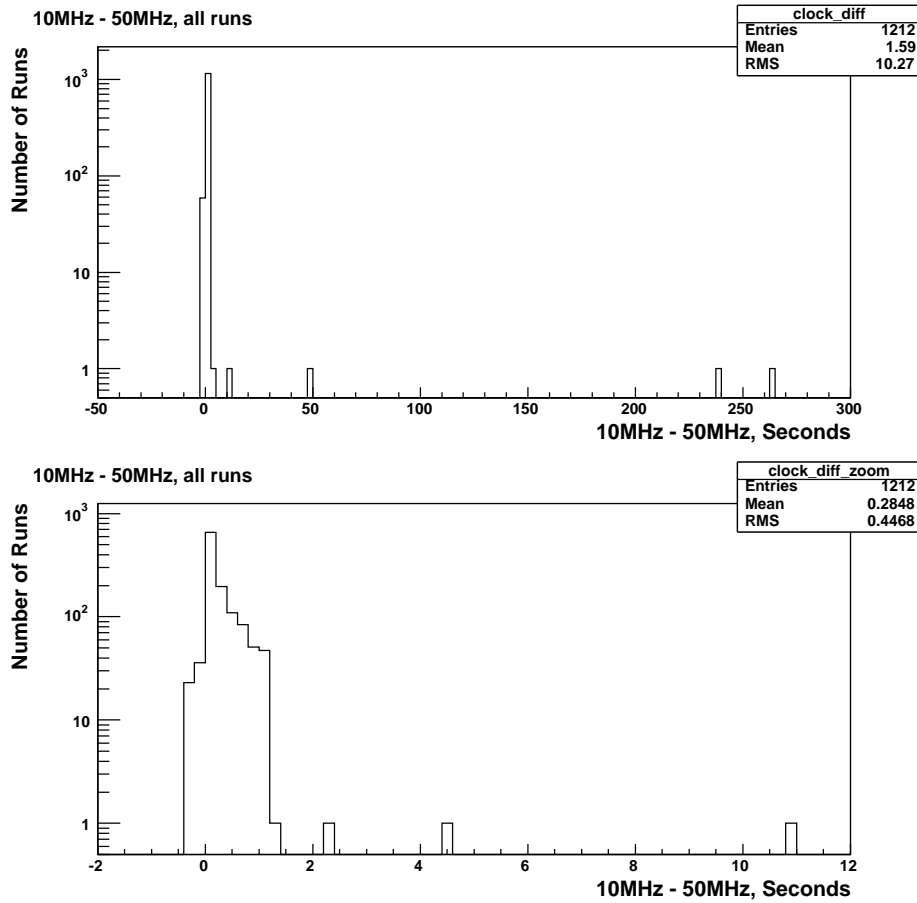
Figure 5.2: Differences between the run-by-run livetimes measured using the 10 MHz and 50 MHz clocks. The upper plot shows all runs, and the lower plot shows a restricted range of the same data.

(PGT) events in the data stream. The pulsed global trigger is issued at a frequency of 5 Hz, driven by the 50 MHz clock. A rough measure of the raw detector livetime can be made simply by counting all of the PGT events in the data set and dividing by 5. This is not independent of the 50 MHz clock times, and it is a coarser time measure than using the 10 MHz or 50 MHz clocks. However, it is a very simple technique that does not depend on events actually having the correct recorded times, since it requires only that the oscillator is still running and driving the pulsed trigger at 5 Hz. Two effects can potentially bias the PGT measurement. PGT triggers can be missed if the trigger for an event takes place in

Table 5.1: Raw livetimes for the 1212-run salt data set, measured using the 10 MHz and 50 MHz clocks and the PGT-counting method

| Measurement | Raw Livetime |
| --- | --- |
| 10 MHz Clock | 398.591 days |
| 50 MHz Clock | 398.581 days |
| PGT Count | 398.569 days |

coincidence with the pulsed trigger. When such a coincidence takes place, there will not be a record of the pulsed trigger in the data. However, for typical event rates, this should only happen around once every 400,000 events (slightly more often when the event rates are high). A trigger monitoring process that is sometimes run during data taking (called the "Nhit monitor") also prevents the recording of PGT triggers, but the PGT events in this case can later be identified and added back into the PGT counting.

A comparison of the raw livetimes calculated using the 10 MHz and 50 MHz clocks and the PGT counting method is shown in Table 5.1.

### 5.5.2  Cut-Corrected livetimes

During data processing, raw 10 MHz and 50 MHz livetimes for each run are calculated and stored, as well as the amounts of livetime removed by data selection cuts. Conditions for several data selection cuts can be met simultaneously, so "overlaps" between the cuts must be carefully accounted for when the cut-corrected final livetimes are calculated. The Livetime Summary Processor (LSP) in SNOMAN accesses stored information about periods of time removed by each cut and compiles the livetime and cut-related "deadtime" as a function of time, handling all of the overlaps between cut periods. LSP livetimes are based on the 10 MHz clock, and can be calculated using a very fine time binning. The LSP cut-corrected livetimes calculated with a 0.01-second time binning are used for the final SNO livetimes. A detailed discussion of the LSP processor and definitions of cut-related deadtime can be found in  [106]

Table 5.2: Summary of raw and corrected livetime, for all 1212 runs in the salt data set. The total cut "deadtime" does not equal the sum of the individual deadtimes due to overlap between the cuts. The burst cut should not have been included in the deadtime calculation, but inadvertently was included. The corrected livetime includes a correction for orphan-related deadtime, described in Section 5.4.

| Measurement | Time | % of Raw Livetime |
|---|---|---|
| Raw 10 MHz Livetime | 398.591 days | 100% |
| Raw 50 MHz Livetime | 398.581 days | 100% |
| Burst Cut | 3869.70 sec | 0.011% |
| Retrigger Cut | 47.53 sec | $1.38 \times 10^{-4}\%$ |
| NHIT Burst Cut | 15709.50 sec | 0.046% |
| Muon Follower Short | 6.741 days | 1.7% |
| Missed Muon Follower Short | 25350.35 sec | 0.074% |
| Combined Runlogger Deadtime | 7.110 days | 1.816% |
| Orphan-Related Deadtime | <5204 sec | 0.012 % |
| Corrected Livetime | 391.432 days | 98.2% |

A comparison of the amounts of time cut by each of the data-selection cuts in the salt phase is shown in Table 5.2. In the LSP livetime calculations for the salt phase, a data-selection cut called the "Burst Cut" was accidentally included, although it was not applied to the final data set. The Burst Cut cuts at most only 3870 seconds the data in the full salt data set, so rather than repeating the LSP livetime corrections, the maximum amount of time cut by the burst cut is taken to represent a small systematic uncertainty in the final livetimes.

The muon follower cut dominates the cut-related deadtime, removing nearly 2% of the total livetime. The fractional time removed by the data-selection cuts on a run-by-run basis is shown in Figure 5.3. Runs with outlying values tend to be short, such that the fractional deadtime is more sensitive to statistical fluctuations in the muon rate.

The PGT-counting method for verifying livetime is particularly valuable for checking cut-
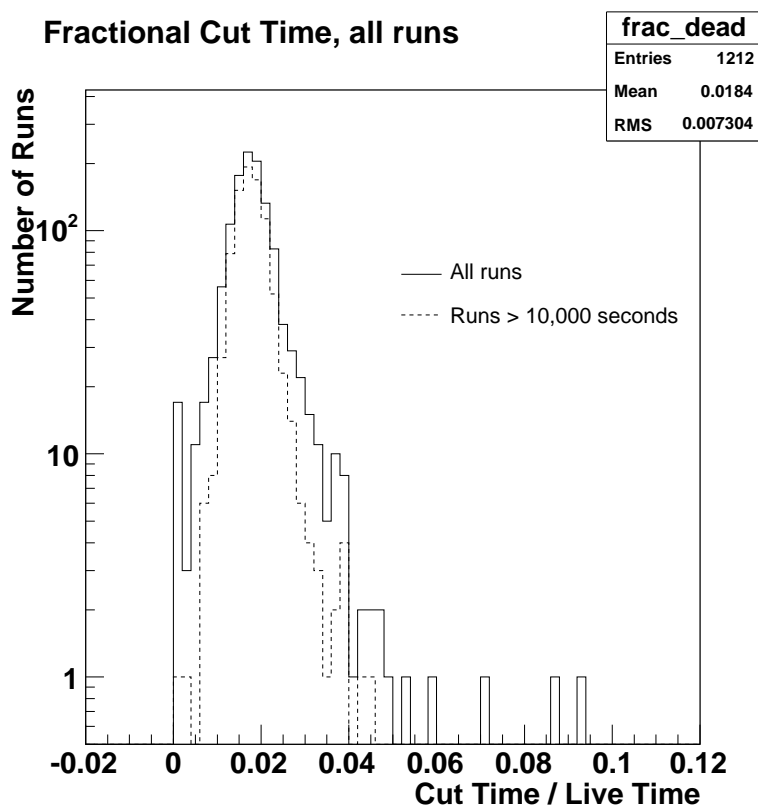
Figure 5.3: Fraction of the time in each run that is cut by data selection cuts. The dashed line shows only those runs with raw livetimes greater than 10,000 s. The distribution is narrower for runs that are longer, indicating that outliers are due to short runs. Fluctuations in the muon rate can have a larger effect on the fractional cut time for shorter runs.

corrected livetimes. All events that fall into time windows that are cut by data-selection cuts are tagged in the processed data structure that stores the events. By counting the number of PGT events that have been tagged by the data selection cuts, a coarse measure can be made of the cut-related deadtime. The PGT measurement of cut-corrected livetimes does not require complex calculations to include overlaps between the cuts, since it simply collects the number of events that are tagged by any of the data-selection cuts. Comparisons of the cut-corrected PGT and LSP livetimes are shown in Figure 5.4. About a dozen runs have differences between the LSP and PGT cut-corrected livetimes in excess of 50 seconds. These differences are not understood in all cases, although they may be due to PGT triggers

being lost due to coincidences with other events. This is particularly likely to happen during extremely high rate conditions, such as those caused by large instrumental bursts. However, even these differences are small enough that they are essentially insignificant. Cut-corrected livetimes are summarized in Table 5.3.
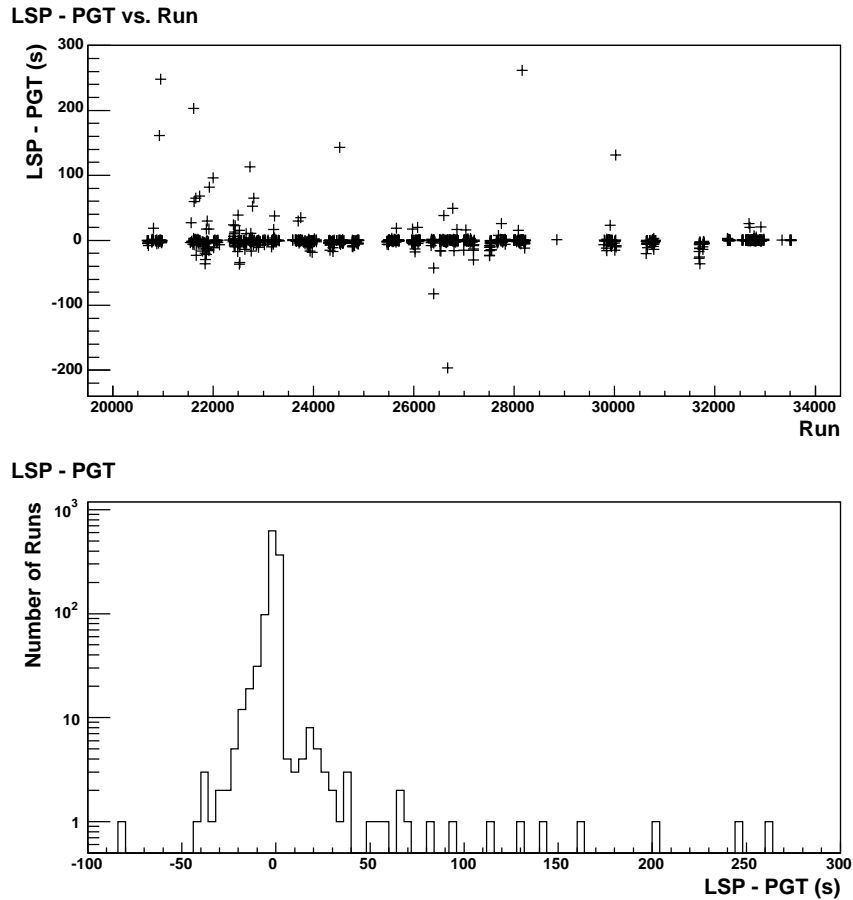


Figure 5.4: Run-by-run differences in the LSP cut-corrected livetimes and the PGT cut-corrected livetimes, shown as a function of run number and as a histogram for all of the runs in the salt phase data set. The run number is a 5-digit sequential identification number for each data run

.

The total livetimes appear to agree to within 0.002 days, or approximately 170 seconds. This level of agreement is artificial, however, since the LSP livetimes incorrectly include up

Table 5.3: Cut-corrected livetimes for the 1212-run salt data set, calculated by the LSP processor in SNOMAN and using the PGT-counting method. Orphan burst periods have not been subtracted, but all time cut by data-selection cuts has been subtracted.

| Measurement | Cut-Corrected Livetime |
|---|---|
| LSP | 391.481 days |
| PGT Count | 391.483 days |

to 3870 seconds of Burst Cut deadtime. Additionally, the fact that the 50 MHz clock is slightly slow would mean that the PGT livetimes should be longer by about 340 seconds. So the actual difference between the LSP and PGT time measurements for the full data set is probably closer to 4000 seconds (0.05 days). This difference is reasonably explained by PGT triggers being lost due to coincidences with other events. We will take the difference between the PGT and LSP livetimes (with the burst cut deadtime added back in to the LSP measurement to avoid double-counting) as an estimate of the maximum actual difference between the two measurements, and apply it as a small systematic uncertainty in the LSP results.

### 5.5.3  Orphan Corrections

As described in Section 5.4, the extreme event rates associated with large bursts of instrumental events can overwhelm the data acquisition system. In such situations, events may not be properly assembled by the Builder and some time may be effectively "dead" for the detection of neutrino events. Unfortunately, no robust technique has yet been determined for automatically identifying and cutting these periods from the data. However, they represent only a small correction to neutrino livetime. The amount of affected time has been estimated by searching for time periods during which the overall number of PMT hits being recorded in triggered events drops below 50% of the average value for the run, accompanied by an increase in the rate of orphan events. In the salt phase data, occasional event rate instabilities sometimes mimic these conditions, so hand-scanning was necessary to identify

the periods of mis-built data. A conservative estimate of the total time affected amounts to $< 5204$ s. Overlaps between the affected periods and existing data cuts can be subtracted using the PGT-counting method, and the final amount of orphan-related "deadtime" that is not cut by existing cuts is estimated to be $< 4186.6$ s. The final livetimes are corrected to account for this effect. Because of the inherent uncertainty in identifying periods of time affected by orphan bursts, a generous estimate of the maximum amount of time affected by orphan bursts is taken as a systematic uncertainty in the total livetime measurement.

### 5.5.4  Final Salt Livetime

With orphan burst periods subtracted, the total livetime for the salt phase is 391.432 days. Three sources of uncertainty are included in the final livetime estimates: uncertainty due to the difference between the LSP and PGT measurements, uncertainty in the final LSP livetimes due to the misapplication of the Burst Cut, and uncertainty in the effects of orphan bursts on livetime. These are of comparable size, so no single uncertainty dominates. When the burst cut dead time is added back into the total LSP time, the discrepancy between PGT and LSP livetimes amounts to 0.013% of the total salt livetime. Uncertainty in livetime due to the misapplication of the burst cut in the LSP calculations is 0.012% of the total salt livetime. The uncertainty due to orphan-related problems is estimated to be 0.011%. Added in quadrature, these sources of uncertainty lead to a total estimated systematic uncertainty of 0.021% on the final livetime. This is small enough that the livetime uncertainty has no effect on the major physics results in the salt phase.

### 5.5.5  Differential Livetimes

For the day-night solar neutrino measurements, livetimes must be separately calculated in two time bins. "Day" is defined as any time when the sun is above the horizon, and "night" as any time when the sun is below the horizon. The location of the sun relative to the detector zenith can be characterized by the solar zenith angle, which is the angle between the vector to the sun's position and the detector zenith. The cosine of the zenith angle is positive during the day, negative at night, and zero when the sun crosses the horizon. The

Table 5.4: Raw and cut-corrected livetimes for day, night, and day + night, calculated by the LSP processor in SNOMAN and using the PGT-counting method. The amounts of time subtracted to account for orphan bursts are also given, as well as the final orphan-corrected LSP livetimes, with 0.021% systematic uncertainties. When the entries in the day and night columns do not appear to add up exactly to the entry in the "total" column, it is due to rounding in the final digit.

| Measurement | Day | Night | Total |
|---|---|---|---|
| LSP Raw | 179.831 days | 218.760 days | 398.591 days |
| PGT Raw | 179.818 days | 218.750 days | 398.569 days |
| LSP Cut-Corrected | 176.535 days | 214.946 days | 391.481 days |
| PGT Cut-Corrected | 176.534 days | 214.947 days | 391.483 days |
| Orphan bursts | 2035.4 s | 2156.2 s | 4191.6 s |
| Final Livetimes | $(176.511\pm0.037)$ days | $(214.921\pm0.045)$ days | $(391.432\pm0.082)$ days |

determination of whether time during a run takes place during the day or the night depends only on knowledge of the absolute time, which is used to calculate the location of the sun. Since the absolute time is known very accurately and the LSP livetimes are calculated in fine bins of 0.01 seconds, there is essentially no uncertainty in the splitting of livetime into the two time bins.

Livetimes were calculated separately day and night using the LSP processor and verified using the PGT counting method. Day and night livetimes are subject to a 0.021% systematic uncertainty, similar to the full livetime, since there are no significant differences in the sources of systematic uncertainty day and night. Day, night, and total livetimes are summarized in Table 5.4. Calibrations and maintenance work on the detector take place primarily during the day, so a larger fraction of the total neutrino livetime is at night.

Livetimes calculated in many bins with respect to the solar zenith angle are required for calculating the predicted neutrino fluxes in MSW neutrino oscillation models. A comparison of the LSP and PGT cut-corrected livetimes for 24 zenith angle bins is shown in Figure 5.5,

76

which also shows the amount of time cut from the data and the amount of time affected by orphan bursts as a function of zenith angle. There are no apparent zenith-angle dependencies in the amount of time cut, the degree of agreement between LSP and PGT times, or the frequency of orphan bursts. The largest bin in the distribution of orphan-burst deadtime in Figure 5.5 is dominated by an extended (700 second) orphan burst at the end of a single run.
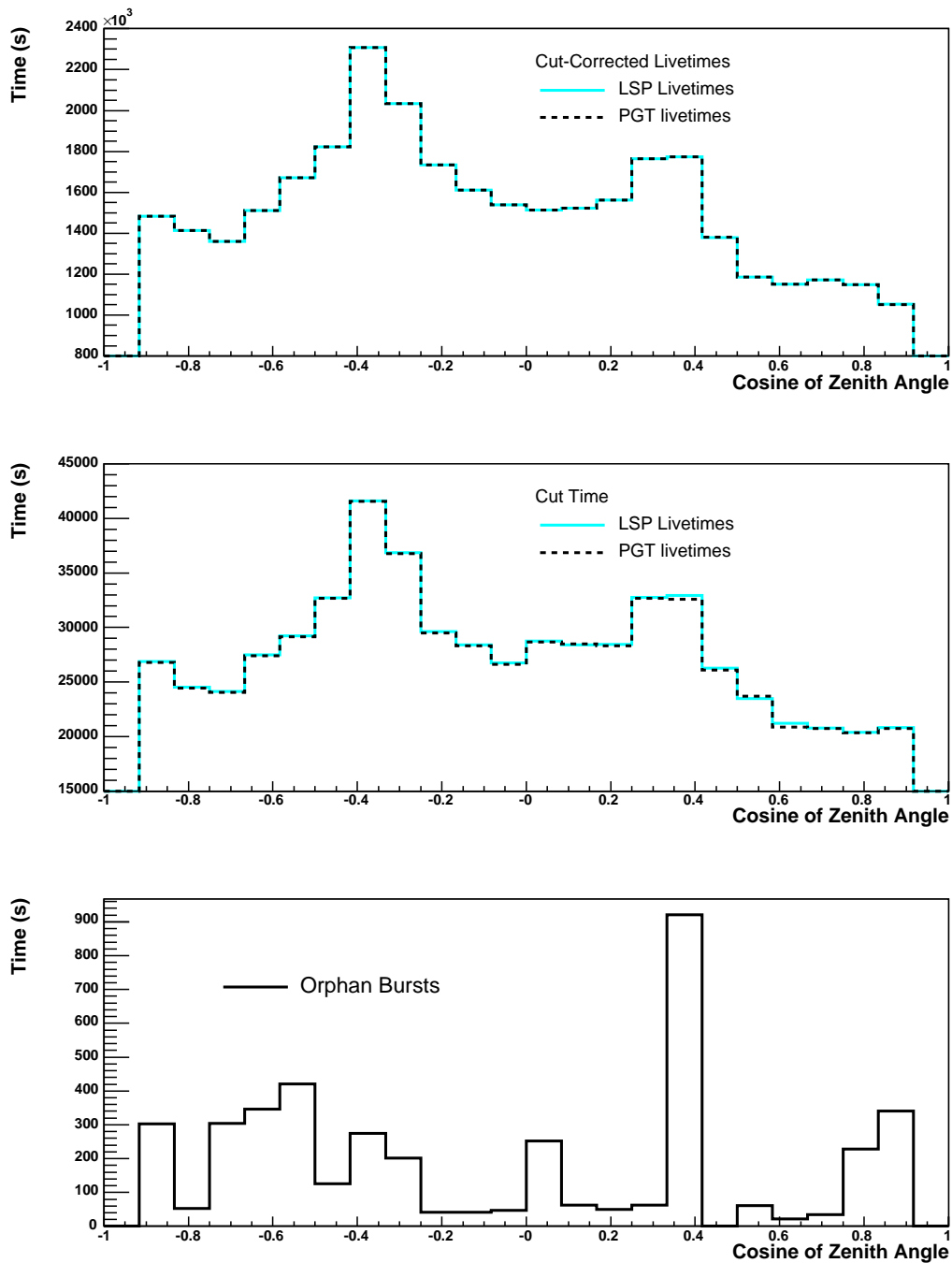
Figure 5.5: Cut-corrected livetime as a function of zenith angle (top panel). The lower two figures show the time cut by data cuts and the corrections due to orphan bursts as a function of zenith angle.

Chapter 6

# THE SALT PHASE DATA SET

## 6.1 Overview

During data processing, all data selection cuts are applied, and event energies, positions, and directions are assigned. Event vertices and directions are reconstructed based on the timing of the PMT hits in each event, and event energies are estimated using the reconstruction information along with the total number of PMT hits in the event. Reconstruction and energy estimation require inputs from calibration and Monte Carlo, as well as a run-by-run description of specific detector conditions. A number of additional derived quantities are also calculated during data processing, including the direction of the event relative to the location of the sun, and the values of parameters characterizing the "isotropy" of the light detected in the event.

The reconstructed, reduced data set consists primarily of neutrino events and low-energy backgrounds. Radioactive background events populate the low-energy end of the event spectrum, and are much more prevalent in the outer regions of the detector. Fiducial volume and energy threshold cuts largely isolate the neutrino events from these backgrounds. Extensive study is then performed to estimate the residual contribution of backgrounds to the neutrino data set after all data selection and fiducial volume cuts have been applied. After enormous amounts of work by a variety of working groups within the collaboration, the final data set consists of calibrated, reconstructed neutrino events and a small number of well-characterized backgrounds. With the data set, background estimates, an accurate livetime, and a series of Monte Carlo simulations of signal and background properties, the basic ingredients are in place to extract solar neutrino physics, through the procedure outlined in chapter 8.

## 6.2  Reconstruction and Energy

Over the course of the SNO experiment, a number of different event vertex and direction reconstruction algorithms have been studied and employed in analysis. The reconstruction algorithm used in this thesis is the same as the one used for salt phase publications, and is described more extensively in [110].

When a physics event takes place in the detector, Cherenkov light from one or more electrons impinges on a collection of PMTs. The timing of the individual PMT hits can be used to reconstruct the location from which the light originated. If $\vec{x}_{fit}$ is the vector representing the reconstructed ("fit") location of the event with respect to the detector center, and $\vec{x}_{PMT}$ represents the location of a particular PMT, we can define a "time residual",

$$T_{\mathrm{res}} = T_{\mathrm{pmt}} - T_{\mathrm{fit}} - \frac{|\vec{x}_{fit} - \vec{x}_{PMT}|}{c_{avg}}, \tag{6.1}$$

where $T_{\mathrm{fit}}$ is the fitted event time, $T_{\mathrm{pmt}}$ is the time when the PMT was hit, and $c_{avg}$ is the mean photon group velocity. The fitting procedure searches for the event vertex time $T_{fit}$ and position $\vec{x}_{fit}$ that minimizes the time residuals for the PMT hits in the event. This is accomplished using a maximum likelihood fit to a probability density function (PDF) describing the expected time residual distribution. The PDF is derived from Monte Carlo simulations and laserball calibration data, and is dominated by a primary peak of in-time light, with a width of $\sim 1.5$ ns. The time residual distribution also has early and late peaks due to pre-pulsing and after-pulsing in the PMTs, as well as structures representing reflected and scattered light. The more complex late-light structures are approximated as a constant for large time residuals ($> 15$ ns), and an overall offset is chosen to match the rate of noise hits.

The direction of the event is reconstructed after the location of the event vertex has been determined. A second maximum likelihood fit is performed, using a PDF based on Monte Carlo simulations. The fit determines the event direction that best reproduces the PMT hits in the event, under the assumption that the light is radiated by a single electron, at a Cherenkov angle of $\sim 42°$. Event direction is primarily important for identifying the electrons produced in the ES reaction, which are typically single Cherenkov cone events.

### 6.2.1  Energy Estimation

The most straightforward measure of an event's energy is simply the number of photomultiplier tubes that register light due to that event (the Nhit value for the event). For events in the MeV range, the number of hit PMTs is essentially a count of the number of Cherenkov photons produced by the particle, which is proportional to its energy. However, the actual number of hit PMTs in an event is a function of the event position and direction as well as its energy, due to variations in photon attenuation and PMT efficiency as a function of event position/direction. The strategy for assigning calibrated energies to events is to model the dependence of the photon collection efficiency as a function of event position and direction, and then to correct the number of hits in a given event to the expected number of hits had that event been at the center of the detector. The corrected Nhit value is then translated to an estimated energy in MeV using a "look-up table" generated from Monte Carlo simulations of electron interactions. The absolute scale of the energy conversion is set by comparison to data from the $^{16}$N calibration source. Only prompt PMT hits in an event are included in the energy calibration process, defined as those that arrive within $\pm 10$ ns of the reconstructed event time. Reflected, or "late", light is much more difficult to characterize. The PMT dark noise is taken into account, which adds roughly 2 PMT hits per event (although these are not likely to be prompt hits).

### 6.2.2  Event Observables

After data processing, reconstruction, and energy estimation, each event is assigned values for several "event observables" that are derived from the raw data for the event. The event-by-event quantities that we will use in later analysis are:

- *Effective Kinetic Energy:* The energy estimation process determines the total energy $E$ associated with each Cherenkov event. For analysis, we use an energy variable $T_{eff} = E - 0.511$, which is the effective kinetic energy for the event under the assumption that the light comes from a single energetic electron.

- *Weighted Radial Position:* The radial position $r$ for the reconstructed event vertex is calculated. A radial parameter $\rho = (r/r_{AV})^3$ is used to characterize radial profiles in the detector, where $r_{AV} = 600.5$ cm is the radius of the AV. Signals that are distributed isotropically throughout the spherical detector volume will have "flat" distributions in the $\rho$ variable.

- *Isotropy:* A variety of methods exist for parameterizing the isotropy of the distribution of light in an event. For the salt analysis, a parameter called $\beta_{14}$ was chosen. The $\beta_{14}$ parameter efficiently separates neutron-like and electron-like events, and also allows a relatively simple propagation of systematic uncertainties. $\beta_{14}$ is described extensively in [111].

  For an individual event, the position of each PMT hit $i$ can be described by a vector $\vec{x}_i$ defined relative to the reconstructed event vertex. If an event produces light that is spread out over a large portion of the detector, the angle between two individual PMT position vectors $\vec{x}_i$ and $\vec{x}_j$ will, on average, be relatively large. For events with less isotropic light distributions, the average angle $\theta_{ij}$ between pairs of PMT hits $\vec{x}_i$ and $\vec{x}_j$ will be smaller. The spatial distribution of PMT hits can be described in terms of Legendre polynomials $P_l$ in the cosine of the pair-wise angle $\theta_{ij}$ between PMT hits in an event. The "beta parameters" are functions of these Legendre polynomials,

  $$\beta_l = \frac{2}{N(N-1)} \sum_{i=1}^{N-l} \sum_{j=i+1}^{N} P_l(\cos\theta_{ij}), \tag{6.2}$$

  where N is the total number of hit PMTs in the event. The parameter

  $$\beta_{14} \equiv \beta_1 + 4\beta_4 \tag{6.3}$$

  is used in the salt analysis. This parameter was chosen because it provides good separation between neutron-like and electron-like events, and allows simple parameterizations for propagating systematic uncertainties. Events that are more isotropic have *smaller* values of $\beta_{14}$.

- *Direction relative to the sun:* For each event, the direction of the Cherenkov-radiating particle(s) is estimated. For solar neutrino analysis, the coordinate system that is most

useful for describing the direction of an event is one defined relative to the position of the sun. Elastic scattering events will tend to be peaked in the direction defined by the vector from the sun to the event vertex. Charged-current events will be slightly backward peaked in this coordinate system, while neutral current events will have no directional preference. For each event, the location of the sun is calculated based on the event time, and the direction is expressed as a cosine of the angle between the event trajectory and the solar position, $\cos\theta_\odot$, defined such that the forward-peaked elastic scattering neutrino events have $\cos\theta_\odot \sim 1$.

- *Time and Zenith Angle:* The time of each event is stored in several formats. For the day-night analysis, the relevant quantity is the position of the sun with respect to the detector zenith at the time when the event was detected. For each event, we define the "zenith angle" $\theta_Z$ as the angle between the detector zenith and the vector from the center of the detector to the solar position. For each event, the value of $\cos\theta_Z$ is stored. Events during the day have positive values of $\cos\theta_Z$ and events during the night have negative values. During the night, the zenith angle associated with a given neutrino event determines how much of the earth the neutrino passed through to reach the detector.

Different classes of events in the data set will have different distributions in these variables, allowing the various contributions to be statistically separated. This is important for many of the analyses of backgrounds as well as for the final extraction of solar neutrino signals.

## 6.3   Backgrounds

The dominant backgrounds in the data set are due to radioactivity in the detector materials. The $D_2O$ itself is the "cleanest" part of the detector, while the AV, $H_2O$, and the PMTs have higher levels of radioactive contaminants. The number of background events detected is therefore largest at higher radii. A fiducial volume cut of $r < 550$ cm or $\rho < 0.77$ eliminates many of these backgrounds. The number of observed Cherenkov events due to

$\beta - \gamma$ decays increases at lower energies, so an energy cut of $T_{eff} > 5.5$ MeV additionally restricts the number of backgrounds. The fiducial volume and energy cuts are illustrated in Figure 6.1.
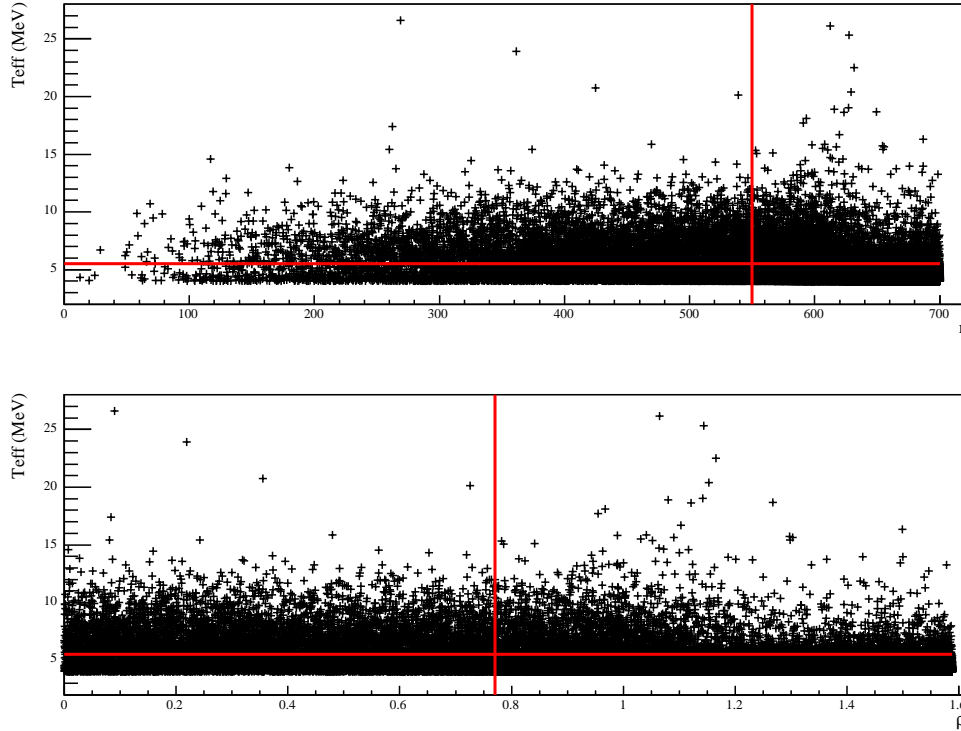


Figure 6.1: Scatter plot of $T_{eff}$ vs. radius for events above $T_{eff} =4$ MeV and within 700 cm. The bottom plot shows the same thing, but using the $\rho$ radial variable, defined as $(r/600.5)^3$. The lines show the analysis energy threshold at 5.5 MeV and the fiducial volume cut at $r = 550$ cm.

A variety of analysis techniques are used to characterize sources of backgrounds and to evaluate the number of background events in the final fiducial volume and energy range. Levels of backgrounds can vary as a function of time. For the day-night analysis, the backgrounds need to be separately characterized day and night. Variations in background levels over a variety of time scales could potentially alias into day-night variations because of the specific time sampling of the runs in the salt data set, so the average rate of backgrounds in the day and night portions of the data need not be the same. Background studies are done

separately on the full day and night portions of the salt data set, and an overall day-night asymmetry in the estimated numbers of events is calculated.

Suppose that a particular background source contributes $N$ events within the signal region. The analysis can then be repeated to determine the numbers of events that occur during the day and during the night, $N_D$ and $N_N$. Rather than characterize the number of background events separately day and night, we can also characterize them in terms of the total, $N$, and the day-night rate asymmetry $A$,

$$A \equiv 2\frac{(\frac{N_N}{T_N} - \frac{N_D}{T_D})}{(\frac{N_N}{T_N} + \frac{N_D}{T_D})}, \tag{6.4}$$

where $T_N$ and $T_D$ are the night and day livetimes. This is a more convenient parameterization for separating systematic uncertainties in the total background rates from systematic uncertainties in the day-night split. If $N$ and $A$ are known for a particular background, we can calculate the day and night numbers of events using:

$$
\begin{aligned}
N_D &= N\frac{(2-A)T_D}{A(T_N - T_D) + 2(T_N + T_D)} \\
N_N &= N\frac{(2+A)T_N}{A(T_N - T_D) + 2(T_N + T_D)}.
\end{aligned} \tag{6.5}
$$

Background studies for the salt phase are described in [38]. The day-night asymmetries in background rates are considered in reference [112]. The background sources and the estimated numbers of events in the final data set are summarized below, as well as the day-night asymmetries estimated for each source.

### 6.3.1  Instrumental Backgrounds

The set of cuts designed to remove individual instrumental events and bursts of instrumental events is very effective. However, some instrumental events may still remain after all of the "low-level" cuts are applied. Two additional "high-level" cuts are placed on the reconstructed data, requiring that the events have isotropy and timing properties that are characteristic of Cherenkov light. Neutrino candidate events are required to have $\beta_{14}$ values between -0.12 and 0.95, and greater than 55% of their PMT hits occurring in a prompt timing window (between -2 and 5 nanoseconds around the fitted event time). These cuts help to eliminate the "AV events" as well as other instrumental events from the final sample.

After the application of the high-level cuts, very few instrumental events remain in the data set. The residual contamination with instrumental events is estimated to be less than 3 events, using a "bifurcated analysis" that is described in [108]. The acceptance of the low-level and high-level cuts for neutrino events is estimated using calibration data and Monte Carlo simulations.

In the $D_2O$ phase, the AV events could be efficiently cut from the data using an isotropy cut, but this cut was relaxed in the salt phase to account for high-isotropy neutron capture events. Two methods were used to estimate the number of AV events in the final data set, one based on fitting the data isotropy distributions to the expected distributions for CC and NC events, and the other based on estimates of the AV background in the $D_2O$ phase. An upper limit of 6.55 AV events is derived from a combination of the two analyses.

The $< 3$ event contamination due to instrumental events is so small that the day-night asymmetry is barely relevant, but it has nevertheless been estimated as $(-18 \pm 65)\%$. For the AV events, the asymmetry is estimated to be $(68 \pm 31)\%$.

### 6.3.2   Internal Photodisintegration Backgrounds

Small amounts of uranium and thorium persist in the heavy water despite extensive purification. $^{208}$Tl from the $^{232}$Th chain and $^{214}$Bi from the $^{238}$U chain can both emit gamma rays with energies above the 2.2 MeV required to break up the deuteron. The neutrons produced from these photodisintegration reactions cannot be distinguished from the neutrons produced by NC neutrino interactions. The levels of these backgrounds must be measured independently to determine their contribution to the final data set.

Regular assays of the water are used to make "ex-situ" measurements of the levels of radioactive contaminants. Three techniques are used to measure the levels of precursor isotopes to Tl and Bi in the heavy water, as described in  [93],  [94], and  [95]. A total of 22 assays took place throughout the duration of the salt phase.

An independent measure of the levels of Bi and Tl comes from "in-situ" analysis of the low-energy data. In the energy window $4 < T_{eff} < 4.5$, the decays of $^{208}$Th and $^{214}$Bi are the dominant contribution to the event rate. $^{208}$Tl decay events tend to produce light that

is more isotropic than that produced by $^{214}$Bi, and this difference is used to statistically extract the contributions from each background in the restricted energy window. The extracted numbers can be converted to equivalent concentrations of U and Th (assuming secular equilibrium) and compared with the results from the ex-situ techniques. The in-situ analysis gives concentrations of $0.85^{+0.44}_{-0.42}$(stat.)$^{+0.42}_{-0.44}$(syst.)$\times 10^{-15}$ g Th/g D$_2$O and $8.28^{+0.83}_{-0.81}$(stat.)$^{+1.10}_{-1.94}$(syst.)$\times 10^{-15}$ g U/g D$_2$O [38].

Results from the in-situ and ex-situ techniques are consistent with each other, and can be combined to estimate the number of photodisintegration backgrounds due to internal radioactivity in the final data set. A total of $91.3^{+30.4}_{-31.5}$ neutron events are estimated to be present in the data set.

In the salt phase, $^{24}$Na can be produced by neutron capture on $^{23}$Na in the heavy water brine. $^{24}$Na decays with a half life of 15 hours, releasing a 2.75 MeV gamma that is another source of internal photodisintegration neutrons. $^{24}$Na activation can take place in the neck region of the detector, or during the recirculation of the heavy water. In the neck region and in the external water systems, the heavy water is not as well shielded against ambient neutrons. Activation also occurs in the detector volume when some calibration sources are deployed. Estimates of the total contribution of photodisintegration neutrons from $^{24}$Na give 10.2±2.5 events in the signal region.

The total internal photodisintegration neutron background is $101.5^{+30.7}_{-31.8}$ events. For the $^{214}$Bi and $^{208}$Tl photodisintegration backgrounds, the in-situ measurement technique was used to separately determine the day and night neutron production rates. The $^{24}$Na analysis was also repeated day and night. Combined, the day and night photodisintegration backgrounds from the three sources have a day-night asymmetry estimated at $A = (23 \pm 29)\%$.

### 6.3.3 Internal Cherenkov

Betas and gammas from U and Th chain decays also produce Cherenkov radiation in the detector. Although the energy released in these events is below the energy threshold used for analysis, the energy resolution of the detector is broad enough that a small number of

these events appear to have energies within the signal region.

To calibrate response to Cherenkov backgrounds, a controlled quantity of $^{222}$Rn was injected into the D$_2$O and allowed to decay. The energy distribution of the "radon spike" data was fit to Monte Carlo distributions to extract the ratio of Cherenkov backgrounds to photodisintegration neutrons for U and Th chain contaminants. This was then combined with the measured photodisintegration background values to obtain a total of $3.6^{+1.0}_{-0.9}$ Cherenkov background events in the final data set. The day-night asymmetry is $A = (42 \pm 36)\%$.

### 6.3.4 External Cherenkov

Radioactivity in the materials outside the heavy water can also lead to Cherenkov events in the data set, when gamma rays travel into the fiducial volume or mis-reconstruction accidentally places them there. The external Cherenkov background was modeled with a set of radial probability density functions derived from uranium and thorium calibration sources and a controlled radon spike in the H$_2$O region. Fits of the data to these distributions give upper limits on the contributions of external Cherenkov backgrounds from the AV, H$_2$O, and PMTs. The combined upper limit for Cherenkov backgrounds in the signal region is 18.5 events, with a day-night asymmetry of $(10 \pm 16)\%$.

### 6.3.5 Other Backgrounds

A variety of additional background sources may also contribute events in the signal region. These include alpha reactions on materials in the detector, cosmic ray spallation products that have not been cut from the data, fission products from $^{238}$U, and reactor and atmospheric neutrinos. More detail can be found in [107] and [38].

The total number of neutrons from "other" backgrounds is estimated to be $23.6^{+21.4}_{-5.3}$, with $15.8^{+21.3}_{-4.6}$ of these coming from atmospheric neutrino interactions. The large positive uncertainty on the atmospheric neutrino backgrounds accounts for disagreement between atmospheric neutrino Monte Carlo calculations and the number of multiplets of events in the data set (see Section 5.3). Atmospheric neutrino products also contribute an estimated $3.2^{+4.6}_{-4.4}$ gamma rays events to the final data set, from excitation of $^{16}$O. The major sources

of "other backgrounds" are not expected to vary diurnally,so the day-night asymmetry on these neutrons and gammas is taken to be zero.

### 6.3.6   External Neutrons

In addition to contributing to the "external Cherenkov" backgrounds, radioactivity associated with the AV can produce neutron backgrounds, through photodisintegration or $(\alpha, n)$ processes. These neutrons will have a distinct radial profile in the salt data, falling off toward the interior of the detector. In contrast, the neutrons produced by NC interactions and those produced by internal photodisintegration backgrounds have an essentially flat radial profile. The contribution of external neutron backgrounds to the data set is determined in the same fits that are used to extract the neutrino signal contributions to the data set, by including a probability distribution function that models the radial distribution of external neutrons. The PDF is derived from Monte Carlo simulations.

### 6.3.7   Background Summary

Table 6.1 summarizes all of the backgrounds evaluated for the salt phase, with their day-night asymmetries, with the exception of the external neutrons. The external neutron backgrounds are determined in the final signal extraction fits that are used to separate the solar neutrino signals.

## 6.4   The Final Data Set

After all data selection cuts and fiducial volume cuts, the data set contains 4722 events above an energy of $T_{eff} = 5.5$ MeV and within a radius of 550 cm. The expected contributions of backgrounds to this data set were summarized in the previous section. Of these 4722 events, 2134 were detected during the day and 2588 during the night. The event rates and the day-night rate asymmetry, defined according to Equation 6.4, are given in Table 6.2.

The distributions of the day, night, and total data sets in the variables $T_{eff}$ , $\rho$ , $\beta_{14}$ and $\cos\theta_\odot$ are shown in Figures 6.2 and 6.3. The number of events and the event rate are shown as a function of zenith angle in Figure 6.4.

Table 6.1: Estimated numbers of background events in the salt data set, with day-night asymmetries and uncertainties for all major sources of background. From [112]. The day-night asymmetries have been obtained by repeating the analysis used to estimate the total background values, using the day and night data separately. The asymmetries have been assumed to be zero for the "other neutron" and "internal $\gamma$" backgrounds.

| Background | Total number of expected events | Asymmetry (%) |
|---|---|---|
| Instrumental Contamination | $< 3$ (95% CL) | $A = -18 \pm 65$ |
| AV Events | $< 6.55$ | $A = 68 \pm 31$ |
| AV $\beta - \gamma$ | $< 7$ | $A = -27.5 \pm 33.4$ |
| H$_2$O $\beta - \gamma$ | $< 3$ | $A = -3.0 \pm 2.0$ |
| PMT $\beta - \gamma$ | $< 11$ | $A = 1.9 \pm 3.1$ |
| Sum of external $\beta - \gamma$'s | $< 18.5$ | $A = -10 \pm 16$ |
| Internal photodisintegration | $101.5^{+30.7}_{-31.8}$ | $A = 23 \pm 29$ |
| Internal Cherenkov tail | $3.64 \pm 0.81^{+0.62}_{-0.31}$ | $A = 42 \pm 36$ |
| Other neutron backgrounds | $23.6^{+21.4}_{-5.3}$ | $A = 0$ |
| Internal $\gamma$ background | $3.2^{+4.6}_{-4.4}$ | $A = 0$ |

Table 6.2: Numbers of events, event rates, and raw rate day-night asymmetry. Livetimes are: 176.511 days of Day data, and 214.921 days of Night data. Uncertainties on the rates and asymmetry are statistical.

| | |
|---|---|
| Num. Events Day | 2134 |
| Num. Events Night | 2588 |
| Event Rate Day | 12.0899/day $\pm$ 0.2617/day |
| Event Rate Night | 12.0416/day $\pm$ 0.2367/day |
| Rate Asymmetry | -0.0040 $\pm$ 0.0292 |
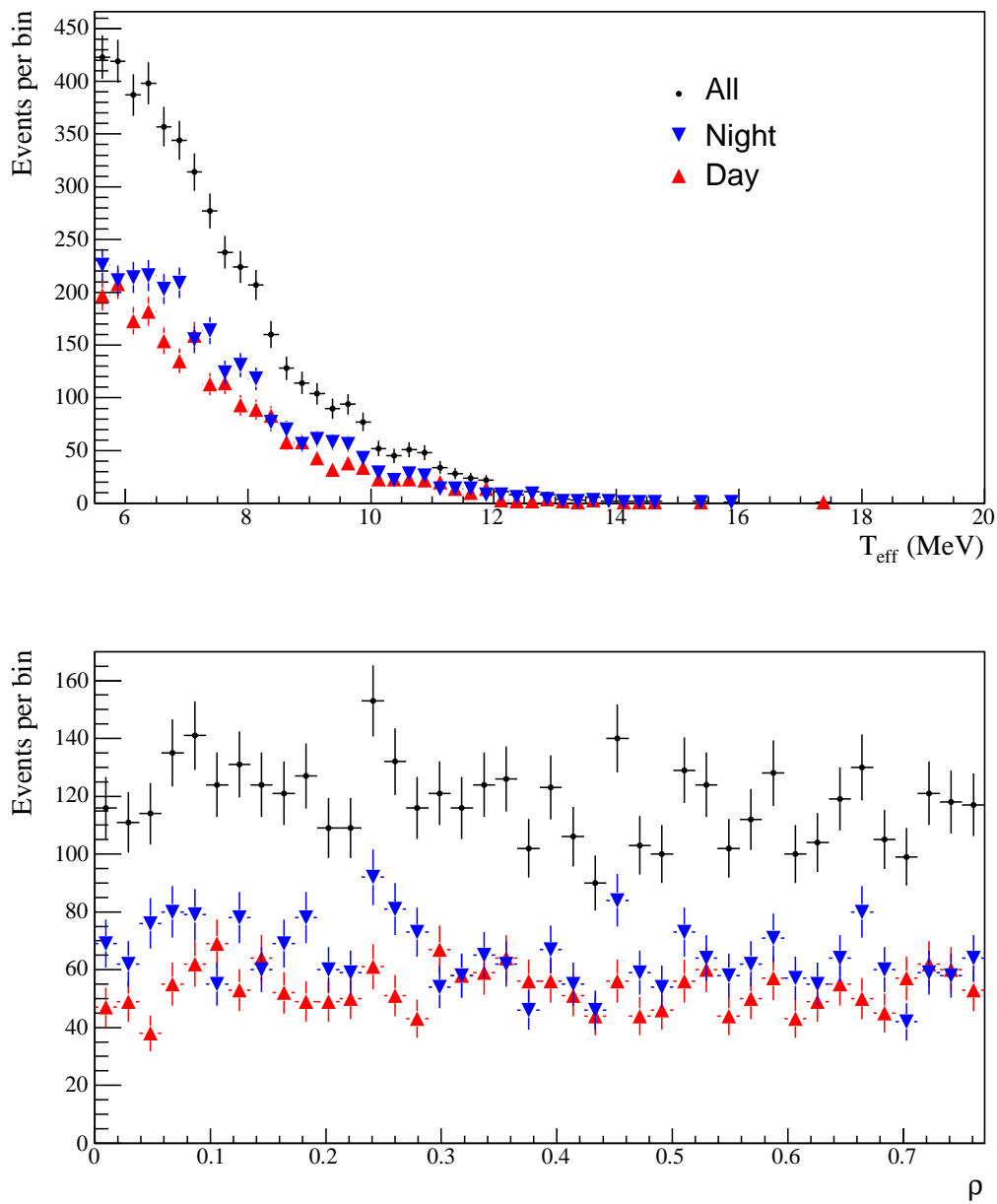
Figure 6.2: $T_{eff}$ and $\rho$ distributions for the day and night data and the full day+night data set.
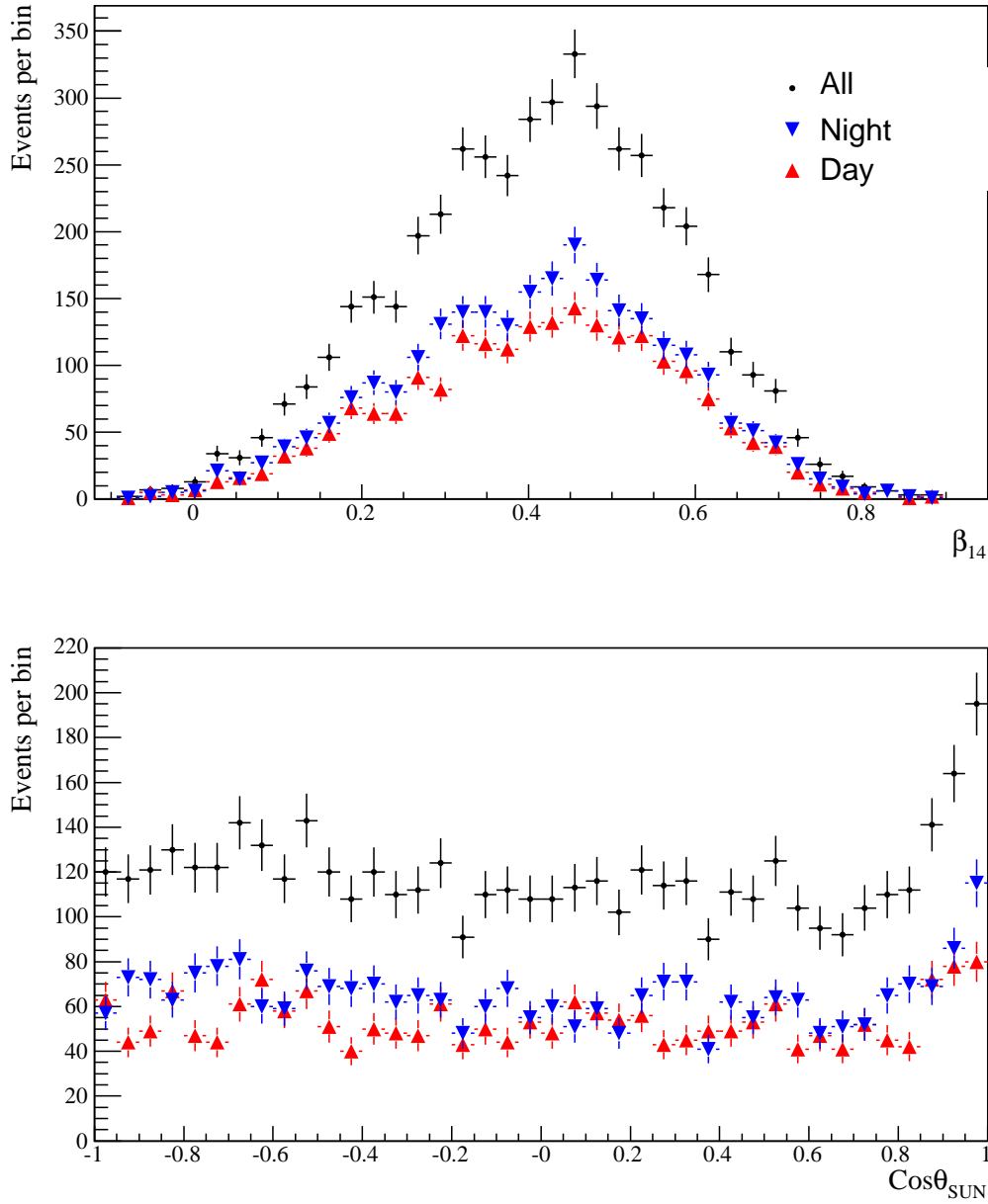
Figure 6.3: $\beta_{14}$ and $\cos\theta_\odot$ distributions for the day and night data and the full day + night data set.
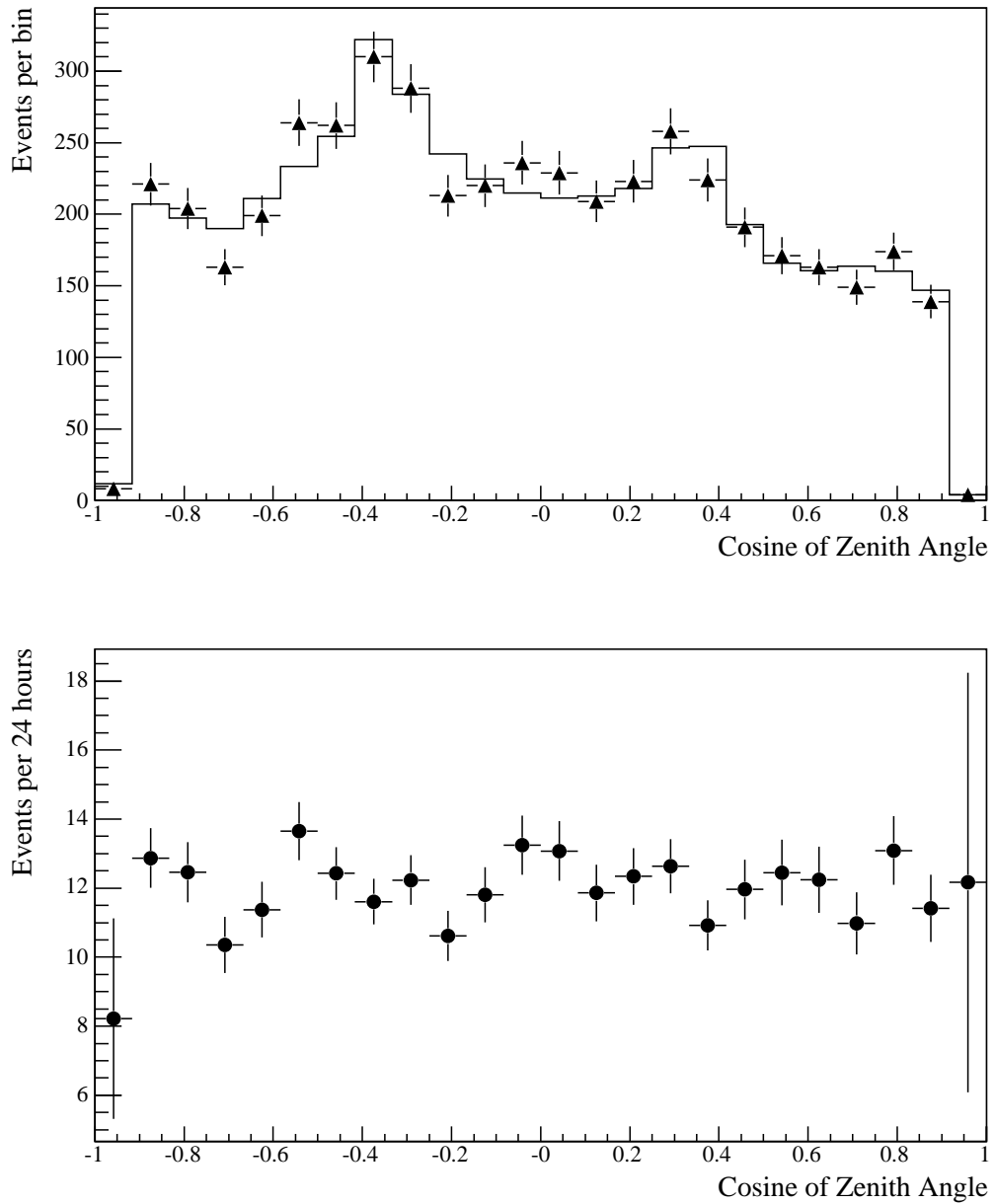
Figure 6.4: Number of events and event rate as a function of zenith angle for the salt data. In the top panel, the histogram shows the expected number of events given a constant event rate equal to the average event rate from the salt phase, 12.06 neutrino candidate events/day.

Chapter 7

# DETECTOR RESPONSE AND SYSTEMATIC UNCERTAINTIES

## 7.1 Overview

The final 4722-event salt data set contains an unknown number of CC, NC, ES, and "external neutron" background events, as well as the estimated backgrounds summarized in Table 6.1. The CC, NC, ES, and external neutron events each have different expected distributions in the four major event-by-event observables: energy, isotropy, radius, and direction relative to the sun. These distributions will be used to estimate the total number of each type of event in the data set, given the data distributions shown in Figures 6.2 and 6.3.

When a particle interaction in SNO occurs with a particular energy, photon distribution, vertex location, and particle direction, the values of $T_{eff}$ , $\beta_{14}$ , $\rho$, and $\cos\theta_\odot$ that are associated with the detected event depend on detector "response parameters" such as energy scale, energy resolution, and vertex resolution. Detector response characteristics also determine the overall efficiency for detecting particle interactions within the selected fiducial volume and energy ranges. To decompose the data set into neutrino signal and background components, and to interpret the results in terms of absolute neutrino fluxes, we require an accurate model of detector response to many different classes of events. For most SNO analysis, a carefully calibrated description of the detector within the SNOMAN Monte Carlo package provides a model of detector response.

The major response parameters that affect the extraction of solar neutrino physics are the energy scale, the energy resolution, the means and widths of the isotropy distributions, the accuracy of the reconstructed vertex positions in the x, y, and z dimensions, the radial position accuracy, the vertex resolution, the angular resolution, and the neutron capture efficiency. Systematic uncertainties in any of these response parameters will translate into systematic uncertainties in the neutrino fluxes derived from the data. The general strategy

for evaluating uncertainties in detector response parameters is to compare data from calibration sources to Monte Carlo simulations. The Monte Carlo is calibrated to reproduce the major features of the detector. Differences between calibration event distributions and Monte Carlo predictions indicate errors in the detector response model. When it is possible to identify the cause of a discrepancy, the error can be explicitly corrected. In other cases, the size of the difference between data and MC is taken as a measure of systematic uncertainty. Limitations in the calibration process or limitations in the Monte Carlo modeling will also translate into systematic uncertainties in detector response.

In general, calibration sources in SNO cannot sample the entire relevant ranges of event energies, isotropies, positions, or times. To the extent that it is possible, multiple calibration sources are used to study differences in detector response as a function of event energy, or for different particle interactions in the detector. Regularly scheduled calibrations with the $^{16}$N are used to monitor temporal variations in response, typically once a month. We rely on the Monte Carlo to model the remaining differences between calibration events and signal events.

For the day-night analysis, systematic uncertainties in detector response separate into two categories: day-night "correlated" uncertainties, and differential, "uncorrelated" uncertainties. Any systematic uncertainty that affects the day and night results in the same way will ultimately have no effect on the day-night asymmetry measurements. For example, suppose that the estimated uncertainty in the energy scale leads to a 1% uncertainty in the night and day CC fluxes $\Phi_{\rm CC}^N$ and $\Phi_{\rm CC}^D$. When we construct the asymmetry ratio $A \equiv 2(\Phi_{\rm CC}^N - \Phi_{\rm CC}^D)/(\Phi_{\rm CC}^N + \Phi_{\rm CC}^D)$, a correlated shift of 1% in the night and day fluxes will "cancel out", leaving the asymmetry unchanged. Most of the systematic uncertainties in detector response parameters that affect the measurement of solar neutrino fluxes are correlated day and night. For example, a large contribution to the systematic uncertainty in energy scale comes from uncertainty in how the $^{16}$N calibration source is modeled. The fundamental energy scale uncertainty due to source modeling applies equally to data taken at any time of day, so it produces a day-night correlated effect.

Differential uncertainties - systematic uncertainties that affect the day and night data differently - must be evaluated separately. Detector calibrations are primarily done during

the day, so day-night variations in detector response must be investigated using signals that are always present in the detector. Differential uncertainties for the day-night analysis will be reviewed in detail in the later sections of this chapter, after a brief summary of the day-night correlated systematic uncertainties that are relevant for the integral flux results.

## 7.2   Systematic Uncertainties for the Integral Flux Analysis

The major systematic uncertainties that are relevant for extracting solar neutrino flux results are summarized below. These uncertainties are extensively described in [38].

- *Energy Response:*   Energy response is primarily evaluated with the $^{16}$N source. Monthly calibrations with the $^{16}$N source at the center of the detector are used to study temporal stability of the energy scale. Changes in the attenuation of the $D_2O$ during the salt phase led to a steady decrease in the measured energy for $^{16}$N events over time. The time variation in energy scale was added to the Monte Carlo simulations so that the final energy scale would be approximately constant with time. Residual scatter of the $^{16}$N energies with time is taken as one measure of systematic uncertainty in the determination of the absolute energy scale. Periodic "scans" in which the source is deployed at many locations around the detector are used to study the variation of energy response with position. As an example, a comparison of the mean energies for $^{16}$N data and MC as a function of radius is shown in figure 7.1. Additional effects like uncertainties in the stability of the PMT gains and thresholds also contribute to energy scale uncertainty. The final energy scale uncertainty is estimated to be 1.15% including all of these effects [113]. The energy resolution uncertainty is also evaluated using $^{16}$N, and is estimated to be 3.4% near the energy threshold for the analysis. The resolution varies as a function of energy, such that the resolution uncertainty is 10% for the 19.8 MeV gammas produced by the pT source.

- *Vertex reconstruction:*   Vertex reconstruction response parameters include the position accuracy in $x$, $y$, $z$, or $r$, and vertex resolution. Vertex position accuracy is evaluated by comparing the average reconstructed position of $^{16}$N events to the po-
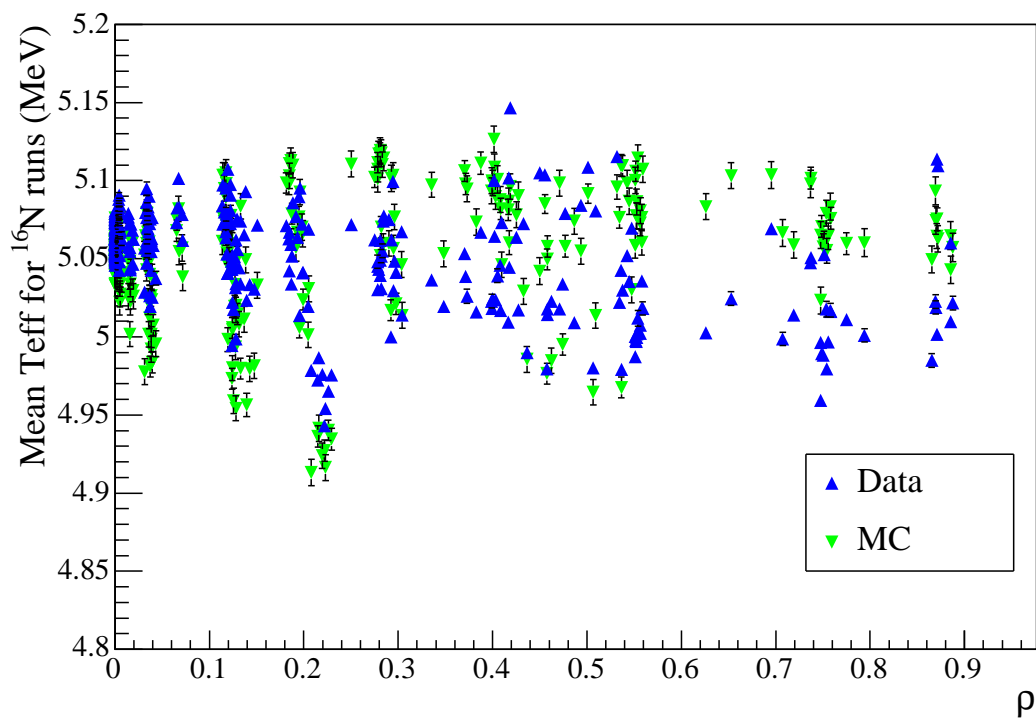
Figure 7.1: Comparison of the mean values of $T_{eff}$ for data and MC for $^{16}$N runs as a function of the radial parameter $\rho$. The mean $T_{eff}$ values are obtained by fitting a Gaussian function over a restricted range around the mean energies. The scatter of points gives one measure of systematic uncertainty in the overall energy scale, due to variations in detector response as a function of position.

sition of the calibration source. The source positioning system is accurate to within around 2 cm when the source is placed along the vertical ($z$) axis of the detector. The difference between the reconstructed position and the source position can be compared to the difference between the reconstructed position of $^{16}$N source Monte Carlo simulations and the input position used in the simulations. The difference between the data and Monte Carlo "vertex shifts" is used to evaluate systematic uncertainties in reconstructed positions. Systematic offsets in the linear dimensions $x$, $y$, or $z$ will shift the effective fiducial volume region closer to the acrylic vessel on one side of the detector. Systematic offsets in the radial dimension are more dangerous, since they will change the effective fiducial volume.

In the salt phase, a systematic offset in the $z$ direction is apparent in $^{16}$N reconstructed positions. In the $x$ and $y$ dimensions, the offsets are characteristic of the $\sim$2 cm positioning accuracy of the source manipulator system[1], but in the $z$ direction, a systematic offset of closer to 6 cm is observed. The differences between data and MC for $x$, $y$ and $z$ positions for center $^{16}$N runs are shown in Figure 7.2, as a function of the Julian date. The $z$ offset has been extensively studied. It is believed to be caused by a change in the "timing center" for the laserball calibration source, which is used to set the absolute timing reference for all PMT channels.[2] The systematic error in $z$ is corrected by adding 5.5 cm to the $z$ coordinate for every event in the data set. Systematic uncertainties of 2 cm in the $x$ and $y$ dimensions and 6 cm in the $z$ dimension account for uncertainty in the absolute vertex positioning accuracy [114] [115].

Errors in the index of refraction used in the Monte Carlo would lead to a scaling of all event positions in radius. Such a radial scaling error would affect the number of events reconstructing within the fiducial volume. $^{16}$N calibration runs taken at several

---

[1]When sources are deployed along the $z$ axis, positioning accuracy is typically around 2 cm. When deployed off-axis, the positioning accuracy is around 5 cm in $x$, $y$, and $z$. Runs taken in single-axis mode are used for most of the reconstruction studies, and off-axis runs are used as checks.

[2]Calibration constants are determined for each electronics channel using the laserball data. These constants are used to derive the calibrated PMT hit times in an event. If the laserball timing center shifts a few centimeters, the calibrated times of PMT hits in an event will be wrong, leading to a shift in the reconstructed position.
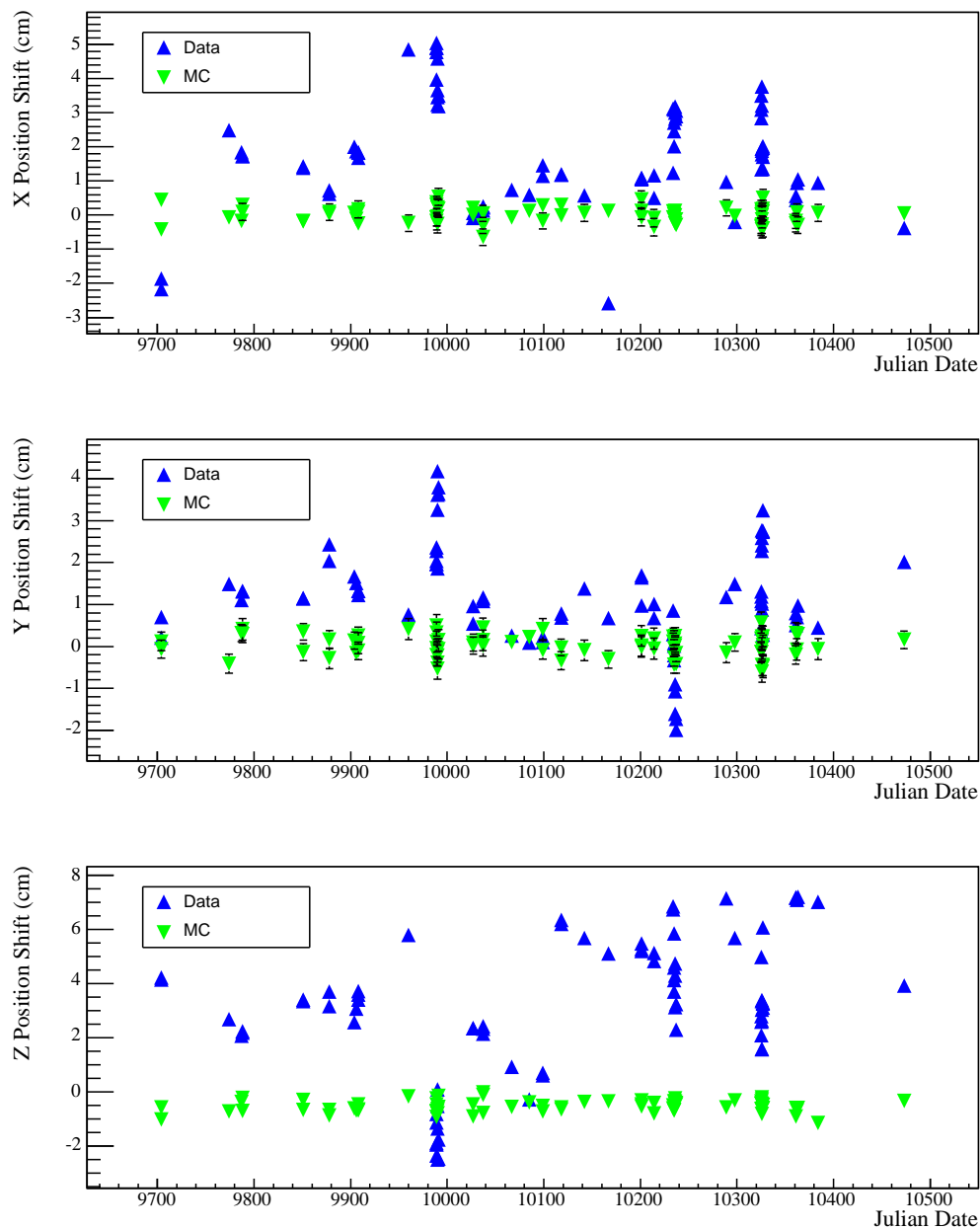
Figure 7.2: Comparison of data and MC vertex shifts for $^{16}$N runs in the salt phase, as a function of Julian date. For data, the vertex shift is defined as the reconstructed position minus the source manipulator position. For MC, the vertex shift is defined as the reconstructed position minus the position used to generate the MC events. The reconstructed positions are determined by fitting a Gaussian to the vertex position distributions, over a restricted range close to the mean.

positions along the $z$ axis are used to look for radial scaling in the reconstructed positions. This is combined with checks using the apparent position of the acrylic vessel in neutrino and low-energy background data to constrain radial scaling errors. The uncertainty in the radial scaling of event vertices is estimated to be 1%, corresponding to 5.5 cm at the boundary of the fiducial volume [116].

- *Angular resolution:* Angular response uncertainties are also evaluated using $^{16}$N data. The decay gammas from $^{16}$N travel an average of 30 cm away from the source before they scatter electrons. The vector from the source position to the reconstructed vertex position for each event gives a measure of that event's direction. The distribution of angles between the actual event direction and the reconstructed event direction is fit to a functional form,

$$R = N[e^{\beta_S(\cos\theta-1)} + \alpha_M e^{\beta_M(\cos\theta-1)}],\tag{7.1}$$

  where $N$ is the overall normalization, $\beta_S$ parameterizes the angular distribution for electrons scattered through small angles, $\beta_M$ parameterizes the distribution for larger angles, and the ratio of the two components is given by $\alpha_M$. Comparing the data and MC angular response, systematic uncertainties are estimated for each of the parameters in the analytic angular response function. The parameter that most strongly affects neutrino signal properties is $\beta_S$. The systematic uncertainty in $\beta_S$ is estimated to be 16% [117].

- *Isotropy Response:* The $\beta_{14}$ distributions for monoenergetic data are well approximated by simple Gaussians. Isotropy response can therefore be characterized by a mean and width, which will be different for neutron and electron events. These response parameters are evaluated using both $^{16}$N data and $^{252}$Cf neutron calibration data. From the $^{16}$N studies, the uncertainty on the $\beta_{14}$ mean is estimated to be 0.85%, and the uncertainty on the $\beta_{14}$ width is 0.94%. From the $^{252}$Cf studies, the uncertainty on the mean is 0.48% and the uncertainty on the width is 0.67%. Extensive discussion of the $\beta_{14}$ parameter and systematic uncertainties can be found in [111].

The differences in the isotropy mean for $^{16}$N data and MC are shown as a function of radial position in figure 7.3.
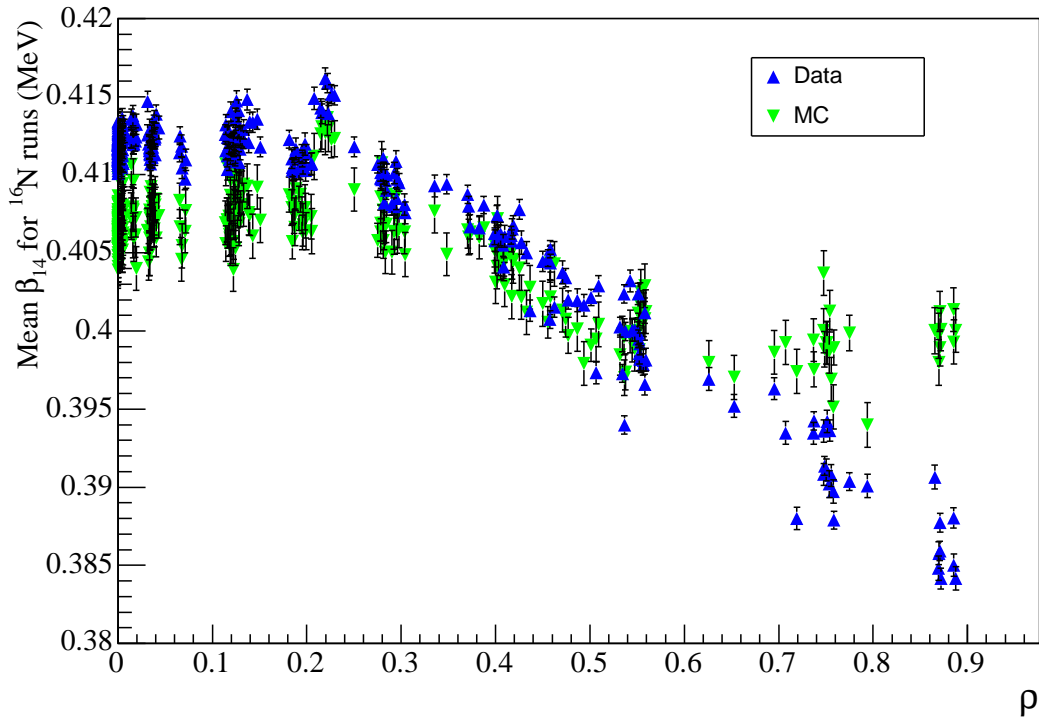


Figure 7.3: Comparison of the mean values of $\beta_{14}$ for data and MC for $^{16}$N runs as a function of the radial parameter $\rho$. The mean $\beta_{14}$ values are obtained by fitting a Gaussian function over a restricted range around the mean value. Only $^{16}$N events with energies near the mean energy are used. The scatter of points gives one measure of systematic uncertainty in the overall isotropy mean.

- *Neutron Capture and Detection Efficiencies:* The neutron capture efficiency is critical for interpreting the measured number of NC neutron events in terms of the underlying solar neutrino flux, as well as for evaluating the contributions of background neutron sources to the data set. The capture efficiency is evaluated using the $^{252}$Cf source. The absolute source strength is measured in four different ways.[3] The measured number

---

[3]These include the Frisch Grid and Si(Li) techniques, which use an array of $^{3}$He neutron detectors to

of neutron events from the source is then compared to the expected number, and the capture efficiency is mapped out as a function of the position of the calibration source. The efficiency for detecting NC neutrons within the fiducial volume and above the analysis energy threshold, assuming that they are produced isotropically in the acrylic vessel, is $(40.7 \pm 0.5^{+0.9}_{-0.8}\%)$, including statistical and systematic uncertainties [118].

- *Energy-Dependent Systematic Uncertainties:* Several systematic uncertainties, like the energy resolution uncertainty, vary as a function of energy. Energy-dependent uncertainties in energy scale, radial scale and isotropy response have been investigated with multiple calibration sources. These uncertainties are incorporated in the measurement of the integral neutrino fluxes, as well as in the extraction of the electron energy spectrum from the CC and ES reactions. Details can be found in [119].

- *Background Uncertainties:* Systematic uncertainties in background estimates also need to be included in the final analysis. Only the neutron backgrounds and the gamma ray backgrounds from atmospheric neutrino interactions are directly subtracted from the final results. All other sources of background are treated as uncertainties on the derived neutrino fluxes. The sizes and uncertainties on the different background sources are indicated in Table 6.1.

- *Theoretical Uncertainties:* Theoretical uncertainties that affect the final results arise from uncertainties in the weak interaction coupling $g_A$, uncertainties in the neutrino reaction cross sections, and uncertainties in radiative corrections. Combined, these amount to ~1% systematic uncertainties in the final neutrino results for the CC and NC reactions, and a ~0.5% uncertainty in the ES results.

- *Other Systematic Uncertainties:* Additional systematic uncertainties related to signal acceptance include any uncertainty in the overall livetime and uncertainties in the

directly measure the source strength, as well as two techniques using data from the source in SNO, one based on the multiplicity of events and one based on a time-series analysis. See [38]

signal loss due to data selection cuts. The livetime uncertainty, from Chapter 5 is 0.021%. The measured signal losses are less than 1% for each of the three neutrino signals, with uncertainties of around 0.1% [120].

## 7.3 Differential Detector Response for the Day-Night Analysis

### 7.3.1 Overview

The day-night analysis is sensitive to any systematic uncertainty that is capable of affecting the day and night neutrino data differently. This includes uncertainties in the diurnal stability of detector response as well as uncertainties in the stability of detector response with respect to event direction and the time of year. Uncertainties in the day-night asymmetries of backgrounds must be considered, as well as day-night variations in signal acceptance. Systematic uncertainties that affect the day-night analysis will be described in detail below.

### 7.3.2 Long-Term Variations

Variations in detector response over long timescales could potentially cause artificial day-night asymmetries. Although a given variation in response may affect all times of day equally, the relative lengths of day and night change with the seasons. It is therefore possible that long-term variations in response could preferentially affect either the day or the night portions of the total data set. As an example, if the energy scale is incorrectly calibrated for a period of time during the winter, it will preferentially affect the night portion of the data.

Extraction of solar neutrino signals is most sensitive to the energy scale and $\beta_{14}$ mean. For the day-night analysis, we consider long-term variations in just these two response parameters. Because long-term variations in the detector are fairly well modeled, comparisons of calibration data and Monte Carlo as a function of time do not tend to show systematic response variations on long time scales. To limit the possible effect of long term variations for the day-night analysis, we construct "worst-case" models for energy and isotropy variation that exaggerate the possible temporal changes in response. Even worst-case models for long-term variations have only small effects on the extracted day-night asymmetry, so

there is no need for detailed modeling of drifts in detector response.

To construct the worst-case models, we break the salt phase into periods of time bounded by the equinoxes. Using comparisons of data and MC for $^{16}$N calibrations, we then construct models for energy scale variations that systematically overestimate the relative energy scale during the summer and underestimate it during the winter, and vice versa. The worst-case models are chosen to produce maximal variation in the day-night asymmetry. The worst-case drift model for the energy scale is shown in Figure 7.4. The two step-function curves in Figure 7.4 are taken as estimates of the variation in the energy scale as a function of time. These models, as well as the corresponding worst-case drift models for isotropy variation, are taken from reference [121]. They are summarized in Table 7.1.

Table 7.1: Worst-case drift models for energy and isotropy. For energy, a given worst-case scenario is modeled by multiplying the energy scale by the numbers in the "Energy scale 1" or "Energy scale 2" column, for the date ranges given. For isotropy, the worst-case scenarios are modeled by shifting the mean isotropy by the amounts given in the "$\beta_{14}$ shift 1" or "$\beta_{14}$ shift 2" column.

| Julian Dates | Energy scale 1 | Energy scale 2 | $\beta_{14}$ shift 1 | $\beta_{14}$ shift 2 |
|---|---|---|---|---|
| up to 9762 | 0.998 | 1.003 | 0.0032 | 0.0053 |
| 9762 to 9942 | 1.003 | 0.998 | 0.0055 | 0.0025 |
| 9942 to 10127 | 0.998 | 1.006 | 0.0015 | 0.0064 |
| 10127 to 10308 | 1.005 | 0.998 | 0.0064 | 0.0002 |
| 10308 and up | 1.000 | 1.007 | 0.0016 | 0.0062 |

### 7.3.3   Directional Systematics

The directions of ES and CC events in the detector are correlated with the location of the sun when the events take place. Both signals will therefore illuminate different portions of the detector day and night. During the day, ES events will preferentially illuminate the bottom half of the detector, while at night they will preferentially illuminate the top. The CC events will preferentially sample the opposite halves of the detector day and night,
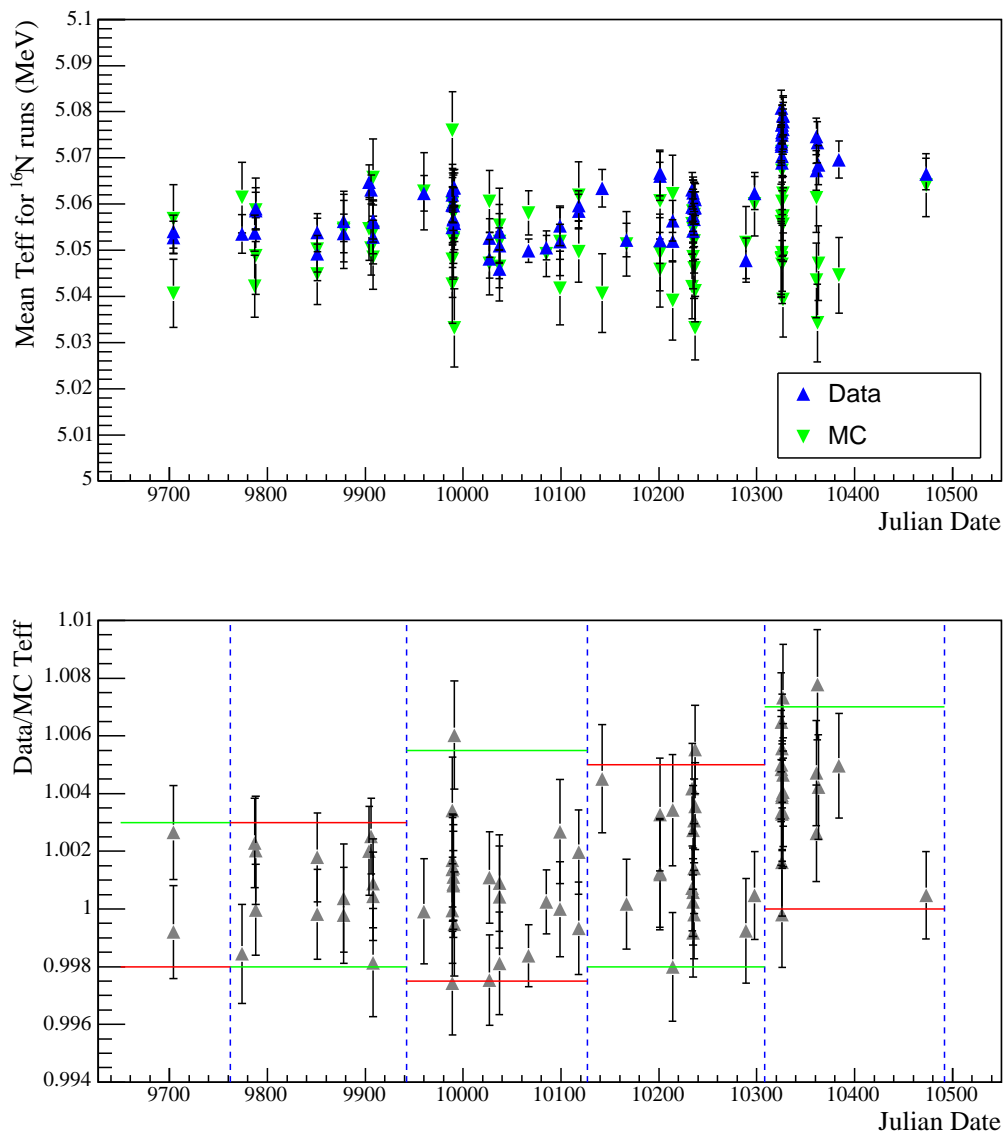
Figure 7.4: The top figure shows a comparison of the mean $T_{eff}$ for data and MC for $^{16}$N runs with the source near the center of the detector, as a function of Julian date. The bottom figure shows the ratio of the data and MC values. The dashed lines show the dates of the spring and autumn equinoxes. The alternating horizontal lines show the two worst-case energy scale drift models.

although their direction dependence is weaker. Because of the directionality of these signals, geometric asymmetries in the detector can cause effective day-night asymmetries in the ES and CC signals. The SNO detector is not perfectly spherically symmetric, with the neck region representing a significant difference between the upper and lower hemispheres.

$^{16}$N calibration data is used to evaluate differences in detector response as a function of event direction. Using calibration data taken with the source at many locations in the detector, the major detector response parameters (energy scale, energy resolution, vertex shift, vertex resolution, isotropy, and angular resolution) are evaluated as a function of the direction of the event, in terms of the polar and azimuthal angles $\theta$ and $\phi$ relative to the center of the detector. Monte Carlo simulations are used to predict the $\theta, \phi$ distributions for CC and ES events for night and day. The MC distributions are used to weight the measured variations in $^{16}$N with direction. The signal-weighted day values of each systematic uncertainty and the corresponding night values are used to estimate the effective day-night asymmetry due to directional variations.

For the highly-directional ES signal, directional systematic uncertainties can be quite large. They will have less of an effect on the CC signal. The NC signal samples the same portion of the detector day and night, so there are no direction-related systematic uncertainties in the NC day night asymmetry.

The sizes of the directional systematics, from [122], are summarized in Table 7.2.

### 7.3.4   Background Systematics

Systematic uncertainties in the day-night asymmetries of backgrounds were summarized in the previous chapter, in Table 6.1. In addition, uncertainties in the total amplitudes of backgrounds can affect the day-night measurement. Unlike other systematic uncertainties, uncertainties in background numbers are additive with respect to the total numbers of signal events in the data set. They do not cancel out in the asymmetry ratio, and may have an effect on the measured day-night asymmetries.

Table 7.2: Day-night systematic uncertainties due to directional variations in detector response. The uncertainties for the CC and ES signals are anticorrelated, since the two signals tend to illuminate opposite hemispheres of the detector at a given time.

| Response Parameter | CC Uncertainty | ES Uncertainty |
|---|---|---|
| Directional Energy Scale | $\pm$ 0.09% | $\mp$ 0.79% |
| Directional Energy Resolution | $\pm$ 0.13% | $\mp$ 1.3% |
| Directional Isotropy | $\pm$0.09% | $\mp$0.82% |
| Directional Radial Scale | $\pm$ 0.02% | $\mp$ 0.15% |
| Directional Vertex Resolution | $\pm$ 0.13% | $\mp$ 1.4% |
| Directional Angular Resolution ($\beta_S$) | $\pm$ 0.6% | $\mp$ 5.3% |

## 7.4  Diurnal Variations

Because calibrations take place almost entirely during daytime hours, there are few direct tests of the stability of detector response with respect to the diurnal cycle. For most solar neutrino analysis, daytime evaluations of detector response are assumed to apply equally well to the entire data set, including data taken at night. This assumption is reasonable since the major contributions to detector response uncertainties are not correlated to time of day. However, detector conditions may vary day to night, and these variations must be explicitly considered for the day-night analysis. Temperature variations, variations in the amount of personnel activity in the laboratory, variations in the high voltage supplied to the detector, and variations in the nearby mining activities could all contribute to variations in the day and night detector response.

To evaluate uncertainties in diurnal response, we rely on signals that are constantly present in the detector. Low-energy background events provide the highest statistics, and can be separated into a number of different categories to provide consistency checks. Studies using the low-energy backgrounds have a limited ability to test stability within the fiducial volume and energy regions used for solar neutrino analysis, since background events are lower in energy and tend to have high radii. Neutron events following muon interactions in

the detector resemble neutrino data much more closely, but are limited by statistics. Limits on diurnal response from muon follower studies are primarily a check on the low-energy background results, except in the case of diurnal isotropy variation. The neutrino results are very sensitive to the isotropy parameter, and neither the muon follower analysis nor the low-energy background analysis provides a high-precision test of diurnal variations in this parameter. For diurnal isotropy response, a combination of both analyses is used. The muon follower analysis will be presented in detail later in this chapter.

For energy-related systematic uncertainties, the best test of diurnal response variations comes from the rate stability of low energy backgrounds. The rate of low-energy events falls steeply as a function of energy. Therefore, variations in energy scale or energy resolution will translate directly into variations in the rate of backgrounds measured within a given monitoring window. Comparisons of the day and night rates of low-energy backgrounds can be used to limit day-night asymmetries in energy scale and energy resolution. For the final limits used in the day-night analysis, radioactive backgrounds in the region of the acrylic vessel are used.

For vertex position accuracy and resolution uncertainties, a "hot spot" located on the acrylic vessel provides a stationary point for comparing day and night response. There is no way to test for diurnal variations in angular response using low-energy background data because none of the signals have a well-specified direction. However, angular response variation is only a significant source of systematic uncertainty for the elastic scattering signal. The ES day-night asymmetry is very statistics limited, and plausible levels of diurnal variation in angular response would be unlikely to affect the measured values.

The low-energy background categories that are used in studies of diurnal variations are described below. Background events are selected within an energy range defined by requiring that the number of PMT hits that occur within a 20 ns prompt timing window is between 25 and 40. This corresponds roughly to energies between 4.5 and 6.5 MeV, which means that these studies are sensitive to energy scale variations around the energy threshold used for neutrino analysis.

- *AV "Hot Spot":* Near the top of the acrylic vessel (AV), there is a region with elevated

levels of radioactivity. This "hot spot" is of unknown origin. The hot spot's stationary position and constant presence in the detector make it a useful test for diurnal stability of reconstruction response.

- *AV radioactivity:* Low energy background events are selected within a spherical shell that extends from 585 cm to 615 cm in radius. This region includes events from radioactivity in the AV itself as well as events in the high-radius region of the $D_2O$ and part of the $H_2O$.

- *$D_2O$:* Low energy background events are selected within a radius of 450 cm. To separate these from events that enter the $D_2O$ from beyond 600 cm, events are selected that have outward-going reconstructed directions.

- *$H_2O$:* Low energy events within a spherical shell between a radius of 650 cm and 680 cm are selected. Only outward-going events are accepted, to separate $H_2O$ radioactivity from PMT radioactivity.

- *PMT:* Radioactivity from the PMTs is selected within a spherical shell between radii of 725 cm and 900 cm. Only events with directions pointing toward the inner parts of the detector are selected.

To mitigate any artificial day-night asymmetries due to changes in the levels of radioactive impurities in the detector, day-night studies using low-energy backgrounds must be done on time scales that are short compared to the characteristic time scales for background variations. For the rate stability tests, the day-night asymmetries are calculated on a run-by-run basis, using only those runs that sample time during the day and during the night. A maximum likelihood technique is then used to fit for the overall value of the day-night asymmetry in the background rate. For determining the $\beta_{14}$ stability day to night, the data is binned in two-day intervals. The two-day binning improves statistics, while still avoiding bias due to gradual changes in background levels. The run-by-run rate asymmetries for each category of background are shown in Figure 7.5. The low-energy background studies show
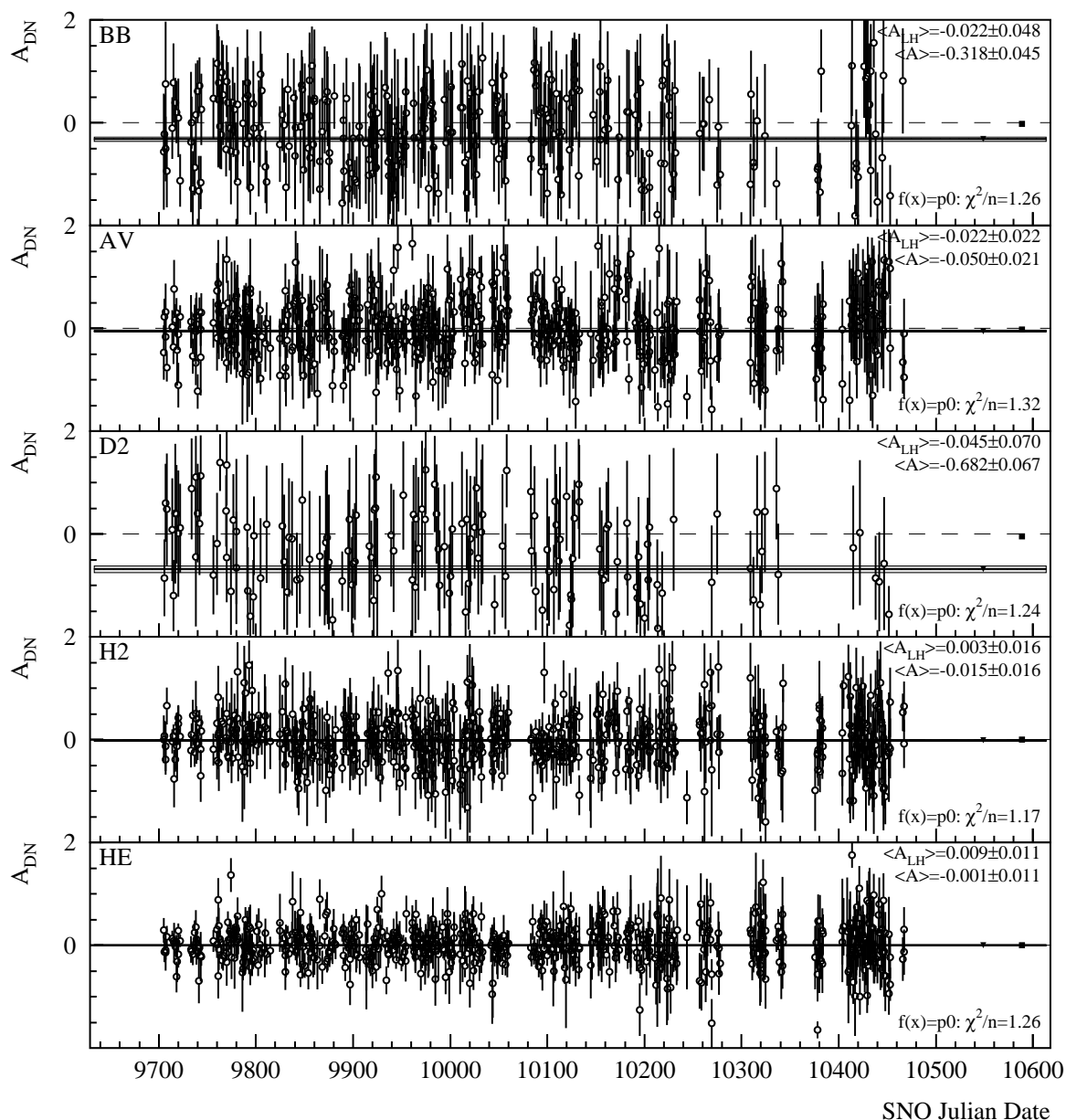
Figure 7.5: Asymmetries in the rates of low energy backgrounds, calculated on a run-by-run basis through the salt run period. Only runs with some livetime during the day and some during the night appear. The figure labeled "BB" corresponds to the hot spot, the figures labeled "AV", "D2", and "H2" correspond to the acrylic vessel, $D_2O$ and $H_2O$ backgrounds. The figure labled "HE" shows the PMT backgrounds. On the far right of each plot are the overall asymmetries determined from several different techniques. The filled box and the dashed line show the average asymmetry calculated using a Poissonian likelihood method. The filled triangle and the black line show the asymmetry determined from a Gaussian weighted average. The grey line shows a straight-line fit. Figure provided by J. Wendland.

no evidence for diurnal variations in detector response. The limits placed on each response parameter from the low-energy background analysis are summarized in Table 7.3.

Table 7.3: Limits on the diurnal variation of response parameters from low-energy backgrounds. Taken from [123]. For each response parameter, the value quoted in the table represents a limit on the difference between the day and night values of that parameter. In some cases this is expressed as a percentage difference and in others it is expressed in terms of a day-night shift in the parameter value.

| Response Parameter | Uncertainty | Limit based on: |
|---|---|---|
| Diurnal Energy Scale | ± 0.4% | AV background rate |
| Diurnal Energy Resolution | ± 0.5% | AV background rate |
| Diurnal Isotropy | 0.006 | AV background |
| Diurnal Radial Scale | ± 0.3% | Hot spot location |
| Diurnal Vertex Resolution | ± 1.26 cm | Hot spot location |

### 7.4.1 Muon Followers

Muon interactions in the detector can produce secondary neutrons through a variety of processes, including photodisintegration and nuclear spallation. For solar neutrino analyses, time windows following every muon event are cut from the data set, so that these neutrons (and other interaction products) do not constitute a background. However, muon follower neutrons can also be used as an excellent (albeit statistics-limited) calibration source for evaluating detector response to solar neutrinos. They are isotropically distributed in space and occur at all times of day, resembling the NC signal itself.[4] Isolating these neutrons and comparing their characteristics day and night yields limits on diurnal variation in detector response parameters. In particular, the "muon followers" can give additional constraints on diurnal isotropy variation.

---

[4]Reference [108] investigated possible differences between muon-induced neutron characteristics and NC signal characteristics, including event-rate or energy dependent effects, and no significant differences were found.

Candidate muon events are identified by the presence of light detected in the OWL PMTs. The conditions for assigning the "muon" tag during data-processing are that the event contains at least five OWL hits, that it has a total Nhit $> 150$, and that it passes a few minimal tests rejecting other event classes.[5] This is a loose definition of "muon" that is used to ensure that the muon follower cut is conservatively applied, minimizing any potential muon-induced backgrounds. The "muons" so-identified include many instrumental events as well as actual physics events.

The total number of events tagged as muons using the loose conditions described above is 35407 for the full 1212-run salt data set. This set of muon candidates contains a number of instrumental events. It also contains events for which the full muon-follower sample window is not available in the data set. These are muon candidates that occur within twenty seconds of a boundary between two data files, in which case the "follower" period is truncated because the data processing takes place on a file-by-file basis. To create a slightly "cleaner" muon sample, we can apply a basic set of cuts meant to eliminate instrumental events and events taking place within a minute of a subrun boundary.[6] The "clean" muon sample contains 27537 candidate muons. A comparison of the Nhit distributions for these two sets of muons is shown in figure 7.6. Applying the extra set of cuts reduces the number of lower-Nhit instrumental events and results in an Nhit spectrum that looks more like the expected distribution for muons (see, for example, [125]). For the purposes of muon follower studies, both the original, inclusive sample of muon candidates and the "clean" sample are reasonable choices. We will use the "clean" sample, but will repeat the analysis for the full sample to test for any biases due to this choice.

The time window defining the muon-follower cut is 20 seconds. Immediately after a muon interacts in the detector, Michel electrons and prompt gamma rays may be observed, as well as "retrigger" events, since muons frequently saturate the detector with light. Later,

---

[5]More specifically, that no hits are registered by the neck PMTs, that the width of the timing distribution for the PMT pulses does not exceed 90ns, that the event is not an orphan, that it is not associated with any of the non-physics event triggers, and (to avoid instrumental "ringing"), that it has occurred at least 5 $\mu$s after the last event with OWL hits.

[6]Following [124], the cuts applied are the QvT, Q/NHit, Crate Isotropy, "Ring of Fire", Neck event, "HIB",Flasher Geometry, and the Subrun Boundary cuts.
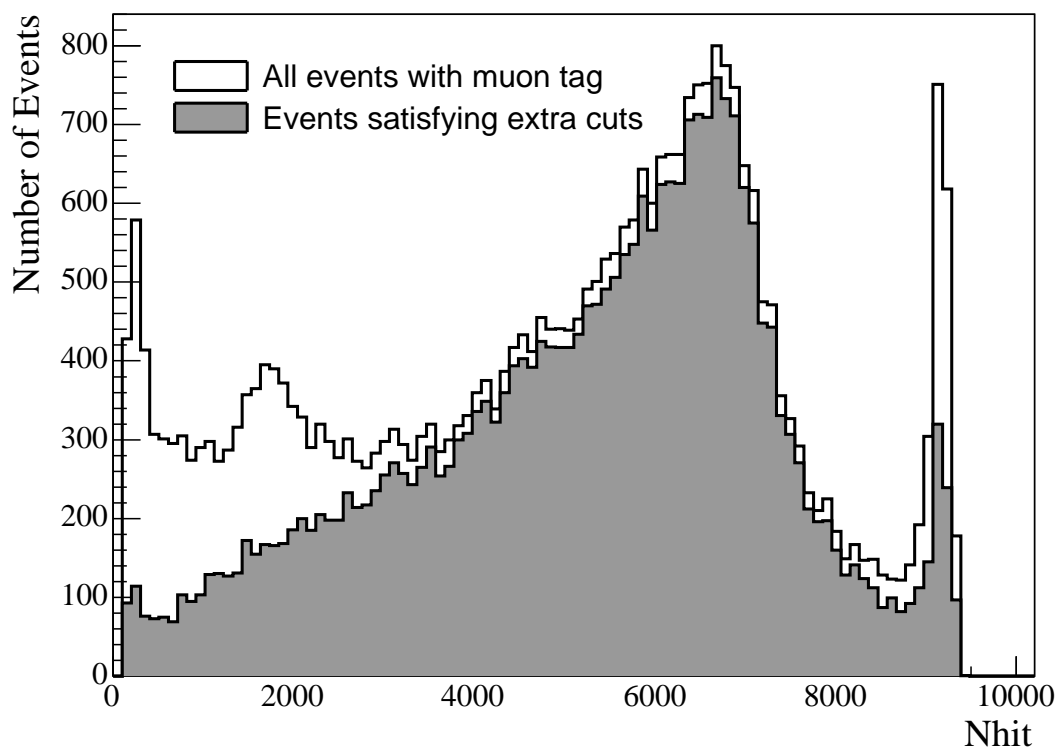
Figure 7.6: The Nhit distributions for the set of all candidate muons selected by the muon tag, and for the "clean" sample of muons that satisfy an additional set of data selection cuts described in the text. Many of the lower-Nhit events that are tagged as muons have the characteristics of instrumental events and are removed by the additional cuts.

neutrons produced by the muon will capture on $^{35}$Cl with a characteristic capture time of around 5.5 ms. A variety of unstable muon-capture and spallation products may also be produced by a muon, and these may decay throughout the 20 second window. Finally, the 20 second window may contain background events in accidental coincidence with the muon. More detail on backgrounds to the muon follower neutron sample can be found in references [107], [108], [125], and [126].

To construct a sample of muon-follower *neutrons*, selecting only those events taking place between $50\mu$s and 20ms after the muon will eliminate the prompt events from the sample and substantially limit spallation and muon capture products in the muon follower sample. For the purposes of studying diurnal variation, remaining muon-related backgrounds can be ignored on the assumption that they are not correlated to the diurnal cycle. Using a restricted time window to select muon-follower neutrons also reduces the probabilities of coincidences with low-energy backgrounds from radioactivity in the detector. To further separate the muon follower neutrons from any low energy backgrounds, we will also place a cut rejecting events with $T_{eff}$ less than 4.0 MeV. Figure 7.7 shows the energies of all of the muon follower events in the sample (within a 600 cm fiducial volume) as a function of the time since the initiating muon, along with lines indicating the time and energy cuts used in this analysis.

Highly energetic muons can produce hundreds of secondary neutrons through deep inelastic scattering reactions. These neutrons will be correlated in time and space to the muon, so they can potentially bias the characteristics of the muon follower sample. To reduce this bias, we will apply a cut on the "multiplicity" of followers for each muon. We will define the multiplicity as the number of events in the full 20 second muon follower window that pass the standard set of data cleaning cuts and reconstruct within 600cm, with energies ($T_{eff}$) greater than 3.5 MeV. A comparison of the multiplicity distributions for the fully inclusive and the "clean" muon samples is shown in figure 7.8. Some of the muon candidates rejected by the extra cuts that are used in this analysis have large multiplicities, indicating that the rejected set includes some muon deep inelastic scattering events as well as instrumental backgrounds. For selecting a sample of muon-follower neutrons, we will require a multiplicity less than 15. The choice of a multiplicity cut is somewhat arbitrary,
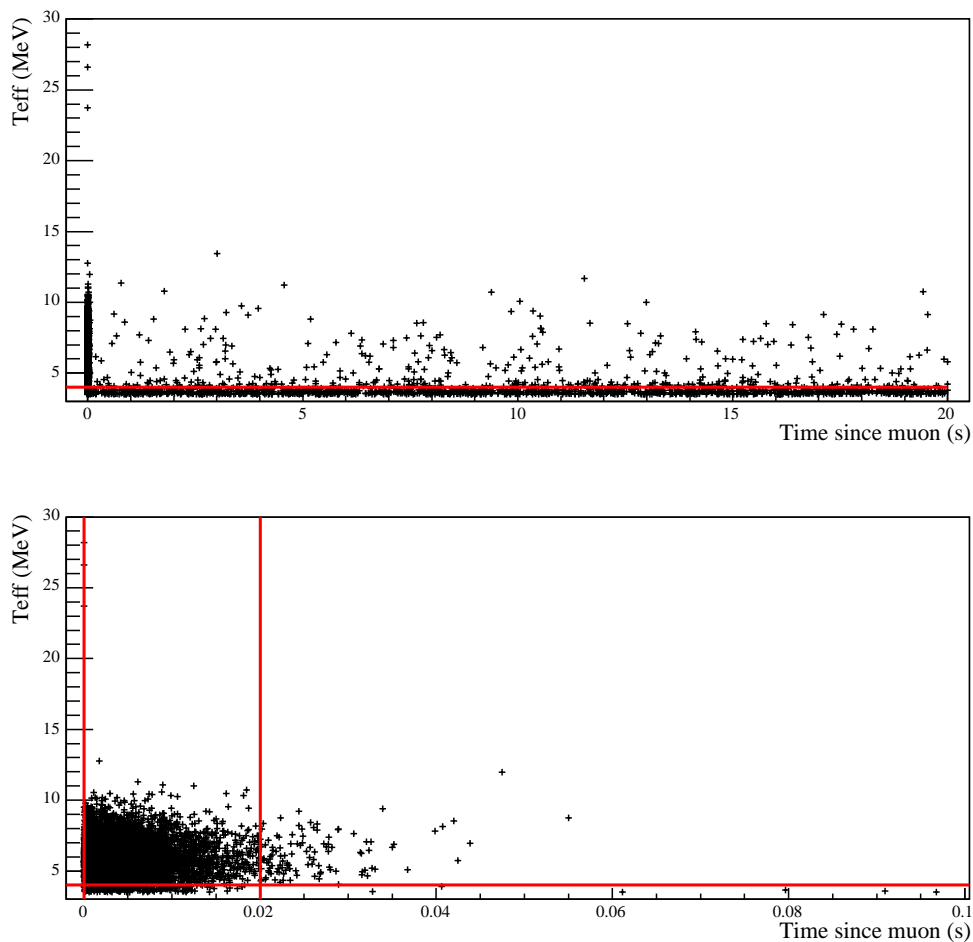
Figure 7.7: Energy ($T_{eff}$) vs. time since the initiating muon, for all muon follower events within a radius of 600 cm and above 3.5 MeV. Only muon followers for the "clean" muon sample are shown. The top panel shows the full 20 second time window, with a line indicating the energy cut of 4.0 MeV that is used in the analysis. The lower panel shows a reduced time period, and shows the upper and lower boundaries of the time window cut that is placed to restrict the muon follower sample.

so we will vary the multiplicity cut to ensure that the results are not sensitive to the cut.

**Multiplicity distribution for "clean" muons**



**Multiplicity distribution for muon candidates rejected by cuts**
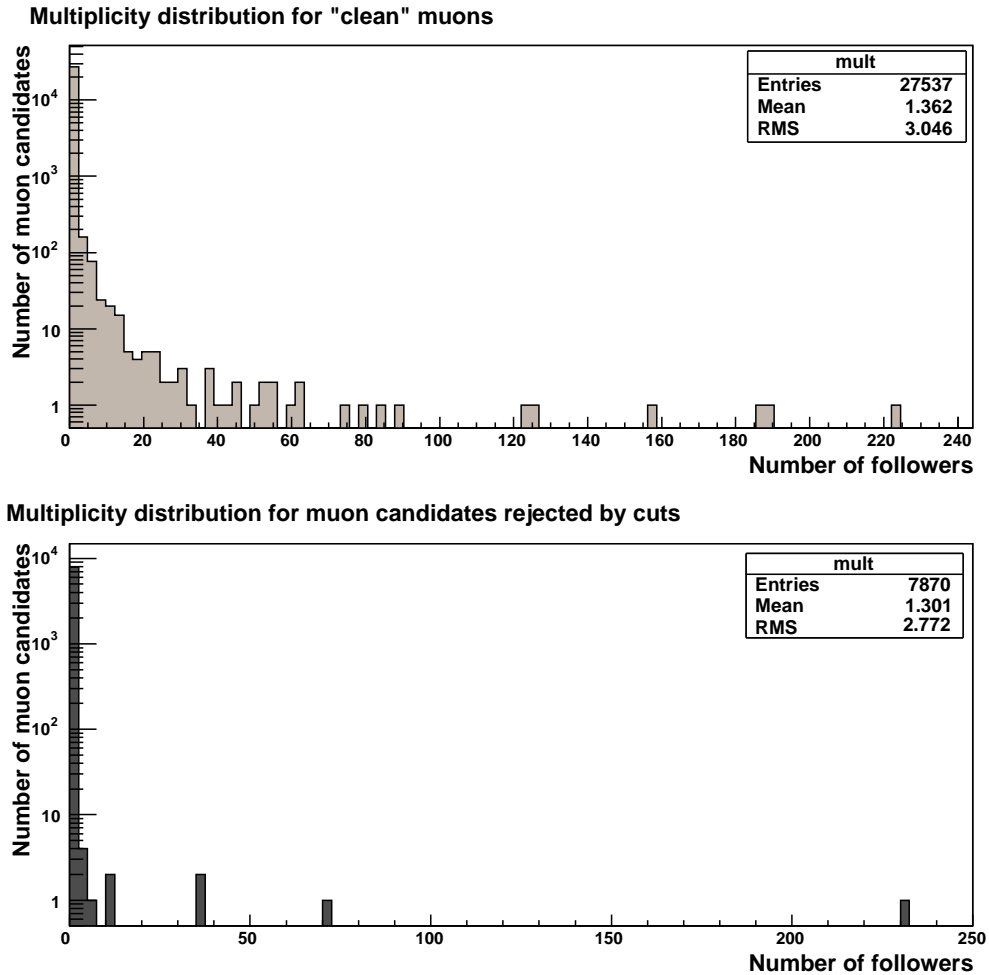


Figure 7.8: Muon "multiplicity". The top panel shows the "clean" muon candidate set. The lower panel shows the muon candidates that are rejected by the set of cuts that is applied to obtain the "clean" set. Some of the events that fail these cuts have high multiplicity, indicating that the extra set of cuts rejects some events that are muon events.

The final muon follower sample can be used to study diurnal variation in energy and isotropy. It contains 1314 events that take place during the day, and 1564 events that take place during the night, over the course of the salt data set.[7] Figures 7.9 and 7.10 compare

---

[7]Comparisons of the rates of muon and muon follower candidates day and night show no evidence for diurnal variations. A more thorough analysis needs to be done before the rates can be interpreted as true

Table 7.4: Energy mean, energy width, and isotropy mean from Gaussian fits to the day and night muon follower distributions. The final column gives the day-night asymmetry.

| Measurement | Night Value | Day Value | Asymmetry |
|---|---|---|---|
| Energy Mean | 5.768 ± 0.057 | 5.660 ± 0.0668 | 0.0190 ± 0.0154 |
| Energy Width | 1.476 ± 0.046 | 1.471 ± 0.053 | 0.0037 ± 0.0475 |
| Isotropy Mean | 0.3206 ± 0.0043 | 0.3145 ± 0.0045 | 0.0191 ± 0.0197 |

the energy and isotropy distributions of the day and night muon followers to the Monte Carlo NC distributions for the same fiducial volume and energy cuts. Simple Gaussian fits are performed to the distributions in figures 7.9 and 7.10 to extract the mean day and night energy and isotropy values, as well as the energy resolution. The asymmetry in these parameters can then be computed, defined as the difference between the night and day values divided by the average value. The results are summarized in Table 7.4.

To search for biases in this study, the fits were repeated with several different variations. The results are shown in figure 7.11. The points in the figure correspond to the following variations on the analysis:

- 1. *Standard:* The standard set of cuts. We require that the initiating muon candidate is in the "clean" sample of muon candidates, and that it have a multiplicity of fewer than 15 followers. Muon followers are included if they have passed all standard data selection cuts, reconstruct within 600 cm, have energies $T_{eff} > 4.5$ MeV, and occur 50 $\mu$s to 20 ms after the candidate muon.

- 2. *Fiducial:* Instead of accepting muon follower events within 600 cm and above 4.0 MeV, the cuts used in the neutrino analysis were applied, so that only followers within 550cm and above 5.5MeV were kept. This substantially reduces the statistics available for the fits. However, it is useful for testing diurnal stability within the analysis region.

rates of muon events or muon follower neutrons.
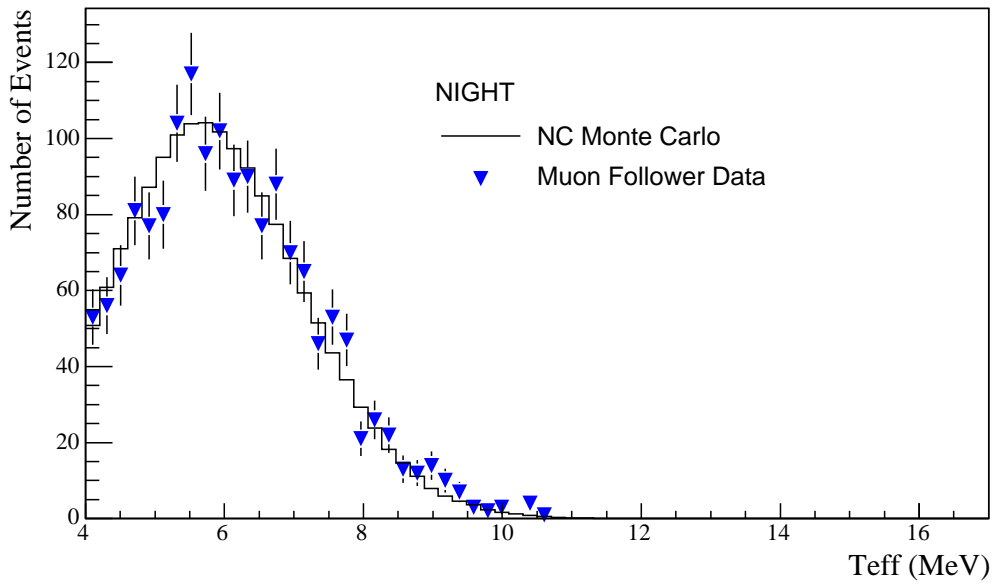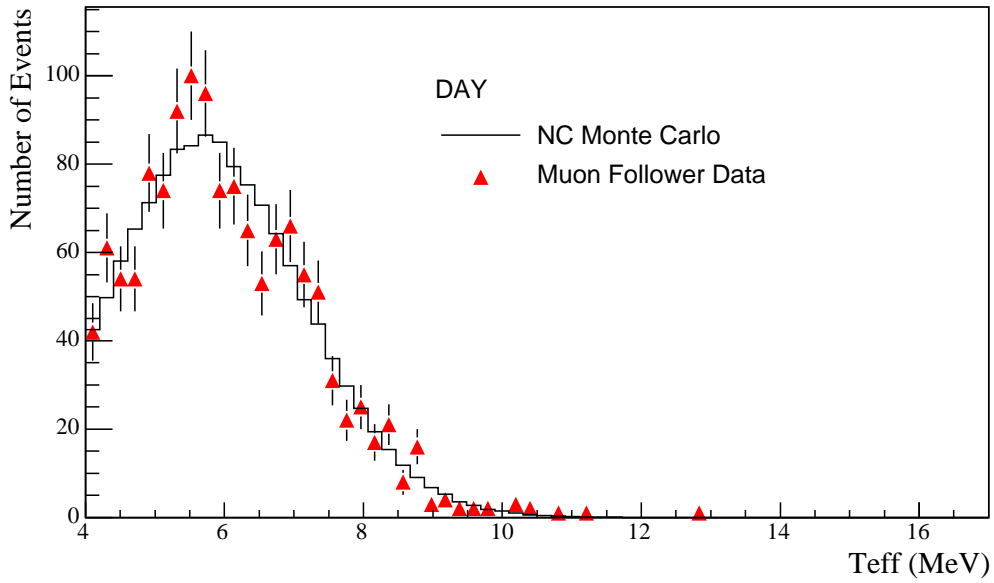
Figure 7.9: Day and night $T_{eff}$ distributions for muon followers above $T_{eff}$ =4.0 MeV and within a radius 600 cm. The histograms show Monte Carlo distributions for the NC signal, assuming the same energy and fiducial volume cuts. The MC histograms have been normalized to the number of events in each data distribution.
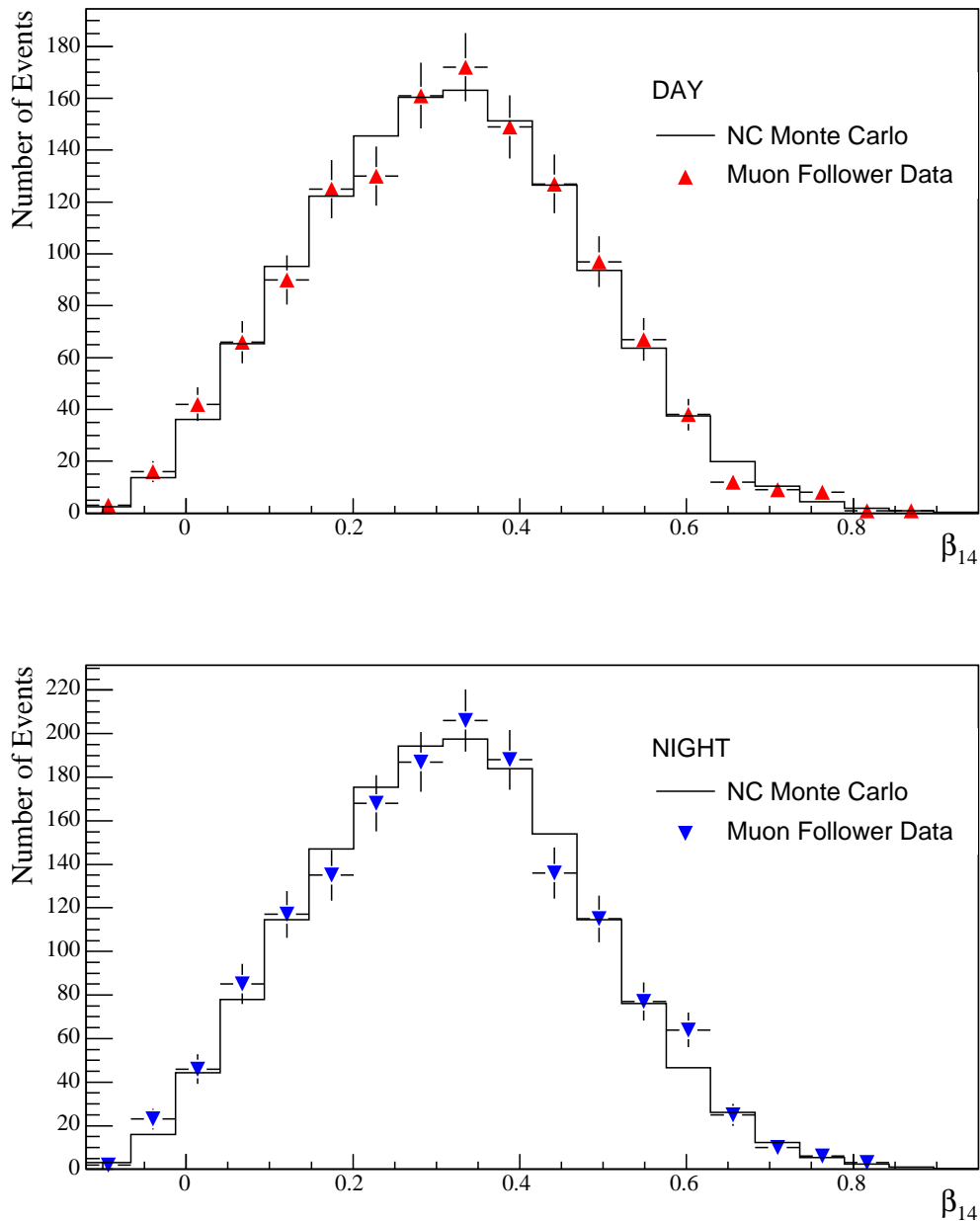
Figure 7.10: Day and night $\beta_{14}$ distributions for muon followers above $T_{eff}$ =4.0 MeV and within a radius 600 cm. The histograms show Monte Carlo distributions for the NC signal, assuming the same energy and fiducial volume cuts. The MC histograms have been normalized to the number of events in each data distribution.

- 3. *High Multiplicity:* The multiplicity cut is removed, so that all neutron events from high-multiplicity spallation interactions are kept.

- 4. *Low Multiplicity:* Only those muon followers for muon events with multiplicities up to 5 events are kept. This tests for bias due to the spatial clustering of higher multiplicity events.

- 5. *Long Time:* The time cut is relaxed so that followers between $50\mu$s and 1s are kept.

- 6. *All Muon Candidates:* The inclusive sample of muon candidates is used rather than the "clean" sample.

- 7. *Restricted Fit Range:* Rather than performing a Gaussian fit over the full range of each distribution, the fit is restricted to a range defined by plus or minus 1.5 $\sigma$ on either side of the mean value. This tests whether fluctuations in the tails of the distributions bias the results.

## 7.5    Systematic Uncertainties Conclusions

For the integral flux analysis, systematic uncertainties are estimated primarily through comparisons of calibration data with Monte Carlo. The Monte Carlo models many features of the detector state, so residual differences between data and MC represent systematic uncertainties in detector response. For the day-night analysis, comparisons of data and MC for the $^{16}$N source are used to limit differential uncertainties with respect to long time periods and with respect to event direction. For diurnal variations, we rely on in-situ techniques using low energy backgrounds and muon follower neutrons.

The muon followers are unfortunately a statistics limited test of diurnal variations in detector response. They may also be subject to biases due to the spatial clustering of muon followers for high-multiplicity muons. Nevertheless, of the signals that can be used for in-situ day-night studies, they are the most like the neutrino data. Unlike the low-energy backgrounds, muon followers can be used to test for diurnal response variations
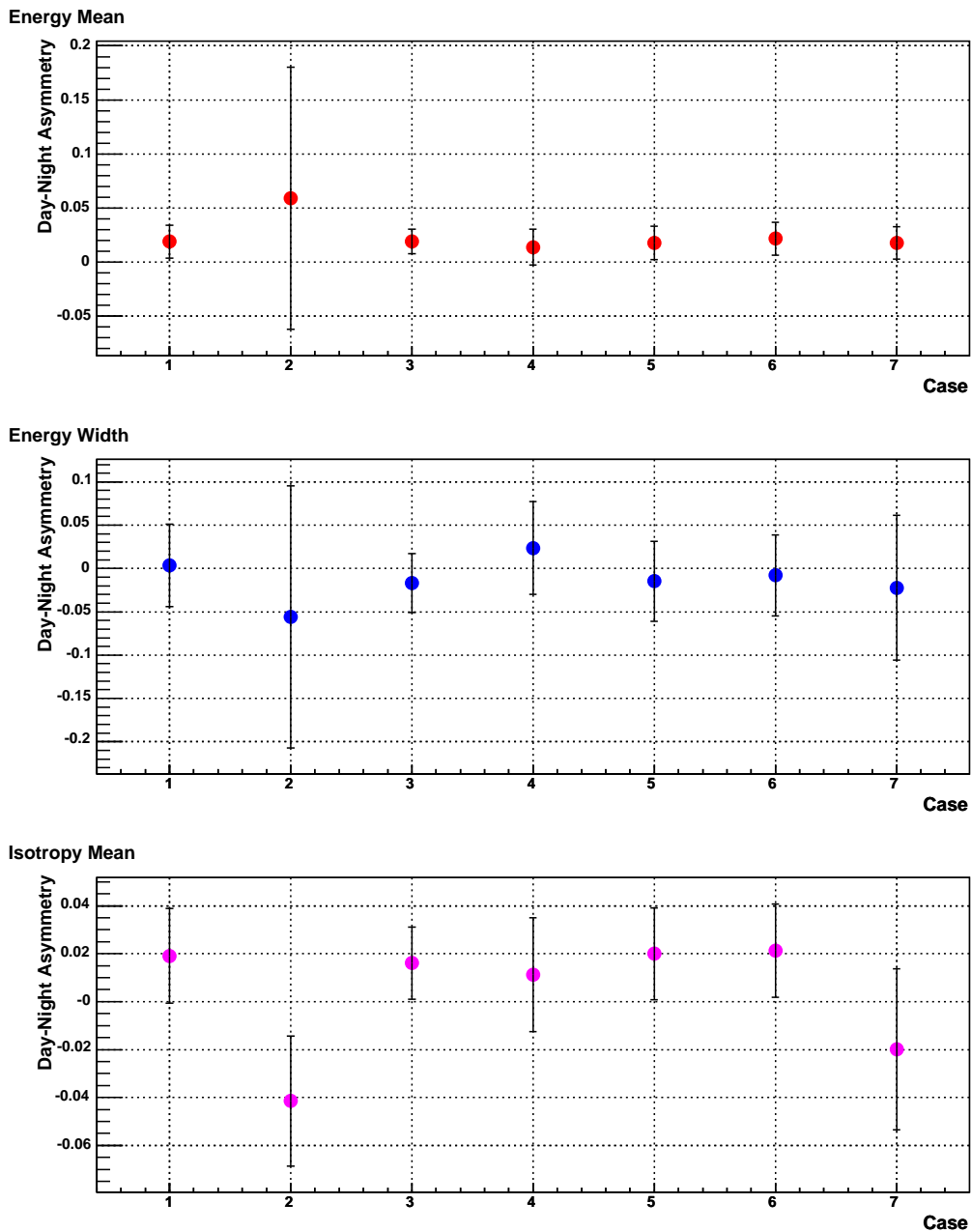
Figure 7.11: Day-night asymmetries in the energy mean, energy width, and isotropy mean for muon followers, for the seven different analysis variations described in the text. The points in each figure should not be viewed as independent, since there are substantial overlaps in the data used in each case.

within the fiducial volume and energy ranges used for analysis of neutrino data. The day-night asymmetries derived from the muon follower studies as well as those derived from the low-energy background studies are all consistent with no asymmetry, within statistical fluctuations of $\sim 1\sigma$. In assigning final systematic uncertainties in diurnal response, the muon follower analysis is viewed primarily as a check on the measurements that were made with low-energy backgrounds.

The high-statistics measurements from low-energy background studies are used to limit diurnal variations in energy scale and energy resolution. The radioactive hot spot is the only source available to study diurnal variations in radial vertex accuracy, and vertex resolution, so systematic uncertainties in these parameters are taken from studies of the diurnal stability of the hot spot position. The systematic uncertainties in diurnal variations of energy scale, energy response, radial vertex accuracy, and vertex resolution are all taken directly from Table 7.3.

For diurnal isotropy variation, limits derived from the low energy background study suffer from poor statistical precision. For this systematic, the limit from the muon follower analysis has been combined with the limit from the low-energy background analysis.[8] Since the muon follower asymmetry in the isotropy mean is consistent with zero, we take the statistical uncertainty in the difference between the night and day isotropy values as a measure of the systematic uncertainty in diurnal isotropy response. From Table 7.4, this gives a limit $\sim 0.006$ in the difference between the day and night values. Combining the muon follower limit with the one from Table 7.3, the final limit on day-night variation in the isotropy mean is 0.0043. The effects of each differential uncertainty on the measurements of the day-night asymmetry parameters will be discussed in Chapter 9.

---

[8]To be completely consistent, the uncertainties derived from the muon follower studies for energy scale and energy resolution should also be combined with low-energy background uncertainties for the final estimates. However, for energy systematics, the low-energy background studies alone provide strong constraints on diurnal variation so the addition of the muon follower information would have little effect.

Chapter 8

# SIGNAL EXTRACTION AND SOLAR NEUTRINO FLUXES

## 8.1   Overview

The central solar neutrino physics goals of the SNO experiment are to measure the total
$^8$B active solar neutrino flux through the NC reaction, and to test for flavor change by
comparing the fluxes measured through the CC and NC reactions. On an event-by-event
basis, it is not possible to tell whether a given event in the final salt data set is due to
CC, NC, ES, or background. The goal of the "signal extraction" process is to determine,
through a statistical fit, the most likely contribution of each class of events to the 4722-event
data set. The measured CC, NC, and ES reaction rates can then be compared to model
predictions to make statements about solar neutrino physics.

The Standard Solar Model predicts the total flux and the spectrum of neutrinos incident
at the surface of the earth. To calculate the predicted event rates in SNO, the neutrino
flux predictions are combined with the cross sections, numbers of target particles in the
detector, detector livetime, and models for the detector response and detection efficiency
for each type of event. These calculations can be done analytically or through Monte Carlo
simulations to determine predicted numbers of events $N_{\mathrm{CC}}^{\mathrm{pred.}}$, $N_{\mathrm{NC}}^{\mathrm{pred.}}$, and $N_{\mathrm{ES}}^{\mathrm{pred.}}$ for the salt
data set. $N_{\mathrm{CC}}^{\mathrm{pred.}}$ and $N_{\mathrm{ES}}^{\mathrm{pred.}}$ represent the predicted number of CC and ES reactions taking
place within the fiducial volume that result in electrons with energies above the analysis
threshold of 5.5 MeV. $N_{\mathrm{NC}}^{\mathrm{pred.}}$ represents the predicted number of NC neutrons within the
fiducial and energy cuts, which are produced by interactions of active neutrinos carrying at
least 2.2 MeV.

The signal extraction process produces the corresponding *measured* numbers of events
of each type, $N_{\mathrm{CC}}$, $N_{\mathrm{NC}}$, and $N_{\mathrm{ES}}$. The ratios $N_\alpha/N_\alpha^{\mathrm{pred.}}$ for $\alpha = $ CC, NC, ES express
each measurement as a fraction of the SSM prediction for that signal. Since the SSM

prediction corresponds to a specific total flux of $^8$B solar neutrinos, we can then express each measurement in terms of an equivalent $^8$B flux:

$$\Phi_\alpha = \frac{N_\alpha}{N_\alpha^{\text{pred.}}} \times \Phi_{8B}, \quad \alpha = \{\text{CC, NC, ES}\}. \tag{8.1}$$

For the salt-phase analysis, the predicted numbers of events are calculated assuming a $^8$B flux of $\Phi_{8B} = 5.05 \times 10^6$ cm$^{-2}$s$^{-1}$ from the "BP00" solar model [127]. This older version of the Standard Solar Model provides consistency with analysis from the first phase of the SNO experiment. Once SNO's measured neutrino interaction rates are converted to equivalent $^8$B fluxes, they can be compared with the predictions from more recent versions of the SSM. The "BP04" model from 2004 [128] predicts a $^8$B flux of $5.79 \pm 1.33 \times 10^6$ cm$^{-2}$s$^{-1}$, while the "BS05" model from 2005 [69] predicts $5.69 \pm 0.91 \times 10^6$ cm$^{-2}$s$^{-1}$. The models depend on different sets of inputs, including different calculations of the radiative opacities in the sun. For more details on variations in solar model calculations, see [69] and references therein.

The quantities described in Equation 8.1 will be referred to as the CC, NC, and ES "fluxes". They represent the equivalent flux of $^8$B neutrinos (integrated over the full $^8$B spectrum) that would be inferred from the event rate measured in each reaction channel. Implicit in the conversion from a measured number of events to "flux units" are assumptions about the flux of hep neutrinos relative to $^8$B neutrinos, as well as about the energy spectra of the solar neutrinos, since these are inputs to the Monte Carlo predictions. These assumptions do not represent model dependencies in the final results, however, since they are only used to normalize the measured numbers of events to a convenient reference.

In the flux units defined by Equation 8.1, the neutral current flux $\Phi_{\text{NC}}$ can be directly compared to the SSM prediction for the total neutrino flux as a test of the solar model prediction. The ratios $\Phi_{\text{CC}}/\Phi_{\text{NC}}$ and $\Phi_{\text{CC}}/\Phi_{\text{ES}}$ can both be used to test for flavor change of solar neutrinos, with the CC to NC ratio giving the greater statistical power. If neutrinos do not change flavor, then all three fluxes should be equal (within statistics), and these ratios should be equal to 1. If neutrinos do change flavor, than the CC to NC flux ratio will give a measure of the fraction of active $^8$B neutrinos that arrive at the detector as electron flavor.

The central purpose of this thesis is to determine the day-night asymmetries in the mea-

sured fluxes for each signal. For the day-night measurement, signal extraction is performed separately in two time bins, and the day-night asymmetry parameters are constructed out of the day and night fluxes. To ensure consistency with the "integral flux" measurements for the salt phase, the signal extraction procedure that was developed for the day-night work closely follows the procedure used in [129] and the integral flux portion of [38]. In this chapter, this procedure will be described, and integral flux results will be presented.[1]

## 8.2  Signal Extraction

The signal extraction procedure relies on an accurate description of the behavior of each signal class in the SNO detector, which can be obtained from analytic parameterizations of detector response, from calibration data, or from Monte Carlo. For the work in this thesis, Monte Carlo simulations are used to construct the characteristic distributions of each class of event with respect to radius, energy, isotropy, and direction relative to the sun. These distributions are normalized and treated as probability density functions (PDFs) in the signal extraction fits. For each signal $\alpha$ ($\alpha$ = CC, NC, ES, or backgrounds), the Monte Carlo distributions define a multi-dimensional PDF $f_\alpha(\vec{x})$, where $\vec{x}$ represents a vector in the space defined by $T_{eff}$ , $\rho$, $\beta_{14}$ , and $\cos\theta_\odot$ . $f_\alpha(\vec{x})$ gives the relative probability that an event of type $\alpha$ will occur with a specific set of values for the event-by-event measureables. A particular model for the physics content of the data set is fully specified by these PDFs along with the amplitudes for each signal, which are simply the number of events of each type, $N_\alpha$.

Each actual event $i$ in the data set corresponds to a specific point $\vec{x}_i$ in the coordinate space defined by the SNO measureables. The total number of events in the data set $n$ is assumed to be a Poisson random variable with mean value $\nu$. The goal of the signal extraction algorithm is to find the set of PDF amplitudes $\vec{N}_\alpha$ such that the probability of obtaining the actual set of data points is maximized. The probability of obtaining the data

---

[1]Note that the analysis techniques and cuts used for the published flux results for the $D_2O$ phase and the 254-day portion of the salt phase were both developed in blind analyses. Because the cuts and analysis techniques for the 391-day salt phase were the same as those used for the 254-day results, additional blindness was not imposed. For more details on this important part of SNO data analysis, see [129] or [35].

set can be simply expressed as

$$\mathcal{L}(\vec{N}_\alpha) = \nu^n \frac{e^{-\nu}}{n!} \prod_{i=1}^n \left( \sum_\alpha N_\alpha f_\alpha(\vec{x_i}) \right). \tag{8.2}$$

This expression for the probability, or "likelihood", includes the Poissonian variation in the total number of events as well as the dependence on the PDF amplitudes. Note that the vector $(\vec{N}_\alpha)$ is the vector of PDF amplitudes, which are just the numbers of events of each signal class, so $\nu = \sum_\alpha N_\alpha$. The vector $\vec{x_i}$ is the vector of coordinate values for event $i$. To maximize the likelihood, we minimize its negative logarithm:

$$-\mathrm{log}\mathcal{L}(\vec{\mathcal{N}}_\alpha) = \sum_\alpha \mathcal{N}_\alpha - \sum_{\rangle=\infty}^{\backslash} \mathrm{log}\left( \sum_\alpha \mathcal{N}_\alpha \{_\alpha(\vec{\S}_\rangle) \right). \tag{8.3}$$

Equation 8.3 is the "Extended Maximum Likelihood" equation [130]. Given the set of PDFs $f_\alpha(\vec{x})$, $\mathrm{log}\mathcal{L}(\vec{\mathcal{N}}_\alpha)$ can be calculated for any set of PDF amplitudes $\vec{N}_\alpha$. The minimization package MINUIT [131], as implemented in ROOT [132], is used to find the set of PDF amplitudes that provide the best fit.

## 8.3    PDFs

To fully describe the data set, we need to construct PDFs for each signal class (CC, NC, and ES) as well as several backgrounds. Neutrons produced within the fiducial volume (from photodisintegration, atmospheric neutrino interactions, or other sources) will share the same features as the NC signal neutrons. These "internal" neutron backgrounds are therefore included in the signal extraction fits as a fixed amplitude contribution to the total number of neutrons. Neutrons from external sources have a different radial profile. A separate PDF is included to describe these external neutrons, and the amplitude of this background is allowed to vary in the fit. A PDF is also included to describe the small background contribution from "internal gammas" due to atmospheric neutrino products. The amplitude of the internal gamma contribution is held fixed in the fit, at 3.6 events. Within the fiducial volume and energy ranges used for analysis, the other types of background events from Table 6.1 do not have sufficiently distinct distributions to warrant the use of additional

PDFs in the signal extraction fits. All of the other sources of background will be treated as systematic uncertainties on the final extracted results.[2]

The PDFs describing the CC, NC, and ES signal distributions in energy, radius, isotropy and direction are derived from Monte Carlo simulations of $^8$B and hep neutrinos. Signal events are generated for the specific running conditions of each run in the data set. The final MC distributions therefore reflect the correct time sampling of the data as well as any variations in the number of working phototubes or other detector parameters, to the extent that these are modeled in the Monte Carlo.

The external neutron (EXTN) background PDF is identical to the NC PDF in the energy, direction, and isotropy variables. It only differs in the radial variable, which distinguishes these events from the NC signal and internal neutron backgrounds. The external neutron radial PDF is taken from Monte Carlo simulations of radioactivity at the location of the acrylic vessel. The internal gamma (INTG) background PDF is "flat" in radius and direction. Its energy and isotropy distributions are taken from the distributions of events from a $^{16}$N calibration run at the center of the detector.

The projections of the PDFs for CC, NC, ES, and EXTN in each of the four variables are shown in Figures 8.1 and 8.2. The $\beta_{14}$ parameter allows statistical separation of neutron-like and electron-like events. The $\cos\theta_\odot$ parameter is most helpful at distinguishing the ES signal, while the $\rho$ parameter allows the external neutron background to be discriminated from the NC signal. The binning and ranges used for each dimension are summarized in Table 8.1.

### 8.3.1  Correlations and Bias

Because of the underlying physics, as well as the geometry and response of the detector, the values of the four event variables for events may be correlated. For example, higher energy events tend to be less isotropic, so they have higher values of $\beta_{14}$ than low energy events. To a lesser extent, isotropy and radius are correlated, as well as energy and direction

---

[2]A number of the backgrounds cannot be directly subtracted from the signal extraction results because it is not know which of the signals they would subtract from, so their amplitudes are treated as uncertainties on each of the flux results.

Table 8.1: Ranges and bin sizes used for the PDFs over each of the four signal extraction variables. Note that the final bin in $T_{eff}$ is wider to ensure Gaussian statistics in that bin.

| Dimension | Range | Binning |
|---|---|---|
| $T_{eff}$ | 5.5 MeV to 20.0 MeV | 0.5 MeV bins; |
| | | final bin from 13.5 to 20.0 MeV |
| $\beta_{14}$ | -0.12 to 0.95 | 100 bins (bin width 0.0107) |
| $\rho$ | 0 to $(550.\text{cm}/600.5\text{cm})^3 = 0.77$ | 40 bins (bin width 0.0193) |
| $\cos\theta_{\odot}$ | -1 to 1 | 100 bins (bin width 0.02) |

relative to the sun. Ideally, one would generate enough Monte Carlo events to fully populate a 4-dimensional PDF, preserving all of the correlations. In practice, several factorizations of the full 4-d PDF give reasonable approximations, with less demanding requirements in terms of Monte Carlo statistics.

The strongest correlations are between isotropy and energy. For this reason, a two-dimensional PDF in $T_{eff}$ and $\beta_{14}$ is absolutely necessary, if not a three dimensional one including $\rho$ as well. The variation of the $\beta_{14}$ distribution as a function of energy for CC and NC Monte Carlo events is shown in Figure 8.3. The PDF factorization that was used in [129] and is used in this thesis is to take

$$f(T_{eff}, \beta_{14}, \rho, \cos\theta_{\odot}) = f(T_{eff}, \beta_{14}) \times f(\rho) \times f(\cos\theta_{\odot}). \tag{8.4}$$

Studies performed by multiple authors [107], [119], [133] showed that signal extraction using the PDF factorization in Equation 8.4 results in slightly biased results. Fits using 100 "fake" MC data sets with fixed numbers of CC, NC, ES, and EXTN events showed that the extracted number of CC events was around 1% lower than the actual number, with a three-sigma significance. The NC extracted numbers showed essentially no evidence for bias, and the ES extracted numbers showed a 1.44% bias, but at a lower significance ($1.6\sigma$). The largest bias is in the extracted number of external neutron events. The fit overestimates

the number of external neutron events by 11.5%, at a greater than $4\sigma$ significance.

To reduce signal extraction bias, a second factorization of the PDF was also used in [38]. In this factorization, the PDF was taken as

$$f(T_{eff}, \beta_{14}, \rho, \cos\theta_\odot) = f(T_{eff}, \beta_{14}, \rho) \times f(\cos\theta_\odot | T_{eff}), \qquad (8.5)$$

where $f(\cos\theta_\odot | T_{eff})$ is a conditional PDF for $\cos\theta_\odot$ given $T_{eff}$. Factorization 8.5 was used in the analysis of the CC energy spectrum in [38] and [119].

Since signal extraction bias has a small effect on neutrino signal results, and since the effect is the same for day and night, the approach used in this thesis is to perform signal extraction using the factorization in Equation 8.4. The final results will be corrected for the biases measured in [133]. These corrections will be given in the next section.

### 8.3.2   Constrained and Unconstrained Analyses

In the salt phase analysis, the $\beta_{14}$ parameter is a powerful tool for separating neutron events from ES or CC events. In the $D_2O$ phase of the experiment, the CC and NC events had similar isotropy distributions, so isotropy was not useful for signal extraction. The radial profile of the NC reaction in the $D_2O$ phase was helpful for distinguishing these events from CC or ES events, but not sufficient for a statistically precise signal extraction. A more powerful signal extraction was possible when the expected energy distributions for each event class were included in the fits. The NC energy spectrum is fixed by the energy of the neutron capture process. The CC and ES spectra, on the other hand, depend on the underlying neutrino spectrum. The Monte Carlo PDFs are based on an undistorted $^8B$ spectral shape, introducing a model dependence into the signal extraction used for the $D_2O$ analysis.

In the salt phase, it is possible to remove the spectrum shape constraint and produce a "model-independent" measure of the solar neutrino reaction rates. Because of the additional isotropy parameter, we can perform an "energy-unconstrained" fit, in which the energy spectrum shapes of the CC and ES signals are allowed to vary. For comparison to previous results, we can also perform an "energy-constrained" fit assuming an undistorted neutrino

spectrum. In either case, the neutron energy profile is fixed, since it is independent of the underlying neutrino spectrum.

In the unconstrained fit, the CC and ES amplitudes are allowed to vary in each energy bin, while the NC signal and the EXTN background are each associated with a single, overall amplitude. The correlations between $\beta_{14}$ and $T_{eff}$ are incorporated by using a conditional $\beta_{14}$ PDF, giving a different $\beta_{14}$ distribution for each energy bin. The unconstrained fit produces measured CC and ES energy spectra, which can then be compared to model predictions to test for spectral distortions. For calculating solar neutrino fluxes and day-night asymmetries, the extracted numbers of CC and ES events in each of the energy bins can be added up to calculate the total number of each type of event.

The signal extraction bias discussed in the previous section is energy-dependent, and has slightly different effects on the constrained and unconstrained analyses. Studies comparing the results of signal extraction performed with both sets of factorizations were used to determine a set of "bias corrections" to apply to results obtained with the factorization in Equation 8.4 [133]. These bias corrections will be applied to all of the flux and spectrum results in this thesis. They are summarized in Tables 8.2. They do not vary diurnally and therefore they will have no effect on the measured day-night asymmetries.

Table 8.2: Multiplicative corrections applied to flux results to account for signal extraction bias, for the energy-constrained and energy-unconstrained fits. From [133]. The corrections are given for the energy constrained and energy-unconstrained fluxes, as well as for the bin-by-bin results for ES and CC in the unconstrained case. These are applied for the integral flux results as well as for the day and night flux results.

| Signal | Constrained | Unconstrained |
|---|---|---|
| NC | 1.0009 | 0.9967 |
| CC | 1.0120 | 1.0163 |
| ES | 0.9858 | 0.9857 |
| EXTN | 0.8962 | 0.8488 |

| Energy | CC correction | ES correction |
|---|---|---|
| 5.75 | 0.9993 | 1.0783 |
| 6.25 | 1.0237 | 1.0224 |
| 6.75 | 1.0171 | 1.0909 |
| 7.25 | 1.0319 | 1.0348 |
| 7.75 | 1.0218 | 0.9995 |
| 8.25 | 1.0121 | 0.9828 |
| 8.75 | 1.0213 | 0.9567 |
| 9.25 | 1.0164 | 0.9733 |
| 9.75 | 1.0205 | 1.0073 |
| 10.25 | 1.0155 | 1.0850 |
| 10.75 | 1.0226 | 0.9451 |
| 11.25 | 1.0118 | 1.0021 |
| 11.75 | 1.0150 | 1.0262 |
| 12.25 | 1.0251 | 1.1016 |
| 12.75 | 1.0262 | 1.0477 |
| 13.25 | 1.0271 | 1.0148 |
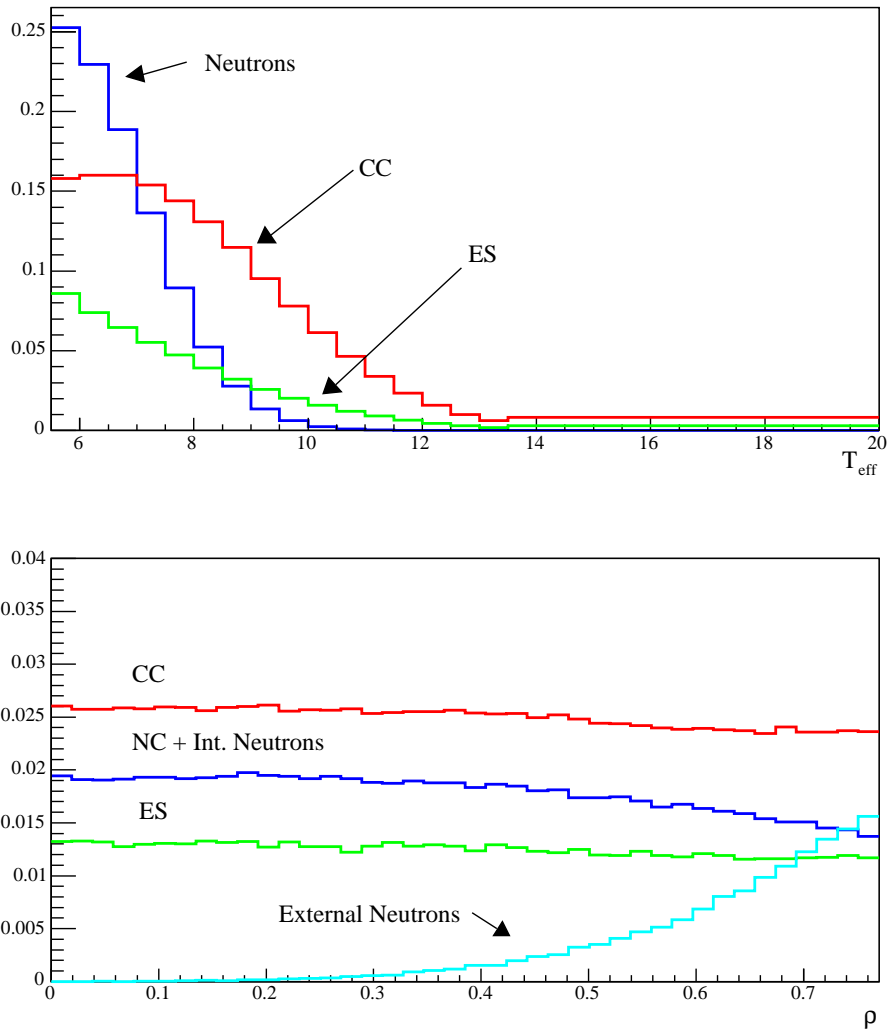
Figure 8.1: Probability density functions from Monte Carlo simulations, showing the distributions of each signal class over the event-by-event measureables $T_{eff}$ and $\rho$. The normalizations are arbitrary, and were chosen to emphasize the differences in PDF shapes. For the $T_{eff}$ , distributions, the "Neutrons" PDF describes NC signal neutrons, internal neutron backgrounds and "external neutrons". However, the external neutrons have a different radial profile from the signal and internal neutron backgrounds. For the radial profile, the internal and external neutrons are treated separately. The PDF used for the "internal gamma" background is not shown.
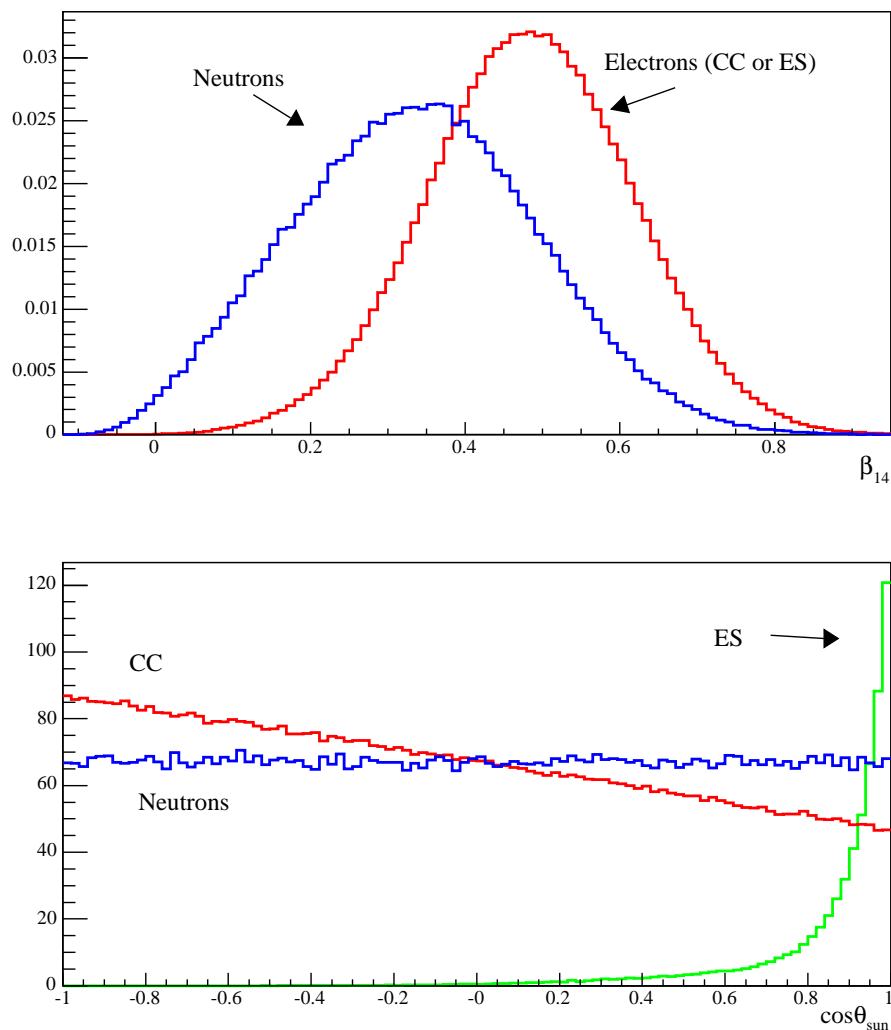
Figure 8.2: Probability density functions from Monte Carlo simulations, showing the distributions of each signal class over the event-by-event measureables $\beta_{14}$ and $\cos\theta_\odot$ . The normalizations are arbitrary, and were chosen to emphasize the differences in PDF shapes. The "Neutrons" PDF describes NC signal neutrons, internal neutron backgrounds and "external neutrons". The PDF used for the "internal gamma" background is not shown.
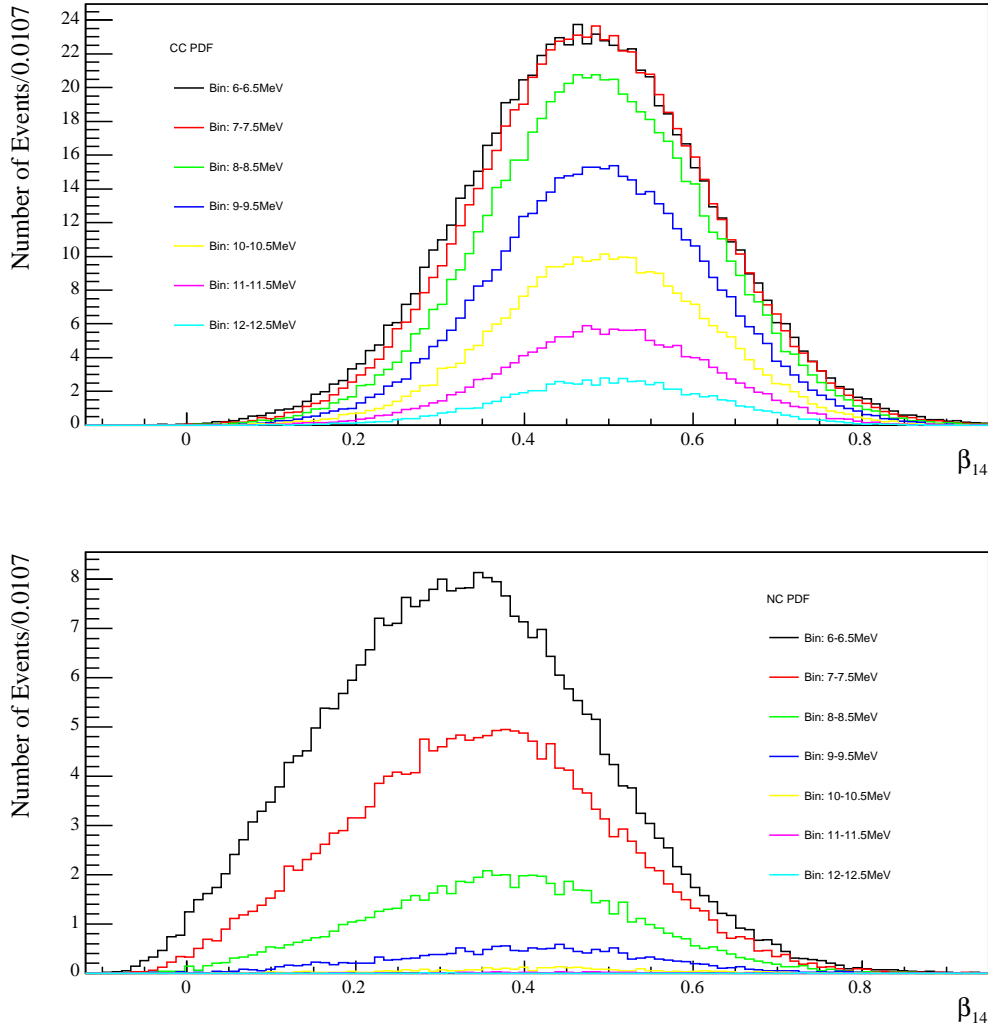
Figure 8.3: $\beta_{14}$ distributions for CC events (top figure) and the neutron events (bottom figure). Each histogram represents the contents of one 0.5 MeV bin in the two-dimensional $T_{eff}$ -$\beta_{14}$ PDFs. The selected energy bins range from 6 MeV to 12 MeV, in 1 MeV steps. At higher energies, events tend to be less isotropic and therefore have larger values of the isotropy parameter $\beta_{14}$ . The plots were produced by projecting the two-dimensional $T_{eff}$ -$\beta_{14}$ PDFs onto the $\beta_{14}$ axis, and the overall normalizations for the $\beta_{14}$ curves in the figure reflect the relative number of events in each energy range.

## 8.4  Predicted Numbers of Events

For the salt analysis, Monte Carlo simulations were performed to generate $^8$B neutrinos equivalent to 200 times the Standard Solar Model (SSM), and hep neutrinos equivalent to 2000 times the SSM. The interactions of these neutrinos in SNO were then propagated, using the livetime and detector conditions appropriate for the 1212-run salt data set. Weighting the $^8$B and hep contributions by the appropriate scaling factors, the MC can then give predictions for the total number of CC, NC, and ES events in the salt data set, assuming SSM neutrino fluxes. For the NC reaction, the Monte Carlo is not used to obtain the final predicted number of events. The rate of neutral current interactions of $^8$B and hep neutrinos within the detector volume is calculated to be 13.1715 neutrons per day for the Standard Solar Model. This rate is combined with the salt phase livetime and the measured neutron capture efficiency within the fiducial region in order to determine the predicted number of NC events.

A number of corrections must then be applied to the predicted numbers of events, to account for elements of the Monte Carlo simulations (or the external NC calculation) that are not quite accurate. These correction factors are described below and summarized in Table 8.3. For use in the day-night analysis, the correction factors appropriate for day and night are given along with those appropriate for the integral flux analysis.

- *Livetime:* The Monte Carlo does not model the "deadtime" due to data selection cuts. The predicted number of events from the CC and NC MC calculations must be adjusted downward for the appropriate final livetimes. The NC calculation is done externally with the correct livetime, so this correction is not needed for the NC prediction. The livetime correction will be slightly different for day and night.

- *Cut Acceptance:* The set of data-selection cuts that are applied to the data are not modeled in the MC. The Monte Carlo predictions are corrected to account for the measured signal loss due to these cuts, which is taken from [120].

- *SSM Fluxes:* The Monte Carlo generates neutrino events using an older version of

the Standard Solar Model, in which the total $^8$B flux was $5.15 \times 10^6$ cm$^{-2}$s$^{-1}$. We correct the predicted number of events to an equivalent $^8$B flux of $5.05 \times 10^6$ cm$^{-2}$s$^{-1}$, appropriate for the "BP00" solar model prediction [127].

- *Orbital Eccentricity:* The actual flux of neutrinos arriving at the surface of the earth depends on the season, because the distance between the earth and the sun changes with time. The earth's orbital eccentricity is modeled in the MC, so the ES and CC predictions do not need to be corrected for this effect. However, the NC prediction does need to be corrected. For the day-night analysis, the eccentricity corrections are slightly different for day and night.

- *CC interactions with O, Na, and Cl:* CC reactions are also possible on $^{17}$O, $^{18}$O, $^{23}$Na, $^{35}$Cl and $^{37}$Cl in the detector. These CC interactions are not modeled in the Monte Carlo, and result in a slight correction to the CC prediction[134].

- *Simulation Errors:* A small fraction of Monte Carlo simulated events fail to be fully propagated due to "geometry errors". The number of predicted events is scaled upward to account for the measured rate of these simulation failures.

- *Target Deuterons :* The Monte Carlo detector model uses a slightly incorrect value for the number of target deuterons in the heavy water volume. This results in another small correction to the predicted reaction rates for the CC reaction [135].

- *Target electrons:* The Monte Carlo uses a slightly incorrect value for the number of target electrons. The ES prediction must be corrected for this [135].

- $g_A$: The neutrino-deuteron interaction cross sections that are used in the Monte Carlo come from effective field theory calculations [92]. An updated value of the weak axial coupling, $g_A$, is suggested in reference [136]. A correction is made to the predicted numbers of CC and NC events to account for the difference.

- $L_{1,A}$ : The effective field theory calculations of the neutrino cross sections [92] are normalized to potential-model calculations of the cross sections [137] by fixing the two-body axial exchange-current counter term $L_{1,A}$. A correction is applied to the CC and NC predictions to account for an updated $L_{1,A}$ value, that is appropriate for normalizing to a more recent potential-model calculation [138].

- *Radiative Corrections:* Radiative corrections to the CC, NC, and ES cross sections are not modeled in the MC. The correction to the NC prediction is a simple scaling; for CC and ES, energy-dependent corrections are applied. This is done by individually weighting each simulated MC event by an energy-dependent weight function. These weight functions, derived from reference [139], are parameterized as follows:

$$w_{CC} = 1.0318 - 7.45 \times 10^{-4} \cdot E_{gen} + 4.72 \times 10^{-6} \cdot E_{gen}^2 \qquad (8.6)$$
$$w_{ES} = 0.9764 - 7.81 \times 10^{-4} \cdot T_{eff} - 1.31 \times 10^{-4} \cdot T_{eff}^2 + 3.64 \times 10^{-6} \cdot T_{eff}^3,$$

where $T_{eff}$ is the measured kinetic energy of the electron, and $E_{gen}$ is the true total energy of the electron (the energy at which the electron was generated by the Monte Carlo).

The radiative corrections for CC and ES are applied on an event-by-event basis to the simulated events used for building PDFs. The other corrections are applied to the total predicted number of events for each signal. The predicted numbers of events, with all of these corrections applied, are

$$N_{CC} = 6558.43 \text{ events}$$
$$N_{NC} = 2056.21 \text{ events}$$
$$N_{ES} = 598.838 \text{ events.} \qquad (8.7)$$

These correspond to the total predicted number of events within the appropriate fiducial region and over the livetime period sampled by the salt data set. They assume neutrino fluxes from the BP00 model, which corresponds to a $^8$B flux of $5.05 \times 10^6$ cm$^{-2}$s$^{-1}$. All detector acceptance factors and correction factors have been included.

Table 8.3: Flux corrections for the day-night and integral flux analyses. $w_{CC}$ and $w_{ES}$ refer the radiative correction weightings that must be applied to the CC and ES events when building the PDFs, as described in the text. The radiative corrections $w_{CC}$ and $w_{ES}$ are applied on an event-by-event basis to the Monte Carlo, but the other corrections are applied multiplicatively to the total predicted numbers of events.

| Correction | CC | ES | NC |
|---|---|---|---|
| Correct flux to $5.05 \times 10^6$ cm$^{-2}$s$^{-1}$ $^8$B flux | 0.9806 | 0.9806 | 0.9806 |
| Mean orbital radius, all | 1.00 | 1.00 | 1.00101 |
| Mean orbital radius, day | | | 0.99534 |
| Mean orbital radius, night | | | 1.00555 |
| CC on O and Na isotopes | 1.0081 | 1.0 | 1.0 |
| Number of deuterons in MC | 1.01228 | 1.0 | 1.0 |
| Number of electrons in MC | 1.0 | 1.0151 | 1.0 |
| Cut acceptance | 0.9943 | 0.9914 | 0.9932 |
| MC geometry error loss fraction | 1.0048 | 1.0029 | 1.00 |
| $g_A = 1.267$ | 1.0111 | 1.0 | 1.0111 |
| Radiative corrections | $w_{CC}$ | $w_{ES}$ | 1.0154 |
| L1A corrections | 0.984 | 1.0 | 0.979 |
| Livetime corrections, all | 0.9820 | 0.9820 | 1.00 |
| Livetime corrections, day | 0.9815 | 0.9815 | 1.00 |
| Livetime corrections, night | 0.9825 | 0.9825 | 1.00 |
| Total, all | 0.9768 $(\times w_{CC})$ | 0.9719 $(\times w_{ES})$ | 0.9799 |
| Total, day | 0.9763 $(\times w_{CC})$ | 0.9714 $(\times w_{ES})$ | 0.9743 |
| Total, night | 0.9773 $(\times w_{CC})$ | 0.9724 $(\times w_{ES})$ | 0.9843 |

## 8.5  Signal Extraction Results

For the day-night results in this thesis, software was written to assemble data sets, build PDFs, and perform signal extraction fits. It was tested by reproducing the 254-day salt phase integral flux results [129], and was used to provide an independent check on the 391-day results [38]. Very close agreement between the integral flux results produced with the signal extraction code used for this thesis and the published integral flux results ensures consistency of the day-night analysis techniques with those used for the integral flux analysis.

Integral flux results are given below for the energy-unconstrained and energy-constrained analysis of the full 391-day data set, using the PDFs from Section 8.3 and the signal extraction algorithm outlined in Section 8.2. These results were produced as a check on the results that were included in [38]. Systematic uncertainties on the integral flux results were not independently propagated for this work. Where systematic uncertainties are presented, they are taken from [38].

### 8.5.1  Unconstrained Analysis

The energy-unconstrained analysis produces spectra for the CC and ES reactions, as well as total numbers of each event class. The total numbers of events extracted in the unconstrained analysis are summarized in Table 8.4. The extracted external neutron background is roughly 128 events, comparable in size to the internal neutron background that is subtracted directly from the fit number of neutrons.

Table 8.4: Extracted numbers of events with statistical uncertainties, for the energy-unconstrained analysis. The results have been corrected for signal extraction bias.

| Signal | Number of Events |
| --- | --- |
| NC | $2011.05 \pm 85.6267$ |
| CC | $2176.15 \pm 80.6055$ |
| ES | $279.09 \pm 27.5824$ |
| EXTN | $128.44 \pm 36.3932$ |

The CC and ES spectrum results are given in Table 8.5, with statistical uncertainties. These spectra are shown, along with the rest of the fit results, in Figures 8.4 and 8.5. The figures show the data distributions compared to the PDFs for each signal, weighted by the results from the fit. The extracted CC spectrum from the salt phase can be used to directly test for spectral distortions due to MSW effects or other physics. A full discussion of the extracted CC spectrum from the salt phase, including evaluation of systematic uncertainties that affect the spectrum shape, can be found in [38] and [119].

Table 8.5: Extracted numbers of CC and ES events with statistical uncertainties, for each bin in energy. The first bin starts at 13.5 MeV. Bins are 0.5 MeV wide except for the last bin, which extends from 13.5 to 20 MeV.

| Bin | Number of CC Events | Number of ES Events |
|-----|---------------------|---------------------|
| 1 | $222.169 \pm 26.6178$ | $54.1508 \pm 12.7645$ |
| 2 | $222.834 \pm 26.6304$ | $43.4742 \pm 10.7496$ |
| 3 | $223.899 \pm 25.4055$ | $40.2792 \pm 11.6255$ |
| 4 | $260.178 \pm 24.2313$ | $26.8759 \pm 9.4733$ |
| 5 | $240.408 \pm 21.5458$ | $22.5799 \pm 8.41284$ |
| 6 | $224.221 \pm 19.2577$ | $21.3781 \pm 7.64691$ |
| 7 | $152.607 \pm 15.4516$ | $27.2277 \pm 7.17492$ |
| 8 | $147.865 \pm 14.2511$ | $16.8214 \pm 6.39091$ |
| 9 | $152.308 \pm 13.7235$ | $6.73268 \pm 4.98067$ |
| 10 | $81.7105 \pm 10.058$ | $12.2176 \pm 5.30856$ |
| 11 | $93.3328 \pm 10.5085$ | $5.44459 \pm 4.04482$ |
| 12 | $57.6347 \pm 8.2396$ | $4.14682 \pm 3.57899$ |
| 13 | $45.3196 \pm 7.16142$ | $1.28879 \pm 2.57518$ |
| 14 | $17.6589 \pm 4.47104$ | $1.95292 \pm 2.09294$ |
| 15 | $15.6628 \pm 4.26846$ | $3.89811 \pm 2.51451$ |
| 16 | $4.67803 \pm 2.3967$ | $2.48311 \pm 1.85543$ |
| 17 | $17.623 \pm 4.40334$ | $0.373384 \pm 1.45906$ |

The numbers of events in Table 8.4 can be converted to neutrino fluxes using the predicted numbers of events in Equation 8.7 and the expression in Equation 8.1. The derived neutrino fluxes, in units of $10^6$ cm$^{-2}$s$^{-1}$, are[3]

$$\Phi_{\mathrm{NC}} = 4.94 \pm 0.21 \,(\mathrm{stat.})\,{}^{+0.38}_{-0.34}\,(\mathrm{syst.})$$

$$\Phi_{\mathrm{CC}} = 1.68 \pm 0.06 \,(\mathrm{stat.})\,{}^{+0.08}_{-0.09}\,(\mathrm{syst.})$$

$$\Phi_{\mathrm{ES}} = 2.35 \pm 0.23 \,(\mathrm{stat.})\,{}^{+0.15}_{-0.15}\,(\mathrm{syst.}) \tag{8.8}$$

The extracted NC flux result from the energy-unconstrained analysis is in good agreement with standard solar model predictions for the $^8$B solar neutrino flux ($5.69 \pm 0.91 \times 10^6$ cm$^{-2}$s$^{-1}$ for Solar Model "BS05"[69]). The CC and ES fluxes are also suppressed relative to the NC flux, providing evidence for solar neutrino flavor change.

Correlation coefficients for these results are given in Table 8.6. The CC and NC results

Table 8.6: Matrix of correlation coefficients for the energy-unconstrained signal extraction.

|      | NC      | CC      | ES      | EXTN    |
|------|---------|---------|---------|---------|
| NC   | 1.0000  | -0.5293 | -0.0642 | -0.3994 |
| CC   | -0.5293 | 1.0000  | -0.1487 | -0.0607 |
| ES   | -0.0642 | -0.1487 | 1.0000  | -0.0121 |
| EXTN | -0.3994 | -0.0607 | -0.0121 | 1.0000  |

are substantially negatively correlated, with a correlation coefficient of -0.529. Using the correlation coefficients in Table 8.6 and the flux results, we can calculate the CC to NC ratio and the CC to ES ratio:

$$\frac{\Phi_{\mathrm{CC}}}{\Phi_{\mathrm{NC}}} = 0.340 \pm 0.023 (\mathrm{stat.})^{+0.029}_{-0.031}(\mathrm{syst.}), \tag{8.9}$$

---

[3]For these results and the rest of the results presented in this chapter, quoted systematic uncertainties come from tables of the systematic shifts of the signal extraction results with respect to variations in each of the response parameters or backgrounds discussed in Chapter 7. These tables were computed by Kevin Graham and were used to calculate the systematic uncertainties quoted in [38]. The results presented in this chapter come from exactly the same analysis procedure as the results in [38] so the same systematic uncertainties apply.
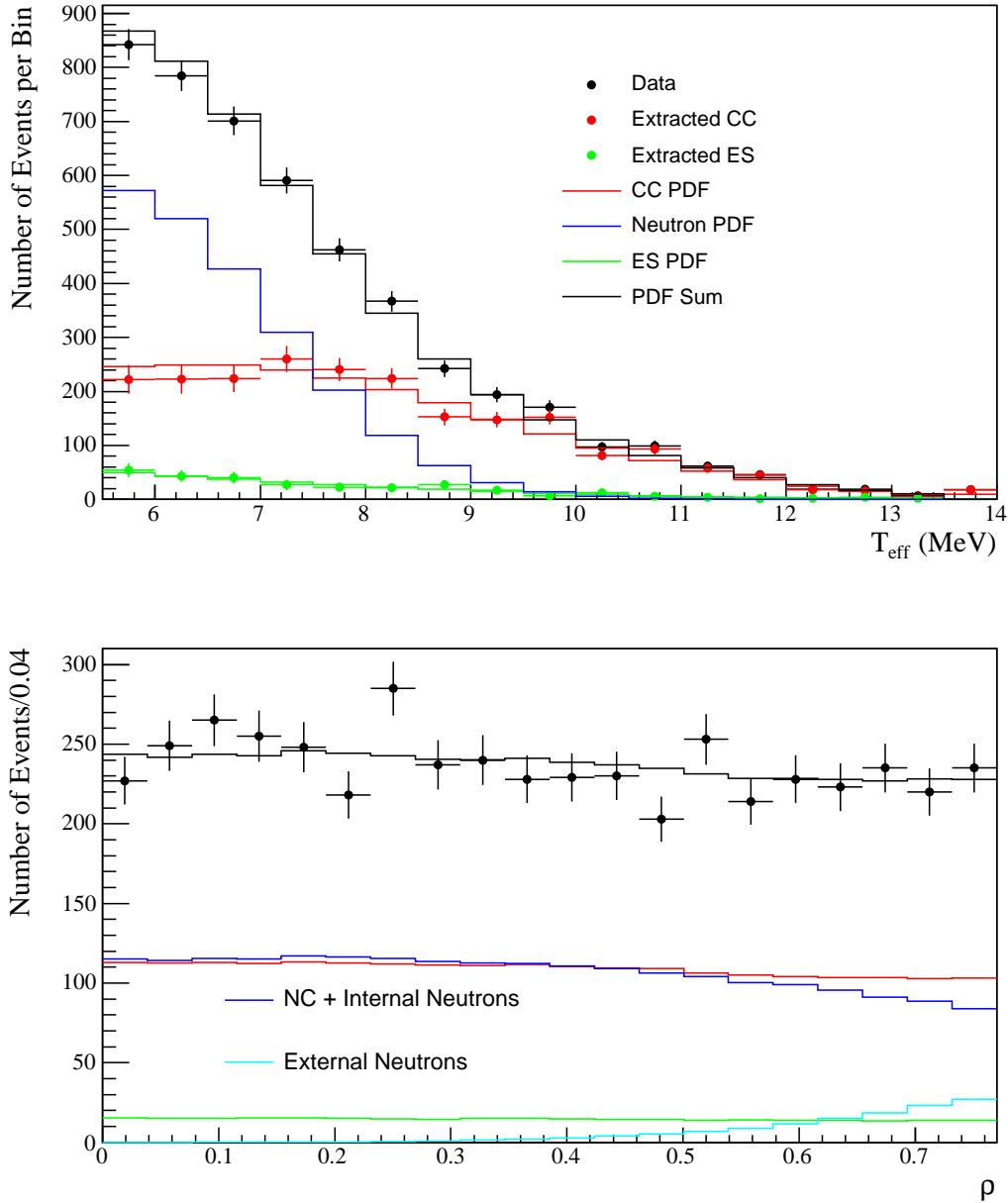
Figure 8.4: Results of the energy-unconstrained signal extraction, compared to data distributions in $T_{eff}$ and $\rho$. The black points show the data distributions. The histograms show the PDFs for each signal, weighted by the fit results. The black histograms shows the sum of the fit results for all signals. The extracted CC and ES spectra are also shown, with statistical uncertainties only. In the $T_{eff}$ distributions, the bins are 0.5 MeV wide except for the final bin, which extends from 13.5 MeV to 20 MeV. For the radial distribution, the neutron PDF is made up of two separate components: one representing NC neutron or neutron backgrounds within the $D_2O$, and one representing the "external" neutron backgrounds.
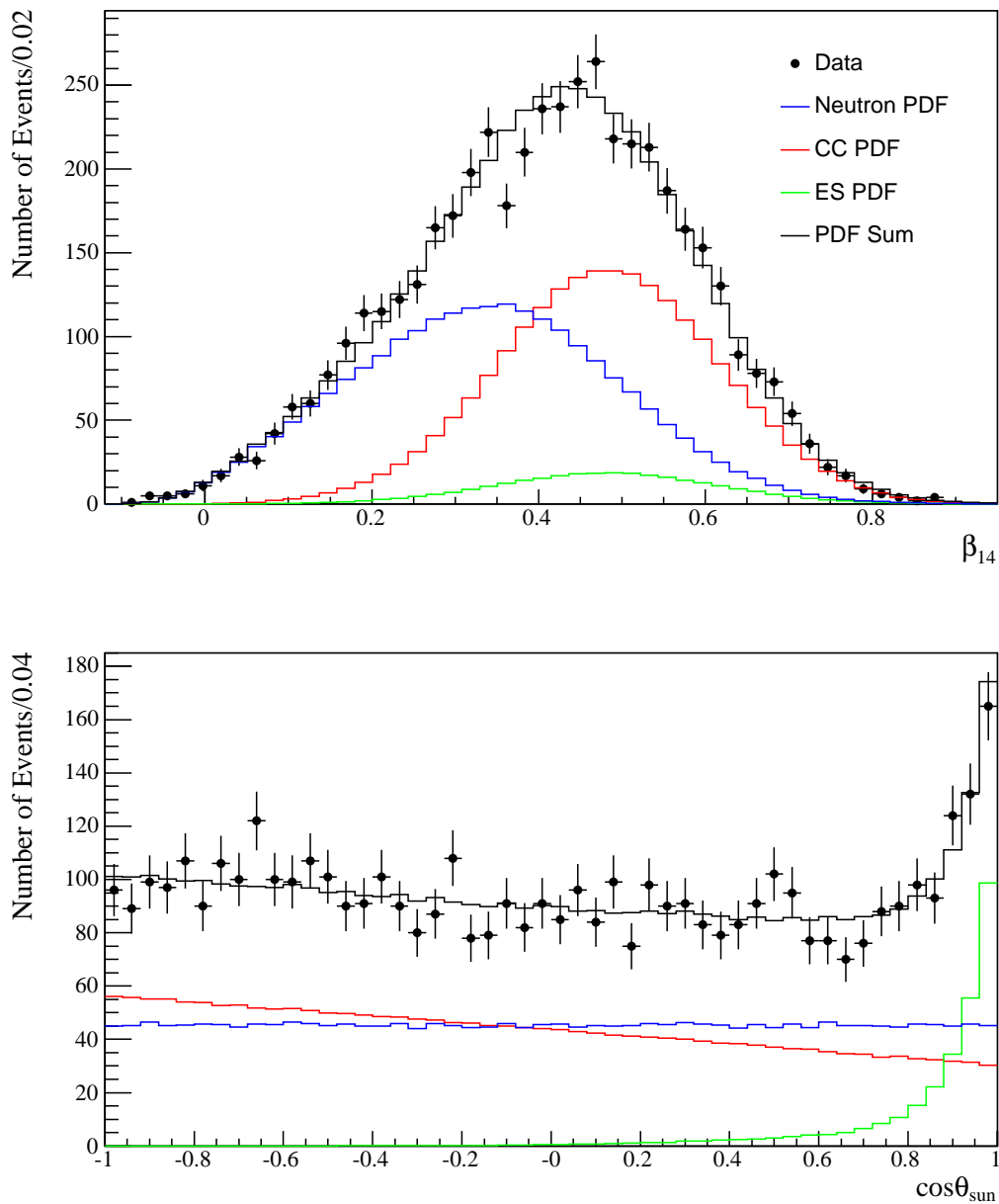
Figure 8.5: Results of the energy-unconstrained signal extraction, compared to data distributions in $\beta_{14}$ and $\cos\theta_\odot$ . The black points show the data distributions. The histograms show the PDFs for each signal, weighted by the fit results. The black histograms shows the sum of the fit results for all signals.

$$\frac{\Phi_{\text{CC}}}{\Phi_{\text{ES}}} = 0.712 \pm 0.075 \text{(stat.)}^{+0.042}_{-0.044} \text{(syst.)}. \tag{8.10}$$

The CC to NC ratio is a direct test of flavor change, as it measures the fraction of the total active neutrino flux from the sun that "survives" as electron flavor. Observation that the CC and ES fluxes are not equivalent is an additional indication of neutrino flavor change, because the elastic scattering flux has a component due to the neutral current scattering of any active neutrino flavor on electrons in the heavy water.

Underlying the three measurements are only two flux parameters: the flux of electron neutrinos $\Phi_e$ and the flux of mu and tau neutrinos, $\Phi_{\mu\tau}$. For an energy threshold of $T_{eff}$ = 5.5 MeV, the elastic scattering flux is approximately given by $\Phi_{\text{ES}} = \Phi_e + 0.1553\Phi_{\mu\tau}$. The CC, NC, and ES fluxes can be combined in several ways to present measurements of $\Phi_e$ and $\Phi_{\mu\tau}$. Subtracting the CC flux from the NC flux gives the most straightforward measurement of the $\mu\tau$ contribution,

$$\Phi_{\mu\tau}(\text{NC}) = 3.26 \pm 0.25 \text{(stat.)}^{+0.40}_{-0.35} \text{(syst.)} \times 10^6 \text{cm}^{-2}\text{s}^{-1}. \tag{8.11}$$

This demonstrates the appearance of mu and tau neutrinos in the solar neutrino flux at the $\sim 7\sigma$. Combining the CC and ES fluxes, we can also measure $\Phi_{\mu\tau}$ without using the NC measurement:

$$\Phi_{\mu\tau}(\text{ES}) = 4.36 \pm 1.52 \text{(stat.)}^{+0.90}_{-0.87} \text{(syst.)} \times 10^6 \text{cm}^{-2}\text{s}^{-1}. \tag{8.12}$$

These results will be discussed in more detail at the end of the chapter.

### 8.5.2 Constrained Analysis

Applying the additional constraint of an undistorted $^8$B neutrino spectrum reduces the statistical and systematic uncertainties on the results, and allows the fluxes to be directly compared with those measured in the pure-$D_2O$ phase. Results for the numbers of events extracted in the energy-constrained analysis are given in Table 8.7. The calculated neutrino fluxes, in units of $10^6$ cm$^{-2}$s$^{-1}$, are

$$
\begin{aligned}
\Phi_{\text{NC}} &= 4.81 \pm 0.19 \,\text{(stat.)} \,^{+0.28}_{-0.27} \,\text{(syst.)} \\
\Phi_{\text{CC}} &= 1.72 \pm 0.05 \,\text{(stat.)} \,^{+0.11}_{-0.11} \,\text{(syst.)} \\
\Phi_{\text{ES}} &= 2.34 \pm 0.23 \,\text{(stat.)} \,^{+0.15}_{-0.14} \,\text{(syst.)}.
\end{aligned}
\tag{8.13}
$$

Table 8.7: Extracted numbers of events with statistical uncertainties, for the energy-constrained analysis. The results have been corrected for signal extraction bias.

| Signal | Number of Events |
|--------|------------------|
| NC | $1960.23 \pm 77.04$ |
| CC | $2234.73 \pm 69.97$ |
| ES | $277.22 \pm 27.49$ |
| EXTN | $130.58 \pm 38.21$ |

The extra constraint on the energy spectra reduces the statistical correlations between the CC and NC signals, as shown in Table 8.8. The constrained fit results are illustrated in Figures 8.6 and 8.7.

Table 8.8: Matrix of correlation coefficients for the energy-constrained signal extraction.

| | NC | CC | ES | EXTN |
|------|--------|--------|--------|----------|
| NC | 1.0000 | -0.4011 | -0.0730 | -0.471456 |
| CC | -0.4011 | 1.0000 | -0.1687 | -0.0375 |
| ES | -0.0730 | -0.1687 | 1.0000 | -0.0121 |
| EXTN | -0.4715 | -0.0375 | -0.0121 | 1.0000 |

For comparison, the flux ratios for the constrained case are

$$\frac{\Phi_{\mathrm{CC}}}{\Phi_{\mathrm{NC}}} = 0.358 \pm 0.021(\text{stat.})^{+0.028}_{-0.029}(\text{syst.}), \tag{8.14}$$

and

$$\frac{\Phi_{\mathrm{CC}}}{\Phi_{\mathrm{ES}}} = 0.736 \pm 0.079(\text{stat.})^{+0.050}_{-0.049}(\text{syst.}). \tag{8.15}$$

The calculated values of $\Phi_{\mu\tau}$ from combining the CC and NC and the CC and ES fluxes are

$$\Phi_{\mu\tau}(\text{NC}) = 3.09 \pm 0.22(\text{stat.})^{+0.30}_{-0.27}(\text{syst.}), \tag{8.16}$$
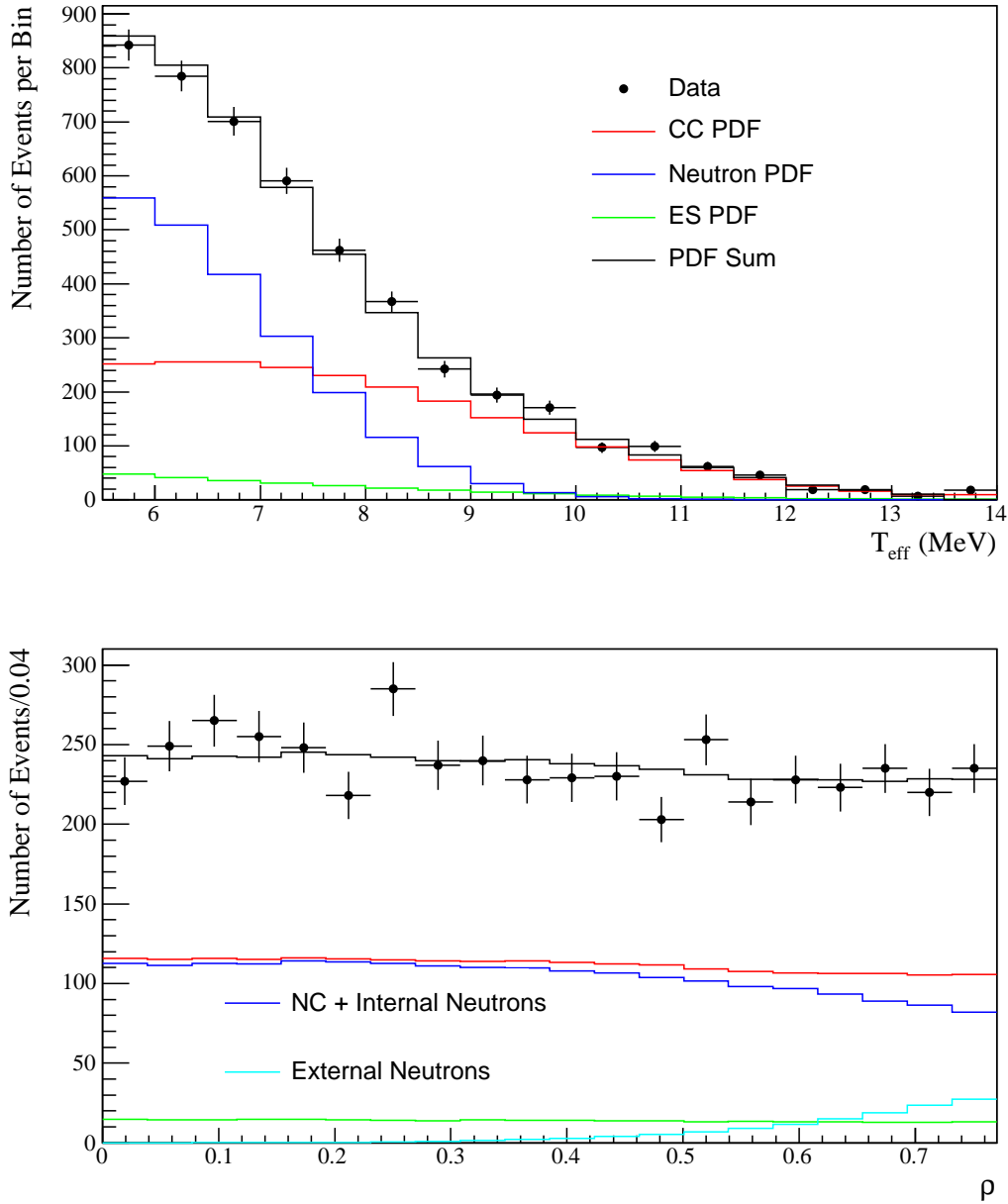
Figure 8.6: Results of the energy-constrained signal extraction, compared to data distributions in $T_{eff}$ and $rho$. The black points show the data distributions. The histograms show the PDFs for each signal, weighted by the fit results. The black histograms shows the sum of the fit results for all signals. In the $T_{eff}$ distributions, the bins are 0.5 MeV wide except for the final bin, which extends from 13.5 MeV to 20 MeV.
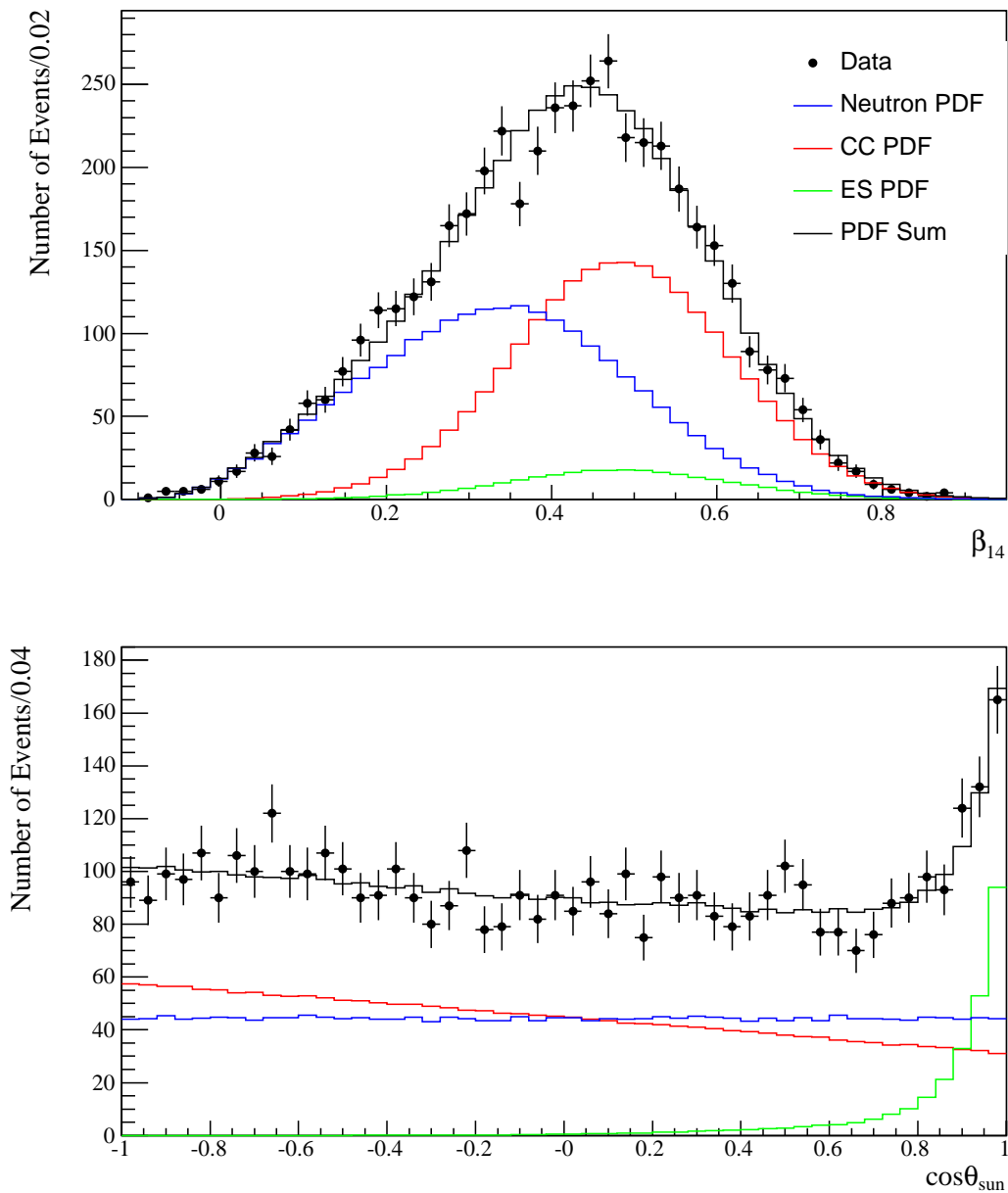
Figure 8.7: Results of the energy-constrained signal extraction, compared to data distributions in $\beta_{14}$ and $\cos\theta_\odot$ . The black points show the data distributions. The histograms show the PDFs for each signal, weighted by the fit results. The black histograms shows the sum of the fit results for all signals.

and

$$\Phi_{\mu\tau}(\text{ES}) = 3.97 \pm 1.56(\text{stat.})^{+0.92}_{-0.89}(\text{syst.}). \tag{8.17}$$

The energy-constrained results agree with the energy-unconstrained results, with smaller statistical uncertainties.

## 8.6    Comparison with Previous Results

Figure 8.8 compares the results for the NC flux from this chapter to previous SNO measurements. The NC flux results from the 391-day salt phase are consistent with the results published for the 254-day subset in [129], and with the results from the pure-$D_2O$ phase, in [35]. The higher neutron capture cross section and higher energy of the neutron capture reaction in the salt phase translate to higher neutron statistics in the salt phase relative to the $D_2O$ phase. The salt phase NC measurements in both the energy-constrained and energy-unconstrained analyses are improvements relative to the energy-constrained analysis in the pure-$D_2O$ phase.

Figure 8.9 shows a similar comparison the results for the CC flux from this chapter with those from previous SNO publications. The salt phase energy-unconstrained CC result has comparable statistical and systematic uncertainties to the energy-constrained analysis of the $D_2O$ phase. The energy-constrained analysis in the salt phase reduces the statistical uncertainties on the CC flux, but increases the systematic uncertainties relative to the energy-unconstrained case. This is largely due to the difference in sensitivity to the energy scale uncertainty. The energy-unconstrained analysis is less sensitive to this particular systematic, although it is more sensitive to variations in the $\beta_{14}$ parameter. The energy-unconstrained CC flux result for the full 391-day salt data set is somewhat higher than the result published in [129] for the 254-day subset of the salt data. The neutral current fluxes for the 391-day and 254-day energy-unconstrained results also differ slightly. Since one of these data sets is a subset of the other, we expect the differences between the two results to be small. To test for possible differences in the analysis between the two salt-phase results, the signal extraction software used to extract the 391-day results was used to reproduce the 254-day results. Agreement with the published results for the 254-day data set demonstrated
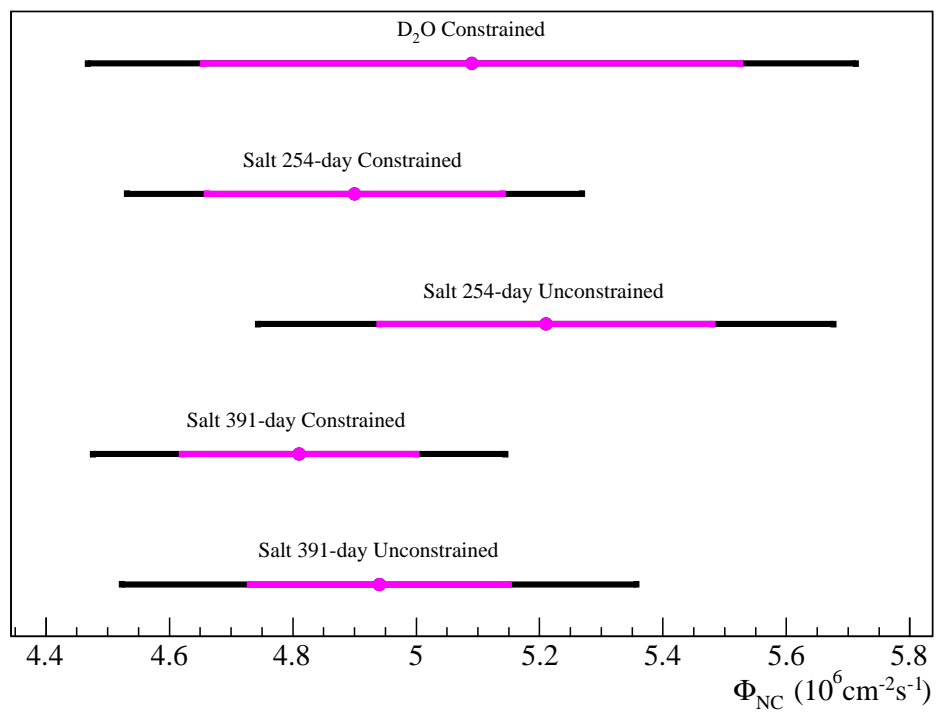
Figure 8.8: Comparison of the measured NC fluxes from the energy-constrained and energy-unconstrained analyses of the 391-day salt data set and the published 254-day salt results and 306-day $D_2O$ results. The smaller bars represent the statistical uncertainties on each result, and the larger bars represent the total uncertainty.
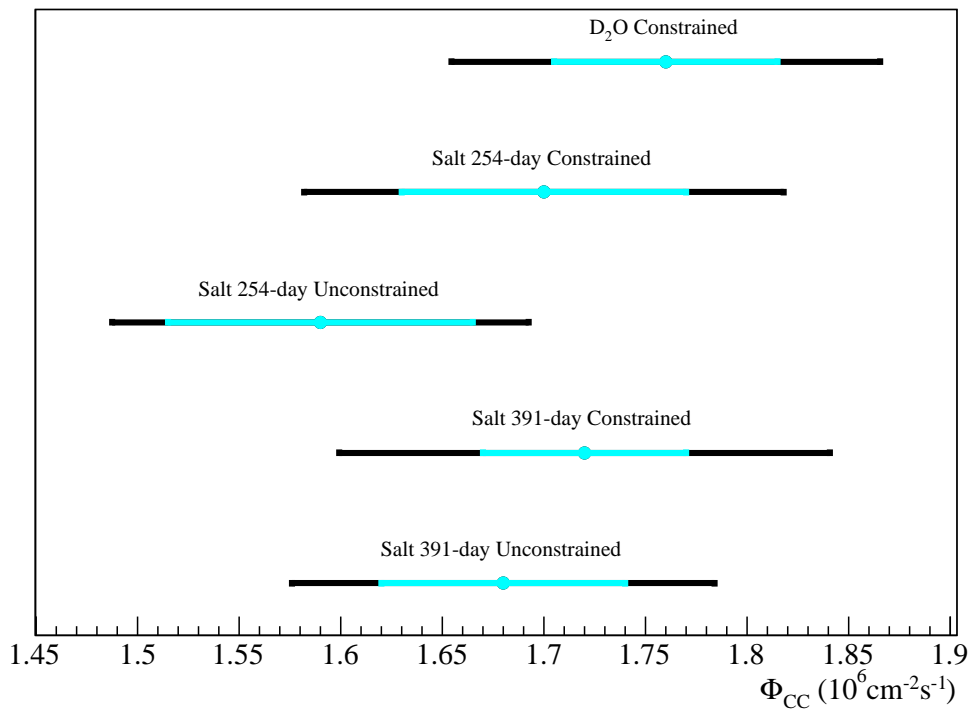
Figure 8.9: Comparison of the measured CC fluxes from the energy-constrained and energy-unconstrained analyses of the 391-day salt data set and the published 254-day salt results and 306-day $D_2O$ results. The smaller bars represent the statistical uncertainties on each result, and the larger bars represent the total uncertainty.

that there were no significant differences in the signal extraction algorithms used for the results. Furthermore, fits were performed in which the signal PDFs for the 254-day and 391-day data sets were interchanged, to test for any differences in the Monte Carlo signal distributions used in each analysis. Although the PDFs used for the signal extraction in each case are constructed out of Monte Carlo simulations customized to the run conditions of each data set, the actual differences between PDFs produced for different data sets are very small. The shift in the energy-unconstrained CC flux result between the 254-day result and the 391-day result does not appear to be due to any differences in the signal extraction or PDFs used for the two analyses.

A simplified signal extraction performed separately on the 254-day data set, the 137-day remainder, and the 391-day total data set gives results summarized in Table 8.9. The table gives the average event rates for each class of events for each phase. For the 391-day results in [38], background estimates and systematic uncertainties were largely re-evaluated for the entire data set. Because of the complications of assigning numbers of background events separately to the 254-day and 137-day subsets of the salt data set, the neutron backgrounds have not been subtracted from the total number of neutrons returned by the fit for Table 8.9. The quoted neutron event rates include backgrounds as well as NC neutrons. A single set of PDFs (those used for the 391-day analysis) were used for these fits, and the contribution due to internal gamma backgrounds was set to zero. To the precision given in the table, none of these modifications to the signal extraction is significant. The 137-day subset of the data shows an enhanced CC event rate and reduced neutron rate relative to the 254-day data set.

Although the variations between the 254-day and 137-day subsets of the salt phase data are consistent with $1\sigma$ statistical fluctuations in the event rates, one additional test for systematic shifts was also performed. Of the detector response parameters, the energy scale is one that is known to vary with time, although this is accounted for in the analysis. To test whether variations in the energy scale could be responsible for a shift in the results, the fits performed for Table 8.9 were repeated, with exaggerated energy scale shifts applied to the Monte Carlo PDFs. Shifting the energy scale for the Monte Carlo up by 3% for the 254-day data set and down by 3% for the 137-day data set gives the results in Table 8.10.

Table 8.9: Event rates for neutron (NC plus internal neutron background), CC, ES, and EXTN events, determined by performing a simplified signal extraction on the 254-day salt data set, the 137-day salt data set, and the full 391-day data set.

|  | 254-day data set | 137-day data set | 391-day data set |
|---|---|---|---|
| Neutron rate | $(5.7 \pm 0.3)$/day | $(5.0 \pm 0.4)$/day | $(5.5 \pm 0.2)$/day |
| CC event rate | $(5.3 \pm 0.2)$/day | $(5.9 \pm 0.4)$/day | $(5.5 \pm 0.2)$/day |
| ES event rate | $(0.7 \pm 0.1)$/day | $(0.8 \pm 0.1)$/day | $(0.7 \pm 0.1)$/day |
| EXTN event rate | $(0.3 \pm 0.1)$/day | $(0.5 \pm 0.2)$/day | $(0.4 \pm 0.1)$/day |

Even such a large relative shift in energy scale (which is inconsistent with the energy scale variations measured through regular $^{16}$N calibrations) do not bring the results for the two subsets of the salt phase into close agreement. Having checked for obvious mistakes that could cause artificial differences between the 254-day and 391-day results, we conclude that any differences are likely due to statistical fluctuations in the event rates.

Table 8.10: Event rates from signal extraction on the 254-day data set with Monte Carlo events shifted up 3% in energy compared to event rates from signal extraction on the remaining 137-day data set, with Monte Carlo events shifted down 3% in energy.

|  | 254-day, MC E-scale 3% up | 137-day, MC E-scale 3% down |
|---|---|---|
| Neutron rate | $(5.6 \pm 0.3)$/day | $(5.1 \pm 0.4)$/day |
| CC event rate | $(5.4 \pm 0.3)$/day | $(5.8 \pm 0.4)$/day |
| ES event rate | $(0.7 \pm 0.1)$/day | $(0.8 \pm 0.1)$/day |
| EXTN event rate | $(0.3 \pm 0.1)$/day | $(0.5 \pm 0.2)$/day |

## 8.7   Discussion and Future Directions

Given the uniqueness of SNO's measurements, perhaps the most important contribution of the salt phase neutrino flux measurements is the independent confirmation of the results

from the first phase of the experiment. Measurements of the solar neutrino reaction rates with deuterium are unlikely to be repeated in any future experiments, so the results from multiple phases of the SNO experiment provide cross-checks and increase the robustness of SNO's results.

The 391-day salt phase results for the NC flux both confirm and improve the NC measurement from the $D_2O$ phase. The energy-unconstrained analysis yields a measurement of $\Phi_{NC} = 4.94 \pm 0.21 \,(\text{stat.}) \, ^{+0.38}_{-0.34} \,(\text{syst.})$, which agrees with Standard Solar Model predictions and surpasses the theory predictions in precision. While the precision on the CC measurement is not dramatically improved in the salt phase compared to the $D_2O$ phase, the use of the $\beta_{14}$ parameter allows the CC flux to be extracted without assuming an undistorted spectrum shape. The energy-unconstrained analysis of the salt phase data therefore allows model-independent extraction of the solar neutrino fluxes. The CC and ES spectra are extracted as additional measurements in the salt phase analysis. Since the CC spectrum directly reflects the underlying neutrino spectrum, it can be used to test for distortions in the $^8B$ solar neutrino spectrum. The measured spectrum, described more fully in [38], is consistent with an undistorted $^8B$ neutrino spectrum, as well as the predicted spectrum for the favored MSW neutrino oscillation parameters.

A comparison of the CC and NC reaction rates in the salt phase provides strong evidence for solar neutrino flavor change. This is illustrated in Figure 8.10, which shows the joint confidence intervals for measurements of $\Phi_e$ and $\Phi_{\mu\tau}$ based on the CC and NC fluxes from the salt phase. The precision on the NC measurement in the salt phase allows a $\sim 7\sigma$ demonstration of the appearance of non-electron neutrinos in the solar neutrino flux.

The implications of these results for the determination of solar neutrino oscillation parameters will be discussed in more detail in Chapter 11. For now, note that the CC to NC flux ratio directly measures the electron neutrino survival probability in the three-neutrino oscillation scenario. In the LMA MSW model for neutrino oscillations, the survival probability is approximately equal to $\sin^2\theta$, where $\theta$ is the mixing angle relevant for solar neutrino oscillations (see Chapter 3). Better measurements of the CC to NC ratio will therefore translate directly into more precise measurements of this fundamental physics parameter, given the LMA MSW model.
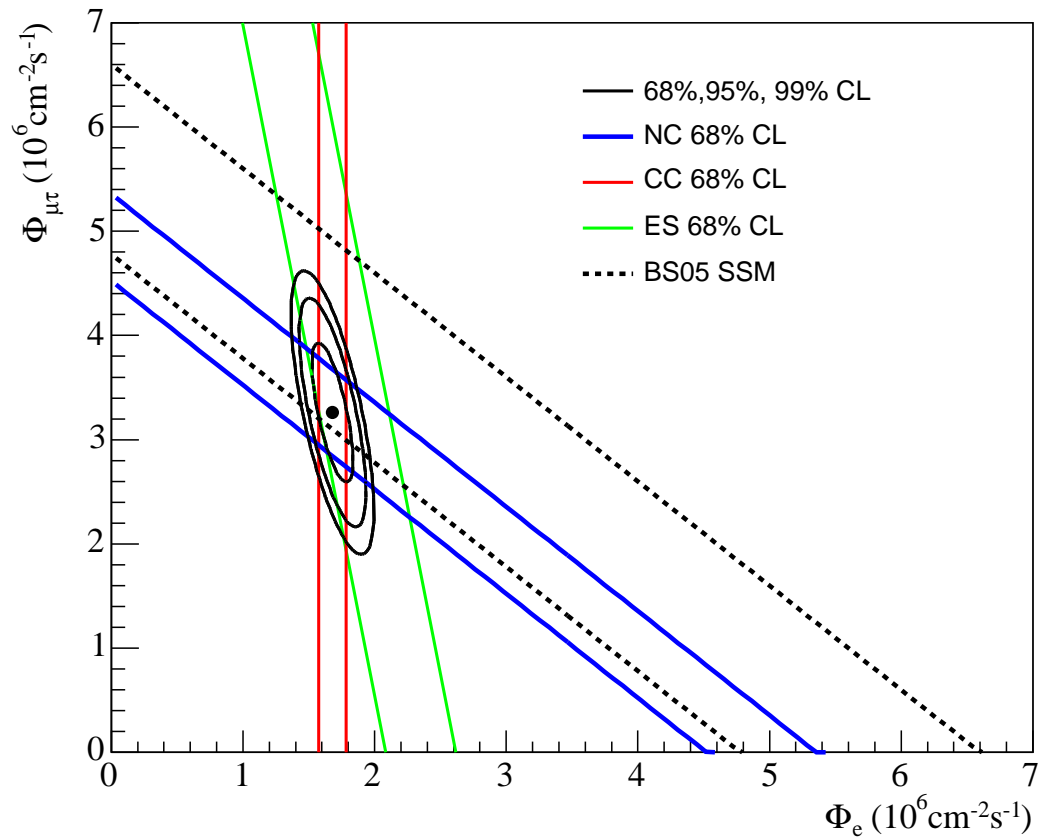
Figure 8.10: 68%,95%, and 99% Confidence intervals for the measurements of $\Phi_{\mu\tau}$ and $\Phi_e$ are shown, where $\Phi_{\mu\tau}$ has been calculated by subtracting $\Phi_{CC}$ from $\Phi_{NC}$. The 68% confidence intervals for the CC, NC, and ES measured fluxes are indicated by the solid bands. The dashed bands show the 68% CL interval for the predicted NC flux from the BS05 Standard Solar Model [69].

Future measurements with SNO will improve on the results presented in this chapter in several ways. The final phase of the SNO experiment, using discrete neutron detectors (NCDs) to measure the NC flux, will provide additional tests of SNO's central neutrino physics results with a dramatically different set of systematic uncertainties, backgrounds, and analysis techniques. The NC flux measured using the NCDs will be completely independent of the measurement of the CC rate using the photomultiplier tube array. Since the correlations between these two parameters contribute substantially to the statistical and systematic uncertainties on the NC flux and the CC to NC ratio, breaking these correlations will improve the overall results.

The results from both the $D_2O$ and salt phases can also be improved and extended with additional work. For both phases, additional analysis could reduce some of the systematic uncertainties in response parameters. Changes in the way that systematic uncertainties are handled in the analysis could also improve the precision of the results. In particular, modeling the dependence of the fluxes on response parameters within the signal extraction fits would improve estimates of systematic uncertainties in the final results.

Work is currently being done to extend the analysis to lower energy thresholds. This will improve the statistics for the flux results, and allow tests for distortions in the CC spectrum shape at lower energies, where the LMA MSW model predicts an effect. The NCD phase provides a unique opportunity to study the CC spectrum shape without the presence of a large number of neutron events in a similar energy range.

Ultimately, the most precise determinations of the NC flux and the CC to NC ratio will come from a combination of the results from SNO's three phases. Investigations are taking place into the best ways to perform a joint analysis of the data from multiple phases. A key element of any technique is a careful determination of the correlations between the systematic uncertainties in each phase.

Chapter 9

# DAY NIGHT RESULTS

## *9.1  Overview*

The previous chapter presented solar neutrino flux measurements using the CC, NC, and ES reactions in the salt phase of SNO. The salt phase flux results demonstrate solar neutrino flavor change and confirm predictions for the total flux of $^8$B neutrinos from the sun. The flavor change indicated by SNO's flux results is interpreted as evidence for solar neutrino oscillations in the MSW framework. Depending on the values of the underlying neutrino parameters $\Delta m^2$ and $\theta$, MSW matter effects could also alter the flavor composition of solar neutrinos passing through the material in the earth. The simplest test for earth matter effects is to repeat the solar neutrino analysis in two time bins, testing for differences in the neutrino fluxes inferred from the daytime SNO data and those inferred from the night data. Given separate night and day measurements $\Phi_\alpha^N$ and $\Phi_\alpha^D$ of the neutrino fluxes for $\alpha = \{\text{CC, NC, ES}\}$ we can construct asymmetry parameters,

$$A_\alpha = 2\frac{\Phi_\alpha^N - \Phi_\alpha^D}{\Phi_\alpha^N + \Phi_\alpha^D}, \quad \alpha = \{\text{CC, NC, ES}\}. \tag{9.1}$$

As described in Chapter 3, the MSW model predicts a "regeneration" of electron neutrinos as the solar neutrinos pass through the earth. A positive day-night asymmetry $A_{\text{CC}}$ would therefore be evidence for the MSW effect. Within the MSW model, negative values of $A_{\text{CC}}$ are unphysical, although they are certainly experimentally possible. The best-fit oscillation parameters from global analyses of all solar and reactor neutrino data are in the LMA region of the MSW parameter space, where day-night asymmetries in the electron neutrino flux are expected to be roughly 2-4% (see Figure 3.5).

In the standard MSW oscillation model, including oscillations only between the three active neutrino flavors, we expect that $A_{\text{NC}}$ should be zero. The neutral current flux is a measure of the total flux of neutrinos from the sun, and the total flux of neutrinos from the

sun does not change day to night. A significant asymmetry in the neutral current flux would be evidence for new physics, such as oscillations into sterile neutrino states. However, a large asymmetry is not an explicit prediction of typical models for sterile neutrino oscillations, as described in Section 3.6.1.

For SNO, measurement of the elastic scattering asymmetry $A_{ES}$ adds very little to what we can learn through measuring $A_{CC}$ and $A_{NC}$, because the elastic scattering signal has such low statistics. The Super-Kamiokande experiment achieves much more precise measurements of $A_{ES}$. However, it is not possible to directly interpret the Super-Kamiokande $A_{ES}$ result in terms of the underlying electron neutrino or total neutrino flux asymmetries without using additional information to disentangle the charged-current and neutral-current contributions to the ES reaction rate. SNO's measurements of the CC and NC fluxes can be combined with the Super-Kamiokande results to aid in such interpretation. The ability to separately measure the CC and NC day-night asymmetries is unique to the SNO experiment.

## 9.2   Signal Extraction

The signal extraction technique used to determine the day and night neutrino fluxes is the same as that described in Section 8.2. Separate PDFs are created for day and night, using the Monte Carlo simulations of signal properties appropriate for the night and day livetime during the salt phase. Individual data events are classified into day or night using the cosine of the zenith angle for each event: events during the day have positive values of $\cos\theta_Z$, and events during the night have negative values. Separate signal extraction fits can then be performed to independently extract the numbers of CC, NC, ES, and EXTN events in each data set. We then construct the day-night asymmetry parameters $A_{CC}$, $A_{NC}$, and $A_{ES}$ from the extracted day and night fluxes. The use of the $\beta_{14}$ parameter in the salt phase enables an energy-unconstrained measurement of the day-night asymmetries that was not possible in the $D_2O$ phase. Electron regeneration is an energy-dependent effect, so the unconstrained analysis is a more consistent test for MSW physics.

The results in Chapter 8 show that the neutrino fluxes extracted through both the

energy-unconstrained and energy-constrained analyses are substantially statistically correlated. Imposing the energy spectrum constraint reduces the correlations relative to the unconstrained analysis, but in both cases the correlations affect the statistical precision that can be achieved for the flux results. These statistical correlations will also affect the asymmetry measurements, and $A_{CC}$ and $A_{NC}$ will be correlated roughly to the extent that the individual fluxes $\Phi_{CC}$ and $\Phi_{NC}$ are correlated.

To reduce these correlations, and to construct a more specific test for MSW physics, we can do a joint fit of the day and night data, requiring the NC flux to be the same for both. This is an additional model constraint, appropriate for three-neutrino oscillation models. In this "NC-constrained" fit, the neutral current asymmetry is zero by construction. This variation on the signal extraction can be combined with the energy spectrum constraint or with the energy-unconstrained technique. There are a total of four variations on the basic signal extraction process that are used in the salt phase day-night analysis. They are summarized below.

- *Energy Unconstrained, NC-Unconstrained:* This is the most model-independent analysis of the day-night asymmetries. In the energy-unconstrained, neutral current unconstrained fit, the CC and ES fluxes are allowed to vary independently day and night and in each energy bin. The amplitudes of the NC signal and the EXTN background are allowed to vary day and night. In this analysis, $A_{CC}$ tests for electron neutrino regeneration, and $A_{NC}$ tests for new physics like sterile neutrinos. $A_{NC}$ and $A_{CC}$ will be substantially correlated, but the individual night and day fluxes for each signal are uncorrelated because they are extracted independently.

- *Energy Constrained, NC-Unconstrained:* Imposing the constraint of an undistorted $^8$B neutrino spectrum, we extract the CC, NC, ES, and EXTN values day and night and construct $A_{CC}$, $A_{NC}$, and $A_{ES}$. The results from this analysis can be directly compared to the energy-constrained day-night asymmetries measured during the $D_2O$ phase. This is a model-dependent variation on the signal extraction, which assumes that the mechanism for solar neutrino flavor change does not depend on neutrino energy.

- *Energy Unconstrained, NC-Constrained:* Applying the constraint that the neutral current asymmetry is zero couples the day and night fits. In the energy-unconstrained case, this means that we are simultaneously fitting for day and night flux values for CC and ES in every energy bin, along with day and night values for the EXTN background and one value for the NC flux. To ensure that detector variations between the day and night data sets are appropriately accounted for in the NC-constrained fit, the signal extraction fit is done directly in terms of "flux units" rather than in terms of numbers of events. Although the neutral current constraint reduces the statistical covariance of the CC and NC fluxes, it also has the side effect of introducing minor correlations between day and night results for the other signals. Propagation of statistical uncertainties in this case must be performed with care. The relevant error propagation formulas are given in Appendix A. This variation on the signal extraction reflects an assumption of standard neutrino oscillations with three active neutrino flavors, such that the total active neutrino flux is constant day and night.

- *Energy Constrained, NC-Constrained:* Constraining both the spectrum and the neutral current asymmetry leads to the most precise measurement. In this case we assume that only active-flavor neutrino oscillations can contribute to the day-night asymmetries, and also assume that any electron neutrino regeneration effects are independent of neutrino energy. This is the most model-dependent of the four analysis variations.

In the $D_2O$ phase of the experiment, only the two energy-constrained versions of the signal extraction procedure were used. When the solar neutrino spectrum is constrained, the relationship between the CC and ES spectra is fixed, and the contribution of the charged-current and neutral-current scattering processes to the ES flux is easily calculated. $A_{\text{CC}}$, $A_{\text{NC}}$, and $A_{\text{ES}}$ depend on only two independent parameters, the asymmetry in the electron neutrino flux, $A_{\text{e}}$, and the asymmetry in the total flux of all flavors, $A_{tot}$. A simple change of variables can be used to calculate $A_{\text{e}}$ and $A_{tot}$ from $A_{\text{CC}}$, $A_{\text{NC}}$, and $A_{\text{ES}}$ if the relationship between the energy spectra of the CC and ES reactions is fixed, using the fact that $\Phi_{\text{ES}} = \Phi_e + \epsilon\Phi_{\mu\tau}$ (with $\epsilon$ depending on the choice of energy threshold used in the

analysis). The elastic scattering asymmetry is, however, so statistically limited that it adds very little to the determination of either $A_{\mathrm{e}}$ or $A_{tot}$.

In the salt phase, the principal results are obtained in an energy-unconstrained analysis. In this case, the relationship between the CC and ES spectra is more complex. For the salt phase analysis, we will take $A_{\mathrm{CC}}$ as a direct measure of the electron neutrino asymmetry $A_{\mathrm{e}}$ , and take $A_{\mathrm{NC}}$ as a direct measure of the total day-night asymmetry $A_{tot}$, rather than doing a change-of-variables using all three measurements. We will therefore not be making much use of the the elastic scattering asymmetry $A_{\mathrm{ES}}$ from the salt phase of SNO, although it will be presented for comparison.

### 9.3   PDFs

A single set of PDFs is used for all four types of fit. They are built using the same Monte Carlo simulated data that is used to create PDFs for the integral flux analysis, separated into day and night components. The day and night PDFs are very similar, but include the slight variations in detector conditions day and night. The relative day and night livetimes are also properly sampled, so that it is possible to use these PDFs for calculating the SSM predicted CC and ES fluxes for day and night. Comparisons of the day and night PDFs for the CC signal are shown in Figure 9.1 as an example of the level of variation day to night. The only distribution that shows noticeable differences between the day and night PDFs is the $\cos\theta_{\odot}$ distribution. At night, the neck region of the detector affects the acceptance for events characterized by large values of $\cos\theta_{\odot}$ . During the day, the opposite is true, which explains the slight difference between the two $\cos\theta_{\odot}$ distributions.

### 9.4   Predicted Numbers of Events

The predictions for the day and night numbers of events assuming the Standard Solar Model are calculated in the same way as those for the flux analysis (Section 8.4). The corrections that need to be applied to the day and night predicted numbers of events differ slightly due to the differences in the fraction of livetime cut by data selection cuts for night and day. For the neutral current prediction, the correction accounting for the eccentricity of the earth's
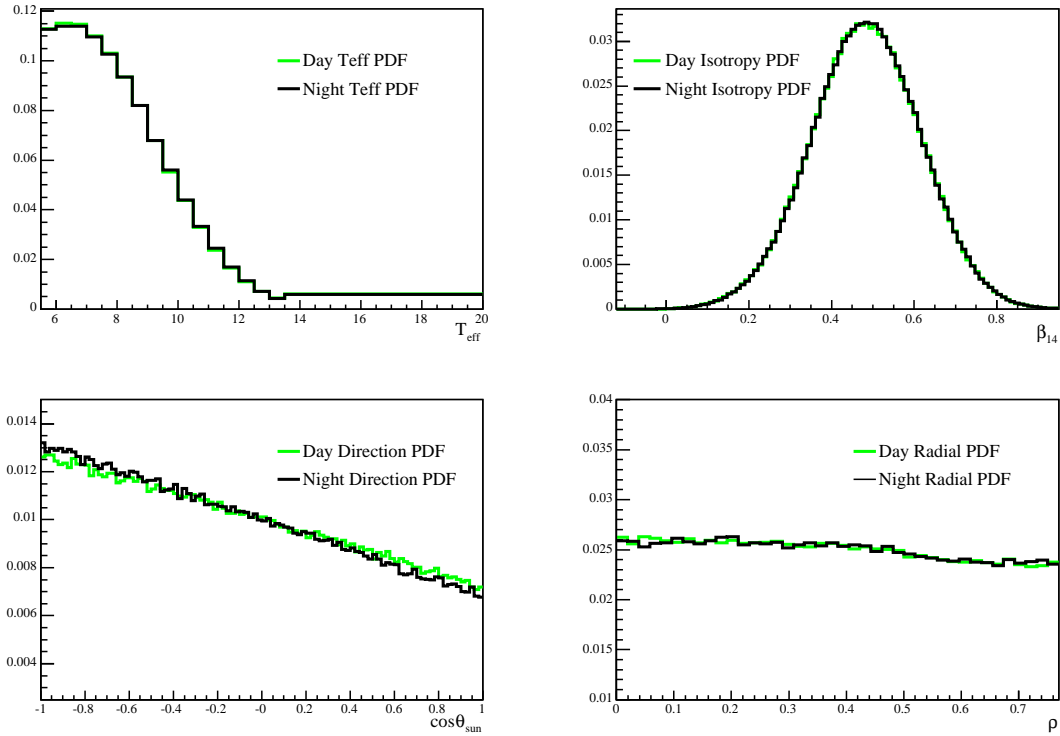
Figure 9.1: Comparisons of the day and night PDFs for the CC signal, projected onto the $T_{eff}$ , $\beta_{14}$ , $\cos\theta_{\odot}$ , and $\rho$ dimensions. The distributions in each dimension have been normalized to unit area.

orbit also differs for the day and night data sets. The day and night correction factors are taken from Table 8.3. Table 9.1 summarizes the predicted numbers of events day and night, assuming the BP00 Standard Solar Model predictions.

## 9.5 Systematic Error Propagation

The systematic uncertainties that must be propagated for the day-night asymmetry measurement were described in detail in Chapter 7. The basic strategy for propagating these systematic uncertainties is to vary the inputs to the signal extraction within their $\pm 1\sigma$ ranges, and then to repeat the fits. The resulting differences in the extracted neutrino fluxes are taken as measures of the one-sigma uncertainty due to variation in each input

Table 9.1: Predicted numbers of events above 5.5 MeV and within 550 cm, with all corrections applied, for day and night. These correspond to a Standard Solar Model with a $^8$B flux of $5.05 \times 10^6$ cm$^{-2}$s$^{-1}$ [127]. The day livetime is 176.511 days, and for night, 214.921 days.

| Signal | Day Prediction | Night Prediction |
|--------|----------------|------------------|
| NC     | 921.921 events | 1134.06 events   |
| CC     | 2934.94 events | 3623.42 events   |
| ES     | 274.923 events | 323.939 events   |

parameter. Uncertainties in the numbers of background events or in their asymmetries are propagated by varying the numbers of events that are fixed in the fit or subtracted from the fit results. Several backgrounds are treated entirely as uncertainties on the final numbers of events, since there is no way to know which signal they would subtract from in the fit. Uncertainties in response parameters are propagated by perturbing the PDFs and repeating the fits.

For the diurnal systematics, the uncertainties given in Section 7.4 represent limits on the estimated differences between the day and night values for each response parameter. These are given either as percentage differences or as absolute differences in the day and night values of the parameters. To propagate these uncertainties, the size of the systematic uncertainty is divided in half and the day and night PDFs are then "smeared" in opposite directions to simulate the relative day-night shift. For example, to propagate the diurnal energy scale uncertainty, the energy values of Monte Carlo events used for the day PDFs will be shifted by +0.2%, while the energy values of the night MC events will be shifted by -0.2%. The signs of the day and night shifts are then reversed to model the opposite variation in the day and night values.

The directional systematics are propagated in a similar manner, except that different shifts are applied to the CC and ES Monte Carlo events. No shift is applied to the NC, EXTN, or internal gamma background PDFs because the directions of these events do not correlate with time of day. The CC and ES Monte Carlo events are shifted in opposite

directions, because of the anticorrelation in the directions of these two event classes. A variation in the directional response of the detector that tends to shift the effective energy scale up for CC events during the day and down at night will have the opposite effect on the ES signal, and vice versa.

Uncertainties in long-term stability of the energy scale and isotropy mean are propagated by applying time-dependent shifts to the Monte Carlo events used to make the PDFs. The time-dependent response functions correspond to the two "worst case" models for response drift, which systematically overestimate or underestimate the values of the response parameters depending on the season.

When the PDFs are perturbed, this has two ways of changing the signal extraction results. First, it may change the relative fraction of events that are assigned to each signal category, because of changes in the shapes of the PDFs. Second, it may change the number of Monte Carlo signal events that are accepted within the fiducial volume and above the energy threshold. This will alter the predicted number of events used to normalize the results. The final systematic uncertainties on the neutrino fluxes include both effects.

Systematic uncertainties on the day-night asymmetries $A_{\mathrm{CC}}$, $A_{\mathrm{NC}}$, and $A_{\mathrm{ES}}$ are determined by calculating the shifts in each day and night extracted fluxes due to variations in each parameter, and then calculating the day-night asymmetry with the perturbed results. The difference is taken as the systematic uncertainty on the day-night asymmetry measurement for each response parameter. Each systematic uncertainty results in two sets of shifted asymmetry results, one for perturbing the day value of the parameter up relative to the night value, and one for the reverse. In the case of worst-case drift models, we obtain one set of results for each of the two worst-case models. For the analysis published in [38] and presented in this chapter, the strategy for assigning final uncertainties on the asymmetries is to take the larger of the two shifts as a measure of the $\pm 1\sigma$ uncertainty due to a particular parameter. These shifts are then added together in quadrature to obtain the total systematic uncertainty.

### 9.6  Data Division

To provide some protection against statistical bias, the salt day-night analysis was developed using a smaller sample of the data set before being applied to the entire data set. Each run was divided into 30 equal-time segments, and 6 of these segments were then randomly chosen to analyze for the 20% data set. After the analysis was finalized using the smaller data set, it was repeated on the full data set. The results based on the 20% data set and the results based on the full data set were consistent. Only the final results will be presented here.

### 9.7  Results for the Energy-Unconstrained and NC-Unconstrained Analysis

The most model-independent of the four analyses involves fitting for the day and night fluxes of all signals independently, and allowing the CC and ES energy spectra to vary. The results of this fit, in numbers of events, are given in Table 9.2.[1] Correlations between the parameters in the fits are given in Table 9.4. The results are illustrated in Figures 9.2, 9.3, 9.4 and 9.5.

Table 9.2: Extracted numbers of events with statistical uncertainties, for the energy-unconstrained analysis.

| Signal | Number of Events Day | Number of Events Night |
|--------|----------------------|------------------------|
| NC     | $879.285 \pm 56.8307$ | $1128.32 \pm 63.8886$ |
| CC     | $1005.72 \pm 54.5089$ | $1173.92 \pm 59.385$  |
| ES     | $118.854 \pm 18.3215$ | $162.169 \pm 20.3837$ |
| EXTN   | $75.8521 \pm 24.5221$ | $50.9351 \pm 26.295$  |

Table 9.3 shows the day and night neutrino fluxes obtained from the results of Table 9.2, using the predicted numbers of events summarized in Table 9.1. From these fluxes, we

---

[1]The results in this table, as well as the rest of the tables throughout this chapter, have been corrected for signal extraction bias.
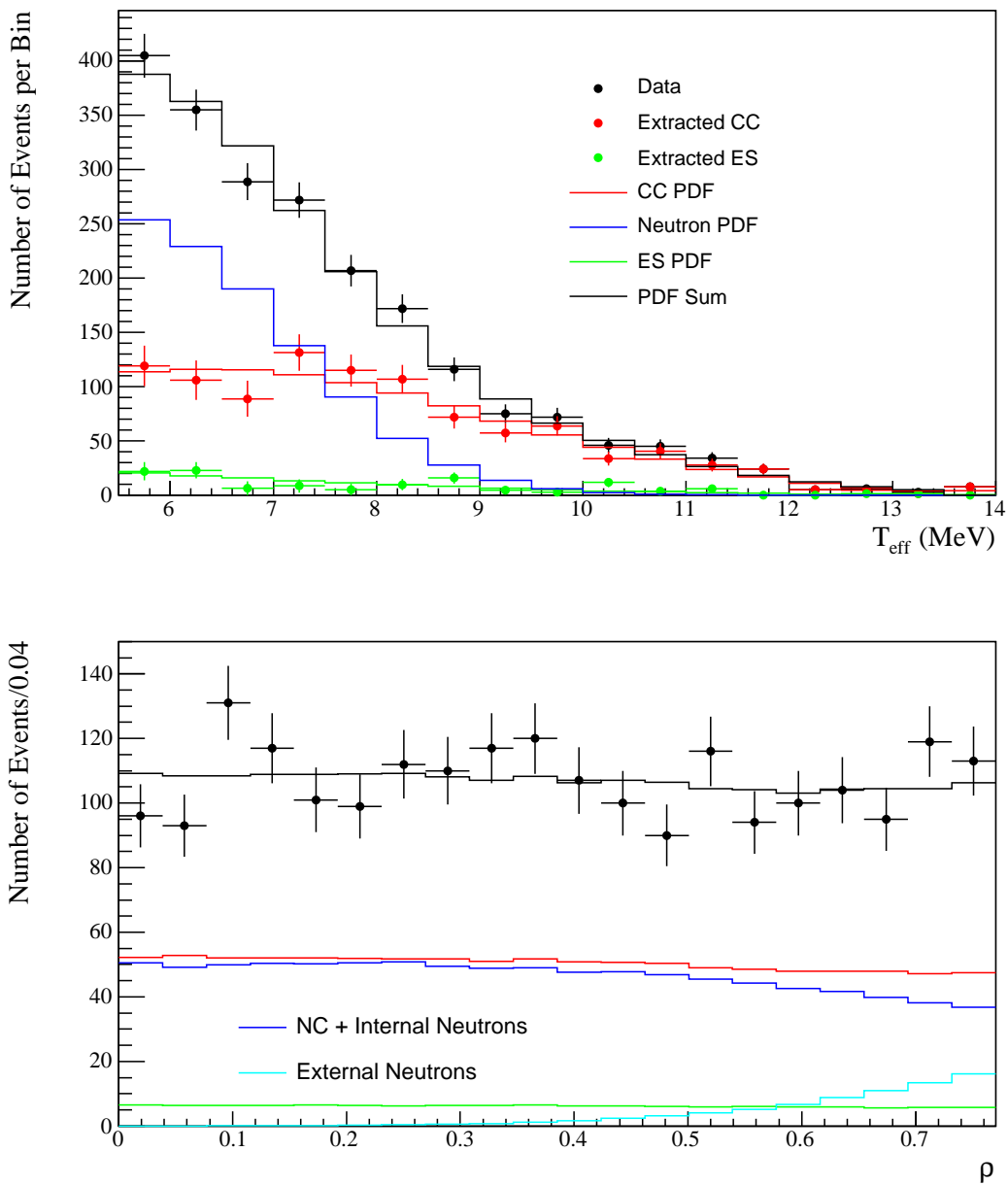
Figure 9.2: Results of the energy-unconstrained, neutral-current unconstrained fit, shown with respect to the $T_{eff}$ and $\rho$ variables, for the Day data. The black points show the data distributions, and the histograms show the PDFs, weighted by the fit results. In the top figure, the extracted CC and ES spectra are also shown.
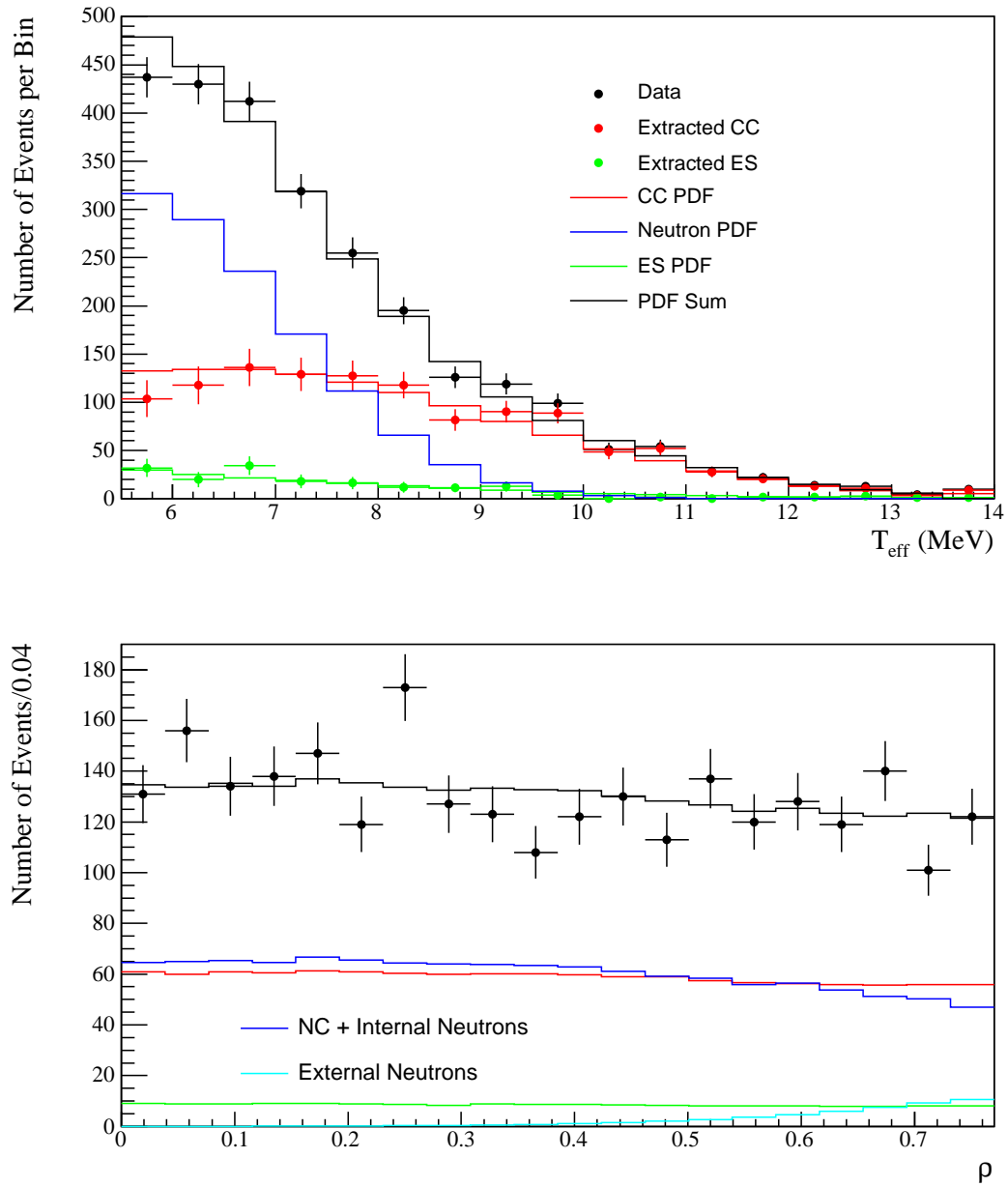
Figure 9.3: Results of the energy-unconstrained, neutral-current unconstrained fit, shown with respect to the $T_{eff}$ and $\rho$ variables, for the Night data. The black points show the data distributions, and the histograms show the PDFs, weighted by the fit results. In the top figure, the extracted CC and ES spectra are also shown.
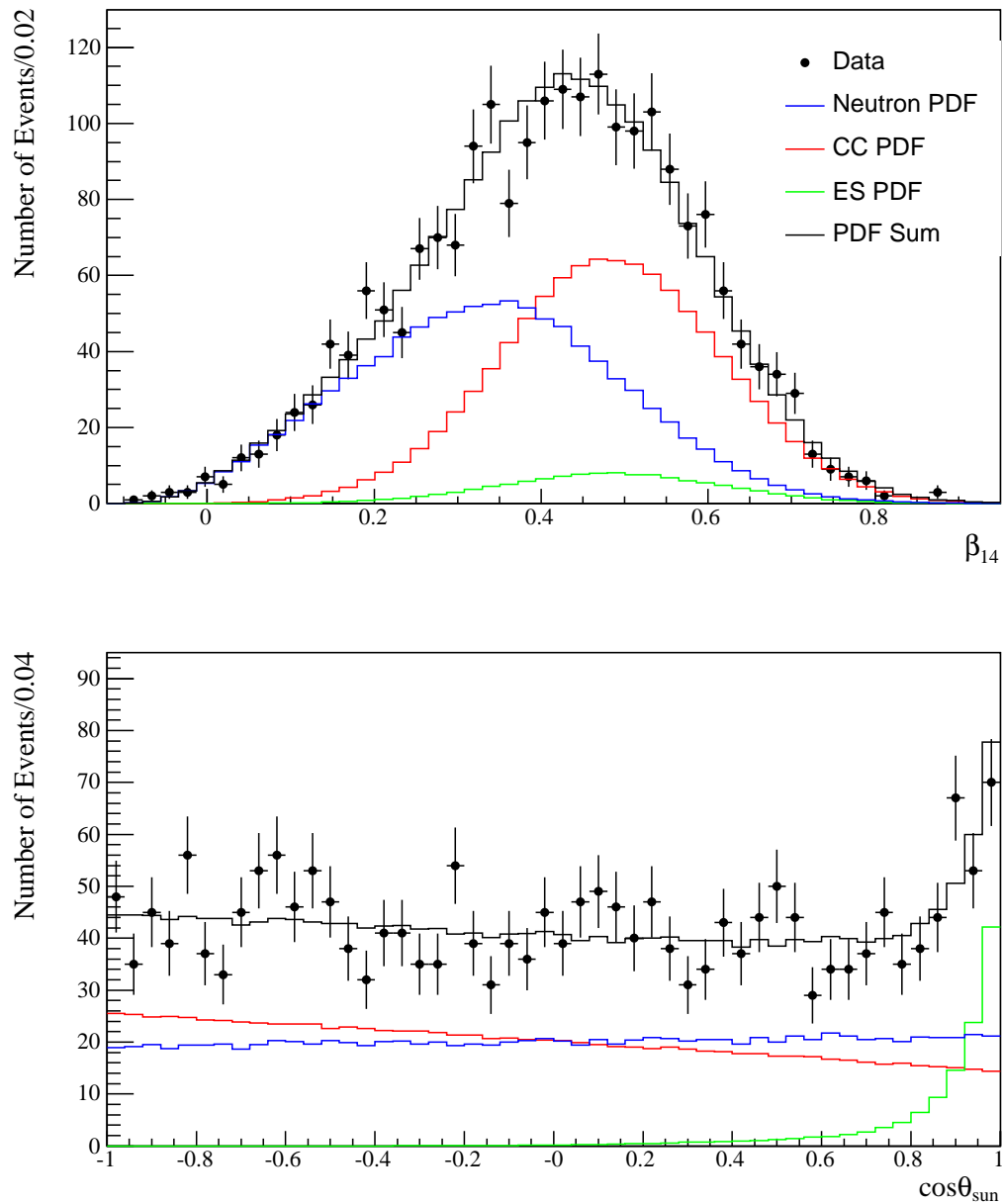
Figure 9.4: Results of the energy-unconstrained, neutral-current unconstrained fit, shown with respect to the $\beta_{14}$ and $\cos\theta_\odot$ variables, for the Day data. The black points show the data distributions, and the histograms show the PDFs, weighted by the fit results.
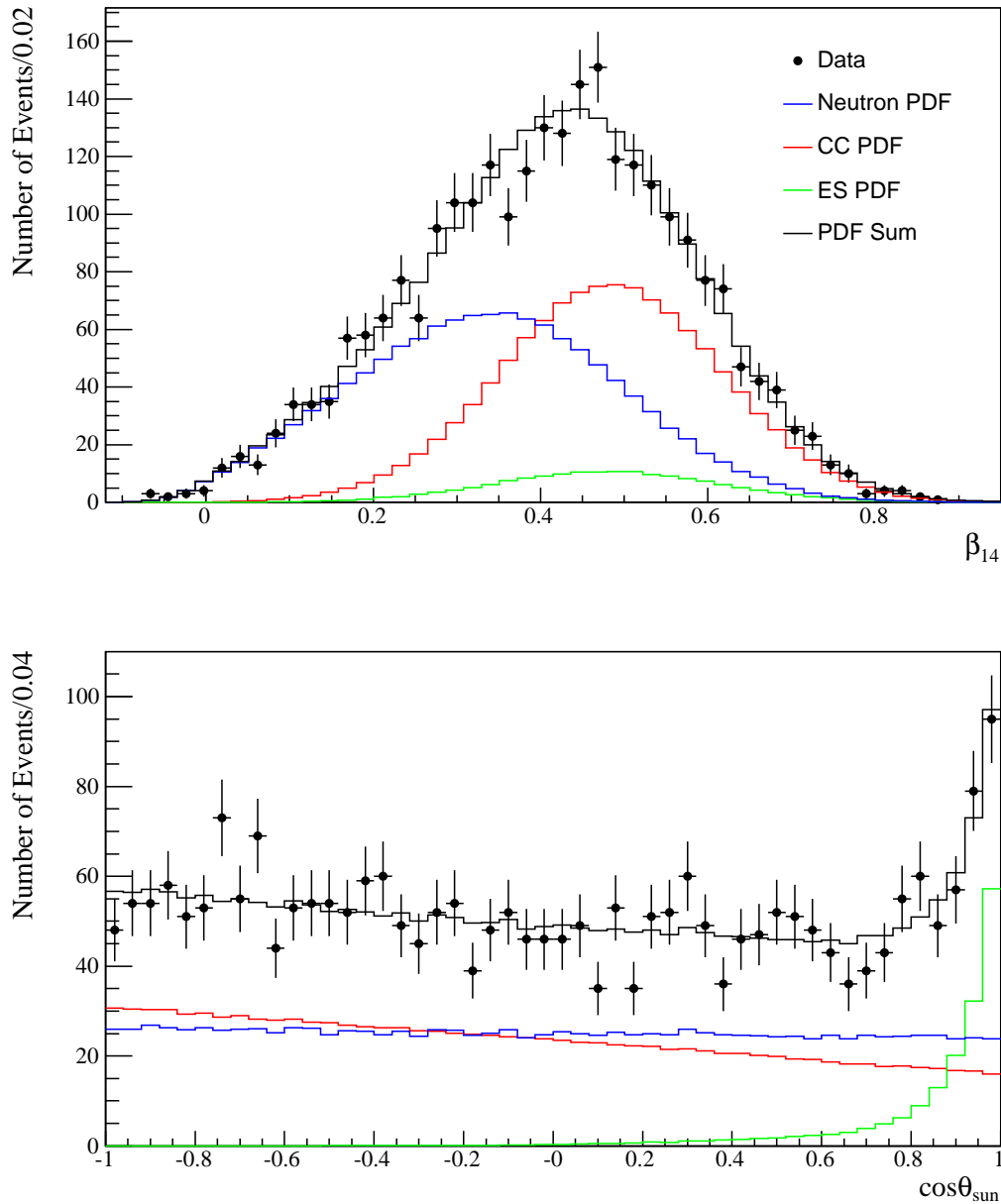
Figure 9.5: Results of the energy-unconstrained, neutral-current unconstrained fit, shown with respect to the $\beta_{14}$ and $\cos\theta_\odot$ variables, for the Night data. The black points show the data distributions, and the histograms show the PDFs, weighted by the fit results.

Table 9.3: Day-night fluxes from an energy-unconstrained, NC-unconstrained signal extraction, with statistical and systematic uncertainties. Fluxes are in units of $10^6$ neutrinos/cm$^2$/sec. The systematic uncertainties on the day and night fluxes include large correlated systematics that cancel in the day-night asymmetry ratio.

| Signal | Day Flux ($10^6$/cm$^2$/s) | Night Flux ($10^6$/cm$^2$/s) |
|--------|------------------------------|--------------------------------|
| NC | $4.81 \pm 0.31$ (stat.) $\pm 0.39$ (syst.) | $5.02 \pm 0.29$ (stat.) $\pm 0.41$ (syst.) |
| CC | $1.73 \pm 0.09$ (stat.) $\pm 0.10$ (syst.) | $1.64 \pm 0.08$ (stat.) $\pm 0.09$ (syst.) |
| ES | $2.17 \pm 0.34$ (stat.) $\pm 0.14$ (syst.) | $2.52 \pm 0.32$ (stat.) $\pm 0.16$ (syst.) |

derive day-night asymmetries for each signal (expressed as percents),

$$A_{\mathrm{CC}}(\%) \;=\; -5.6 \pm 7.4 \,(\text{stat.}) \pm 5.3 \,(\text{syst}) \tag{9.2}$$

$$A_{\mathrm{NC}}(\%) \;=\; 4.2 \pm 8.6 \,(\text{stat.}) \pm 7.2 \,(\text{syst}) \tag{9.3}$$

$$A_{\mathrm{ES}}(\%) \;=\; 14.6 \pm 19.8 \,(\text{stat.}) \pm 3.3 \,(\text{syst}), \tag{9.4}$$

where both statistical and systematic uncertainties have been given. The statistical uncertainties on the asymmetry parameters have been calculated using the expressions in Appendix A. The systematic uncertainties due to each individual variation in detector response or background level are given in Table 9.5. The CC and NC asymmetries are most sensitive to the diurnal $\beta_{14}$ uncertainty, while the ES asymmetry is most sensitive to the directional angular resolution uncertainty. In Table 9.3, systematic uncertainties are also quoted for night and day fluxes. These have been calculated by scaling the uncertainties from the integral flux analysis in [38], with an additional component added by splitting the uncertainty on the associated day-night asymmetry parameter between day and night. The asymmetries are small, so this additional uncertainty is a minor contribution that takes into account uncertainties in the day and night fluxes due to diurnal variations in response.

Within the MSW model, the negative value of $A_{\mathrm{CC}}$ that is measured is unphysical. However, it is statistically consistent with no asymmetry or the presence of very small asymmetries, as are $A_{\mathrm{NC}}$ and $A_{\mathrm{ES}}$. The asymmetries are also statistics-limited, although the systematic uncertainties are almost comparable due to the sensitivity of the fits to diurnal

Table 9.4: Matrices of correlation coefficients for the day and night signal extraction results in the energy-unconstrained, NC-unconstrained analysis.

| DAY | NC | CC | ES | EXTN |
|------|------|------|------|------|
| NC | 1.0000 | -0.5312 | -0.0610 | -0.3815 |
| CC | -0.5312 | 1.0000 | -0.1528 | -0.0704 |
| ES | -0.0610 | -0.1528 | 1.0000 | -0.0147 |
| EXTN | -0.3815 | -0.0704 | -0.0147 | 1.0000 |
| | | | | |
| NIGHT | NC | CC | ES | EXTN |
| NC | 1.0000 | -0.5344 | -0.0693 | -0.4069 |
| CC | -0.5344 | 1.0000 | -0.1390 | -0.0488 |
| ES | -0.0693 | -0.1390 | 1.0000 | -0.0050 |
| EXTN | -0.4069 | -0.0488 | -0.0050 | 1.0000 |

$\beta_{14}$ variation. The statistical correlations between the day-night asymmetry measurements are

$$\rho(A_{\mathrm{CC}}, A_{\mathrm{NC}}) = -0.532$$
$$\rho(A_{\mathrm{CC}}, A_{\mathrm{ES}}) = -0.147$$
$$\rho(A_{\mathrm{ES}}, A_{\mathrm{NC}}) = -0.064. \tag{9.5}$$

## 9.8   Results for the Energy-Constrained and NC-Unconstrained Analysis

Table 9.6 gives the extracted numbers of events day and night when the additional constraint of an undistorted $^8$B neutrino spectrum is used in the signal extraction. The correlations between the parameters in this fit are given in Table 9.7.    The day and night fluxes derived from these measurements are given in Table 9.8. From these results, we calculate the day-night asymmetries in the energy-constrained case to be,

$$A_{\mathrm{CC}}(\%) = -2.1 \pm 6.3 \,(\text{stat.}) \pm 3.5 \,(\text{syst}) \tag{9.6}$$

Table 9.5: Shifts in asymmetry parameters due to different systematics, for the NC-unconstrained, energy-unconstrained analysis. Uncertainties have been rounded and symmetrized by taking the larger of the two shifts for each parameter. See Appendix B for more details.

| Systematic | $\Delta A_{\mathrm{NC}}$ | $\Delta A_{\mathrm{CC}}$ | $\Delta A_{\mathrm{ES}}$ |
|---|---|---|---|
| Internal photodisintegration background total | $\pm$ 0.003 | $\pm$ 0.000 | $\pm$ 0.000 |
| Internal photodisintegration background asym. | $\pm$ 0.015 | $\pm$ 0.000 | $\pm$ 0.000 |
| Other neutron background total | $\pm$ 0.001 | $\pm$ 0.000 | $\pm$ 0.000 |
| Internal gamma background total | $\pm$ 0.000 | $\pm$ 0.000 | $\pm$ 0.000 |
| Diurnal energy scale | $\pm$ 0.015 | $\pm$ 0.004 | $\pm$ 0.007 |
| Directional energy scale | $\pm$ 0.000 | $\pm$ 0.001 | $\pm$ 0.014 |
| Worst case energy drift | $\pm$ 0.010 | $\pm$ 0.002 | $\pm$ 0.001 |
| Diurnal energy resolution | $\pm$ 0.006 | $\pm$ 0.003 | $\pm$ 0.004 |
| Directional energy resolution | $\pm$ 0.001 | $\pm$ 0.001 | $\pm$ 0.003 |
| Diurnal $\beta_{14}$ shift | $\pm$ 0.064 | $\pm$ 0.050 | $\pm$ 0.017 |
| Worst case $\beta_{14}$ drift | $\pm$ 0.015 | $\pm$ 0.014 | $\pm$ 0.006 |
| Directional $\beta_{14}$ shift | $\pm$ 0.002 | $\pm$ 0.002 | $\pm$ 0.004 |
| Directional radial scaling | $\pm$ 0.000 | $\pm$ 0.000 | $\pm$ 0.003 |
| Diurnal radial scaling | $\pm$ 0.012 | $\pm$ 0.008 | $\pm$ 0.007 |
| Directional vertex resolution | $\pm$ 0.000 | $\pm$ 0.000 | $\pm$ 0.001 |
| Diurnal vertex resolution | $\pm$ 0.006 | $\pm$ 0.002 | $\pm$ 0.002 |
| Directional angular resolution | $\pm$ 0.001 | $\pm$ 0.001 | $\pm$ 0.020 |
| Internal $\beta\gamma$ background total | $\pm$ 0.000 | $\pm$ 0.001 | $\pm$ 0.000 |
| Internal $\beta\gamma$ background asym. | $\pm$ 0.001 | $\pm$ 0.001 | $\pm$ 0.000 |
| External $\beta\gamma$ background total | $\pm$ 0.003 | $\pm$ 0.002 | $\pm$ 0.000 |
| External $\beta\gamma$ background asym. | $\pm$ 0.004 | $\pm$ 0.003 | $\pm$ 0.000 |
| AV background total | $\pm$ 0.001 | $\pm$ 0.001 | $\pm$ 0.000 |
| AV background asym. | $\pm$ 0.002 | $\pm$ 0.002 | $\pm$ 0.000 |
| Instrumental background total | $\pm$ 0.001 | $\pm$ 0.000 | $\pm$ 0.000 |
| Instrumental background asym. | $\pm$ 0.002 | $\pm$ 0.001 | $\pm$ 0.000 |
| Cut acceptance | $\pm$ 0.004 | $\pm$ 0.003 | $\pm$ 0.003 |
| Total | $\pm$ 0.072 | $\pm$ 0.053 | $\pm$ 0.032 |

Table 9.6: Extracted numbers of events with statistical uncertainties, for the energy-constrained analysis. The results have been corrected for signal extraction bias.

| Signal | Number of Events Day | Number of Events Night |
|--------|----------------------|------------------------|
| NC | 867.955 ± 51.1508 | 1086.81 ± 57.1508 |
| CC | 1013.17 ± 47.379 | 1225.38 ± 51.4433 |
| ES | 123.845 ± 18.4016 | 155.943 ± 20.4264 |
| EXTN | 78.7018 ± 25.7787 | 50.9472 ± 27.6205 |

$$A_{\text{NC}}(\%) = 1.8 \pm 7.9 \,(\text{stat.}) \pm 5.2 \,(\text{syst}) \tag{9.7}$$

$$A_{\text{ES}}(\%) = 6.6 \pm 19.8 \,(\text{stat.}) \pm 5.7 \,(\text{syst}). \tag{9.8}$$

The spectrum constraint improves the statistical precision, and also reduces the systematic uncertainties. The asymmetries are consistent with what is calculated for the energy-unconstrained case. Systematic uncertainties for these results are given in detail in Table 9.9. Compared with the unconstrained analysis, the CC and NC asymmetries are less sensitive to the $\beta_{14}$ uncertainties, while the ES asymmetry is more so. Energy scale uncertainties is also more important for the CC asymmetry measurement in this analysis, similar to what is seen for the energy-constrained integral flux measurements. The statistical correlations between the parameters are reduced, with

$$\rho(A_{\text{CC}}, A_{\text{NC}}) = -0.402$$

$$\rho(A_{\text{CC}}, A_{\text{ES}}) = -0.171$$

$$\rho(A_{\text{ES}}, A_{\text{NC}}) = -0.070. \tag{9.9}$$

## 9.9 Results for the Energy-Unconstrained and NC-Constrained Analysis

When we impose the requirement that the neutral current asymmetry $A_{\text{NC}}$ must be zero, we couple the day and night results. To correctly account for day-night differences in the signal response, day and night PDFs are separately included for the NC signal, but only

Table 9.7: Matrices of correlation coefficients for the day and night signal extraction results in the energy-constrained, NC-unconstrained analysis.

| DAY | NC | CC | ES | EXTN |
|------|--------|--------|--------|--------|
| NC | 1.0000 | -0.4050 | -0.0586 | -0.4542 |
| CC | -0.4050 | 1.0000 | -0.1809 | -0.0468 |
| ES | -0.0586 | -0.1809 | 1.0000 | -0.0163 |
| EXTN | -0.4542 | -0.0468 | -0.0163 | 1.0000 |
| | | | | |
| NIGHT | NC | CC | ES | EXTN |
| NC | 1.0000 | -0.3990 | -0.0852 | -0.4772 |
| CC | -0.3990 | 1.0000 | -0.1574 | -0.0311 |
| ES | -0.0852 | -0.1574 | 1.0000 | -0.0070 |
| EXTN | -0.4772 | -0.0311 | -0.0070 | 1.0000 |

a single amplitude for the NC flux is allowed to float in the fit. The energy-unconstrained NC-constrained fit involves more than 70 parameters, including 17 bins each for the day and night CC and ES fluxes, but just one amplitude for the average NC flux. Because the CC and ES day and night extracted fluxes are correlated with the NC flux, the fit induces small correlations between the day and night extracted CC and ES fluxes that were not present in the previous two analyses.

Th neutrino fluxes extracted in this case are given in Table 9.10. The matrix of correlation coefficients for the day and night results is given in Table 9.12. In this analysis, $A_{\mathrm{NC}}$ is zero by construction, and we extract only the CC and ES asymmetries,

$$A_{\mathrm{CC}}(\%) \quad = \quad -3.7 \pm 6.3 \,(\mathrm{stat.}) \pm 3.2 \,(\mathrm{syst}) \tag{9.10}$$

$$A_{\mathrm{ES}}(\%) \quad = \quad 15.3 \pm 19.8 \,(\mathrm{stat.}) \pm 3.0 \,(\mathrm{syst}). \tag{9.11}$$

Due to the anticorrelation of the CC and NC asymmetries, constraining the NC asymmetry to be zero reduces the size of the CC asymmetry. The statistical uncertainty on

Table 9.8: Day-night integral fluxes from an energy-constrained, NC-unconstrained signal extraction, with statistical and systematic uncertainties. Fluxes are in units of $10^6$ neutrinos/cm$^2$/sec. The systematic uncertainties on the day and night fluxes include large correlated systematics that cancel in the day-night asymmetry ratio.

| Signal | Day Flux ($10^6$/cm$^2$/s) | Night Flux ($10^6$/cm$^2$/s) |
|--------|----------------------------|------------------------------|
| NC | $4.75 \pm 0.28$ (stat.) $\pm 0.29$ (syst.) | $4.84 \pm 0.25$ (stat.) $\pm 0.30$ (syst.) |
| CC | $1.74 \pm 0.08$ (stat.) $\pm 0.11$ (syst.) | $1.71 \pm 0.07$ (stat.) $\pm 0.11$ (syst.) |
| ES | $2.27 \pm 0.34$ (stat.) $\pm 0.16$ (syst.) | $2.43 \pm 0.32$ (stat.) $\pm 0.17$ (syst.) |

the CC asymmetry is the same as in the energy-constrained, NC-unconstrained analysis, and the systematic uncertainty is comparable. The systematic uncertainties on the CC and ES asymmetries are given in Table 9.11. Compared to the energy-unconstrained, NC-unconstrained analysis, the systematic uncertainties on the CC and ES asymmetries are substantially reduced with the extra constraint. The correlation between the extracted CC and ES asymmetries in this analysis is

$$\rho(A_{\mathrm{CC}}, A_{\mathrm{ES}}) = -0.214. \tag{9.12}$$

Table 9.9: Shifts in asymmetry parameters due to different systematics, for the NC-unconstrained, energy-constrained analysis. Uncertainties have been rounded and symmetrized by taking the larger of the two shifts for each parameter. See Appendix B for more details.

| Systematic | $\Delta A_{\mathrm{NC}}$ | $\Delta A_{\mathrm{CC}}$ | $\Delta A_{\mathrm{ES}}$ |
|---|---|---|---|
| Internal photodisintegration background total | $\pm 0.003$ | $\pm 0.000$ | $\pm 0.000$ |
| Internal photodisintegration background asym. | $\pm 0.015$ | $\pm 0.000$ | $\pm 0.000$ |
| Other neutron background total | $\pm 0.000$ | $\pm 0.000$ | $\pm 0.000$ |
| Internal gamma background total | $\pm 0.000$ | $\pm 0.000$ | $\pm 0.000$ |
| Diurnal energy scale | $\pm 0.003$ | $\pm 0.014$ | $\pm 0.003$ |
| Directional energy scale | $\pm 0.001$ | $\pm 0.001$ | $\pm 0.012$ |
| Worst case energy drift | $\pm 0.005$ | $\pm 0.006$ | $\pm 0.006$ |
| Diurnal energy resolution | $\pm 0.004$ | $\pm 0.003$ | $\pm 0.004$ |
| Directional energy resolution | $\pm 0.001$ | $\pm 0.001$ | $\pm 0.009$ |
| Diurnal $\beta_{14}$ shift | $\pm 0.044$ | $\pm 0.029$ | $\pm 0.035$ |
| Worst case $\beta_{14}$ drift | $\pm 0.015$ | $\pm 0.007$ | $\pm 0.026$ |
| Directional $\beta_{14}$ shift | $\pm 0.001$ | $\pm 0.003$ | $\pm 0.023$ |
| Directional radial scaling | $\pm 0.000$ | $\pm 0.000$ | $\pm 0.004$ |
| Diurnal radial scaling | $\pm 0.012$ | $\pm 0.008$ | $\pm 0.008$ |
| Directional vertex resolution | $\pm 0.000$ | $\pm 0.000$ | $\pm 0.001$ |
| Diurnal vertex resolution | $\pm 0.005$ | $\pm 0.001$ | $\pm 0.003$ |
| Directional angular resolution | $\pm 0.001$ | $\pm 0.002$ | $\pm 0.021$ |
| Internal $\beta\gamma$ background total | $\pm 0.000$ | $\pm 0.000$ | $\pm 0.000$ |
| Internal $\beta\gamma$ background asym. | $\pm 0.001$ | $\pm 0.001$ | $\pm 0.000$ |
| External $\beta\gamma$ background total | $\pm 0.003$ | $\pm 0.002$ | $\pm 0.000$ |
| External $\beta\gamma$ background asym. | $\pm 0.004$ | $\pm 0.004$ | $\pm 0.000$ |
| AV background total | $\pm 0.001$ | $\pm 0.001$ | $\pm 0.000$ |
| AV background asym. | $\pm 0.002$ | $\pm 0.002$ | $\pm 0.000$ |
| Instrumental background total | $\pm 0.001$ | $\pm 0.001$ | $\pm 0.000$ |
| Instrumental background asym. | $\pm 0.002$ | $\pm 0.001$ | $\pm 0.000$ |
| Cut acceptance | $\pm 0.004$ | $\pm 0.003$ | $\pm 0.003$ |
| Total | $\pm 0.052$ | $\pm 0.035$ | $\pm 0.057$ |

Table 9.10: Day-night integral fluxes from an energy-unconstrained signal extraction, with the constraint $A_{\mathrm{NC}} \equiv 0$.

| Signal | Day Flux ($10^6/\mathrm{cm}^2/\mathrm{s}$) | Night Flux ($10^6/\mathrm{cm}^2/\mathrm{s}$) |
|--------|--------------------------------------------|-----------------------------------------------|
| CC | $1.71 \pm 0.08$ (stat.) $\pm 0.09$ (syst.) | $1.65 \pm 0.08$ (stat.) $\pm 0.09$ (syst.) |
| ES | $2.18 \pm 0.34$ (stat.) $\pm 0.14$ (syst.) | $2.53 \pm 0.32$ (stat.) $\pm 0.16$ (syst.) |
| NC | $4.93 \pm 0.21$ (stat.) $\pm 0.36$ (syst.) | |

Table 9.11: Shifts in asymmetry parameters due to different systematics, for the NC-constrained, energy-unconstrained analysis. Uncertainties have been rounded and symmetrized by taking the larger of the two shifts for each parameter.See Appendix B for more details.

| Systematic | $\Delta A_{\mathrm{CC}}$ | $\Delta A_{\mathrm{ES}}$ |
|---|---|---|
| Internal photodisintegration background total | ± 0.002 | ± 0.001 |
| Internal photodisintegration background asym. | ± 0.007 | ± 0.002 |
| Other neutron background total | ± 0.000 | ± 0.000 |
| Internal gamma background total | ± 0.000 | ± 0.000 |
| Diurnal energy scale | ± 0.009 | ± 0.009 |
| Directional energy scale | ± 0.001 | ± 0.014 |
| Worst case energy drift | ± 0.006 | ± 0.002 |
| Diurnal energy resolution | ± 0.002 | ± 0.004 |
| Directional energy resolution | ± 0.001 | ± 0.002 |
| Diurnal $\beta_{14}$ shift | ± 0.022 | ± 0.009 |
| Worst case $\beta_{14}$ drift | ± 0.013 | ± 0.003 |
| Directional $\beta_{14}$ shift | ± 0.001 | ± 0.005 |
| Directional radial scaling | ± 0.000 | ± 0.003 |
| Diurnal radial scaling | ± 0.013 | ± 0.009 |
| Directional vertex resolution | ± 0.000 | ± 0.001 |
| Diurnal vertex resolution | ± 0.001 | ± 0.002 |
| Directional angular resolution | ± 0.002 | ± 0.019 |
| Internal $\beta\gamma$ background total | ± 0.001 | ± 0.000 |
| Internal $\beta\gamma$ background asym. | ± 0.001 | ± 0.000 |
| External $\beta\gamma$ background total | ± 0.002 | ± 0.000 |
| External $\beta\gamma$ background asym. | ± 0.003 | ± 0.000 |
| AV background total | ± 0.001 | ± 0.000 |
| AV background asym. | ± 0.002 | ± 0.000 |
| Instrumental background total | ± 0.001 | ± 0.000 |
| Instrumental background asym. | ± 0.001 | ± 0.000 |
| Cut acceptance | ± 0.003 | ± 0.003 |
| Total | ± 0.032 | ± 0.030 |

Table 9.12: Matrix of correlation coefficients for the day and night signal extraction results in the energy-unconstrained, NC-constrained analysis. The day and night parameters are indicated by "D" and "N". When the NC flux is constrained to be the same day and night, this introduces small correlations between the day and night extracted values of the other parameters.

|        | NC      | CC D    | CC N    | ES D    | ES N    | EXTN D  | EXTN N  |
|--------|---------|---------|---------|---------|---------|---------|---------|
| NC     | 1.0000  | -0.3868 | -0.4252 | -0.0413 | -0.0514 | -0.2667 | -0.3138 |
| CC D   | -0.3868 | 1.0000  | 0.1645  | -0.1855 | 0.0199  | -0.2075 | 0.12137 |
| CC N   | -0.4252 | 0.1645  | 1.0000  | 0.0176  | -0.1672 | 0.1134  | -0.1626 |
| ES D   | 0.0413  | -0.1855 | 0.0176  | 1.0000  | 0.0021  | -0.0286 | 0.0130  |
| ES N   | -0.0514 | 0.0199  | -0.1672 | 0.0021  | 1.0000  | 0.0137  | -0.0185 |
| EXTN D | -0.2667 | -0.2075 | 0.1134  | -0.0286 | 0.0137  | 1.0000  | 0.0837  |
| EXTN N | -0.3138 | 0.12137 | -0.1626 | 0.0130  | -0.0185 | 0.0837  | 1.0000  |

## 9.10 Results for the Energy-Constrained, NC-Constrained Analysis

Finally, we can apply both the spectrum shape constraint and the NC constraint. Results are given in Table 9.13, with correlations given in Table 9.14. From these, we derive the

Table 9.13: Day-night integral fluxes from an energy-unconstrained signal extraction, with the constraint $A_{\mathrm{NC}} \equiv 0$.

| Signal | Day Flux ($10^6/\mathrm{cm}^2/\mathrm{s}$) | Night Flux ($10^6/\mathrm{cm}^2/\mathrm{s}$) |
|--------|---------------------------------------------|-----------------------------------------------|
| CC     | $1.74 \pm 0.08$ (stat.) $\pm 0.11$ (syst.)  | $1.71 \pm 0.07$ (stat.) $\pm 0.11$ (syst.)    |
| ES     | $2.27 \pm 0.34$ (stat.) $\pm 0.16$ (syst.)  | $2.43 \pm 0.32$ (stat.) $\pm 0.17$ (syst.)    |
| NC     | $4.80 \pm 0.19$ (stat.) $\pm 0.27$ (syst.)  ||

final set of asymmetry results,

$$A_{\mathrm{CC}}(\%) = -1.5 \pm 5.8 \,(\mathrm{stat.}) \pm 2.7 \,(\mathrm{syst}) \qquad (9.13)$$

Table 9.14: Matrix of correlation coefficients for the day and night signal extraction results in the energy-constrained, NC-constrained analysis. The day and night parameters are indicated by "D" and "N". When the NC flux is constrained to be the same day and night, this introduces small correlations between the day and night extracted values of the other parameters.

|        | NC      | CC D    | CC N    | ES D    | ES N    | EXTN D  | EXTN N  |
|--------|---------|---------|---------|---------|---------|---------|---------|
| NC     | 1.0000  | -0.2838 | -0.3076 | -0.0394 | -0.0633 | -0.3242 | -0.3737 |
| CC D   | -0.2838 | 1.0000  | 0.0873  | -0.2036 | 0.0180  | -0.1649 | 0.1061  |
| CC N   | -0.3076 | 0.0873  | 1.0000  | 0.0121  | -0.1796 | 0.0997  | -0.1277 |
| ES D   | -0.0394 | -0.2036 | 0.0121  | 1.0000  | 0.0025  | -0.0328 | 0.0147  |
| ES N   | -0.0633 | 0.0180  | -0.1796 | 0.0025  | 1.0000  | 0.0205  | -0.0267 |
| EXTN D | -0.3242 | -0.1649 | 0.0997  | -0.0328 | 0.0205  | 1.0000  | 0.1211  |
| EXTN N | -0.3737 | 0.1061  | 0.1061  | -0.1277 | 0.0147  | -0.0267 | 1.0000  |

$$A_{\mathrm{ES}}(\%) \quad = \quad 7.0 \pm 19.7 \,(\mathrm{stat.}) \pm 5.4 \,(\mathrm{syst}). \tag{9.14}$$

This analysis leads to the smallest statistical and systematic uncertainties of the four variations, as well as the smallest asymmetry values. Systematic uncertainties are given in Table 9.15. The CC asymmetry is less sensitive to $\beta_{14}$ variations and more sensitive to energy scale variations relative to the energy-unconstrained version, while the ES asymmetry is more sensitive to the $\beta_{14}$ systematics. The correlation between the CC and ES asymmetries in this analysis is comparable to that in the energy-unconstrained version,

$$\rho(A_{\mathrm{CC}}, A_{\mathrm{ES}}) \quad = \quad -0.217 \tag{9.15}$$

## 9.11  Asymmetries as a Function of Energy

The two energy-unconstrained variants of the day-night analysis produce extracted spectra for the CC and ES reactions. The CC day and night spectra can be compared to test for energy-dependent electron neutrino regeneration effects. Figures 9.6 and 9.7 show the day and night extracted CC spectra for the NC-unconstrained and NC-constrained versions of

Table 9.15: Shifts in asymmetry parameters due to different systematics, for the NC-constrained, energy-constrained analysis. Uncertainties have been rounded and symmetrized by taking the larger of the two shifts for each parameter.See Appendix B for more details.

| Systematic | $\Delta A_{\text{CC}}$ | $\Delta A_{\text{ES}}$ |
|---|---|---|
| Internal photodisintegration background total | $\pm 0.001$ | $\pm 0.001$ |
| Internal photodisintegration background asym. | $\pm 0.005$ | $\pm 0.003$ |
| Other neutron background total | $\pm 0.000$ | $\pm 0.000$ |
| Internal gamma background total | $\pm 0.000$ | $\pm 0.000$ |
| Diurnal energy scale | $\pm 0.014$ | $\pm 0.005$ |
| Directional energy scale | $\pm 0.001$ | $\pm 0.012$ |
| Worst case energy drift | $\pm 0.008$ | $\pm 0.005$ |
| Diurnal energy resolution | $\pm 0.003$ | $\pm 0.004$ |
| Directional energy resolution | $\pm 0.001$ | $\pm 0.010$ |
| Diurnal $\beta_{14}$ shift | $\pm 0.015$ | $\pm 0.029$ |
| Worst case $\beta_{14}$ drift | $\pm 0.006$ | $\pm 0.026$ |
| Directional $\beta_{14}$ shift | $\pm 0.003$ | $\pm 0.022$ |
| Directional radial scaling | $\pm 0.001$ | $\pm 0.003$ |
| Diurnal radial scaling | $\pm 0.011$ | $\pm 0.011$ |
| Directional vertex resolution | $\pm 0.000$ | $\pm 0.002$ |
| Diurnal vertex resolution | $\pm 0.001$ | $\pm 0.005$ |
| Directional angular resolution | $\pm 0.002$ | $\pm 0.020$ |
| Internal $\beta\gamma$ background total | $\pm 0.000$ | $\pm 0.000$ |
| Internal $\beta\gamma$ background asym. | $\pm 0.001$ | $\pm 0.000$ |
| External $\beta\gamma$ background total | $\pm 0.002$ | $\pm 0.000$ |
| External $\beta\gamma$ background asym. | $\pm 0.004$ | $\pm 0.000$ |
| AV background total | $\pm 0.001$ | $\pm 0.000$ |
| AV background asym. | $\pm 0.002$ | $\pm 0.000$ |
| Instrumental background total | $\pm 0.001$ | $\pm 0.000$ |
| Instrumental background asym. | $\pm 0.001$ | $\pm 0.000$ |
| Cut acceptance | $\pm 0.003$ | $\pm 0.003$ |
| Total | $\pm 0.027$ | $\pm 0.054$ |

the energy-unconstrained analysis, respectively. In both figures, the spectrum bins have been normalized such that the sum of all bins reproduces the CC flux results from Sections 9.7 and 9.9. The bin-by-bin spectrum results are given in Tables 9.16 and 9.17. The day and night spectra are consistent with one another in both cases.

Table 9.16: Extracted CC spectra for day and night, from the energy-unconstrained, NC-unconstrained analysis, in units of $10^6$ neutrinos/cm$^2$/sec. The units are chosen such that the sum of all bins gives the total day or night CC flux. The first bin starts at 5.5 MeV. Bins are 0.5 MeV wide, except for the final bin, which extends from 13.5 MeV to 20 MeV.

| Bin | Day CC Flux | Night CC Flux |
|-----|-------------|---------------|
| 1 | $0.205 \pm 0.032$ | $0.145 \pm 0.0268$ |
| 2 | $0.182 \pm 0.030$ | $0.164 \pm 0.0267$ |
| 3 | $0.153 \pm 0.028$ | $0.190 \pm 0.026$ |
| 4 | $0.226 \pm 0.028$ | $0.180 \pm 0.024$ |
| 5 | $0.198 \pm 0.025$ | $0.178 \pm 0.022$ |
| 6 | $0.184 \pm 0.023$ | $0.164 \pm 0.019$ |
| 7 | $0.124 \pm 0.018$ | $0.114 \pm 0.015$ |
| 8 | $0.099 \pm 0.015$ | $0.126 \pm 0.015$ |
| 9 | $0.110 \pm 0.015$ | $0.124 \pm 0.014$ |
| 10 | $0.058 \pm 0.011$ | $0.067 \pm 0.010$ |
| 11 | $0.070 \pm 0.012$ | $0.073 \pm 0.011$ |
| 12 | $0.048 \pm 0.010$ | $0.039 \pm 0.007$ |
| 13 | $0.042 \pm 0.008$ | $0.029 \pm 0.007$ |
| 14 | $0.0088 \pm 0.0038$ | $0.018 \pm 0.005$ |
| 15 | $0.0082 \pm 0.0040$ | $0.015 \pm 0.005$ |
| 16 | $0.0025 \pm 0.0028$ | $0.0042 \pm 0.0025$ |
| 17 | $0.014 \pm 0.005$ | $0.012 \pm 0.004$ |

Using the day and night CC spectra, we can construct day-night asymmetries as a function of energy for the two energy-unconstrained analyses. The results are shown in
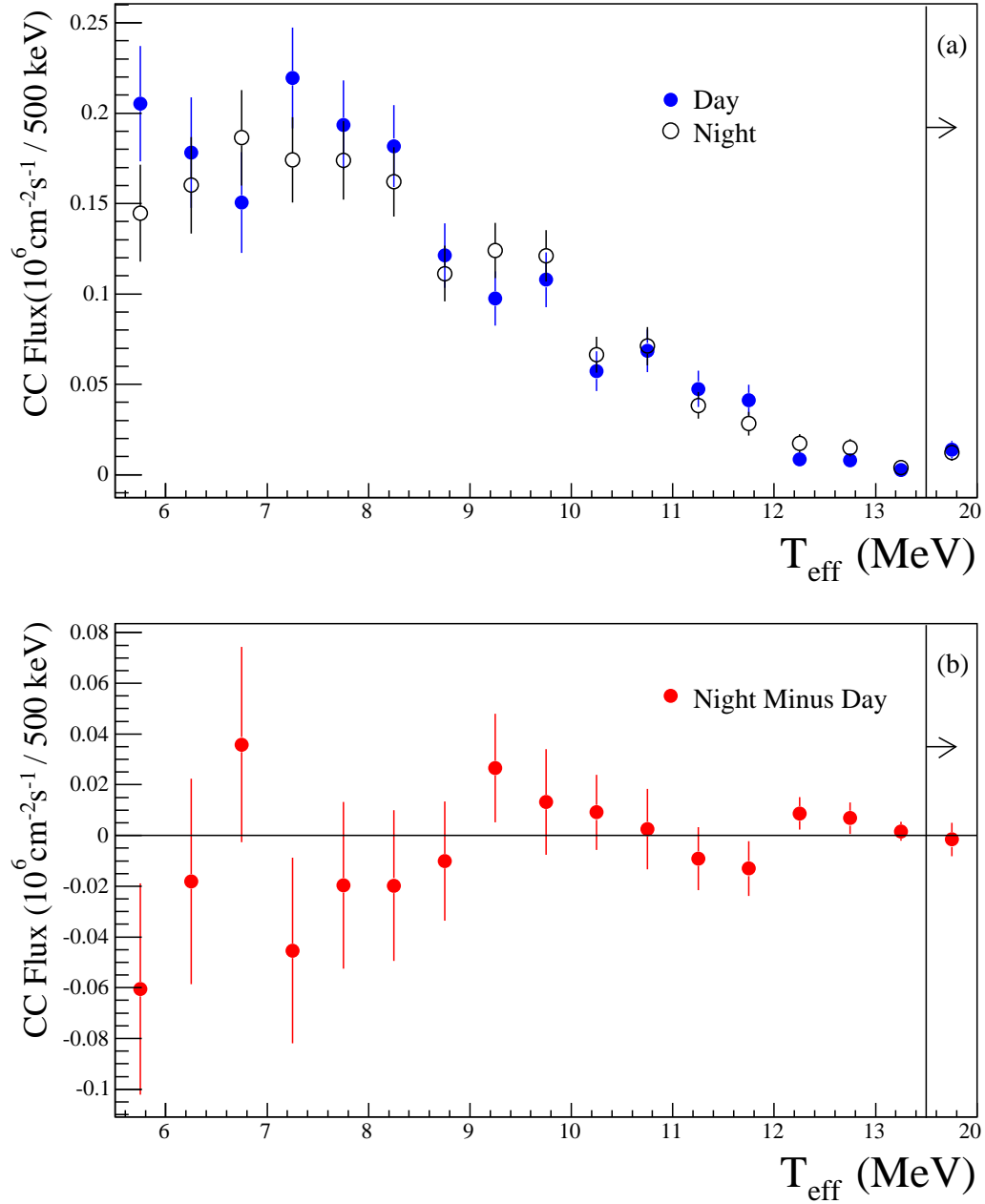
Figure 9.6: Day and night CC extracted spectra and the differences between the results in each bin, for the energy-unconstrained, neutral-current unconstrained analysis. Uncertainties are statistical only. The bins in the figures are 0.5 MeV wide, except for the final bin, which extends from 13.5 MeV to 20 MeV.
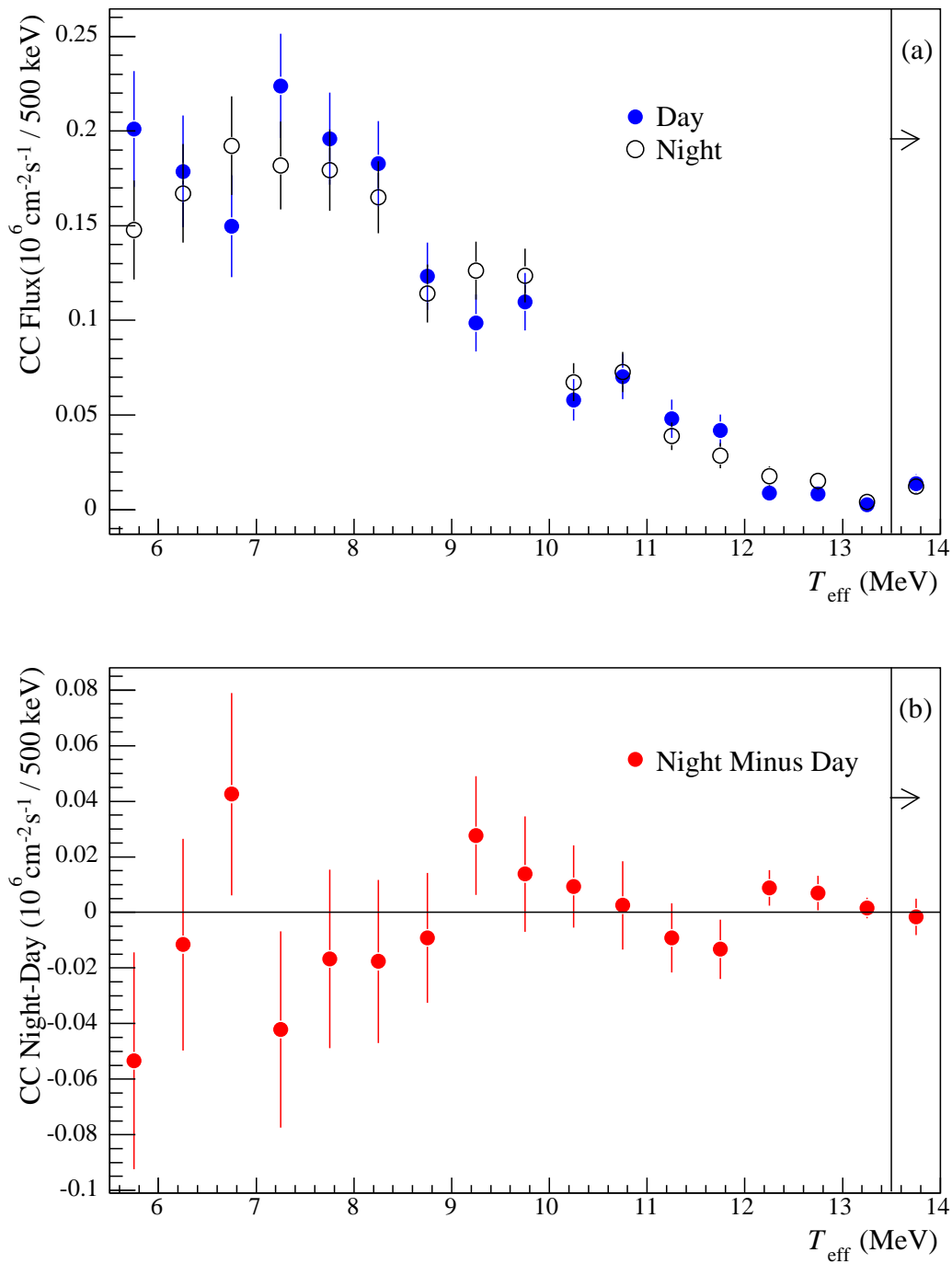
Figure 9.7: Day and night CC extracted spectra and the differences between the results in each bin, for the energy-unconstrained, neutral-current constrained analysis. Uncertainties are statistical only. The bins in the figures are 0.5 MeV wide, except for the final bin, which extends from 13.5 MeV to 20 MeV.

Table 9.17: Extracted CC spectra for day and night, from the energy-unconstrained, NC-constrained analysis, in units of $10^6$ neutrinos/cm$^2$/sec. The units are chosen such that the sum of all bins gives the total day or night CC flux. The first bin starts at 5.5 MeV. Bins are 0.5 MeV wide, except for the final bin, which extends from 13.5 MeV to 20 MeV.

| Bin | Day CC Flux | Night CC Flux |
|-----|-------------|---------------|
| 1 | $0.201 \pm 0.030$ | $0.148 \pm 0.026$ |
| 2 | $0.179 \pm 0.030$ | $0.167 \pm 0.027$ |
| 3 | $0.150 \pm 0.027$ | $0.192 \pm 0.026$ |
| 4 | $0.224 \pm 0.028$ | $0.182 \pm 0.024$ |
| 5 | $0.196 \pm 0.025$ | $0.179 \pm 0.022$ |
| 6 | $0.183 \pm 0.023$ | $0.165 \pm 0.019$ |
| 7 | $0.123 \pm 0.018$ | $0.114 \pm 0.016$ |
| 8 | $0.099 \pm 0.015$ | $0.126 \pm 0.016$ |
| 9 | $0.110 \pm 0.015$ | $0.124 \pm 0.015$ |
| 10 | $0.058 \pm 0.011$ | $0.067 \pm 0.010$ |
| 11 | $0.070 \pm 0.012$ | $0.073 \pm 0.011$ |
| 12 | $0.048 \pm 0.010$ | $0.039 \pm 0.007$ |
| 13 | $0.042 \pm 0.009$ | $0.029 \pm 0.007$ |
| 14 | $0.0088 \pm 0.0039$ | $0.018 \pm 0.005$ |
| 15 | $0.0082 \pm 0.0041$ | $0.015 \pm 0.005$ |
| 16 | $0.0025 \pm 0.0028$ | $0.0042 \pm 0.0026$ |
| 17 | $0.014 \pm 0.005$ | $0.012 \pm 0.004$ |

Figure 9.8. Also shown in the figure is the predicted day-night asymmetry as a function of energy for a point in the LMA region of the MSW parameter space. The LMA prediction corresponds to $\Delta m^2 = 7 \times 10^{-5}$ eV$^2$ and $\tan^2 \theta = 0.40$, which was the best-fit point for a global analysis prior to the release of the 391-day salt phase results (see, for example, the analysis in [129]). As can be seen from the figure, the prediction is nearly a flat line, and very close to zero asymmetry. For the best-fit MSW parameters, the predicted day-night asymmetries are very small. The SNO salt results are consistent with these predictions, and with no asymmetry at all.

The energy spectra and asymmetries as a function of energy for the NC-unconstrained and NC-constrained case are very similar, with comparable uncertainties on each bin. The addition of the $A_{\mathrm{NC}} = 0$ constraint does reduce the errors on each bin value by a small amount, but it also reduces the bin-to-bin correlations. These bin-to-bin correlations affect the statistical uncertainty on the total CC flux that is calculated by adding up all of the bins. The bin-to-bin correlations explain why the uncertainties on the calculated $A_{\mathrm{CC}}$ values for the two analyses can be quite different, while the uncertainties on the individual bins are nearly the same. The matrices of correlation coefficients for the spectral bins can be found in Appendix C.

## 9.12   Comparing SNO's Day-Night Asymmetry Measurements

In the pure-D$_2$O phase of the SNO experiment, measurements of the day-night asymmetry were performed in an energy-unconstrained analysis [140]. The asymmetries measured were

$$
\begin{aligned}
A_{\mathrm{NC}}^{D_2O}(\%) &= -20.4 \pm 16.9 \,(\text{stat.}) \,^{+2.4}_{-2.5}(\text{syst.}) \\
A_{\mathrm{CC}}^{D_2O}(\%) &= 14.0 \pm 6.3 \,(\text{stat.}) \,^{+1.5}_{-1.4}(\text{syst.}) \\
A_{\mathrm{ES}}^{D_2O}(\%) &= -17.4 \pm 19.5 \,(\text{stat.}) \,^{+2.4}_{-2.2}(\text{syst.}).
\end{aligned}
\tag{9.16}
$$

Using the fact that $\Phi_{\mathrm{ES}} = (1-\epsilon)\Phi_e + \epsilon\Phi_{tot}$, where $\epsilon = 0.1543$, the three measurements were combined to express an asymmetry in the electron neutrino flux, $A_e$ , and an asymmetry in the total neutrino flux $A_{tot}$,

$$
A_e^{D_2O} = 12.8 \pm 6.3(\text{stat.}) \,^{+1.5}_{-1.4}(\text{syst.})
\tag{9.17}
$$

186
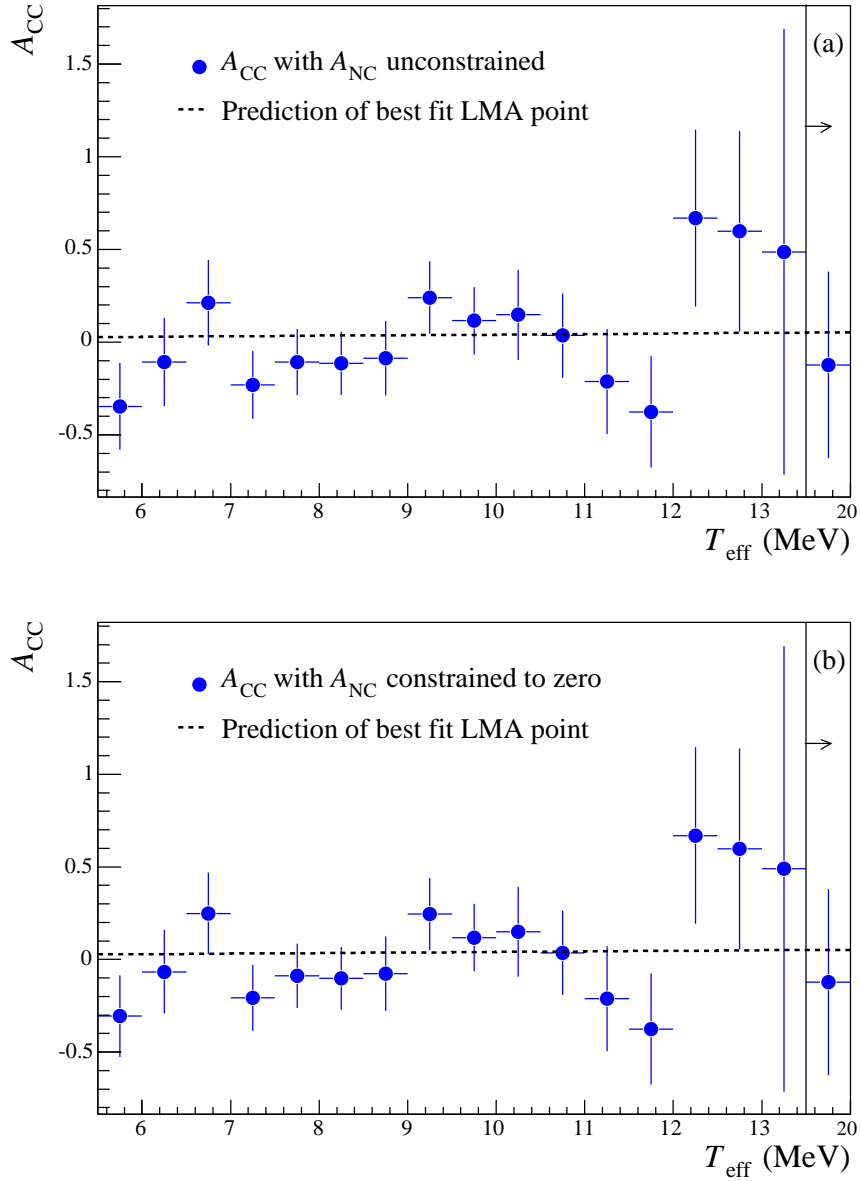


Figure 9.8: Day-night asymmetry in the CC flux, calculated in each energy bin, for (a) the NC-unconstrained analysis and (b) the NC-constrained analysis. Bins are 0.5 MeV wide, except for the final bin, which extends from 13.5 MeV to 20 MeV. Error bars represent statistical errors only. In both figures, the dashed line indicates the predicted asymmetry as a function of energy for the MSW model specified by $\Delta m^2 = 7 \times 10^{-5}\text{eV}^2$ and $\tan^2 \theta = 0.40$, which was the best-fit point for a global analysis prior to the release of the 391-day salt phase results.

$$A_{tot}^{D_2O} = -24.2 \pm 16.1(\text{stat.})\,{}^{+2.4}_{-2.5}(\text{syst.}), \qquad (9.18)$$

with a correlation coefficient of -0.602. Adding the constraint $A_{tot} = 0$ led to a smaller measurement of the day-night asymmetry for electron neutrinos due to the anticorrelation of the two asymmetries,

$$A_e^{D_2O} = 7.0 \pm 4.9(\text{stat.})\,{}^{+1.3}_{-1.2}(\text{syst.}). \qquad (9.19)$$

The two measurements of $A_e$ from the $D_2O$ phase are compared to the four measurements of $A_{CC}$ from the salt phase in Figure 9.9. Despite the fact that the livetime for the salt phase is longer (391 days compared to 306 days for the $D_2O$ analysis), the statistical uncertainties on the salt $A_{CC}$ measurements are slightly larger than the uncertainties on $A_e$ from the $D_2O$ phase. For the salt phase, the large number of NC events in the data set limits the precise measurement of the CC rate or asymmetry. The systematic uncertainties in the salt phase are also larger, dominated by uncertainty in the diurnal stability of the isotropy parameter. For both statistical and systematic uncertainties, the salt phase analysis produces a slightly less precise day-night asymmetry measurement than was possible with only $D_2O$ in the detector. One distinct advantage of the salt phase analysis, however, is that the electron neutrino asymmetry can be extracted without making assumptions about the solar neutrino energy spectrum.

The four variations on signal extraction produce measurements of $A_{CC}$ that differ in their model assumptions as well as in their sensitivities to different sources of uncertainty. The results are all consistent with one another, and are consistent with no day-night asymmetry in the electron neutrino flux. They are also consistent with the predictions for the LMA region of the solar neutrino oscillation parameter space, which gives electron neutrino day-night asymmetries in the range 2% to 4%.

Figure 9.10 shows a comparison of the measured $A_{tot}$ from the $D_2O$ phase with measurements of $A_{NC}$ from the salt phase. Measurements of $A_{NC}$ are improved in the salt phase due to the enhanced neutral current sensitivity. Systematic uncertainties are larger for the salt phase results, dominated by uncertainty in diurnal isotropy variation. The measured neutral current asymmetries are consistent with no asymmetry, as expected for standard neutrino oscillations.
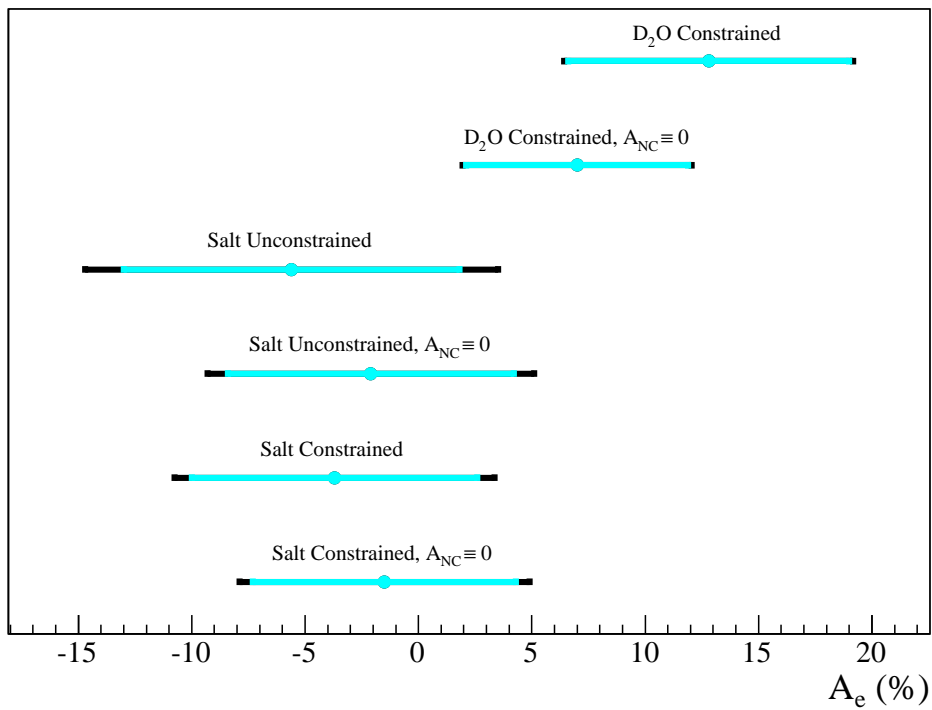
Figure 9.9: Comparisons of measurements of the day-night asymmetry in the electron neutrino flux for the $D_2O$ and salt phases, using different signal extraction techniques. The smaller bars for each measurement show the statistical uncertainties, and the larger bars show the total uncertainty. For the $D_2O$ phase results, the asymmetry $A_e$ is constructed using information from both the CC and ES reactions. In the salt phase, we take $A_e = A_{CC}$.

For testing MSW neutrino oscillation physics, the most appropriate analysis to consider is the energy-unconstrained, NC-constrained version. Standard neutrino oscillations within the MSW framework take place only between active neutrinos, causing energy-dependent flavor change. The most model-independent measurement comes from the energy-unconstrained, NC-unconstrained analysis, which is the most appropriate analysis for testing non-standard physics that might produce an asymmetry in the NC flux. The two energy-constrained analyses are primarily useful for comparing to previous results.
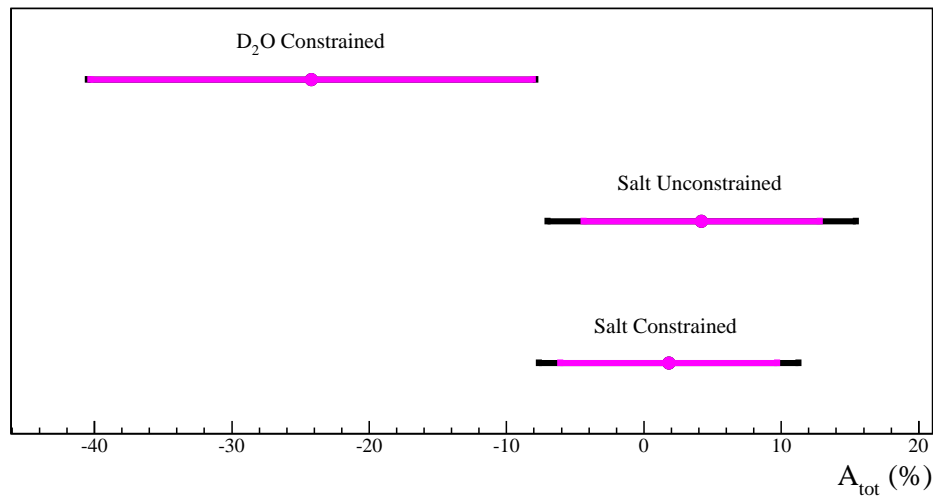


Figure 9.10: Comparisons of measurements of the day-night asymmetry in the total flux of active neutrinos for the $D_2O$ and salt phases, using different signal extraction techniques. The smaller bars for each measurement show the statistical uncertainties, and the larger bars show the total uncertainty. For the $D_2O$ phase results, the asymmetry $A_{tot}$ is constructed using information from both the NC and ES reactions. In the salt phase, we take $A_{tot} = A_{NC}$.

## 9.13  Discussion and Future Directions

Electron neutrino regeneration is a unique prediction of the MSW effect that potentially has a very clean signature, because most systematic uncertainties associated with the measurement of neutrino fluxes will cancel in the asymmetry ratio. For small day-night asymmetries of a few percent, measurements of the asymmetries at SNO are unfortunately too

statistics-limited to provide strong tests of MSW physics. However, the day-night asymmetry measurements offer independent consistency checks on the neutrino oscillation model, supporting the conclusion that the LMA region of the MSW parameter space describes solar neutrino oscillations.

In this chapter, results have been presented for the day-night asymmetries in solar neutrino fluxes measured through the CC, NC, and ES reactions in the salt phase of SNO. The first model-independent measurements and tests of the CC-asymmetry as a function of energy have been presented. The measured CC asymmetries directly test for electron neutrino regeneration, while the NC asymmetries can be viewed as a test for non-standard neutrino physics that might change the flux of active neutrinos arriving at the SNO detector day and night. The ability to separately test for the electron-neutrino and active-neutrino asymmetries is unique to SNO. Super-Kamiokande relies on the ES signal, which has a combined sensitivity to electron and non-electron flavors.

The salt phase day-night asymmetry measurements are summarized in Figures 9.11 and 9.12, which show the joint statistical confidence intervals for the CC and NC asymmetry measurements in the energy-unconstrained and energy-constrained analyses. The correlations between the two asymmetry measurements are indicated by the slopes of the semi-major axes of the error ellipses, and a comparison between the two figures shows how the energy constraint reduces the CC-NC covariance and overall uncertainties. Each figure also shows the CC asymmetry that is derived when the neutral current asymmetry is constrained to be zero.

### 9.13.1 Combining Measurements

In the $D_2O$ phase, the day-night asymmetry for electron neutrinos was determined to be $A_e = (7.0 \pm 4.9^{+1.3}_{-1.2})\%$, in an analysis with a constrained energy spectrum and $A_{NC}$ constrained to zero. The results for the comparable analysis for salt are found in Section 9.10, giving a CC asymmetry $A_{CC} = (-1.5 \pm 5.8 \pm 2.7)\%$. Combining these using a standard weighted average, we obtain a combined measurement of the electron neutrino asymmetry:

$$A_e(\text{ salt } + D_2O) = (3.7 \pm 4.0)\%. \tag{9.20}$$
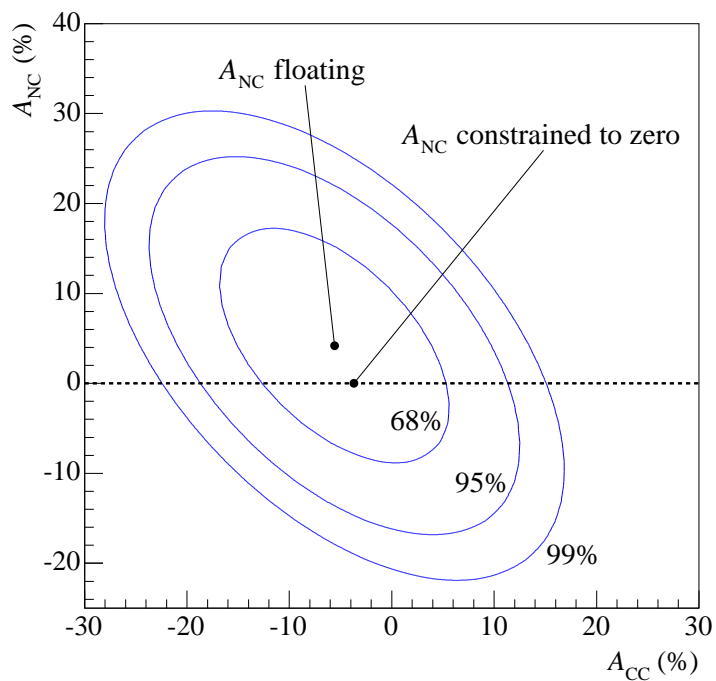
Figure 9.11: Joint statistical confidence intervals for $A_{CC}$ and $A_{NC}$ in the energy-unconstrained, NC-unconstrained analysis. The points indicate the best fit values for the NC-unconstrained and NC-constrained versions of the energy-unconstrained signal extraction.

192
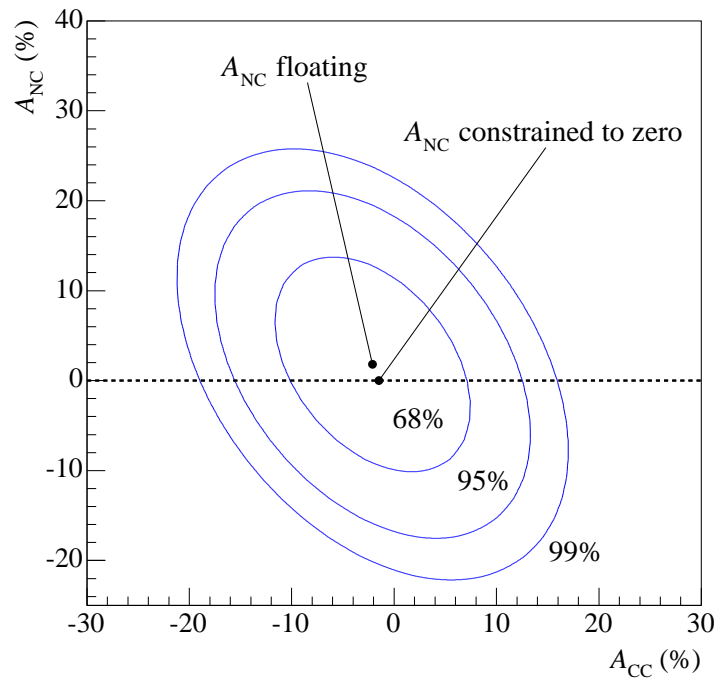


Figure 9.12: Joint statistical confidence intervals for $A_{\rm CC}$ and $A_{\rm NC}$ in the energy-constrained, NC-unconstrained analysis. The points indicate the best fit values for the NC-unconstrained and NC-constrained versions of the energy-constrained signal extraction.

In general, measurements from the two phases of SNO cannot be casually combined because of correlations between the systematic uncertainties for each phase. For the day-night measurements, the statistical uncertainties dominate, so a simple combination is reasonable. Caution is also generally required when manipulating ratios of Gaussian variables, which are not themselves Gaussian. However, the fractional uncertainties on the numerator and denominator of SNO's asymmetry ratios are sufficiently small that the Gaussian approximation is reasonable as long as we are not trying to make statements at very high confidence levels [141].

We can go one step further and combine SNO's result with the asymmetry measured by the Super-Kamiokande experiment. Super-Kamiokande measures an elastic scattering asymmetry $A_{ES} = (2.1 \pm 2.0^{+1.2}_{-1.3})\%$ [142]. Because ES interactions can be initiated by either $\nu_e$ or $\nu_{\mu\tau}$, the day-night asymmetry for ES events is diluted by a factor of $(\Phi_e + \epsilon(\Phi_{tot} - \Phi_e))/((1 - \epsilon)\Phi_e)$. For the Super-Kamiokande energy threshold of 5 MeV (total energy), the relative cross sections for neutral current and charged current scattering give a value of 0.1576 for $\epsilon$. Using the CC and NC fluxes from Chapter 8 as measures of $\Phi_e$ and $\Phi_{tot}$, the factor by which the Super-Kamiokande result is diluted is 1.55. With the simplifying assumption that the day-night effect is energy-independent, we can scale the Super-Kamiokande asymmetry by 1.55 to obtain $A_{e,\text{SK}} = (3.3 \pm 3.1^{+1.9}_{-2.0})\%$. Combining this with the SNO value, we get $A_{e,\text{combined}} = (3.5 \pm 2.7)\%$.

Chapter 10

# COMMENTS ON POSSIBLE IMPROVEMENTS TO THE DAY-NIGHT ANALYSIS

## 10.1 General Comments

The day-night asymmetry measurement is ultimately statistics-limited, and even combining results from all three phases of the SNO experiment will not overcome that limitation well enough to make strong statements about day-night effects. As confidence grows in the current best-fit LMA oscillation solution, there is diminishing hope of being able to resolve earth matter effects with current-generation experiments. Nevertheless, the day-night asymmetry measurements offer a unique opportunity to test directly for matter effects in neutrino oscillations. Even if it is impossible to discover evidence for matter effects with these measurements, the day-night asymmetry measurement still tests predictions of MSW models.

Several possible improvements and extensions to the SNO day-night analysis could be pursued. Although the measurements are limited by statistics, the systematic uncertainties for the salt-phase analysis are almost certainly substantially overestimated. This is because the techniques used to limit diurnal variation in detector response for the $D_2O$ phase data, which were extended for the salt phase analysis, are not sufficient to effectively measure diurnal variations in isotropy response. Because of the sensitivity of the salt-phase signal extraction results to variations in $\beta_{14}$ , any uncertainty in the diurnal or long-term variation in this parameter translates into large uncertainties in the asymmetry results for CC and NC events. From first principles, there are few effects that could lead to diurnal isotropy variations, so realistic day-night variations in isotropy response are probably much smaller than can be measured with the in-situ techniques described in Chapter 7. It may be possible to explore how underlying detector conditions such as temperature or high-voltage

stability impact the measured isotropy of events. If limits can be placed on the diurnal variations in detector conditions, smaller uncertainties on $\beta_{14}$ variation could be derived. Alternatively, calibration data taken during the night-time hours could be used, possibly in combination with other techniques, to provide better limits on isotropy response. Some preliminary explorations into these issues are provided in the second section of this chapter. Although these modifications to the analysis may be worth doing in an effort to assign correct systematic uncertainties, they will not have a large impact on the precision of the results.

Extensions to the day-night analysis could also be explored in future work. Measurements of the day-night asymmetry parameters characterize the average asymmetry over the full SNO energy spectrum and over a range of solar neutrino trajectories through the earth. However, electron neutrino regeneration is an energy-dependent and zenith-angle-dependent effect. The salt phase analysis includes the first construction of the CC asymmetry as a function of energy, shown in Figure 9.8, but a complete investigation of systematic uncertainties on the day and night spectra has not been performed, nor has the zenith angle dependence been explored. For the LMA MSW solution, expected variations with energy and zenith angle may be too small to be resolved, given SNO's limited statistics. However, the current analysis may not be the most sensitive for addressing the expected physics. Judicious choices of energy thresholds and zenith angle binning could isolate the more interesting subsets of SNO's data set, but the best approach is probably to perform an unbinned maximum likelihood fit, including the zenith angle and energy information for each event.

Extending the analysis to include energy and zenith angle dependence would require re-thinking how backgrounds and systematic uncertainties are handled. Measuring backgrounds as a function of the solar zenith angle is likely to be difficult. One approach to addressing backgrounds would be to raise the energy threshold used in the analysis in order to eliminate low-energy background events altogether. This does not eliminate the neutron backgrounds, but if the analysis is only concerned with searching for electron neutrino regeneration, separating the neutron backgrounds from the NC events may not be necessary. Estimating and modeling systematic uncertainties as a function of zenith angle is also likely to be quite challenging. If a binned analysis is performed, some of the same in-situ tech-

196

niques that are used for limiting day-night variations in response could be used to study stability over the set of zenith and/or energy bins. However, limitations in the statistics available for in-situ studies will be a significant problem. If an unbinned maximum likelihood technique is used, then new strategies will be needed for estimating uncertainties and modeling the dependence of the extracted neutrino fluxes on systematic variations in detector response.

If the current best-fit oscillation parameters apply, even the most subtle and complex analysis of the day-night effect is unlikely to have enough statistical power to see evidence for earth regeneration effects. Nevertheless, combining data from all three phases of SNO will improve the statistics of the day-night measurement somewhat. Measurements of the day-night asymmetry parameters in the NCD phase are likely to be improvements on the measurements in the salt and $D_2O$ phases. In the NCD phase, the covariance between the CC and NC measurements is broken, since the NC flux is measured through an independent set of detectors. This will lead to a more statistically precise measurement of the electron neutrino asymmetry compared to the previous phases. Systematic uncertainties should be small, comparable to those for the day-night measurement in the $D_2O$ phase, since the results will not be sensitive to isotropy response variations. Combining all three phases is expected to result in a final uncertainty on the electron neutrino asymmetry measurement of around 2.5%.

## 10.2  Comments on Improving Systematic Uncertainties for the Salt Day-Night Analysis

The overall strategy for estimating systematic uncertainties for the salt day-night analysis was based on the methods used for the $D_2O$ phase of the experiment. In the $D_2O$ phase, signal extraction was most sensitive to variations in energy response parameters. Diurnal, long term, and directional variations in energy response can be relatively well characterized using low-energy background studies and [16]N calibrations. In the salt phase, the signal extraction (in the energy-unconstrained analysis) is most sensitive to the isotropy parameter $\beta_{14}$. Low-energy background rates cannot be used to limit diurnal variations in isotropy,

and comparisons of the day and night $\beta_{14}$ values for background events give poor limits. From low-energy background studies, the limit on the diurnal shift in $\beta_{14}$ was estimated to be 0.006. Including extra information from muon follower studies reduced the value of the diurnal isotropy shift to 0.0043.

The results in Chapter 9 show that diurnal isotropy variation is the largest systematic uncertainty on the primary day-night asymmetry results. Although the uncertainties are still dominated by the statistical uncertainty, the isotropy systematics are large enough to merit re-evaluation if the analysis is repeated in the future. Some possible approaches are sketched in this section.

An important consideration in testing for diurnal variations is the distinction between day-night variations that are due to true diurnal changes in detector response, and those that arise due to an aliasing of long term or occasional effects into an effective day-night variation, because to the particular time-sampling of the data set. The tests and checks described below are presented assuming that the intent is to assess true diurnal variations. A thorough re-evaluation of systematic uncertainties for the day-night analysis also needs to consider how to estimate systematic uncertainties due to the aliasing of long-term or occasional variations into day-night variations.

### 10.2.1   Night Calibration Data

During the salt phase, a handful of calibration runs were taken during nighttime hours. These can be used to test directly for systematic variations in detector response day and night. Because they sample a very limited set of points in the time span of the salt phase, they have not been used in the evaluation of diurnal response uncertainties for the day-night analysis. To use these runs as the basis for estimates of systematic uncertainties would require a significant assumption: that the source of any day-night variations in detector response is stable enough that a few individual night-time runs sample the effect sufficiently. With careful thought, it may be possible to argue that such an assumption is reasonable. More likely, these runs could be used as part of a suite of day and night response comparisons used to derive systematic uncertainties.

Early in the salt phase, the $^{252}$Cf calibration source was left in the detector for a 24-hour period, to provide checks on diurnal response. Figure 10.1 shows a comparison of the (normalized) isotropy distributions for the day and night portions of this 24 hour run. The distributions agree well. A Gaussian fit within a restricted range of the mean gives $0.30945 \pm 0.00032$ for the mean isotropy value during the day, and $0.30948 \pm 0.00034$ for the night.
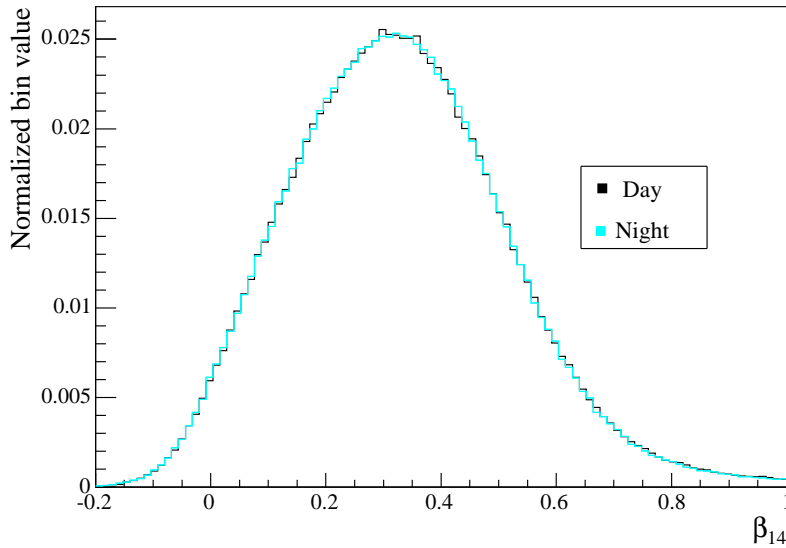


Figure 10.1: Comparison of normalized isotropy distributions for the day and night portions of run 21023, a 24-hour $^{252}$Cf run.

During the salt phase, three $^{16}$N scans were taken that included night-time runs. Although these only sample three points in the time spanned by the full data set, they can be used to check for systematic variations in day-night response. Figure 10.2 shows the mean isotropy values for the day and night runs. The night runs agree well with the day runs. The average value of the day isotropy means in this analysis is 0.41168 for the day data, with an RMS spread of 0.00070. For the night runs, the average is 0.41186 with an RMS spread of 0.00063.

These calibration runs can be used to give additional checks on diurnal variations in
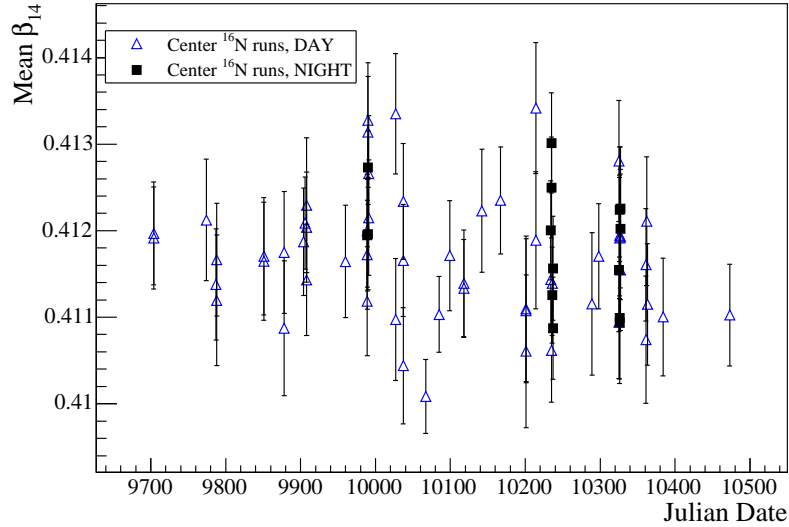
Figure 10.2: Comparison of mean isotropy values for day and night $^{16}$N runs at the center of the detector. The mean isotropy values were determined from a gaussian fit to $^{16}$N events with energies near the mean energy for each run.

response. None of them show evidence for day-night variations.

### 10.2.2 Characterizing Low-Level Detector Stability

Particularly when considering the isotropy parameter, a worthwhile approach may be to determine what low-level detector changes could actually cause diurnal variations in detector response. Temperature variations, seismic activity, personnel activity, or changes in the high-voltage supplied to the detector are some of the conditions that could systematically vary day to night. In principle, these variations could cause changes in the average isotropy for events, most likely through variations in the numbers of noise PMT hits recorded in the events. If a mechanism can be supplied for systematic variations in the optical properties of the detector day and night, that could also affect the isotropy measured for each event.

For directly studying the effect of noise on isotropy response, Monte Carlo data could be used. Variations of isotropy could be mapped out as a function of variations in noise rate. Data from the pulsed global trigger (PGT) gives a measure of the actual noise rates in

each run. Day-night variations in the noise measured through PGT could then be used to limit how much the isotropy parameter could vary day and night. Most likely, the isotropy parameter will be fairly insensitive to noise variations at the level that occur during ordinary running. As an example of the day-night noise variations measured through PGT, Figure 10.3 shows the mean Nhit value for PGT events day and night, as a function of run number. The day and night mean number of noise hits generally agree to within a fraction of one PMT hit.
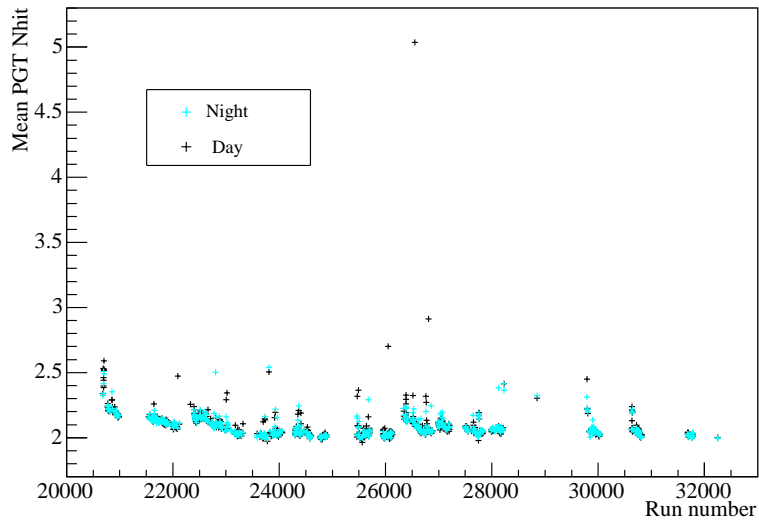


Figure 10.3: Preliminary comparisons of day and night values for the (arithmetic) mean Nhit for PGT events during salt phase runs. The day and night means are shown for the majority of salt phase runs. Day (night) PGT means are only shown for runs that have non-zero day (night) livetime. Files of PGT events for runs after run number 32249 were not available when the figure was produced, so the figure is only included as an illustration of day-night variations for a portion of the data set.

To study the possible effects of variations in detector high-voltage or threshold stability on energy scale, two sets of $^{16}$N calibration runs were taken during the salt phase, during which the high-voltage and threshold settings were varied. These runs can also be used to determine the effect of threshold and gain variations on isotropy. The mean isotropy values for these runs are shown in figure 10.4. The isotropy means do not show clear sys-

tematic trends as a function of variation in high voltage or threshold, and the differences between isotropy means for the different runs are at the level of 0.002-0.004. If it is possible to argue that day-night variations in high voltage or threshold are smaller than those explored with this set of special calibrations, these points could be used to provide another check on diurnal isotropy variation. Variations in optical response that could affect
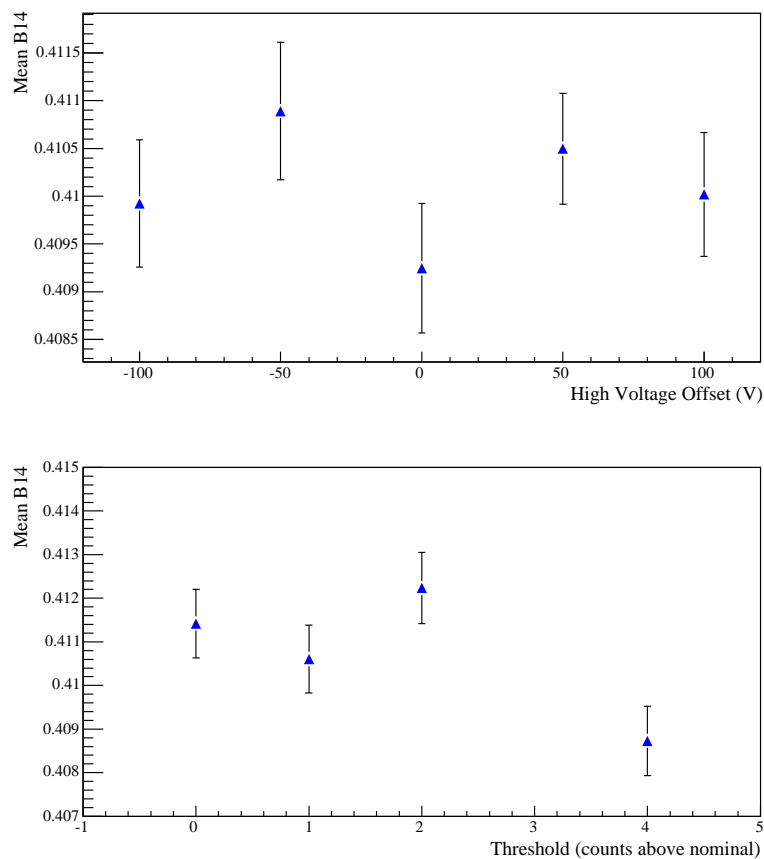


Figure 10.4: Preliminary comparisons of the mean $\beta_{14}$ values for $^{16}$N runs with varying high-voltage and threshold settings. The isotropy mean is determined by fitting a gaussian to the isotropy distribution for events near the mean energy for all $^{16}$N events in the run. The mean energy of $^{16}$N events does change when gain or threshold varies, so a more careful study of isotropy variations due to gain and threshold variations may need to consider how the correlation between energy and isotropy affects interpretation.

isotropy may be harder to constrain. In general, approaching systematic uncertainties in

diurnal response from the perspective of low-level detector stability requires more complex arguments. Given an underlying detector change that could induce day-night variations in isotropy (or another response variable), the effects of the change on the measured response must be explored through Monte Carlo or other means, and then arguments must be made about the underlying detector stability. The effort to make more sophisticated arguments may not be worthwhile. However, for exploring zenith angle or energy dependent day-night analyses, perhaps such techniques would become more useful.

*10.2.3   Approaches to Error Propagation*

With further study, some of the approaches sketched in this chapter could result in a reduced systematic uncertainty in the diurnal shift of the isotropy parameter. The systematic uncertainty in the isotropy mean was likely overestimated for the analysis presented in this thesis. Since the day-night analysis is statistics-limited, there is not much to be gained by any more subtle treatment of systematic uncertainties. However, a few other improvements could, in principle, be made in how the error propagation is treated. These improvements may be more relevant for other analyses, including the integral flux analysis, and some of them have been implemented in other SNO thesis work.

The standard technique for propagating systematic uncertainties in SNO's measurements is to perturb the Monte Carlo events used to construct PDFs, in such a way as to simulate shifts in the response parameters equal to plus or minus the $1\sigma$ systematic uncertainty. The shifted PDFs are substituted into the signal extraction process, and the resulting shift in each extracted physics result is taken as the uncertainty in that result due to a $1\sigma$ uncertainty in that parameter.

Typically, the systematic shifts in the extracted physics parameters are not symmetric around the central value. For the day-night analysis, the uncertainties were symmetrized by taking the larger of the two shifts as a measure of the plus and minus systematic error. This can be viewed as a conservative approach, but averaging the two shifts would be just as reasonable. For the integral flux analysis, the asymmetric uncertainties were retained, and the plus and minus shifts were separately added in quadrature to obtain the final result. In

many cases, the signal extraction process is not likely to be sensitive enough that the asymmetric errors are truly meaningful. The fact that they are asymmetric may be an artifact of statistics rather than an indication of asymmetric dependencies on response variations. In such cases, it is reasonable to take the average of the plus and minus shifts as an estimated symmetric uncertainty. For the cases in which we believe that the systematic uncertainty truly is asymmetric, the plus and minus shifts should be treated with an asymmetric model for error propagation (see, for example, reference [143]).

Ultimately, the best approach to handling systematic uncertainties is to model the dependence on response parameters directly in the signal extraction process. Approaches to this have been described in [119] and [144]. Future day-night work should incorporate these techniques, which account for correlations between systematic uncertainties and make use of information from the neutrino data itself as well as information from calibrations and in-situ studies.

Chapter 11

## CONCLUSIONS AND IMPLICATIONS

This thesis has presented measurements of the day-night asymmetries in solar neutrino fluxes using data from the salt phase of the Sudbury Neutrino Observatory. SNO has a unique ability to test directly for day-night asymmetries in the electron neutrino flux using the charged current (CC) reaction of neutrinos on deuterium. The neutral current (NC) reaction allows a test for the day-night asymmetry in the total active solar neutrino flux. The elastic scattering (ES) day-night asymmetry has some sensitivity to non-electron neutrinos as well as electron neutrinos, but is highly statistics-limited. Because the light produced by neutron capture reactions in the salt phase is more isotropic than the light produced by electron events, the neutrino signals can be statistically separated without imposing constraints on the energy spectrum of the incoming neutrinos. This enables a model-independent measurement of the day-night asymmetries in the salt phase, in which the CC spectrum day and night are also extracted from the data and can be used to test for distortions in the solar neutrino spectrum.

The day-night analysis in the salt phase has been performed with four variations on the maximum likelihood fits used to extract the day and night neutrino fluxes from the data. The first is the model-independent analysis, in which the day and night neutrino fluxes are extracted independently and the CC and ES spectrum shapes are allowed to vary. The second includes the additional constraint that the NC flux does not vary between day and night. This assumption is appropriate for tests for a day-night asymmetry given standard three-neutrino oscillations within the MSW model. The third and fourth variations on the analysis impose the additional constraint of an undistorted $^8$B neutrino spectrum. Constraining the energy spectrum reduces the statistical and systematic uncertainties on the results, but represents an assumption that the neutrino flavor change mechanism is energy independent.

The CC day-night asymmetries from the four analyses are summarized in Table 11.1. All asymmetries are consistent with zero. They are also consistent with the small asymmetries that are predicted for the Large Mixing Angle region of the MSW parameter space. The day and night CC energy spectra extracted in the two shape-unconstrained versions of the fit were given in Chapter 9, and show no evidence for day-night variations as a function of energy. Table 11.1 also gives a comparison of the day-night asymmetries in the neutral cur-

Table 11.1: Summary of salt day-night asymmetries for the CC and NC reactions.

| Fit variation | CC Asymmetry |
|---|---|
| Shape-Unconstrained, NC-Unconstrained | $A_{CC} = [-5.6 \pm 7.4(\text{stat.}) \pm 5.3(\text{syst.})]\%$ |
| Shape-Unconstrained, NC-Constrained | $A_{CC} = [-3.7 \pm 6.3(\text{stat.}) \pm 3.2(\text{syst.})]\%$ |
| Shape-Constrained, NC-Unconstrained | $A_{CC} = [-2.1 \pm 6.3(\text{stat.}) \pm 3.5(\text{syst.})]\%$ |
| Shape-Constrained, NC-Constrained | $A_{CC} = [-1.5 \pm 5.8(\text{stat.}) \pm 2.7(\text{syst.})]\%$ |
| Fit variation | NC Asymmetry |
| Shape-Unconstrained, NC-Unconstrained | $A_{NC} = [4.2 \pm 8.6(\text{stat.}) \pm 7.2(\text{syst.})]\%$ |
| Shape-Constrained, NC-Unconstrained | $A_{NC} = [1.8 \pm 7.9(\text{stat.}) \pm 5.2(\text{syst.})]\%$ |

rent flux. The day-night asymmetries in the elastic scattering flux can be found in Chapter 9. The NC and ES day-night asymmetries measured in the salt phase are also consistent with zero. The uncertainties are dominated by statistical uncertainty, but the systematic uncertainties are not negligible, particularly for the model-independent measurement. For the CC and NC asymmetries, the systematic uncertainties are dominated by uncertainty in the diurnal stability of the isotropy variable.

In addition to the day-night asymmetry measurements, measurements of the integral fluxes from the salt phase were produced as a check on those published in [38]. The measured solar neutrino fluxes from a model-independent analysis, in units of $10^6 \text{cm}^{-2}\text{s}^{-1}$, are:

$$\Phi_{\text{NC}} = 4.94 \pm 0.21\,(\text{stat.})\,^{+0.38}_{-0.34}\,(\text{syst.})$$
$$\Phi_{\text{CC}} = 1.68 \pm 0.06\,(\text{stat.})\,^{+0.08}_{-0.09}\,(\text{syst.})$$

$$\Phi_{\mathrm{ES}} \quad = \quad 2.35 \pm 0.23\,(\mathrm{stat.})\,^{+0.15}_{-0.15}\,(\mathrm{syst.}). \tag{11.1}$$

The measured NC flux agrees with theoretical predictions for the total $^8$B solar neutrino flux. A comparison of the CC and NC fluxes demonstrates the appearance of non-electron neutrinos in the solar neutrino flux.

Measurements of the CC, NC, and ES fluxes in the salt phase confirm the predictions of the Standard Solar Model and demonstrate solar neutrino flavor change in a model-independent analysis. Solar neutrino flavor change is interpreted as evidence for neutrino oscillations within the MSW model, which additionally predicts spectral distortions and day-night variations in solar neutrino flavor. The CC spectrum analysis and the day-night analysis in SNO can test for these effects. As described in [38] and [119], the extracted CC energy spectrum from the salt phase is consistent with an undistorted $^8$B solar neutrino spectrum, as well as with the spectrum predicted by the LMA model. The day-night measurements in this thesis are also consistent with no effect, as well as with the LMA predictions. For the favored region of the MSW parameter space, the expected distortions in the energy spectrum and the expected earth matter effects are subtle.

The day-night CC spectra in this thesis were used along with the integral fluxes for the NC and ES measurements and the $D_2O$ phase results in an MSW oscillation analysis for [38]. The allowed regions using only the SNO data are shown in Figure 11.1. The best fit point corresponds to $\Delta m^2 = 5.0^{+6.2}_{-1.8}$ and $\tan^2 \theta = 0.45^{+0.11}_{-0.10}$. When combined with the results of other solar neutrino experiments, only one region remains in the MSW plot, as shown in the top panel of Figure 11.2. The best-fit parameters for the global solar analysis are $\Delta m^2 = 6.5^{+4.4}_{-2.3}$ and $\tan^2 \theta = 0.45^{+0.09}_{-0.08}$. The addition of the other solar neutrino experiments increases the value of $\Delta m^2$ by a small amount, but does not have much of an effect on $\tan^2 \theta$, which is already strongly constrained by the electron neutrino survival probability measured through the CC and NC reactions in SNO. With the inclusion of the reactor antineutrino data from KamLAND, the parameter space is restricted much more tightly in $\Delta m^2$, as shown in the bottom panel of Figure 11.2, with best fit point $\Delta m^2 = 8.0^{+0.6}_{-0.4}$ and $\tan^2 \theta = 0.45^{+0.09}_{-0.07}$. The KamLAND experiment provides strong constraints on $\Delta m^2$, which are complementary to the constraints on $\tan^2 \theta$ that come from the SNO CC to NC ratio.
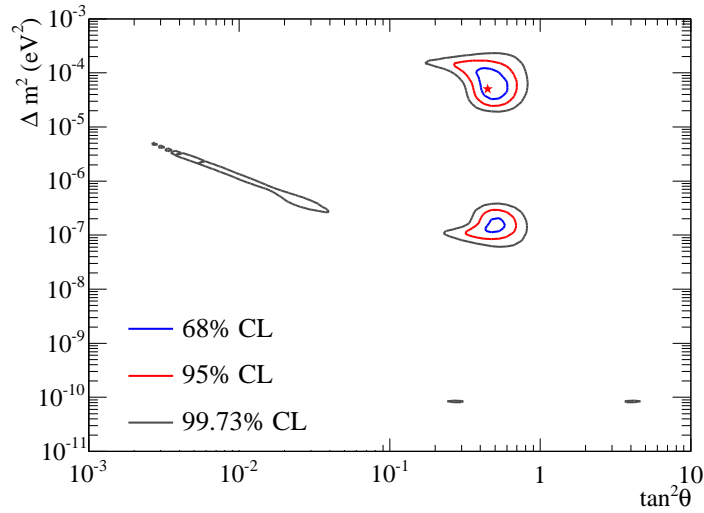
Figure 11.1: Results for an MSW oscillation analysis using only data from the $D_2O$ and salt phases of SNO. The best-fit point corresponds to $\Delta m^2 = 5.0^{+6.2}_{-1.8}$ and $\tan^2 \theta = 0.45^{+0.11}_{-0.10}$. Figure from [38].

The agreement between the SNO and KamLAND experiments within the MSW model is a strong argument that the MSW effect is a correct explanation for solar neutrino flavor change. Observation of spectral distortions or earth matter effects would be direct evidence of the MSW effect. Future spectrum measurements at SNO with a lower energy threshold may see distortions in the CC spectrum, and additional data from the NCD phase will improve the precision of the day-night asymmetry. However, further exploration of matter enhanced neutrino oscillations will require next-generation experiments. Experiments with sensitivity to lower energy neutrinos will test the energy-dependence of the LMA electron neutrino survival probability. To observe the predicted day-night asymmetry, extremely large detectors may be required, running over time periods as long as a decade.
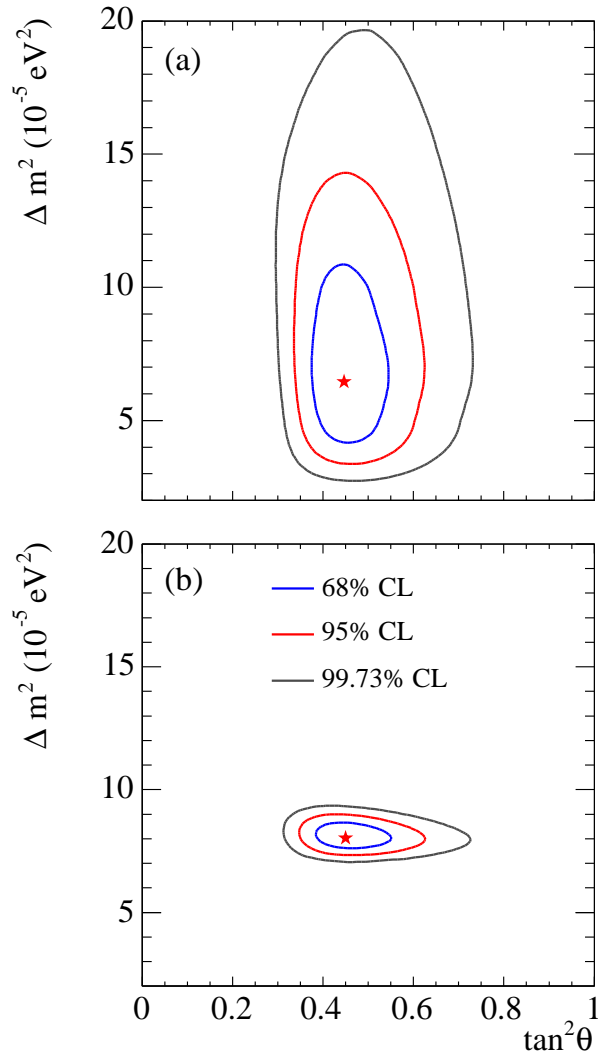
Figure 11.2: Global MSW analysis using SNO plus other solar neutrino experiments (a), and including the KamLAND experiment (b). The best fit point for the top panel is $\Delta m^2 = 6.5^{+4.4}_{-2.3}$ and $\tan^2 \theta = 0.45^{+0.09}_{-0.08}$, and for the lower panel, $\Delta m^2 = 8.0^{+0.6}_{-0.4}$ and $\tan^2 \theta = 0.45^{+0.09}_{-0.07}$. Figure from [38].

# BIBLIOGRAPHY

[1] W. Pauli, "Letter to the Physical Society of Tubingen," Reproduced in [2].

[2] L. Brown, "The idea of the neutrino," *Phys. Today*, p. 23, Sept. 1978.

[3] E. Fermi, "Trends to a theory of beta radiation. (in Italian)," *Nuovo Cim.*, vol. 11, pp. 1–19, 1934.

[4] H. Bethe and R. Pierls *Nature*, vol. 133, no. 532, 1934.

[5] C. Sutton, *Spaceship Neutrino.* Cambridge University Press, 1992.

[6] C. Cowan *et al.*, "Detection of the free neutrino: a confirmation," *Science*, vol. 124, no. 103, p. 3212, 1956.

[7] F. Reines, "Search for the free neutrino," in *Weak Neutral Currents* (D. Cline, ed.), pp. 2–63, Addison-Wesley, 1997.

[8] E. Majorana, "Theory of the symmetry of electrons and positrons," *Nuovo Cim.*, vol. 14, pp. 171–184, 1937.

[9] R. Davis, "An attempt to detect the neutrinos from a nuclear reactor by the $^{3}7\text{Cl}(\bar{\nu}, e^-)^{37}\text{Ar}$ reaction," *Bull. of American Phys. Soc., Series 2*, vol. 1.

[10] T. D. Lee and C.-N. Yang, "Question of parity conservation in weak interactions," *Phys. Rev.*, vol. 104, pp. 254–258, 1956.

[11] C. S. Wu, E. Ambler, R. W. Hayward, D. D. Hoppes, and R. P. Hudson, "Experimental test of parity conservation in beta decay," *Phys. Rev.*, vol. 105, pp. 1413–1414, 1957.

[12] E. D. Commins and P. H. Bucksbaum, "Weak interactions of leptons and quarks," Cambridge, USA: Univ. Pr. ( 1983) 473p.

[13] T. D. Lee and C.-N. Yang, "Parity nonconservation and a two component theory of the neutrino," *Phys. Rev.*, vol. 105, pp. 1671–1675, 1957.

[14] M. Goldhaber, L. Grodzins, and A. W. Sunyar, "Helicity of neutrinos," *Phys. Rev.*, vol. 109, pp. 1015–1017, 1958.

[15] L. Hoddeson, L. Brown, M. Riordan, and M. Dresden, "The rise of the standard model: Particle physics in the 1960s and 1970s.," Prepared for 3rd International Symposium on the History of Particle Physics: The Rise of the Standard Model, Stanford, California, 24-27 Jun 1992.

[16] F. J. Hasert *et al.*, "Search for elastic muon neutrino electron scattering," *Phys. Lett.*, vol. B46, pp. 121–124, 1973.

[17] F. J. Hasert *et al.*, "Observation of neutrino-like interactions without muon or electron in the gargamelle neutrino experiment," *Phys. Lett.*, vol. B46, pp. 138–140, 1973.

[18] A. C. Benvenuti *et al.*, "Observation of muonless neutrino induced inelastic interactions," In Cline, D.B. (ed.): *Weak neutral currents* 5.19-5.22.

[19] P. Galison, "The discovery of neutral currents," in *Weak Neutral Currents* (D. Cline, ed.). Reading, USA: Addison-Wesley (1997).

[20] G. Arnison *et al.*, "Experimental observation of isolated large transverse energy electrons with associated missing energy at s**(1/2) = 540-GeV," *Phys. Lett.*, vol. B122, pp. 103–116, 1983.

[21] M. Banner *et al.*, "Observation of single isolated electrons of high transverse momentum in events with missing transverse energy at the CERN anti-p p collider," *Phys. Lett.*, vol. B122, pp. 476–485, 1983.

[22] G. Arnison *et al.*, "Experimental observation of lepton pairs of invariant mass around 95-GeV/c\*\*2 at the CERN SPS collider," *Phys. Lett.*, vol. B126, pp. 398–410, 1983.

[23] P. Bagnaia *et al.*, "Evidence for $Z^0 \longrightarrow e^+e^-$ at the CERN anti-p p collider," *Phys. Lett.*, vol. B129, pp. 130–140, 1983.

[24] G. Danby *et al.*, "Observation of high-energy neutrino reactions and the existence of two kinds of neutrinos," *Phys. Rev. Lett.*, vol. 9, pp. 36–44, 1962.

[25] M. L. Perl *et al.*, "Evidence for anomalous lepton production in e+ e- annihilation," *Phys. Rev. Lett.*, vol. 35, pp. 1489–1492, 1975.

[26] K. Kodama *et al.*, "Observation of tau-neutrino interactions," *Phys. Lett.*, vol. B504, pp. 218–224, 2001, hep-ex/0012035.

[27] D. N. Schramm, "Cosmology and the weak interaction," Proc. of Wien '89 Int. Symp. on Weak and Electromagnetic Interactions in Nuclei, Montreal, Canada, May 15-19, 1989.

[28] G. Steigman, "Neutrinos and big bang nucleosynthesis," 2005, hep-ph/0501100.

[29] "A combination of preliminary electroweak measurements and constraints on the standard model," 2004, hep-ex/0412015.

[30] S. Eidelman *et al.*, "Review of particle physics," *Phys. Lett.*, vol. B592, p. 1, 2004.

[31] R. Davis, D. S. Harmer, and K. C. Hoffman, "Search for neutrinos from the sun," *Phys. Rev. Lett.*, vol. 20, pp. 1205–1209, 1968.

[32] Y. Fukuda *et al.*, "Measurement of the flux and zenith-angle distribution of upward through-going muons by Super-Kamiokande," *Phys. Rev. Lett.*, vol. 82, pp. 2644–2648, 1999, hep-ex/9812014.

[33] E. Aliu *et al.*, "Evidence for muon neutrino oscillation in an accelerator- based experiment," *Phys. Rev. Lett.*, vol. 94, p. 081802, 2005, hep-ex/0411038.

[34] Q. R. Ahmad *et al.*, "Measurement of the charged current interactions produced by B-8 solar neutrinos at the Sudbury Neutrino Observatory," *Phys. Rev. Lett.*, vol. 87, p. 071301, 2001, nucl-ex/0106015.

[35] Q. R. Ahmad *et al.*, "Direct evidence for neutrino flavor transformation from neutral-current interactions in the Sudbury Neutrino Observatory," *Phys. Rev. Lett.*, vol. 89, p. 011301, 2002, nucl-ex/0204008.

[36] K. Eguchi *et al.*, "First results from KamLAND: Evidence for reactor anti- neutrino disappearance," *Phys. Rev. Lett.*, vol. 90, p. 021802, 2003, hep-ex/0212021.

[37] T. Araki *et al.*, "Measurement of neutrino oscillation with KamLAND: Evidence of spectral distortion," *Phys. Rev. Lett.*, vol. 94, p. 081801, 2005, hep-ex/0406035.

[38] B. Aharmim *et al.*, "Electron energy spectra, fluxes, and day-night asymmetries of B-8 solar neutrinos from the 391-day salt phase SNO data set," 2005, nucl-ex/0502021.

[39] A. Aguilar *et al.*, "Evidence for neutrino oscillations from the observation of anti-nu/e appearance in a anti-nu/mu beam," *Phys. Rev.*, vol. D64, p. 112007, 2001, hep-ex/0104049.

[40] D. B. Kaplan, A. E. Nelson, and N. Weiner, "Neutrino oscillations as a probe of dark energy," *Phys. Rev. Lett.*, vol. 93, p. 091801, 2004, hep-ph/0401099.

[41] R. Fardon, A. E. Nelson, and N. Weiner, "Dark energy from mass varying neutrinos," *JCAP*, vol. 0410, p. 005, 2004, astro-ph/0309800.

[42] R. Stefanski, "The status of MiniBooNE," *Nucl. Phys. Proc. Suppl.*, vol. 110, pp. 420–422, 2002.

[43] B. Kayser, "The neutrino future," 2005. Proceedings of the XXXXth Rencontres de Moriond Session: Electroweak Interactions and Unified Theories, La Thuile, Italy.

[44] W. B. Rolnick, "The fundamental particles and their interactions," Reading, USA: Addison-Wesley (1994) 466 p.

[45] E. K. Akhmedov, "Neutrino physics," 1999, hep-ph/0001264.

[46] B. Kayser, "Neutrino mass, mixing, and oscillation," 2001, hep-ph/0104147.

[47] B. Kayser and R. N. Mohapatra, "The nature of massive neutrinos," In Caldwell, D.O. (ed.): *Current aspects of neutrino physics* 17-38.

[48] B. Pontecorvo, "Inverse beta processes and nonconservation of lepton charge," *Sov. Phys. JETP*, vol. 7, pp. 172–173, 1958.

[49] B. Pontecorvo, "Neutrino experiments and the question of leptonic-charge conservation," *Sov. Phys. JETP*, vol. 26, pp. 984–988, 1968.

[50] Z. Maki, M. Nakagawa, and S. Sakata, "Remarks on the unified model of elementary particles," *Prog. Theor. Phys.*, vol. 28, p. 870, 1962.

[51] M. Apollonio *et al.*, "Search for neutrino oscillations on a long base-line at the CHOOZ nuclear power station," *Eur. Phys. J.*, vol. C27, pp. 331–374, 2003, hep-ex/0301017.

[52] S. T. Petcov, "Towards complete neutrino mixing matrix and CP-violation," *Nucl. Phys. Proc. Suppl.*, vol. 143, pp. 159–166, 2005, hep-ph/0412410.

[53] A. Bandyopadhyay, S. Choubey, S. Goswami, S. T. Petcov, and D. P. Roy, "Update of the solar neutrino oscillation analysis with the 766-Ty KamLAND spectrum," *Phys. Lett.*, vol. B608, pp. 115–129, 2005, hep-ph/0406328.

[54] M. C. Gonzalez-Garcia and M. Maltoni, "Status of global analysis of neutrino oscillation data," 2004, hep-ph/0406056.

[55] J. N. Bahcall, M. C. Gonzalez-Garcia, and C. Pena-Garay, "Solar neutrinos before and after Neutrino 2004," *JHEP*, vol. 08, p. 016, 2004, hep-ph/0406294.

[56] C. Aalseth *et al.*, "Neutrinoless double beta decay and direct searches for neutrino mass," 2004, hep-ph/0412300. Part of APS study on neutrino physics.

[57] H. V. Klapdor-Kleingrothaus, I. V. Krivosheina, A. Dietz, and O. Chkvorets, "Search for neutrinoless double beta decay with enriched Ge-76 in Gran Sasso 1990-2003," *Phys. Lett.*, vol. B586, pp. 198–212, 2004, hep-ph/0404088.

[58] C. Weinheimer, "Direct neutrino mass experiments: Present and future," *Nucl. Phys. Proc. Suppl.*, vol. 118, pp. 279–286, 2003.

[59] A. Osipowicz *et al.*, "KATRIN: A next generation tritium beta decay experiment with sub-eV sensitivity for the electron neutrino mass," 2001, hep-ex/0109033.

[60] S. R. Elliott and J. Engel, "Double beta decay," *J. Phys.*, vol. G30, p. R183, 2004, hep-ph/0405078.

[61] C. Giunti, "Phenomenology of absolute neutrino masses," 2004, hep-ph/0412148.

[62] H. V. Klapdor-Kleingrothaus *et al.*, "Latest results from the Heidelberg-Moscow double-beta-decay experiment," *Eur. Phys. J.*, vol. A12, pp. 147–154, 2001, hep-ph/0103062.

[63] H. V. Klapdor-Kleingrothaus, "From nuclear physics to physics beyond the standard model: first evidence for lepton number violation and the Majorana character of neutrinos," *Int. J. Mod. Phys.*, vol. D13, pp. 2107–2126, 2004.

[64] C. Albright *et al.*, "The neutrino factory and beta beam experiments and development," 2004, physics/0411123.

[65] R. N. Mohapatra *et al.*, "Theory of neutrinos," 2004, hep-ph/0412099. Part of the APS neutrino study.

[66] H. Bethe, "Energy production in stars," *Phys. Rev.*, vol. 55, p. 436, 1939.

[67] L. C. Stonehill, J. A. Formaggio, and R. G. H. Robertson, "Solar neutrinos from CNO electron capture," *Phys. Rev.*, vol. C69, p. 015801, 2004, hep-ph/0309266.

[68] J. N. Bahcall, M. H. Pinsonneault, S. Basu, and J. Christensen-Dalsgaard, "Are standard solar models reliable?," *Phys. Rev. Lett.*, vol. 78, pp. 171–174, 1997, astro-ph/9610250.

[69] J. N. Bahcall, A. M. Serenelli, and S. Basu, "New solar opacities, abundances, helioseismology, and neutrino fluxes," *Astrophys. J.*, vol. 621, pp. L85–L88, 2005, astro-ph/0412440.

[70] B. T. Cleveland *et al.*, "Measurement of the solar electron neutrino flux with the Homestake chlorine detector," *Astrophys. J.*, vol. 496, pp. 505–526, 1998.

[71] J. N. Bahcall, "Solar models and solar neutrinos: Current status," 2004, hep-ph/0412068.

[72] C. Cattadori, N. Ferrari, and L. Pandola, "Results from radiochemical experiments with main emphasis on the gallium ones," *Nucl. Phys. Proc. Suppl.*, vol. 143, pp. 3–12, 2005.

[73] V. N. Gavrin, "Measurement of the solar neutrino capture rate in SAGE and the value of the pp-neutrino flux at the earth," *Nucl. Phys. Proc. Suppl.*, vol. 138, pp. 87–90, 2005.

[74] M. Altmann *et al.*, "Complete results for five years of GNO solar neutrino observations," 2005, hep-ex/0504037.

216

[75] Y. Fukuda *et al.*, "Solar neutrino data covering solar cycle 22," *Phys. Rev. Lett.*, vol. 77, pp. 1683–1686, 1996.

[76] S. Fukuda *et al.*, "Determination of solar neutrino oscillation parameters using 1496 days of Super-Kamiokande-I data," *Phys. Lett.*, vol. B539, pp. 179–187, 2002, hep-ex/0205075.

[77] L. Wolfenstein, "Oscillations among three neutrino types and CP violation," *Phys. Rev.*, vol. D18, pp. 958–960, 1978.

[78] S. Mikheyev and A. Y. Smirnov *Sov. J. Nucl. Phys.*, vol. 42, p. 913, 1985.

[79] E. K. Akhmedov, M. A. Tortola, and J. W. F. Valle, "A simple analytic three-flavour description of the day- night effect in the solar neutrino flux," *JHEP*, vol. 05, p. 057, 2004, hep-ph/0404083.

[80] P. C. de Holanda, W. Liao, and A. Y. Smirnov, "Toward precision measurements in solar neutrinos," *Nucl. Phys.*, vol. B702, pp. 307–332, 2004, hep-ph/0404042.

[81] A. M. Dziewonski and D. L. Anderson, "Preliminary reference earth model," *Phys. Earth Planet. Interiors*, vol. 25, pp. 297–356, 1981.

[82] E. Lisi and D. Montanino, "Earth regeneration effect in solar neutrino oscillations: an analytic approach," *Phys. Rev.*, vol. D56, pp. 1792–1803, 1997, hep-ph/9702343.

[83] M. C. Gonzalez-Garcia, C. Pena-Garay, and A. Y. Smirnov, "Zenith angle distributions at Super-Kamiokande and SNO and the solution of the solar neutrino problem," *Phys. Rev.*, vol. D63, p. 113004, 2001, hep-ph/0012313.

[84] M. Blennow, T. Ohlsson, and H. Snellman, "Day-night effect in solar neutrino oscillations with three flavors," *Phys. Rev.*, vol. D69, p. 073006, 2004, hep-ph/0311098.

[85] C.-W. Chiang and L. Wolfenstein, "The sign of the day-night asymmetry for solar neutrinos," *Phys. Rev.*, vol. D63, p. 057303, 2001, hep-ph/0010213.

[86] C. Giunti, M. C. Gonzalez-Garcia, and C. Pena-Garay, "Four-neutrino oscillation solutions of the solar neutrino problem," *Phys. Rev.*, vol. D62, p. 013005, 2000, hep-ph/0001101.

[87] J. N. Bahcall, M. C. Gonzalez-Garcia, and C. Pena-Garay, "Solar neutrinos before and after KamLAND," *JHEP*, vol. 02, p. 009, 2003, hep-ph/0212147.

[88] M. Cirelli, G. Marandella, A. Strumia, and F. Vissani, "Probing oscillations into sterile neutrinos with cosmology, astrophysics and experiments," *Nucl. Phys.*, vol. B708, pp. 215–267, 2005, hep-ph/0403158.

[89] J. Boger *et al.*, "The Sudbury Neutrino Observatory," *Nucl. Instrum. Meth.*, vol. A449, pp. 172–207, 2000, nucl-ex/9910016.

[90] F. Duncan, M. Chen, *et al.*, "The QPhysics package," SNO internal C++-based MSW and physics interpretation package.

[91] J. N. Bahcall, "Neutrino astrophysics," Cambridge, UK: Univ. Pr. (1989) 567p.

[92] M. Butler, J.-W. Chen, and X. Kong, "Neutrino deuteron scattering in effective field theory at next-to-next-to-leading order," *Phys. Rev.*, vol. C63, p. 035501, 2001, nucl-th/0008032.

[93] I. Blevis *et al.*, "Measurement of Rn-222 dissolved in water at the Sudbury Neutrino Observatory," *Nucl. Instrum. Meth.*, vol. A517, pp. 139–153, 2004, nucl-ex/0305022.

[94] T. C. Andersen *et al.*, "A radium assay technique using hydrous titanium oxide adsorbent for the Sudbury Neutrino Observatory," *Nucl. Instrum. Meth.*, vol. A501, pp. 386–398, 2003, nucl-ex/0208015.

[95] T. C. Andersen *et al.*, "Measurement of radium concentration in water with Mn-coated beads at the Sudbury Neutrino Observatory," *Nucl. Instrum. Meth.*, vol. A501, pp. 399–417, 2003, nucl-ex/0208010.

[96] D. F. Cowen *et al.*, "The Sudbury Neutrino Observatory electronics chain," *IEEE Trans. Nucl. Sci.*, vol. 42, pp. 925–932, 1995.

[97] J. R. Klein, M. S. Neubauer, R. Van Berg, and F. Newcomer, "The SNO trigger system," SNO Technical report SNO-STR-97-036, University of Pennsylvania.

[98] M. Neubauer, "Evidence for electron neutrino flavor change through measurement of the $^8$B solar neutrino flux at the sudbury neutrino observatory," 2001. Ph.D Thesis, University of Pennsylvania.

[99] J. Orrell, "The 50 MHz clock document," Dec. 2000. SNO internal document.

[100] M. R. Dragowsky *et al.*, "The N-16 calibration source for the Sudbury Neutrino Observatory," *Nucl. Instrum. Meth.*, vol. A481, pp. 284–296, 2002, nucl-ex/0109011.

[101] N. J. Tagg *et al.*, "The Li-8 calibration source for the Sudbury Neutrino Observatory," *Nucl. Instrum. Meth.*, vol. A489, pp. 178–188, 2002, nucl-ex/0202024.

[102] A. W. P. Poon *et al.*, "A compact H-3(p,gamma)He-4 19.8-MeV gamma-ray source for energy calibration at the Sudbury Neutrino Observatory," *Nucl. Instrum. Meth.*, vol. A452, pp. 115–129, 2000, physics/9910011.

[103] W. R. Nelson, H. Hirayama, and D. W. O. Rogers, "The EGS4 code system," 1985. SLAC-0265.

[104] "MCNP: A general Monte Carlo N-particle transport code," http://laws.lanl.gov/x5/MCNP/index.html.

[105] A. Kling, F. Barao, M. Nakagawa, L. Tavora, and P. Vaz, "Advanced Monte Carlo for radiation physics, particle transport simulation and applications. Proceedings, Conference, MC2000, Lisbon, Portugal, October 23-26, 2000,"

[106] N. McCauley, "Producing a background free data set for measurement of the charge current flux and day-night asymmetry at the Sudbury Neutrino Observatory," 2001. Ph.D Thesis, Oxford University.

[107] A. Marino, "Evidence for neutrino oscillations in the Sudbury Neutrino Observatory," 2004. Ph.D Thesis, University of California, Berkeley.

[108] V. Rusu, "Measurement of the total $^8$B solar neutrino flux at the Sudbury Neutrino Observatory," 2003. Ph.D Thesis, University of Pennsylvania.

[109] J. Formaggio, "An analysis of high multiplicity events in the extended salt data set," Dec. 2004. SNO internal report.

[110] M. Boulay, "Direct evidence for weak flavor mixing with the Sudbury Neutrino Observatory," 2001. Ph.D Thesis, Queen's University.

[111] J. Dunmore, "Separation of CC and NC events in the Sudbury Neutrino Observatory," 2004. Ph.D Thesis, Oxford University.

[112] S. Oser, "Day-night background summary," Jan. 2005. SNO internal report.

[113] K. Graham, "Energy response for the salt phase," 2004. SNO Internal Document.

[114] K. Miknaitis and A. Hallin, "Vertex shift studies using $^{16}$n in the salt phase," Sept. 2003. SNO internal report.

[115] K. Graham, "Vertex scale note for the 391-day paper," May 2004. SNO internal report.

[116] M. Boulay, J. Klein, K. Miknaitis, and A. Poon, "Checks on reconstruction using the AV location," Sept. 2003. SNO internal report.

[117] K. Graham, "Angular resolution update," May 2004. SNO internal report.

[118] A. Hime, N. Jelley, M. Kos, J. Loach, J. Maneira, and B. Nickel, "Neutron detection efficiency for the complete salt data set," Dec. 2004. SNO internal report.

[119] J. Wilson, "A measurement of the $^8$B solar neutrino energy spectrum at the Sudbury Neutrino Observatory," 2004. Ph.D Thesis, Oxford University.

[120] M. Dunford, J. Dunmore, A. Marino, N. McCauley, and C. Sims, "Data cleaning document for the salt phase," Feb. 2004. SNO internal report.

[121] S. Oser, "Worst case drift models for salt," 2004. SNO internal report.

[122] K. Graham, "Directional uncertainties for salt," Apr. 2004. SNO internal report.

[123] J. Wendland, "Diurnal studies of radioactive backgrounds during the sno salt phase," Mar. 2004. SNO internal report.

[124] J. Formaggio and K. Miknaitis, "Muon followers during the salt phase," Apr. 2004. SNO internal report.

[125] J. Orrell, "A search for an electron antineutrino signal in the Sudbury Neutrino Observatory," 2004. Ph.D Thesis, University of Washington.

[126] Q. Ahmad, "Muon correlated background at the Sudbury Neutrino Observatory," 2002. Ph.D Thesis, Brown University.

[127] J. N. Bahcall, M. H. Pinsonneault, and S. Basu, "Solar models: Current epoch and time dependences, neutrinos, and helioseismological properties," *Astrophys. J.*, vol. 555, pp. 990–1012, 2001, astro-ph/0010346.

[128] J. N. Bahcall and M. H. Pinsonneault, "What do we (not) know theoretically about solar neutrino fluxes?," *Phys. Rev. Lett.*, vol. 92, p. 121301, 2004, astro-ph/0402114.

[129] S. N. Ahmed *et al.*, "Measurement of the total active B-8 solar neutrino flux at the sudbury neutrino observatory with enhanced neutral current sensitivity," *Phys. Rev. Lett.*, vol. 92, p. 181301, 2004, nucl-ex/0309004.

[130] G. Cowan, "Statistical data analysis," Oxford, UK: Clarendon (1998) 197 p.

[131] F. James and M. Roos, "'MINUIT' a system for function minimization and analysis of the parameter errors and correlations," *Comput. Phys. Commun.*, vol. 10, pp. 343–367, 1975.

[132] R. Brun and F. Rademakers, "ROOT: An object oriented data analysis framework," *Nucl. Instrum. Meth.*, vol. A389, pp. 81–86, 1997.

[133] K. Graham, "Bias studies for the salt paper," 2004. SNO internal report.

[134] R. Robertson, "Solar neutrino interactions with $^{17}$O and $^{18}$O in SNO," Apr. 2003. SNO internal report.

[135] R. Robertson, "Target properties," May 2003. SNO internal report.

[136] J. F. Beacom and S. J. Parke, "On the normalization of the neutrino deuteron cross section," *Phys. Rev.*, vol. D64, p. 091302, 2001, hep-ph/0106128.

[137] S. Nakamura, T. Sato, V. Gudkov, and K. Kubodera, "Neutrino reactions on deuteron," *Phys. Rev.*, vol. C63, p. 034617, 2001, nucl-th/0009012.

[138] S. Nakamura *et al.*, "Neutrino deuteron reactions at solar neutrino energies," *Nucl. Phys.*, vol. A707, pp. 561–576, 2002, nucl-th/0201062.

[139] A. Kurylov, M. J. Ramsey-Musolf, and P. Vogel, "Radiative corrections in neutrino deuterium disintegration," *Phys. Rev.*, vol. C65, p. 055501, 2002, nucl-th/0110051.

[140] Q. R. Ahmad *et al.*, "Measurement of day and night neutrino energy spectra at SNO and constraints on neutrino mixing parameters," *Phys. Rev. Lett.*, vol. 89, p. 011302, 2002, nucl-ex/0204009.

[141] F. James and M. Roos, "Errors on ratios of small numbers of events," *Nucl. Phys.*, vol. B172, p. 475, 1980.

[142] M. B. Smy *et al.*, "Precise measurement of the solar neutrino day/night and seasonal variation in super-kamiokande-i," *Phys. Rev.*, vol. D69, p. 011104, 2004, hep-ex/0309011.

[143] R. Barlow, "Asymmetric systematic errors," 2003, physics/0306138.

[144] M. Smith, "An investigation of matter enhanced neutrino oscillation with the Sudbury Neutrino Observatory," 2002. Ph.D Thesis, University of Washington.

Appendix A

## STATISTICAL ERROR PROPAGATION

Several calculations in this thesis require manipulating the error matrices computed in the fit for standard error propagation. To clarify the procedures used for calculating uncertainties and covariances, the equations used are summarized here.

*A.0.4   Errors and Covariances for CC and ES results in Energy-Unconstrained Analyses*

In the energy-unconstrained analyses, we construct the CC and ES day and night fluxes in terms of the bin-by-bin CC and ES results for day and night:

$$
\begin{aligned}
\text{CC\_d} &= \sum_i \text{CC\_d}_i; \;\; \text{CC\_n} = \sum_i \text{CC\_n}_i \\
\text{ES\_d} &= \sum_i \text{ES\_d}_i; \;\; \text{ES\_n} = \sum_i \text{ES\_n}_i
\end{aligned}
\tag{A.1}
$$

Here, CC_d is the total CC day flux, equal to the sum of the CC fluxes in each energy bin, $\text{CC\_d}_i$, and so on. Standard error propagation dictates that we compute the statistical uncertainty on the total day and night CC and ES fluxes as follows:

$$
\delta \text{CC\_d}^2 = \sum_i \sum_j \left( \frac{\partial \text{CC\_d}}{\partial \text{CC\_d}_i} \right) \left( \frac{\partial \text{CC\_d}}{\partial \text{CC\_d}_j} \right) \delta \text{CC\_d}_i \delta \text{CC\_d}_j
\tag{A.2}
$$

For calculating the covariances between parameters, the error propagation equation reduces to:

$$
\delta \text{CC\_d} \delta \text{ES\_d} = \sum_i \sum_j \left( \frac{\partial \text{CC\_d}}{\partial \text{CC\_d}_i} \right) \left( \frac{\partial \text{ES\_d}}{\partial \text{ES\_d}_j} \right) \delta \text{CC\_d}_i \delta \text{ES\_d}_j
\tag{A.3}
$$

and so forth.

In general, the correlations quoted in the tables in this document are the standard correlation coefficients calculated by taking, for parameters A and B,

$$
\rho_{AB} = \frac{\sigma_{AB}^2}{\sigma_A \sigma_B}
\tag{A.4}
$$

where $\sigma_{AB}^2$ is the error matrix element representing the covariance of parameters A and B.

### A.0.5  Error Propagation for Asymmetry Parameters

In the salt analysis, we extract three neutrino signals (CC, NC, ES) and compute asymmetry parameters for each. For each signal we extract either fluxes or event rates day and night:

$$N_x, D_x \quad x = NC, \, CC, \, ES, \, EXTN. \tag{A.5}$$

We then have an $8 \times 8$ error matrix:

$$\begin{pmatrix} \sigma_N^2 & (\sigma_{DN}^2)^T \\ \sigma_{DN}^2 & \sigma_D^2 \end{pmatrix} \tag{A.6}$$

Where each sub-matrix is $4 \times 4$. In the neutral-current constrained fits, in which the day and night fluxes are extracted simultaneously, the correlations between the constrained NC flux and other parameters can introduce covariances between day and night flux parameters. So in these fits it's possible for the cross terms between day and night to be non-zero.

We define two parameters to characterize the difference between the day and night values, $\Delta_x$ and $A_x$ for x = NC, CC, ES:

$$\begin{aligned} \Delta_x &= N_x - D_x \\ A_x &= 2\frac{N_x - D_x}{N_x + D_x} \end{aligned} \tag{A.7}$$

standard error propagation results in the following expressions for the errors and covariances:

$$\begin{aligned} (\sigma_\Delta^2)_{xy} &= (\sigma_N^2 + \sigma_D^2 - (\sigma_{DN}^2)^T - \sigma_{DN}^2)_{xy} & \text{(A.8)} \\ (\sigma_A^2)_{xy} &= (1 - \frac{A_x^2}{4})(1 - \frac{A_y^2}{4}) \times \left( \frac{(\sigma_D^2)_{xy}}{D_x D_y} + \frac{(\sigma_N^2)_{xy}}{N_x N_y} - \frac{(\sigma_{ND}^2)_{xy}}{N_x D_y} - \frac{(\sigma_{ND}^2)_{xy}^T}{D_x N_y} \right) & \text{(A.9)} \end{aligned}$$

Appendix B

## SHIFTS IN DAY-NIGHT RESULTS DUE TO SYSTEMATIC UNCERTAINTIES

To propagate systematic uncertainties in response parameters, each parameter is perturbed in the Monte Carlo according to its estimated $\pm 1\sigma$ uncertainties. The PDFs used in the analysis are re-built, and the fits are repeated. These perturbations can affect the final results through changes in the PDF shapes, as well as changes in the numbers of Monte Carlo events that are accepted by the fiducial volume and energy threshold cuts. Systematic uncertainties in backgrounds are propagated by changing the numbers of background events included in the signal extraction fits or varying the number of background events subtracted from each signal class after the fit results are obtained.

The tables in this appendix give the shifts in each day and night extracted signal parameter for perturbations in detector response or background levels. For the NC-unconstrained cases, the day and night fits extract the numbers of events for each signal class in the salt data set. The numbers of CC, NC, and ES events are then converted to equivalent neutrino fluxes, using the predicted numbers of events for the Standard Solar Model. The tables below give the shifts in the extracted numbers of events as well as the neutrino fluxes and day-night asymmetries due to each systematic shift. For the NC-unconstrained cases, the signal extraction is performed in terms of the neutrino fluxes for the CC, NC, and ES signals, as well as the number of events for the external neutron background (EXTN). For the NC-constrained fits, tables are given only for the shifts in the fluxes and asymmetries, and not for numbers of events.

Note that, occasionally, both an upward and a downward shift in a particular response parameter can cause a shift of the same sign in an extracted signal. In some cases this reflects the ways that changes in the PDF shapes and normalizations affect the results. In some cases, same-sign shifts likely reflect statistical effects. When the perturbations in response

parameters are extremely small, the corresponding changes in the fit parameters may be too small to be resolved, and the shifts in the extracted parameters will be characteristic of statistical fluctuations.

For the day-night analysis, the systematic shifts in the asymmetry parameters that are given in these tables are symmetrized and added in quadrature to obtain the final systematic uncertainties. A description of the entries in the tables is below.

- *Internal Photodisintegration Background Total:* Varying the amplitude of the internal photodisintegration neutron background up and down, according to the uncertainties from Table 6.1. The up and down shifts of the amplitude are indicated by "intpd_tot_up" and "intpd_tot_down".

- *Internal Photodisintegration Background Asymmetry:* Varying the day-night asymmetry of the internal photodisintegration neutron background, according to the uncertainties from Table 6.1. The up and down shifts of the asymmetry are indicated by "intpd_asym_up" and "intpd_asym_down".

- *Other Neutron Background Total:* Varying the amplitude of the "other neutron" background source up and down. The amplitude of this background is varied according to the uncertainties given in Table 6.1. The up and down shifts of the other neutron amplitude are indicated by "othern_tot_up" and "othern_tot_down".

- *Internal Gamma Background Total:* Varying the amplitude of the internal gamma background up and down. The amplitude is varied according to the uncertainties in Table 6.1. The up and down shifts of the gamma background are indicated by "gamma_tot_up" and "gamma_tot_down".

- *Internal Gamma Background Asymmetry:* Varying the day-night asymmetry in the internal gamma background source, according to the uncertainties in Table 6.1. The up and down shifts of the asymmetry are indicated by "gamma_asym_up" and "gamma_asym_down".

- *Diurnal Energy Scale:* Varying the relative energy scale for day and night, according to the uncertainties in Table 7.3. First the energy scale is shifted up during the day and down during the night ("escale_day_up"), and then the energy scale is shifted down during the day and up during the night ("escale_night_up").

- *Directional Energy Scale:* Varying the relative energy scale for day and night CC and ES events to account for directional variations in detector response, using the uncertainties in Table 7.2. First the energy scale is shifted up during the day and down during the night for CC events, with opposite shifts for ES events ("dir_escale_day_up"). Then the energy scale is shifted down during the day and up during the night for CC events, with opposite shifts for ES events ("dir_escale_night_up").

- *Worst Case Energy Drift:* Varying the energy scale as a function of the Julian Date to simulate worst case models of energy scale drift that could alias into a day-night effect. There are two worst-case drift models, which shift the energy scale up or down in summer relative to winter. The two models are indicated by "escale_wc_1" and "escale_wc_2" corresponding to the shifts given in Table 7.1.

- *Diurnal Energy Resolution:* Varying the relative energy resolution for day and night, according to the uncertainties in Table 7.3. First the energy resolution is smeared up during the day ("eres_day_up"), and then the energy resolution is smeared up during the night ("eres_night_up").

- *Directional Energy Resolution:* Varying the relative energy resolution for day and night CC and ES events to account for directional variations in detector response, using the uncertainties in Table 7.2. First the energy resolution is smeared up during the day day for CC events and up during the night for ES events ("dir_eres_day_up") Then the energy resolution is smeared up during the night for CC events and up during the day for ES events ("dir_eres_night_up").

- *Diurnal Isotropy Mean:* Varying the relative isotropy mean for day and night, according to the uncertainty described in section 7.5. First the isotropy mean is shifted

up during the day and down during the night ("b14_day_up"), and then the isotropy mean is shifted down during the day and up during the night ("b14_night_up").

- *Worst Case Isotropy Drift:* Varying the isotropy mean as a function of the Julian Date to simulate worst case models of isotropy drift that could alias into a day-night effect. There are two worst-case drift models, which shift the isotropy mean up or down in summer relative to winter. The two models are indicated by "b14_wc_1" and "b14_wc_2" corresponding to the shifts given in Table 7.1.

- *Directional Isotropy Mean:* Varying the relative isotropy mean for day and night for CC and ES events to account for directional variations in detector response, using the uncertainties in Table 7.2. First the isotropy mean is shifted up during the day and down during the night for CC events, with opposite shifts for ES events ("dir_b14_day_up"). Then the isotropy mean is shifted down during the day and up during the night for CC events, with opposite shifts for ES events ("dir_b14_night_up").

- *Directional Radial Scaling:* Varying the relative radial scaling for events during the day and night for CC and ES to account for directional variations in detector response, using the uncertainties in Table 7.2. First the event radii are shifted up during the day and down during the night for CC events, with opposite shifts for ES events ("dir_r_scale_day_up"). Then the radii are shifted down during the day and up during the night, with opposite shifts for ES events ("dir_r_scale_night_up").

- *Diurnal Radial Scaling:* Varying the relative radial scaling for events during the day and night, according to the uncertainties in Table 7.3. First the event radii are shifted up during the day and down during the night ("r_scale_day_up"), and then the radii are shifted down during the day and up during the night ("r_scale_night_up").

- *Directional Vertex Resolution:* Varying the vertex resolution for events during the day or night for CC and ES events to account for directional variations in detector response, using the uncertainties in Table 7.2. First the event positions are smeared

during the day for CC events and during the night for ES events ("dir_vres_day_up"). Then the event positions are smeared during the night for CC events and during the day for ES events ("dir_vres_night_up").

- *Diurnal Vertex Resolution:* Varying the vertex resolution day or night, according to the uncertainties in Table 7.3. First the event positions are smeared during the day ("vres_day_up"), and then the event positions are smeared during the night ("vres_night_up").

- *Directional Angular Resolution:* Varying the angular resolution for events during the day or night for CC and ES events to account for directional variations in detector response, using the uncertainties in Table 7.2. First the event directions are smeared during the day for CC events and during the night for ES events ("dir_angres_day_up"). Then the event directions are smeared during the night for CC events and during the day for ES events ("dir_angres_night_up").

- *Internal $\beta\gamma$ Background Total:* Setting the amplitude of the internal Cherenkov background at its nominal value (with nominal day-night asymmetry) and subtracting it alternately from the CC and NC signals. The nominal values are given in Table 6.1. This is indicated in the tables below by "intbg_tot_up". The full amplitude of this background is treated as an uncertainty in this way.

- *Internal $\beta\gamma$ Background Asymmetry:* Setting the amplitude of the internal Cherenkov background at its nominal value and varying the day-night asymmetry up and down. The asymmetry is varied according to the uncertainties in Table 6.1. The up and down shifts in the asymmetry are indicated by "intbg_asym_up" and "intbg_asym_down".

- *External $\beta\gamma$ Background Total:* Setting the amplitude of the external Cherenkov background at its nominal value (with nominal day-night asymmetry) and subtracting it alternately from the CC and NC signals. The nominal values are given in Table 6.1. This is indicated in the tables below by "extbg_tot_up". The full amplitude of this background is treated as an uncertainty in this way.

- *External $\beta\gamma$ Background Asymmetry:* Setting the amplitude of the external Cherenkov background at its nominal value and varying the day-night asymmetry up and down. The uncertainty in the asymmetry is taken from Table 6.1. The up and down shifts in the asymmetry are indicated by "extbg_asym_up" and "extbg_asym_down".

- *AV Background Total:* Setting the amplitude of the "AV event" instrumental background at its nominal value (with nominal day-night asymmetry) and subtracting it alternately from the CC and NC signals. The nominal values are given in Table 6.1. This is indicated in the tables below by "AV_tot_up". The full amplitude of this background is treated as an uncertainty in this way.

- *AV Background Asymmetry:* Setting the amplitude of the "AV event" instrumental background at its nominal value and varying the day-night asymmetry up and down. The asymmetry is varied according to the uncertainties in Table 6.1. The up and down shifts of AV background asymmetry are indicated by "AV_asym_up" and "AV_asym_down".

- *Instrumental Background Total:* Setting the amplitude of the instrumental backgrounds at its nominal value (with nominal day-night asymmetry) and subtracting it alternately from the CC and NC signals. The nominal values are given in Table 6.1. This is indicated in the tables below by "inst_tot_up". The full amplitude of this background is treated as an uncertainty in this way.

- *Instrumental Background Asymmetry:* Setting the amplitude of the instrumental backgrounds at its nominal value and varying the day-night asymmetry up and down. The asymmetry is varied according to the uncertainties in Table 6.1. The up and down shifts of instrumental background asymmetry are indicated by "inst_asym_up" and "inst_asym_down".

Table B.1: Shifts in the numbers of extracted events for each different systematic shift, energy-unconstrained, NC-unconstrained analysis.

| Fit | NC_d | NC_n | CC_d | CC_n | ES_d | ES_n | EXTN_d | EXTN_n |
|---|---|---|---|---|---|---|---|---|
| intpd_tot_up | -12.1130 | -18.5900 | 0.0180 | 0.0200 | 0.0010 | -0.0030 | -0.0048 | -0.0086 |
| intpd_tot_down | 12.5390 | 19.1600 | -0.0030 | 0.0100 | 0.0000 | 0.0040 | 0.0014 | 0.0262 |
| intpd_asym_up | 7.0200 | -7.0300 | -0.0040 | 0.0200 | 0.0020 | -0.0020 | 0.0019 | -0.0049 |
| intpd_asym_down | -7.2240 | 7.1900 | 0.0100 | 0.0000 | 0.0000 | 0.0010 | -0.0028 | 0.0091 |
| othern_tot_up | -9.8720 | -12.0200 | 0.0140 | 0.0200 | 0.0000 | -0.0020 | -0.0039 | -0.0045 |
| othern_tot_down | 4.8200 | 5.8500 | -0.0040 | 0.0000 | 0.0020 | 0.0010 | 0.0018 | 0.0069 |
| gamma_tot_up | -0.5850 | -0.7200 | -1.3020 | -1.5800 | -0.0560 | -0.0650 | -0.0237 | -0.0336 |
| gamma_tot_down | 0.4250 | 0.5300 | 0.9460 | 1.1500 | 0.0410 | 0.0460 | 0.0174 | 0.0258 |
| escale_day_up | -0.6210 | 4.0400 | 1.5240 | -2.2100 | 0.1860 | -0.2490 | -1.0981 | -1.6088 |
| escale_night_up | -0.4950 | 0.7500 | 0.0320 | 1.6000 | 0.0170 | 0.1280 | 0.4451 | -2.5171 |
| dir_escale_day_up | -0.0070 | 0.4300 | 0.0830 | -0.4800 | -0.1490 | 0.0100 | 0.0746 | 0.0431 |
| dir_escale_night_up | 0.2110 | 0.1200 | -0.2890 | 0.1300 | 0.0550 | -0.1240 | 0.0206 | -0.1298 |
| escale_wc_2 | -3.4980 | 1.9000 | 1.3680 | 0.5300 | 0.2750 | -0.1500 | 1.8606 | -2.3155 |
| escale_wc_1 | -0.6530 | 0.4200 | 1.4750 | 1.5200 | 0.1540 | 0.3130 | -0.9808 | -2.2967 |
| eres_day_up | -6.1010 | 0.0000 | 1.3460 | 0.0000 | 0.0920 | 0.0000 | 4.6404 | 0.0000 |
| eres_night_up | 0.0000 | -0.9900 | 0.0000 | -3.7900 | 0.0000 | 0.7360 | 0.0000 | 4.0657 |
| dir_eres_day_up | 1.1260 | -0.0700 | -1.2410 | -0.1000 | -0.0860 | 0.1580 | 0.2017 | 0.0112 |
| dir_eres_night_up | 0.0030 | 0.6500 | 0.0110 | -0.8100 | -0.0210 | 0.0810 | 0.0046 | 0.0796 |
| b14_shift_day_up | 22.6410 | -28.7100 | -22.4640 | 26.5600 | -0.8250 | 1.6230 | -0.3592 | -0.4786 |
| b14_shift_night_up | -25.9560 | 39.3100 | 23.3860 | -30.0700 | 0.9560 | -1.2070 | 1.5829 | -8.0555 |
| b14_wc_1 | 34.3330 | 61.8200 | -33.3790 | -51.7100 | -0.9150 | -2.2060 | -1.0489 | -8.9276 |
| b14_wc_2 | 46.2040 | 50.9800 | -52.7970 | -45.7300 | -1.8490 | -1.8540 | 7.4076 | -3.4363 |
| dir_b14_shift_day_up | 1.6210 | 0.0000 | -2.1950 | 0.0000 | 0.3960 | 0.0000 | 0.1599 | 0.0000 |
| dir_b14_shift_night_up | -1.3910 | 0.0000 | 2.0120 | 0.0000 | -0.5430 | 0.0000 | -0.0715 | 0.0000 |
| dir_r_scale_day_up | 0.0890 | 0.0200 | -0.1150 | 0.0400 | 0.0640 | -0.0740 | -0.0439 | 0.0117 |
| dir_r_scale_night_up | 0.0160 | -0.0200 | 0.0390 | -0.1100 | -0.0750 | 0.1290 | 0.0157 | -0.0003 |
| r_scale_day_up | 2.4960 | -1.5600 | -1.0120 | 0.0000 | -0.1520 | -0.0200 | -1.3504 | 1.5810 |
| r_scale_night_up | -2.4310 | 2.6800 | 0.1100 | -1.1700 | 0.2760 | -0.1990 | 2.0543 | -1.3322 |
| dir_vres_day_up | 0.3390 | 0.0100 | -0.3450 | -0.2400 | -0.0160 | 0.2950 | 0.0224 | -0.0791 |
| dir_vres_night_up | 0.0190 | 0.0200 | -0.0690 | 0.0300 | 0.0690 | 0.0120 | -0.0325 | -0.0643 |
| vertex_res_day_up | 4.5890 | 0.0000 | -1.6100 | 0.0000 | 0.1110 | 0.0000 | -3.0841 | 0.0000 |
| vertex_res_night_up | 0.0000 | -1.9600 | 0.0000 | -0.6100 | 0.0000 | 0.3910 | 0.0000 | 2.1934 |
| dir_angres_day_up | 0.3740 | -0.6800 | -0.2410 | -1.8000 | -0.0030 | 2.4580 | -0.1294 | -0.0099 |
| dir_angres_night_up | -0.3950 | 0.6200 | -1.9500 | -0.6500 | 2.3750 | -0.0280 | -0.0333 | 0.0469 |
| intbg_tot_up | -1.6405 | -2.5127 | -1.6405 | -2.5127 | 0.0000 | 0.0000 | 0.0000 | 0.0000 |
| intbg_asym_up | -1.2452 | -2.8374 | -1.2452 | -2.8374 | 0.0000 | 0.0000 | 0.0000 | 0.0000 |
| intbg_asym_down | -2.0498 | -2.1766 | -2.0498 | -2.1766 | 0.0000 | 0.0000 | 0.0000 | 0.0000 |
| extbg_tot_up | -8.8026 | -7.9643 | -8.8026 | -7.9643 | 0.0000 | 0.0000 | 0.0000 | 0.0000 |
| extbg_asym_up | -8.0683 | -8.5674 | -8.0683 | -8.5674 | 0.0000 | 0.0000 | 0.0000 | 0.0000 |
| extbg_asym_down | -9.5486 | -7.3516 | -9.5486 | -7.3516 | 0.0000 | 0.0000 | 0.0000 | 0.0000 |
| AV_tot_up | -1.8865 | -3.8301 | -1.8865 | -3.8301 | 0.0000 | 0.0000 | 0.0000 | 0.0000 |
| AV_asym_up | -1.4225 | -4.2111 | -1.4225 | -4.2111 | 0.0000 | 0.0000 | 0.0000 | 0.0000 |
| AV_asym_down | -2.3643 | -3.4377 | -2.3643 | -3.4377 | 0.0000 | 0.0000 | 0.0000 | 0.0000 |
| inst_tot_up | -1.4877 | -1.2420 | -1.4877 | -1.2420 | 0.0000 | 0.0000 | 0.0000 | 0.0000 |
| inst_asym_up | -1.0116 | -1.6331 | -1.0116 | -1.6331 | 0.0000 | 0.0000 | 0.0000 | 0.0000 |
| inst_asym_down | -1.9955 | -0.8250 | -1.9955 | -0.8250 | 0.0000 | 0.0000 | 0.0000 | 0.0000 |

Table B.2: Absolute changes in extracted day and night flux parameters and asymmetries for each different systematic shift, for the energy-unconstrained, NC-unconstrained analysis.

| Fit | NC_d | NC_n | CC_d | CC_n | ES_d | ES_n | Anc | Acc | Aes |
|---|---|---|---|---|---|---|---|---|---|
| intpd_tot_up | -0.0663 | -0.0828 | 0.0000 | 0.0000 | 0.0000 | -0.0000 | -0.0027 | -0.0000 | -0.0000 |
| intpd_tot_down | 0.0687 | 0.0853 | 0.0000 | 0.0000 | 0.0000 | 0.0001 | 0.0027 | 0.0000 | 0.0000 |
| intpd_asym_up | 0.0385 | -0.0313 | 0.0000 | 0.0000 | 0.0000 | -0.0000 | -0.0141 | 0.0000 | -0.0000 |
| intpd_asym_down | -0.0396 | 0.0320 | 0.0000 | 0.0000 | -0.0000 | 0.0000 | 0.0145 | -0.0000 | 0.0000 |
| othern_tot_up | -0.0541 | -0.0536 | 0.0000 | 0.0000 | -0.0000 | -0.0000 | 0.0006 | -0.0000 | -0.0000 |
| othern_tot_down | 0.0264 | 0.0260 | 0.0000 | 0.0000 | 0.0000 | 0.0000 | -0.0003 | 0.0000 | -0.0000 |
| gamma_tot_up | -0.0032 | -0.0032 | -0.0022 | -0.0022 | -0.0010 | -0.0010 | 0.0000 | -0.0001 | 0.0001 |
| gamma_tot_down | 0.0023 | 0.0023 | 0.0016 | 0.0016 | 0.0008 | 0.0007 | -0.0000 | 0.0000 | -0.0001 |
| escale_day_up | -0.0294 | 0.0481 | -0.0015 | 0.0008 | -0.0044 | 0.0060 | 0.0151 | 0.0014 | 0.0043 |
| escale_night_up | 0.0268 | -0.0249 | 0.0043 | -0.0016 | 0.0091 | -0.0073 | -0.0102 | -0.0035 | -0.0070 |
| dir_escale_day_up | -0.0000 | 0.0020 | -0.0008 | 0.0002 | 0.0152 | -0.0187 | 0.0004 | 0.0006 | -0.0141 |
| dir_escale_night_up | 0.0012 | 0.0005 | 0.0005 | -0.0006 | -0.0153 | 0.0186 | -0.0001 | -0.0007 | 0.0141 |
| escale_wc_2 | -0.0572 | -0.0082 | -0.0034 | -0.0015 | -0.0073 | -0.0078 | 0.0100 | 0.0011 | 0.0003 |
| escale_wc_1 | -0.0067 | -0.0191 | 0.0018 | -0.0007 | 0.0014 | -0.0018 | -0.0023 | -0.0015 | -0.0013 |
| eres_day_up | -0.0316 | 0.0000 | 0.0029 | 0.0000 | 0.0033 | 0.0000 | 0.0064 | -0.0017 | -0.0015 |
| eres_night_up | 0.0000 | 0.0015 | 0.0000 | -0.0041 | 0.0000 | 0.0116 | 0.0003 | -0.0026 | 0.0045 |
| dir_eres_day_up | 0.0063 | -0.0003 | -0.0019 | -0.0001 | -0.0016 | 0.0047 | -0.0013 | 0.0010 | 0.0025 |
| dir_eres_night_up | 0.0000 | 0.0030 | 0.0000 | -0.0007 | 0.0024 | 0.0013 | 0.0006 | -0.0004 | -0.0006 |
| b14_shift_day_up | 0.1240 | -0.1279 | -0.0386 | 0.0370 | -0.0152 | 0.0253 | -0.0510 | 0.0457 | 0.0166 |
| b14_shift_night_up | -0.1422 | 0.1750 | 0.0403 | -0.0419 | 0.0175 | -0.0188 | 0.0639 | -0.0497 | -0.0152 |
| b14_wc_1 | 0.1923 | 0.2815 | -0.0574 | -0.0721 | -0.0168 | -0.0344 | 0.0146 | -0.0115 | -0.0058 |
| b14_wc_2 | 0.2588 | 0.2321 | -0.0908 | -0.0637 | -0.0339 | -0.0289 | -0.0072 | 0.0144 | 0.0042 |
| dir_b14_shift_day_up | 0.0091 | 0.0000 | -0.0038 | 0.0000 | 0.0073 | 0.0000 | -0.0018 | 0.0022 | -0.0033 |
| dir_b14_shift_night_up | -0.0078 | 0.0000 | 0.0035 | 0.0000 | -0.0100 | 0.0000 | 0.0016 | -0.0020 | 0.0045 |
| dir_r_scale_day_up | 0.0005 | 0.0001 | 0.0002 | -0.0004 | -0.0037 | 0.0042 | -0.0001 | -0.0004 | 0.0033 |
| dir_r_scale_night_up | 0.0001 | -0.0001 | -0.0004 | 0.0003 | 0.0026 | -0.0029 | -0.0000 | 0.0004 | -0.0023 |
| r_scale_day_up | 0.0315 | -0.0247 | 0.0057 | -0.0069 | 0.0056 | -0.0121 | -0.0110 | -0.0076 | -0.0072 |
| r_scale_night_up | -0.0305 | 0.0293 | -0.0069 | 0.0052 | -0.0041 | 0.0077 | 0.0117 | 0.0073 | 0.0049 |
| dir_vres_day_up | 0.0019 | 0.0001 | -0.0006 | -0.0003 | -0.0003 | 0.0029 | -0.0004 | 0.0001 | 0.0013 |
| dir_vres_night_up | 0.0001 | 0.0001 | -0.0001 | -0.0001 | -0.0004 | 0.0002 | -0.0000 | 0.0000 | 0.0002 |
| vertex_res_day_up | 0.0280 | 0.0000 | -0.0026 | 0.0000 | 0.0007 | 0.0000 | -0.0056 | 0.0015 | -0.0003 |
| vertex_res_night_up | 0.0000 | -0.0074 | 0.0000 | -0.0009 | 0.0000 | 0.0044 | -0.0014 | -0.0006 | 0.0017 |
| dir_angres_day_up | 0.0021 | -0.0031 | -0.0007 | -0.0028 | -0.0000 | 0.0383 | -0.0010 | -0.0013 | 0.0148 |
| dir_angres_night_up | -0.0022 | 0.0028 | -0.0036 | -0.0012 | 0.0436 | -0.0004 | 0.0010 | 0.0014 | -0.0197 |
| intbg_tot_up | -0.0090 | -0.0112 | -0.0028 | -0.0035 | 0.0000 | 0.0000 | -0.0004 | -0.0005 | 0.0000 |
| intbg_asym_up | -0.0068 | -0.0127 | -0.0021 | -0.0040 | 0.0000 | 0.0000 | -0.0011 | -0.0012 | 0.0000 |
| intbg_asym_down | -0.0112 | -0.0097 | -0.0035 | -0.0030 | 0.0000 | 0.0000 | 0.0004 | 0.0002 | 0.0000 |
| extbg_tot_up | -0.0482 | -0.0355 | -0.0151 | -0.0111 | 0.0000 | 0.0000 | 0.0030 | 0.0020 | 0.0000 |
| extbg_asym_up | -0.0442 | -0.0382 | -0.0139 | -0.0119 | 0.0000 | 0.0000 | 0.0016 | 0.0007 | 0.0000 |
| extbg_asym_down | -0.0523 | -0.0328 | -0.0164 | -0.0102 | 0.0000 | 0.0000 | 0.0044 | 0.0033 | 0.0000 |
| AV_tot_up | -0.0103 | -0.0171 | -0.0032 | -0.0053 | 0.0000 | 0.0000 | -0.0013 | -0.0014 | 0.0000 |
| AV_asym_up | -0.0078 | -0.0188 | -0.0024 | -0.0059 | 0.0000 | 0.0000 | -0.0021 | -0.0022 | 0.0000 |
| AV_asym_down | -0.0130 | -0.0153 | -0.0041 | -0.0048 | 0.0000 | 0.0000 | -0.0004 | -0.0006 | 0.0000 |
| inst_tot_up | -0.0082 | -0.0055 | -0.0026 | -0.0017 | 0.0000 | 0.0000 | 0.0006 | 0.0004 | 0.0000 |
| inst_asym_up | -0.0055 | -0.0073 | -0.0017 | -0.0023 | 0.0000 | 0.0000 | -0.0003 | -0.0004 | 0.0000 |
| inst_asym_down | -0.0109 | -0.0037 | -0.0034 | -0.0011 | 0.0000 | 0.0000 | 0.0015 | 0.0013 | 0.0000 |

Table B.3: Shifts in the numbers of extracted events for each different systematic shift, for the energy-constrained, NC-unconstrained analysis.

| Fit | NC_d | NC_n | CC_d | CC_n | ES_d | ES_n | EXTN_d | EXTN_n |
|---|---|---|---|---|---|---|---|---|
| intpd_tot_up | -12.1290 | -18.6000 | -0.0800 | -0.2000 | -0.0040 | -0.0150 | 0.0419 | 0.1730 |
| intpd_tot_down | 12.6560 | 19.2600 | 0.0300 | 0.0100 | 0.0020 | 0.0010 | -0.1026 | -0.0017 |
| intpd_asym_up | 7.0760 | -7.0200 | 0.0200 | -0.0100 | 0.0010 | -0.0010 | -0.0503 | -0.0023 |
| intpd_asym_down | -7.2450 | 7.0700 | -0.0400 | 0.0400 | -0.0020 | -0.0150 | 0.0296 | 0.0727 |
| othern_tot_up | -9.8930 | -12.1500 | -0.0600 | -0.1400 | -0.0030 | -0.0110 | 0.0373 | 0.2435 |
| othern_tot_down | 4.8560 | 5.8200 | 0.0200 | 0.0400 | 0.0010 | -0.0160 | -0.0326 | 0.0560 |
| gamma_tot_up | -1.3200 | -1.6000 | -0.5100 | -0.5800 | -0.0620 | -0.0800 | -0.0655 | -0.0850 |
| gamma_tot_down | 0.9640 | 1.1600 | 0.3800 | 0.4200 | 0.0440 | 0.0590 | 0.0446 | 0.0617 |
| escale_day_up | 4.8250 | -2.3300 | -4.0520 | 5.2300 | 0.2610 | -1.0570 | -1.0380 | -1.7681 |
| escale_night_up | -4.6810 | 6.9300 | 5.2100 | -4.6000 | -0.6800 | -0.1470 | 0.1691 | -2.1182 |
| dir_escale_day_up | 0.3920 | -0.1300 | 0.1500 | 0.3000 | -0.7990 | -0.3540 | 0.2477 | 0.1710 |
| dir_escale_night_up | -0.4170 | 0.4200 | 0.2500 | -0.0400 | 0.1740 | -0.2600 | -0.0125 | -0.1161 |
| escale_wc_2 | 3.6120 | 5.5600 | -5.9310 | -2.5500 | 0.1360 | -1.2580 | 2.1504 | -1.7121 |
| escale_wc_1 | 0.8350 | 5.5600 | 0.5700 | -3.6500 | -0.4690 | 0.1910 | -0.9330 | -2.0452 |
| eres_day_up | -3.6470 | 0.0000 | -0.9000 | 0.0000 | -0.5500 | 0.0000 | 5.0946 | 0.0000 |
| eres_night_up | 0.0000 | -0.2600 | 0.0000 | -4.5300 | 0.0000 | 0.3020 | 0.0000 | 4.4624 |
| dir_eres_day_up | 0.6120 | -0.3100 | -0.6600 | -0.2900 | -0.1420 | 0.4590 | 0.1831 | 0.1324 |
| dir_eres_night_up | 0.5370 | 0.5800 | -1.4800 | -0.6200 | 0.8820 | -0.0560 | 0.0553 | 0.0901 |
| b14_shift_day_up | 13.5850 | -17.5500 | -12.2920 | 12.5100 | -1.3060 | 3.8870 | -0.9266 | 0.2051 |
| b14_shift_night_up | -16.3560 | 27.9000 | 12.9100 | -19.8000 | 1.1450 | 0.6330 | 2.2858 | -8.5017 |
| b14_wc_1 | 20.8560 | 42.8800 | -19.1190 | -31.9500 | -0.6650 | -1.8760 | -1.9648 | -10.0440 |
| b14_wc_2 | 24.5950 | 33.6600 | -28.2990 | -28.6100 | -3.5260 | -0.4800 | 6.2745 | -4.2481 |
| dir_b14_shift_day_up | 0.5220 | 1.1400 | 0.7300 | -3.0900 | -1.3290 | 1.9970 | 0.0661 | -0.0437 |
| dir_b14_shift_night_up | -0.1440 | -0.7800 | 0.4700 | 0.0100 | -0.1620 | 0.8740 | -0.1649 | -0.0997 |
| dir_r_scale_day_up | 0.1170 | -0.0300 | -0.1000 | 0.0300 | 0.0240 | -0.0070 | -0.0477 | 0.0117 |
| dir_r_scale_night_up | 0.0110 | -0.0200 | 0.0500 | -0.1100 | -0.1100 | 0.1380 | 0.0470 | -0.0075 |
| r_scale_day_up | 2.2330 | -1.6500 | -0.8900 | 0.0600 | -0.1040 | -0.0720 | -1.2243 | 1.6296 |
| r_scale_night_up | -2.4100 | 2.5500 | 0.1300 | -0.9000 | 0.2250 | -0.1840 | 2.0437 | -1.4178 |
| dir_vres_day_up | 0.2530 | -0.1300 | -0.2700 | -0.0300 | -0.0030 | 0.2310 | 0.0156 | -0.0770 |
| dir_vres_night_up | -0.0700 | 0.1200 | -0.1100 | -0.0700 | 0.2240 | 0.0180 | -0.0495 | -0.0740 |
| vertex_res_day_up | 3.7980 | 0.0000 | -1.1700 | 0.0000 | 0.4810 | 0.0000 | -3.0658 | 0.0000 |
| vertex_res_night_up | 0.0000 | -2.2300 | 0.0000 | -0.5200 | 0.0000 | 0.1770 | 0.0000 | 2.5366 |
| dir_angres_day_up | -0.0180 | -1.0800 | 0.2000 | -1.2400 | -0.0230 | 2.3800 | -0.1607 | -0.0544 |
| dir_angres_night_up | -0.6270 | 0.2000 | -1.9600 | -0.2300 | 2.6470 | -0.0010 | -0.0525 | 0.0307 |
| intbg_tot_up | -1.6405 | -2.5127 | -1.6405 | -2.5127 | 0.0000 | 0.0000 | 0.0000 | 0.0000 |
| intbg_asym_up | -1.2452 | -2.8374 | -1.2452 | -2.8374 | 0.0000 | 0.0000 | 0.0000 | 0.0000 |
| intbg_asym_down | -2.0498 | -2.1766 | -2.0498 | -2.1766 | 0.0000 | 0.0000 | 0.0000 | 0.0000 |
| extbg_tot_up | -8.8026 | -7.9643 | -8.8026 | -7.9643 | 0.0000 | 0.0000 | 0.0000 | 0.0000 |
| extbg_asym_up | -8.0683 | -8.5674 | -8.0683 | -8.5674 | 0.0000 | 0.0000 | 0.0000 | 0.0000 |
| extbg_asym_down | -9.5486 | -7.3516 | -9.5486 | -7.3516 | 0.0000 | 0.0000 | 0.0000 | 0.0000 |
| AV_tot_up | -1.8865 | -3.8301 | -1.8865 | -3.8301 | 0.0000 | 0.0000 | 0.0000 | 0.0000 |
| AV_asym_up | -1.4225 | -4.2111 | -1.4225 | -4.2111 | 0.0000 | 0.0000 | 0.0000 | 0.0000 |
| AV_asym_down | -2.3643 | -3.4377 | -2.3643 | -3.4377 | 0.0000 | 0.0000 | 0.0000 | 0.0000 |
| inst_tot_up | -1.4877 | -1.2420 | -1.4877 | -1.2420 | 0.0000 | 0.0000 | 0.0000 | 0.0000 |
| inst_asym_up | -1.0116 | -1.6331 | -1.0116 | -1.6331 | 0.0000 | 0.0000 | 0.0000 | 0.0000 |
| inst_asym_down | -1.9955 | -0.8250 | -1.9955 | -0.8250 | 0.0000 | 0.0000 | 0.0000 | 0.0000 |

Table B.4: Absolute changes in extracted day and night flux parameters and asymmetries for each different systematic shift, for the energy-constrained, NC-unconstrained analysis.

| Fit | NC_d | NC_n | CC_d | CC_n | ES_d | ES_n | Anc | Acc | Aes |
|---|---|---|---|---|---|---|---|---|---|
| intpd_tot_up | -0.0664 | -0.0828 | -0.0001 | -0.0003 | -0.0001 | -0.0002 | -0.0032 | -0.0001 | -0.0001 |
| intpd_tot_down | 0.0693 | 0.0858 | 0.0000 | 0.0000 | 0.0000 | 0.0000 | 0.0031 | -0.0000 | -0.0000 |
| intpd_asym_up | 0.0388 | -0.0313 | 0.0000 | -0.0000 | 0.0000 | -0.0000 | -0.0146 | -0.0000 | -0.0000 |
| intpd_asym_down | -0.0397 | 0.0315 | -0.0001 | 0.0001 | -0.0000 | -0.0002 | 0.0149 | 0.0001 | -0.0001 |
| othern_tot_up | -0.0542 | -0.0541 | -0.0001 | -0.0002 | -0.0001 | -0.0002 | 0.0002 | -0.0000 | -0.0000 |
| othern_tot_down | 0.0266 | 0.0259 | 0.0000 | 0.0001 | 0.0000 | -0.0002 | -0.0002 | 0.0000 | -0.0001 |
| gamma_tot_up | -0.0072 | -0.0071 | -0.0009 | -0.0008 | -0.0011 | -0.0013 | 0.0001 | 0.0000 | -0.0000 |
| gamma_tot_down | 0.0053 | 0.0052 | 0.0006 | 0.0006 | 0.0008 | 0.0009 | -0.0000 | -0.0000 | 0.0000 |
| escale_day_up | 0.0015 | 0.0177 | -0.0111 | 0.0114 | -0.0033 | -0.0070 | 0.0032 | 0.0132 | -0.0014 |
| escale_night_up | 0.0025 | 0.0043 | 0.0132 | -0.0104 | -0.0034 | -0.0112 | 0.0003 | -0.0138 | -0.0031 |
| dir_escale_day_up | 0.0022 | -0.0006 | -0.0006 | 0.0013 | 0.0038 | -0.0236 | -0.0006 | 0.0012 | -0.0113 |
| dir_escale_night_up | -0.0023 | 0.0019 | 0.0014 | -0.0009 | -0.0138 | 0.0157 | 0.0009 | -0.0014 | 0.0124 |
| escale_wc_2 | -0.0168 | 0.0092 | -0.0161 | -0.0059 | -0.0104 | -0.0248 | 0.0053 | 0.0058 | -0.0056 |
| escale_wc_1 | 0.0017 | 0.0051 | 0.0002 | -0.0080 | -0.0101 | -0.0034 | 0.0007 | -0.0049 | 0.0030 |
| eres_day_up | -0.0179 | 0.0000 | -0.0009 | 0.0000 | -0.0085 | 0.0000 | 0.0037 | 0.0005 | 0.0037 |
| eres_night_up | 0.0000 | 0.0046 | 0.0000 | -0.0051 | 0.0000 | 0.0048 | 0.0009 | -0.0030 | 0.0019 |
| dir_eres_day_up | 0.0034 | -0.0014 | -0.0009 | -0.0004 | -0.0026 | 0.0093 | -0.0010 | 0.0003 | 0.0049 |
| dir_eres_night_up | 0.0030 | 0.0027 | -0.0025 | -0.0004 | 0.0191 | -0.0009 | -0.0001 | 0.0012 | -0.0086 |
| b14_shift_day_up | 0.0744 | -0.0781 | -0.0212 | 0.0174 | -0.0240 | 0.0606 | -0.0318 | 0.0226 | 0.0347 |
| b14_shift_night_up | -0.0896 | 0.1243 | 0.0222 | -0.0276 | 0.0210 | 0.0099 | 0.0444 | -0.0293 | -0.0051 |
| b14_wc_1 | 0.1168 | 0.1953 | -0.0329 | -0.0445 | -0.0122 | -0.0292 | 0.0146 | -0.0075 | -0.0066 |
| b14_wc_2 | 0.1378 | 0.1533 | -0.0487 | -0.0399 | -0.0648 | -0.0075 | 0.0023 | 0.0047 | 0.0256 |
| dir_b14_shift_day_up | 0.0029 | 0.0052 | 0.0013 | -0.0043 | -0.0244 | 0.0312 | 0.0004 | -0.0033 | 0.0233 |
| dir_b14_shift_night_up | -0.0008 | -0.0035 | 0.0008 | 0.0000 | -0.0030 | 0.0136 | -0.0005 | -0.0005 | 0.0068 |
| dir_r_scale_day_up | 0.0007 | -0.0001 | 0.0003 | -0.0004 | -0.0046 | 0.0051 | -0.0002 | -0.0004 | 0.0041 |
| dir_r_scale_night_up | 0.0001 | -0.0001 | -0.0004 | 0.0003 | 0.0021 | -0.0026 | -0.0000 | 0.0004 | -0.0020 |
| r_scale_day_up | 0.0296 | -0.0243 | 0.0060 | -0.0071 | 0.0068 | -0.0124 | -0.0110 | -0.0077 | -0.0080 |
| r_scale_night_up | -0.0300 | 0.0279 | -0.0070 | 0.0059 | -0.0054 | 0.0075 | 0.0118 | 0.0076 | 0.0054 |
| dir_vres_day_up | 0.0014 | -0.0005 | -0.0005 | -0.0000 | -0.0001 | 0.0020 | -0.0004 | 0.0002 | 0.0008 |
| dir_vres_night_up | -0.0004 | 0.0006 | -0.0002 | -0.0002 | 0.0024 | 0.0003 | 0.0002 | -0.0000 | -0.0009 |
| vertex_res_day_up | 0.0236 | 0.0000 | -0.0018 | 0.0000 | 0.0074 | 0.0000 | -0.0048 | 0.0011 | -0.0032 |
| vertex_res_night_up | 0.0000 | -0.0087 | 0.0000 | -0.0008 | 0.0000 | 0.0012 | -0.0017 | -0.0005 | 0.0005 |
| dir_angres_day_up | -0.0001 | -0.0049 | 0.0001 | -0.0020 | -0.0004 | 0.0371 | -0.0010 | -0.0012 | 0.0151 |
| dir_angres_night_up | -0.0035 | 0.0009 | -0.0037 | -0.0006 | 0.0486 | -0.0000 | 0.0009 | 0.0018 | -0.0210 |
| intbg_tot_up | -0.0090 | -0.0112 | -0.0028 | -0.0035 | 0.0000 | 0.0000 | -0.0004 | -0.0004 | 0.0000 |
| intbg_asym_up | -0.0068 | -0.0126 | -0.0021 | -0.0039 | 0.0000 | 0.0000 | -0.0012 | -0.0011 | 0.0000 |
| intbg_asym_down | -0.0112 | -0.0097 | -0.0035 | -0.0030 | 0.0000 | 0.0000 | 0.0004 | 0.0003 | 0.0000 |
| extbg_tot_up | -0.0482 | -0.0355 | -0.0152 | -0.0111 | 0.0000 | 0.0000 | 0.0028 | 0.00022 | 0.0000 |
| extbg_asym_up | -0.0442 | -0.0381 | -0.0139 | -0.0119 | 0.0000 | 0.0000 | 0.0014 | 0.0010 | 0.0000 |
| extbg_asym_down | -0.0523 | -0.0327 | -0.0164 | -0.0102 | 0.0000 | 0.0000 | 0.0043 | 0.0035 | 0.0000 |
| AV_tot_up | -0.0103 | -0.0170 | -0.0033 | -0.0053 | 0.0000 | 0.0000 | -0.0014 | -0.0013 | 0.0000 |
| AV_asym_up | -0.0078 | -0.0187 | -0.0025 | -0.0059 | 0.0000 | 0.0000 | -0.0022 | -0.0021 | 0.0000 |
| AV_asym_down | -0.0130 | -0.0153 | -0.0041 | -0.0048 | 0.0000 | 0.0000 | -0.0004 | -0.0005 | 0.0000 |
| inst_tot_up | -0.0082 | -0.0055 | -0.0026 | -0.0017 | 0.0000 | 0.0000 | 0.0006 | 0.0005 | 0.0000 |
| inst_asym_up | -0.0055 | -0.0073 | -0.0017 | -0.0023 | 0.0000 | 0.0000 | -0.0003 | -0.0003 | 0.0000 |
| inst_asym_down | -0.0109 | -0.0037 | -0.0034 | -0.0011 | 0.0000 | 0.0000 | 0.0015 | 0.0013 | 0.0000 |

Table B.5: Absolute changes in extracted day and night flux parameters and asymmetries for each different systematic shift, for the energy-unconstrained, NC-constrained analysis.

| Fit | phi_nc | phi_cc_d | phi_cc_n | phi_es_d | phi_es_n | EXTN_d | EXTN_n | Acc | Aes |
|---|---|---|---|---|---|---|---|---|---|
| intpd_tot_up | -0.0754 | 0.0014 | -0.0011 | 0.0006 | -0.0006 | 0.3168 | -0.3313 | -0.0015 | -0.0005 |
| intpd_tot_down | 0.0781 | -0.0014 | 0.0012 | -0.0007 | 0.0006 | -0.3290 | 0.3416 | 0.0016 | 0.0005 |
| intpd_asym_up | -0.0001 | 0.0060 | -0.0048 | 0.0025 | -0.0025 | 1.3554 | -1.3860 | -0.0065 | -0.0021 |
| intpd_asym_down | 0.0004 | -0.0062 | 0.0049 | -0.0026 | 0.0025 | -1.3992 | 1.4181 | 0.0067 | 0.0022 |
| othern_tot_up | -0.0537 | -0.0001 | 0.0000 | 0.0000 | 0.0000 | -0.0121 | 0.0064 | 0.0000 | 0.0000 |
| othern_tot_down | 0.0263 | 0.0000 | -0.0000 | 0.0000 | -0.0000 | 0.0059 | -0.0033 | -0.0000 | -0.0000 |
| gamma_tot_up | -0.0032 | -0.0022 | -0.0022 | -0.0010 | -0.0010 | -0.0236 | -0.0320 | -0.0000 | 0.0001 |
| gamma_tot_down | 0.0023 | 0.0016 | 0.0016 | 0.0008 | 0.0007 | 0.0172 | 0.0232 | 0.0000 | -0.0001 |
| escale_day_up | 0.0116 | -0.0077 | 0.0063 | -0.0069 | 0.0090 | -2.5819 | -0.1065 | 0.0085 | 0.0066 |
| escale_night_up | -0.0012 | 0.0085 | -0.0050 | 0.0114 | -0.0090 | 1.4499 | -3.5755 | -0.0081 | -0.0087 |
| dir_escale_day_up | 0.0010 | -0.0009 | 0.0004 | 0.0149 | -0.0187 | 0.0446 | 0.0256 | 0.0008 | -0.0140 |
| dir_escale_night_up | 0.0006 | 0.0006 | -0.0006 | -0.0151 | 0.0186 | 0.0402 | -0.1875 | -0.0007 | 0.0140 |
| escale_wc_2 | -0.0309 | -0.0075 | 0.0021 | -0.0089 | -0.0059 | 0.8904 | -1.3608 | 0.0058 | 0.0018 |
| escale_wc_1 | -0.0136 | 0.0029 | -0.0014 | 0.0023 | -0.0022 | -0.7513 | -2.5359 | -0.0026 | -0.0019 |
| eres_day_up | -0.0145 | 0.0002 | 0.0022 | 0.0025 | 0.0011 | 4.1377 | 0.5785 | 0.0013 | -0.0007 |
| eres_night_up | -0.0000 | 0.0000 | -0.0039 | 0.0001 | 0.0114 | 0.0014 | 4.1403 | -0.0024 | 0.0044 |
| dir_eres_day_up | 0.0024 | -0.0013 | -0.0005 | -0.0014 | 0.0047 | 0.3419 | -0.1568 | 0.0005 | 0.0024 |
| dir_eres_night_up | 0.0014 | -0.0002 | -0.0004 | 0.0023 | 0.0014 | -0.0424 | 0.1003 | -0.0002 | -0.0005 |
| b14_shift_day_up | -0.0145 | -0.0170 | 0.0197 | -0.0058 | 0.0163 | 4.5056 | -5.4890 | 0.0222 | 0.0089 |
| b14_shift_night_up | 0.0319 | 0.0132 | -0.0201 | 0.0064 | -0.0074 | -4.5501 | -1.6452 | -0.0203 | -0.0057 |
| b14_wc_1 | 0.2410 | -0.0645 | -0.0663 | -0.0198 | -0.0311 | -2.6344 | -7.1405 | -0.0025 | -0.0030 |
| b14_wc_2 | 0.2440 | -0.0884 | -0.0657 | -0.0326 | -0.0296 | 7.9912 | -3.9904 | 0.0128 | 0.0034 |
| dir_b14_shift_day_up | 0.0037 | -0.0029 | -0.0005 | 0.0084 | -0.0003 | 0.3342 | -0.2083 | 0.0014 | -0.0039 |
| dir_b14_shift_night_up | -0.0036 | 0.0029 | 0.0006 | -0.0105 | 0.0003 | -0.2092 | 0.1089 | -0.0013 | 0.0049 |
| dir_r_scale_day_up | 0.0001 | 0.0003 | -0.0003 | -0.0035 | 0.0043 | -0.0291 | -0.0349 | -0.0004 | 0.0032 |
| dir_r_scale_night_up | -0.0002 | -0.0003 | 0.0003 | 0.0026 | -0.0028 | 0.0287 | -0.0470 | 0.0004 | -0.0023 |
| r_scale_day_up | 0.0008 | 0.0104 | -0.0107 | 0.0074 | -0.0139 | -0.3003 | 0.4833 | -0.0128 | -0.0088 |
| r_scale_night_up | 0.0013 | -0.0117 | 0.0095 | -0.0058 | 0.0100 | 0.9730 | -0.1750 | 0.0129 | 0.0065 |
| dir_vres_day_up | 0.0007 | -0.0004 | -0.0004 | -0.0001 | 0.0033 | 0.0664 | -0.1597 | -0.0000 | 0.0013 |
| dir_vres_night_up | -0.0001 | -0.0000 | 0.0000 | -0.0003 | 0.0003 | -0.0185 | -0.1083 | 0.0000 | 0.0002 |
| vertex_res_day_up | 0.0124 | -0.0001 | -0.0018 | 0.0016 | -0.0010 | -2.5700 | -0.5865 | -0.0010 | -0.0011 |
| vertex_res_night_up | -0.0045 | 0.0007 | -0.0013 | 0.0004 | 0.0043 | 0.1560 | 2.0502 | -0.0012 | 0.0015 |
| dir_angres_day_up | -0.0010 | -0.0003 | -0.0031 | 0.0001 | 0.0387 | -0.0045 | -0.1204 | -0.0018 | 0.0148 |
| dir_angres_night_up | 0.0006 | -0.0041 | -0.0008 | 0.0434 | -0.0001 | -0.1305 | 0.0791 | 0.0019 | -0.0195 |
| intbg_tot_up | 0.0202 | 0.0028 | 0.0035 | 0.0000 | 0.0000 | 0.0000 | 0.0000 | 0.0005 | 0.0000 |
| intbg_asym_up | 0.0195 | 0.0021 | 0.0040 | 0.0000 | 0.0000 | 0.0000 | 0.0000 | 0.0012 | 0.0000 |
| intbg_asym_down | 0.0209 | 0.0035 | 0.0030 | 0.0000 | 0.0000 | 0.0000 | 0.0000 | -0.0002 | 0.0000 |
| extbg_tot_up | 0.0837 | 0.0151 | 0.0111 | 0.0000 | 0.0000 | 0.0000 | 0.0000 | -0.0021 | 0.0000 |
| extbg_asym_up | 0.0823 | 0.0139 | 0.0119 | 0.0000 | 0.0000 | 0.0000 | 0.0000 | -0.0009 | 0.0000 |
| extbg_asym_down | 0.0850 | 0.0164 | 0.0102 | 0.0000 | 0.0000 | 0.0000 | 0.0000 | -0.0034 | 0.0000 |
| AV_tot_up | 0.0274 | 0.0032 | 0.0053 | 0.0000 | 0.0000 | 0.0000 | 0.0000 | 0.0014 | 0.0000 |
| AV_asym_up | 0.0265 | 0.0024 | 0.0059 | 0.0000 | 0.0000 | 0.0000 | 0.0000 | 0.0022 | 0.0000 |
| AV_asym_down | 0.0283 | 0.0041 | 0.0048 | 0.0000 | 0.0000 | 0.0000 | 0.0000 | 0.0005 | 0.0000 |
| inst_tot_up | 0.0137 | 0.0026 | 0.0017 | 0.0000 | 0.0000 | 0.0000 | 0.0000 | -0.0005 | 0.0000 |
| inst_asym_up | 0.0128 | 0.0017 | 0.0023 | 0.0000 | 0.0000 | 0.0000 | 0.0000 | 0.0004 | 0.0000 |
| inst_asym_down | 0.0146 | 0.0034 | 0.0011 | 0.0000 | 0.0000 | 0.0000 | 0.0000 | -0.0013 | 0.0000 |

Table B.6: Absolute changes in extracted day and night flux parameters and asymmetries for each different systematic shift, for the energy-constrained, NC-constrained analysis.

| Fit | phi_nc | phi_cc_d | phi_cc_n | phi_es_d | phi_es_n | EXTN_d | EXTN_n | Acc | Aes |
|---|---|---|---|---|---|---|---|---|---|
| intpd_tot_up | -0.0754 | 0.0011 | -0.0008 | 0.0007 | -0.0007 | 0.4109 | -0.4404 | -0.0011 | -0.0006 |
| intpd_tot_down | 0.0787 | -0.0015 | 0.0004 | 0.0006 | -0.0001 | -0.3922 | 0.5470 | 0.0011 | -0.0003 |
| intpd_asym_up | 0.0001 | 0.0045 | -0.0035 | 0.0027 | -0.0034 | 1.7995 | -1.8270 | -0.0047 | -0.0025 |
| intpd_asym_down | 0.0004 | -0.0047 | 0.0035 | -0.0027 | 0.0034 | -1.8558 | 1.8477 | 0.0048 | 0.0026 |
| othern_tot_up | -0.0538 | -0.0000 | 0.0001 | 0.0000 | 0.0001 | -0.0231 | 0.0118 | 0.0000 | 0.0000 |
| othern_tot_down | 0.0263 | -0.0000 | -0.0000 | 0.0000 | -0.0000 | 0.0092 | -0.0109 | -0.0000 | -0.0000 |
| gamma_tot_up | -0.0105 | -0.0012 | -0.0007 | -0.0020 | -0.0017 | -0.1465 | 0.0002 | 0.0003 | 0.0002 |
| gamma_tot_down | 0.0077 | 0.0009 | 0.0005 | 0.0014 | 0.0012 | 0.1066 | -0.0011 | -0.0002 | -0.0001 |
| escale_day_up | 0.0100 | -0.0121 | 0.0124 | -0.0034 | -0.0063 | -1.3844 | -1.3878 | 0.0143 | -0.0011 |
| escale_night_up | 0.0034 | 0.0131 | -0.0103 | -0.0011 | -0.0127 | 0.2241 | -1.9494 | -0.0137 | -0.0047 |
| dir_escale_day_up | 0.0009 | -0.0005 | 0.0012 | 0.0052 | -0.0245 | 0.3780 | 0.1289 | 0.0010 | -0.0122 |
| dir_escale_night_up | 0.0002 | 0.0010 | -0.0006 | -0.0124 | 0.0151 | -0.0494 | 0.0068 | -0.0009 | 0.0115 |
| escale_wc_2 | -0.0040 | -0.0176 | -0.0045 | -0.0112 | -0.0244 | 1.5561 | -0.8948 | 0.0076 | -0.0050 |
| escale_wc_1 | 0.0029 | -0.0000 | -0.0077 | -0.0088 | -0.0047 | -0.9126 | -1.8381 | -0.0045 | 0.0020 |
| eres_day_up | -0.0075 | -0.0022 | 0.0009 | -0.0079 | 0.0000 | 4.7134 | 0.4666 | 0.0018 | 0.0035 |
| eres_night_up | 0.0025 | -0.0004 | -0.0048 | 0.0000 | 0.0044 | -0.0844 | 4.5920 | -0.0027 | 0.0017 |
| dir_eres_day_up | 0.0009 | -0.0007 | -0.0005 | -0.0011 | 0.0082 | 0.3735 | 0.0254 | 0.0001 | 0.0038 |
| dir_eres_night_up | 0.0028 | -0.0025 | -0.0003 | 0.0205 | -0.0017 | 0.1275 | 0.1101 | 0.0013 | -0.0096 |
| b14_shift_day_up | -0.0092 | -0.0115 | 0.0100 | -0.0177 | 0.0528 | 2.9496 | -4.0186 | 0.0126 | 0.0288 |
| b14_shift_night_up | 0.0278 | 0.0085 | -0.0172 | 0.0126 | 0.0203 | -3.0552 | -2.9489 | -0.0151 | 0.0028 |
| b14_wc_1 | 0.1601 | -0.0378 | -0.0408 | -0.0149 | -0.0262 | -3.8704 | -7.9523 | -0.0021 | -0.0041 |
| b14_wc_2 | 0.1451 | -0.0493 | -0.0394 | -0.0654 | -0.0074 | 5.9661 | -3.6126 | 0.0056 | 0.0260 |
| dir_b14_shift_day_up | 0.0041 | 0.0010 | -0.0040 | -0.0232 | 0.0301 | 0.0941 | 0.0377 | -0.0029 | 0.0223 |
| dir_b14_shift_night_up | -0.0021 | 0.0009 | -0.0000 | -0.0013 | 0.0128 | -0.0330 | -0.1615 | -0.0005 | 0.0057 |
| dir_r_scale_day_up | 0.0004 | 0.0002 | -0.0003 | -0.0031 | 0.0042 | 0.0396 | 0.0103 | -0.0003 | 0.0031 |
| dir_r_scale_night_up | 0.0001 | -0.0005 | 0.0004 | 0.0035 | -0.0034 | 0.1136 | 0.0111 | 0.0005 | -0.0029 |
| r_scale_day_up | 0.0002 | 0.0092 | -0.0096 | 0.0109 | -0.0165 | 0.1890 | 0.2505 | -0.0111 | -0.0115 |
| r_scale_night_up | 0.0015 | -0.0105 | 0.0089 | -0.0070 | 0.0101 | 0.6426 | 0.0937 | 0.0114 | 0.0072 |
| dir_vres_day_up | 0.0004 | -0.0004 | -0.0000 | 0.0014 | 0.0011 | 0.1326 | -0.1048 | 0.0002 | -0.0002 |
| dir_vres_night_up | 0.0003 | -0.0003 | -0.0001 | 0.0038 | -0.0005 | -0.0096 | -0.0261 | 0.0001 | -0.0019 |
| vertex_res_day_up | 0.0104 | -0.0004 | -0.0010 | 0.0099 | -0.0019 | -2.4309 | -0.5633 | -0.0004 | -0.0051 |
| vertex_res_night_up | -0.0044 | 0.0004 | -0.0011 | 0.0017 | -0.0001 | 0.2745 | 2.2883 | -0.0009 | -0.0008 |
| dir_angres_day_up | -0.0030 | 0.0003 | -0.0021 | -0.0000 | 0.0371 | -0.0128 | -0.1909 | -0.0014 | 0.0149 |
| dir_angres_night_up | -0.0000 | -0.0041 | -0.0004 | 0.0475 | 0.0010 | -0.2138 | -0.0403 | 0.0022 | -0.0202 |
| intbg_tot_up | 0.0202 | 0.0028 | 0.0035 | 0.0000 | 0.0000 | 0.0000 | 0.0000 | 0.0004 | 0.0000 |
| intbg_asym_up | 0.0195 | 0.0021 | 0.0040 | 0.0000 | 0.0000 | 0.0000 | 0.0000 | 0.0011 | 0.0000 |
| intbg_asym_down | 0.0209 | 0.0035 | 0.0030 | 0.0000 | 0.0000 | 0.0000 | 0.0000 | -0.0003 | 0.0000 |
| extbg_tot_up | 0.0837 | 0.0151 | 0.0111 | 0.0000 | 0.0000 | 0.0000 | 0.0000 | -0.0022 | 0.0000 |
| extbg_asym_up | 0.0823 | 0.0139 | 0.0119 | 0.0000 | 0.0000 | 0.0000 | 0.0000 | -0.0010 | 0.0000 |
| extbg_asym_down | 0.0850 | 0.0164 | 0.0102 | 0.0000 | 0.0000 | 0.0000 | 0.0000 | -0.0035 | 0.0000 |
| AV_tot_up | 0.0274 | 0.0032 | 0.0053 | 0.0000 | 0.0000 | 0.0000 | 0.0000 | 0.0013 | 0.0000 |
| AV_asym_up | 0.0265 | 0.0024 | 0.0059 | 0.0000 | 0.0000 | 0.0000 | 0.0000 | 0.0020 | 0.0000 |
| AV_asym_down | 0.0283 | 0.0041 | 0.0048 | 0.0000 | 0.0000 | 0.0000 | 0.0000 | 0.0005 | 0.0000 |
| inst_tot_up | 0.0137 | 0.0026 | 0.0017 | 0.0000 | 0.0000 | 0.0000 | 0.0000 | -0.0005 | 0.0000 |
| inst_asym_up | 0.0128 | 0.0017 | 0.0023 | 0.0000 | 0.0000 | 0.0000 | 0.0000 | 0.0003 | 0.0000 |
| inst_asym_down | 0.0146 | 0.0034 | 0.0011 | 0.0000 | 0.0000 | 0.0000 | 0.0000 | -0.0013 | 0.0000 |

Appendix C

# CORRELATION MATRICES FOR THE DAY AND NIGHT
# SPECTRUM RESULTS

Correlation coefficients have been tabulated for the two energy-unconstrained versions of the day-night analysis. The correlations are shown for each CC energy bin as well as the NC and ES signals and the EXTN background. Although the fit parameters include bin-by-bin amplitudes for the ES signal, the correlations have been presented with respect to the summed ES signal, for convenience. For the NC-unconstrained fits, the day and night parameters are independent. For the NC-constrained fit, the day and night parameters have some minor correlations.

The entries in the tables correspond to the correlation coefficients between each pair of fit parameters. The notation is such that, for example, "ESd" represents the day ES flux, while "ESn" represents the night flux. The parameters "CCd1" through "CCd17" represent the day fluxes in each energy bin for the CC signal, and "CCn1" through "CCn17" are the corresponding night fluxes in each energy bin. The first energy bin begins at 5.5 MeV. Energy bins are 0.5 MeV in width, except for the final bin, which extends from 13.5 to 20 MeV.

Table C.1: Correlation matrix for the day energy-unconstrained, NC-unconstrained fit.

| Signal | NCd | CCd1 | CCd2 | CCd3 | CCd4 | CCd5 | CCd6 | CCd7 | CCd8 | CCd9 |
|---|---|---|---|---|---|---|---|---|---|---|
| NCd | 1.0000 | -0.3478 | -0.3320 | -0.3281 | -0.2488 | -0.2000 | -0.1555 | -0.0877 | -0.0618 | -0.0329 |
| CCd1 | -0.3478 | 1.0000 | 0.1528 | 0.1440 | 0.1124 | 0.0865 | 0.0676 | 0.0425 | 0.0272 | 0.0135 |
| CCd2 | -0.3320 | 0.1528 | 1.0000 | 0.1459 | 0.1147 | 0.0873 | 0.0684 | 0.0440 | 0.0275 | 0.0135 |
| CCd3 | -0.3281 | 0.1440 | 0.1459 | 1.0000 | 0.1073 | 0.0824 | 0.0644 | 0.0407 | 0.0259 | 0.0129 |
| CCd4 | -0.2488 | 0.1124 | 0.1147 | 0.1073 | 1.0000 | 0.0643 | 0.0503 | 0.0322 | 0.0202 | 0.0100 |
| CCd5 | -0.2000 | 0.0865 | 0.0873 | 0.0824 | 0.0643 | 1.0000 | 0.0387 | 0.0243 | 0.0155 | 0.0078 |
| CCd6 | -0.1555 | 0.0676 | 0.0684 | 0.0644 | 0.0503 | 0.0387 | 1.0000 | 0.0190 | 0.0122 | 0.0061 |
| CCd7 | -0.0877 | 0.0425 | 0.0440 | 0.0407 | 0.0322 | 0.0243 | 0.0190 | 1.0000 | 0.0077 | 0.0037 |
| CCd8 | -0.0618 | 0.0272 | 0.0275 | 0.0259 | 0.0202 | 0.0155 | 0.0122 | 0.0077 | 1.0000 | 0.0024 |
| CCd9 | -0.0329 | 0.0135 | 0.0135 | 0.0129 | 0.0100 | 0.0078 | 0.0061 | 0.0037 | 0.0024 | 1.0000 |
| CCd10 | -0.0152 | 0.0061 | 0.0061 | 0.0058 | 0.0045 | 0.0035 | 0.0027 | 0.0017 | 0.0011 | 0.0006 |
| CCd11 | -0.0063 | 0.0030 | 0.0031 | 0.0029 | 0.0023 | 0.0017 | 0.0014 | 0.0009 | 0.0005 | 0.0003 |
| CCd12 | -0.0025 | 0.0011 | 0.0011 | 0.0010 | 0.0008 | 0.0006 | 0.0005 | 0.0003 | 0.0002 | 0.0001 |
| CCd13 | 0.0003 | 0.0001 | 0.0001 | 0.0001 | 0.0001 | 0.0000 | 0.0000 | 0.0000 | 0.0000 | 0.0000 |
| CCd14 | -0.0000 | 0.0000 | 0.0000 | 0.0000 | -0.0000 | -0.0000 | 0.0000 | 0.0000 | 0.0000 | 0.0000 |
| CCd15 | -0.0000 | -0.0000 | -0.0000 | -0.0000 | -0.0000 | 0.0000 | 0.0000 | 0.0000 | 0.0000 | 0.0000 |
| CCd16 | -0.0000 | 0.0000 | 0.0000 | 0.0000 | 0.0000 | 0.0000 | 0.0000 | 0.0000 | 0.0000 | 0.0000 |
| CCd17 | -0.0000 | 0.0000 | 0.0000 | 0.0000 | -0.0000 | 0.0000 | 0.0000 | 0.0000 | 0.0000 | -0.0000 |
| ESd | -0.0610 | -0.0695 | -0.0507 | -0.0525 | -0.0556 | -0.0637 | -0.0648 | -0.0595 | -0.0430 | -0.0495 |
| EXTNd | -0.3815 | -0.0278 | -0.0720 | -0.0337 | -0.0431 | -0.0136 | -0.0129 | -0.0306 | -0.0066 | 0.0015 |

| Signal | CCd10 | CCd11 | CCd12 | CCd13 | CCd14 | CCd15 | CCd16 | CCd17 | ESd | EXTNd |
|---|---|---|---|---|---|---|---|---|---|---|
| NCd | -0.0152 | -0.0063 | -0.0025 | 0.0003 | -0.0000 | -0.0000 | -0.0000 | -0.0000 | -0.0610 | -0.3815 |
| CCd1 | 0.0061 | 0.0030 | 0.0011 | 0.0001 | 0.0000 | -0.0000 | 0.0000 | 0.0000 | -0.0695 | -0.0278 |
| CCd2 | 0.0061 | 0.0031 | 0.0011 | 0.0001 | 0.0000 | -0.0000 | 0.0000 | 0.0000 | -0.0507 | -0.0720 |
| CCd3 | 0.0058 | 0.0029 | 0.0010 | 0.0001 | 0.0000 | -0.0000 | 0.0000 | 0.0000 | -0.0525 | -0.0337 |
| CCd4 | 0.0045 | 0.0023 | 0.0008 | 0.0001 | -0.0000 | -0.0000 | 0.0000 | -0.0000 | -0.0556 | -0.0431 |
| CCd5 | 0.0035 | 0.0017 | 0.0006 | 0.0000 | -0.0000 | 0.0000 | 0.0000 | 0.0000 | -0.0637 | -0.0136 |
| CCd6 | 0.0027 | 0.0014 | 0.0005 | 0.0000 | 0.0000 | 0.0000 | 0.0000 | 0.0000 | -0.0648 | -0.0129 |
| CCd7 | 0.0017 | 0.0009 | 0.0003 | 0.0000 | 0.0000 | 0.0000 | 0.0000 | 0.0000 | -0.0595 | -0.0306 |
| CCd8 | 0.0011 | 0.0005 | 0.0002 | 0.0000 | 0.0000 | 0.0000 | 0.0000 | 0.0000 | -0.0430 | -0.0066 |
| CCd9 | 0.0006 | 0.0003 | 0.0001 | 0.0000 | 0.0000 | 0.0000 | 0.0000 | -0.0000 | -0.0495 | 0.0015 |
| CCd10 | 1.0000 | 0.0001 | 0.0000 | 0.0000 | 0.0000 | -0.0000 | -0.0000 | 0.0000 | -0.0466 | 0.0014 |
| CCd11 | 0.0001 | 1.0000 | 0.0000 | 0.0000 | 0.0000 | 0.0000 | 0.0000 | 0.0000 | -0.0487 | -0.0021 |
| CCd12 | 0.0000 | 0.0000 | 1.0000 | 0.0000 | 0.0000 | 0.0000 | -0.0000 | 0.0000 | -0.0570 | -0.0001 |
| CCd13 | 0.0000 | 0.0000 | 0.0000 | 1.0000 | 0.0000 | -0.0000 | -0.0000 | -0.0000 | 0.0000 | -0.0010 |
| CCd14 | 0.0000 | 0.0000 | 0.0000 | 0.0000 | 1.0000 | -0.0000 | -0.0000 | -0.0000 | -0.0000 | -0.0000 |
| CCd15 | -0.0000 | 0.0000 | 0.0000 | -0.0000 | -0.0000 | 1.0000 | 0.0000 | 0.0000 | -0.0163 | 0.0000 |
| CCd16 | -0.0000 | 0.0000 | -0.0000 | -0.0000 | -0.0000 | 0.0000 | 1.0000 | -0.0000 | -0.0379 | 0.0000 |
| CCd17 | 0.0000 | 0.0000 | 0.0000 | -0.0000 | -0.0000 | 0.0000 | -0.0000 | 1.0000 | 0.0000 | 0.0000 |
| ESd | -0.0466 | -0.0487 | -0.0570 | 0.0000 | -0.0000 | -0.0163 | -0.0379 | 0.0000 | 1.0000 | -0.0147 |
| EXTNd | 0.0014 | -0.0021 | -0.0001 | -0.0010 | -0.0000 | 0.0000 | 0.0000 | 0.0000 | -0.0147 | 1.0000 |

Table C.2: Correlation matrix for the night energy-unconstrained, NC-unconstrained fit.

| Signal | NCn | CCn1 | CCn2 | CCn3 | CCn4 | CCn5 | CCn6 | CCn7 | CCn8 | CCn9 |
|---|---|---|---|---|---|---|---|---|---|---|
| NCn | 1.0000 | -0.3485 | -0.3437 | -0.3060 | -0.2669 | -0.2089 | -0.1571 | -0.1034 | -0.0545 | -0.0317 |
| CCn1 | -0.3485 | 1.0000 | 0.1580 | 0.1400 | 0.1201 | 0.0967 | 0.0671 | 0.0477 | 0.0237 | 0.0143 |
| CCn2 | -0.3437 | 0.1580 | 1.0000 | 0.1379 | 0.1183 | 0.0952 | 0.0661 | 0.0469 | 0.0234 | 0.0141 |
| CCn3 | -0.3060 | 0.1400 | 0.1379 | 1.0000 | 0.1048 | 0.0843 | 0.0586 | 0.0416 | 0.0207 | 0.0125 |
| CCn4 | -0.2669 | 0.1201 | 0.1183 | 0.1048 | 1.0000 | 0.0723 | 0.0505 | 0.0357 | 0.0178 | 0.0107 |
| CCn5 | -0.2089 | 0.0967 | 0.0952 | 0.0843 | 0.0723 | 1.0000 | 0.0404 | 0.0287 | 0.0143 | 0.0086 |
| CCn6 | -0.1571 | 0.0671 | 0.0661 | 0.0586 | 0.0505 | 0.0404 | 1.0000 | 0.0199 | 0.0101 | 0.0060 |
| CCn7 | -0.1034 | 0.0477 | 0.0469 | 0.0416 | 0.0357 | 0.0287 | 0.0199 | 1.0000 | 0.0070 | 0.0042 |
| CCn8 | -0.0545 | 0.0237 | 0.0234 | 0.0207 | 0.0178 | 0.0143 | 0.0101 | 0.0070 | 1.0000 | 0.0021 |
| CCn9 | -0.0317 | 0.0143 | 0.0141 | 0.0125 | 0.0107 | 0.0086 | 0.0060 | 0.0042 | 0.0021 | 1.0000 |
| CCn10 | -0.0138 | 0.0085 | 0.0084 | 0.0074 | 0.0062 | 0.0051 | 0.0033 | 0.0025 | 0.0012 | 0.0007 |
| CCn11 | -0.0067 | 0.0027 | 0.0027 | 0.0024 | 0.0020 | 0.0016 | 0.0012 | 0.0008 | 0.0004 | 0.0002 |
| CCn12 | -0.0010 | 0.0017 | 0.0016 | 0.0014 | 0.0012 | 0.0010 | 0.0006 | 0.0005 | 0.0002 | 0.0001 |
| CCn13 | -0.0008 | 0.0003 | 0.0003 | 0.0002 | 0.0002 | 0.0002 | 0.0001 | 0.0001 | 0.0000 | 0.0000 |
| CCn14 | 0.0001 | 0.0000 | 0.0000 | 0.0000 | 0.0000 | 0.0000 | -0.0000 | 0.0000 | 0.0000 | 0.0000 |
| CCn15 | 0.0000 | -0.0000 | -0.0000 | -0.0000 | -0.0000 | -0.0000 | 0.0000 | 0.0000 | 0.0000 | 0.0000 |
| CCn16 | 0.0000 | -0.0000 | -0.0000 | -0.0000 | -0.0000 | -0.0000 | -0.0000 | 0.0000 | -0.0000 | -0.0000 |
| CCn17 | 0.0000 | -0.0000 | -0.0000 | -0.0000 | -0.0000 | -0.0000 | 0.0000 | 0.0000 | 0.0000 | 0.0000 |
| ESn | -0.0693 | -0.0684 | -0.0463 | -0.0743 | -0.0527 | -0.0483 | -0.0489 | -0.0417 | -0.0692 | -0.0410 |
| EXTNn | -0.4069 | -0.0386 | -0.0372 | -0.0299 | -0.0164 | -0.0254 | 0.0070 | -0.0118 | 0.0002 | -0.0022 |

| Signal | CCn10 | CCn11 | CCn12 | CCn13 | CCn14 | CCn15 | CCn16 | CCn17 | ESn | EXTNn |
|---|---|---|---|---|---|---|---|---|---|---|
| NCn | -0.0138 | -0.0067 | -0.0010 | -0.0008 | 0.0001 | 0.0000 | 0.0000 | 0.0000 | -0.0693 | -0.4069 |
| CCn1 | 0.0085 | 0.0027 | 0.0017 | 0.0003 | 0.0000 | -0.0000 | -0.0000 | -0.0000 | -0.0684 | -0.0386 |
| CCn2 | 0.0084 | 0.0027 | 0.0016 | 0.0003 | 0.0000 | -0.0000 | -0.0000 | -0.0000 | -0.0463 | -0.0372 |
| CCn3 | 0.0074 | 0.0024 | 0.0014 | 0.0002 | 0.0000 | -0.0000 | -0.0000 | -0.0000 | -0.0743 | -0.0299 |
| CCn4 | 0.0062 | 0.0020 | 0.0012 | 0.0002 | 0.0000 | -0.0000 | -0.0000 | -0.0000 | -0.0527 | -0.0164 |
| CCn5 | 0.0051 | 0.0016 | 0.0010 | 0.0002 | 0.0000 | -0.0000 | -0.0000 | -0.0000 | -0.0483 | -0.0254 |
| CCn6 | 0.0033 | 0.0012 | 0.0006 | 0.0001 | -0.0000 | 0.0000 | -0.0000 | 0.0000 | -0.0489 | 0.0070 |
| CCn7 | 0.0025 | 0.0008 | 0.0005 | 0.0001 | 0.0000 | 0.0000 | 0.0000 | 0.0000 | -0.0417 | -0.0118 |
| CCn8 | 0.0012 | 0.0004 | 0.0002 | 0.0000 | 0.0000 | 0.0000 | -0.0000 | 0.0000 | -0.0692 | 0.0002 |
| CCn9 | 0.0007 | 0.0002 | 0.0001 | 0.0000 | 0.0000 | 0.0000 | -0.0000 | 0.0000 | -0.0410 | -0.0022 |
| CCn10 | 1.0000 | 0.0001 | 0.0001 | 0.0000 | 0.0000 | -0.0000 | -0.0000 | -0.0000 | 0.0016 | -0.0116 |
| CCn11 | 0.0001 | 1.0000 | 0.0000 | 0.0000 | -0.0000 | -0.0000 | -0.0000 | -0.0000 | -0.0359 | 0.0011 |
| CCn12 | 0.0001 | 0.0000 | 1.0000 | 0.0000 | 0.0000 | -0.0000 | -0.0000 | -0.0000 | 0.0003 | -0.0057 |
| CCn13 | 0.0000 | 0.0000 | 0.0000 | 1.0000 | 0.0000 | 0.0000 | -0.0000 | 0.0000 | -0.0229 | 0.0003 |
| CCn14 | 0.0000 | -0.0000 | 0.0000 | 0.0000 | 1.0000 | -0.0000 | -0.0000 | -0.0000 | -0.0139 | -0.0002 |
| CCn15 | -0.0000 | -0.0000 | -0.0000 | 0.0000 | -0.0000 | 1.0000 | -0.0000 | -0.0000 | -0.0188 | -0.0000 |
| CCn16 | -0.0000 | -0.0000 | -0.0000 | -0.0000 | -0.0000 | -0.0000 | 1.0000 | 0.0000 | -0.0085 | 0.0000 |
| CCn17 | -0.0000 | -0.0000 | -0.0000 | 0.0000 | -0.0000 | -0.0000 | 0.0000 | 1.0000 | -0.0183 | 0.0000 |
| ESn | 0.0016 | -0.0359 | 0.0003 | -0.0229 | -0.0139 | -0.0188 | -0.0085 | -0.0183 | 1.0000 | -0.0050 |
| EXTNn | -0.0116 | 0.0011 | -0.0057 | 0.0003 | -0.0002 | -0.0000 | 0.0000 | 0.0000 | -0.0050 | 1.0000 |

Table C.3: Correlation coefficients from the energy-unconstrained, NC-constrained analysis.

| Signal | NC | CCd1 | CCn1 | CCd2 | CCn2 | CCd3 | CCn3 | CCd4 | CCn4 | CCd5 |
|---|---|---|---|---|---|---|---|---|---|---|
| NC | 1.0000 | -0.2405 | -0.2663 | -0.2291 | -0.2624 | -0.2262 | -0.2325 | -0.1357 | -0.2015 | -0.1050 |
| CCd1 | -0.2405 | 1.0000 | 0.0641 | 0.0953 | 0.0631 | 0.0865 | 0.0559 | 0.0504 | 0.0485 | 0.0395 |
| CCn1 | -0.2663 | 0.0641 | 1.0000 | 0.0610 | 0.1101 | 0.0602 | 0.0968 | 0.0361 | 0.0818 | 0.0280 |
| CCd2 | -0.2291 | 0.0953 | 0.0610 | 1.0000 | 0.0601 | 0.0915 | 0.0533 | 0.0530 | 0.0462 | 0.0416 |
| CCn2 | -0.2624 | 0.0631 | 0.1101 | 0.0601 | 1.0000 | 0.0594 | 0.0952 | 0.0356 | 0.0805 | 0.0276 |
| CCd3 | -0.2262 | 0.0865 | 0.0602 | 0.0915 | 0.0594 | 1.0000 | 0.0526 | 0.0482 | 0.0456 | 0.0378 |
| CCn3 | -0.2325 | 0.0559 | 0.0968 | 0.0533 | 0.0952 | 0.0526 | 1.0000 | 0.0315 | 0.0708 | 0.0244 |
| CCd4 | -0.1357 | 0.0504 | 0.0361 | 0.0530 | 0.0356 | 0.0482 | 0.0315 | 1.0000 | 0.0273 | 0.0220 |
| CCn4 | -0.2015 | 0.0485 | 0.0818 | 0.0462 | 0.0805 | 0.0456 | 0.0708 | 0.0273 | 1.0000 | 0.0212 |
| CCd5 | -0.1050 | 0.0395 | 0.0280 | 0.0416 | 0.0276 | 0.0378 | 0.0244 | 0.0220 | 0.0212 | 1.0000 |
| CCn5 | -0.1564 | 0.0376 | 0.0664 | 0.0359 | 0.0653 | 0.0354 | 0.0574 | 0.0212 | 0.0485 | 0.0164 |
| CCd6 | -0.0590 | 0.0267 | 0.0157 | 0.0290 | 0.0155 | 0.0257 | 0.0137 | 0.0149 | 0.0119 | 0.0117 |
| CCn6 | -0.1171 | 0.0282 | 0.0439 | 0.0268 | 0.0432 | 0.0265 | 0.0380 | 0.0159 | 0.0323 | 0.0123 |
| CCd7 | -0.0416 | 0.0159 | 0.0111 | 0.0168 | 0.0109 | 0.0152 | 0.0097 | 0.0089 | 0.0084 | 0.0069 |
| CCn7 | -0.0767 | 0.0185 | 0.0324 | 0.0176 | 0.0319 | 0.0174 | 0.0280 | 0.0104 | 0.0237 | 0.0081 |
| CCd8 | -0.0222 | 0.0075 | 0.0059 | 0.0078 | 0.0058 | 0.0071 | 0.0052 | 0.0042 | 0.0045 | 0.0033 |
| CCn8 | -0.0403 | 0.0097 | 0.0156 | 0.0092 | 0.0154 | 0.0091 | 0.0135 | 0.0055 | 0.0115 | 0.0042 |
| CCd9 | -0.0102 | 0.0033 | 0.0027 | 0.0034 | 0.0027 | 0.0032 | 0.0024 | 0.0019 | 0.0021 | 0.0014 |
| CCn9 | -0.0234 | 0.0056 | 0.0096 | 0.0054 | 0.0094 | 0.0053 | 0.0083 | 0.0032 | 0.0070 | 0.0025 |
| CCd10 | -0.0042 | 0.0019 | 0.0011 | 0.0021 | 0.0011 | 0.0018 | 0.0010 | 0.0011 | 0.0009 | 0.0008 |
| CCn10 | -0.0102 | 0.0024 | 0.0065 | 0.0023 | 0.0064 | 0.0023 | 0.0056 | 0.0014 | 0.0046 | 0.0011 |
| CCd11 | -0.0017 | 0.0006 | 0.0005 | 0.0007 | 0.0005 | 0.0006 | 0.0004 | 0.0003 | 0.0004 | 0.0003 |
| CCn11 | -0.0050 | 0.0012 | 0.0017 | 0.0011 | 0.0017 | 0.0011 | 0.0015 | 0.0007 | 0.0013 | 0.0005 |
| CCd12 | 0.0002 | 0.0001 | -0.0000 | 0.0002 | -0.0000 | 0.0001 | -0.0000 | 0.0001 | -0.0000 | 0.0001 |
| CCn12 | -0.0007 | 0.0002 | 0.0016 | 0.0002 | 0.0015 | 0.0002 | 0.0013 | 0.0001 | 0.0011 | 0.0001 |
| CCd13 | 0.0000 | -0.0000 | -0.0000 | 0.0000 | -0.0000 | -0.0000 | -0.0000 | -0.0000 | -0.0000 | -0.0000 |
| CCn13 | -0.0006 | 0.0001 | 0.0002 | 0.0001 | 0.0002 | 0.0001 | 0.0001 | 0.0001 | 0.0001 | 0.0001 |
| CCd14 | -0.0000 | 0.0000 | 0.0000 | 0.0000 | 0.0000 | 0.0000 | -0.0000 | 0.0000 | 0.0000 | 0.0000 |
| CCn14 | 0.0001 | -0.0000 | 0.0000 | -0.0000 | 0.0000 | -0.0000 | 0.0000 | -0.0000 | 0.0000 | -0.0000 |
| CCd15 | -0.0000 | -0.0000 | 0.0000 | -0.0000 | 0.0000 | 0.0000 | -0.0000 | -0.0000 | 0.0000 | 0.0000 |
| CCn15 | -0.0000 | 0.0000 | 0.0000 | 0.0000 | 0.0000 | 0.0000 | 0.0000 | 0.0000 | 0.0000 | 0.0000 |
| CCd16 | 0.0000 | -0.0000 | -0.0000 | 0.0000 | -0.0000 | -0.0000 | -0.0000 | 0.0000 | -0.0000 | -0.0000 |
| CCn16 | -0.0000 | 0.0000 | 0.0000 | 0.0000 | 0.0000 | 0.0000 | -0.0000 | 0.0000 | 0.0000 | 0.0000 |
| CCd17 | -0.0248 | -0.2233 | 0.0066 | 0.0157 | 0.0065 | 0.0136 | 0.0058 | 0.0078 | 0.0050 | 0.0061 |
| CCn17 | 0.0000 | -0.0000 | -0.0000 | -0.0000 | -0.0000 | -0.0000 | -0.0000 | 0.0000 | -0.0000 | -0.0000 |
| ESd | -0.0413 | -0.0838 | 0.0110 | -0.0636 | 0.0108 | -0.0653 | 0.0096 | -0.0712 | 0.0083 | -0.0705 |
| ESn | -0.0514 | 0.0124 | -0.0818 | 0.0118 | -0.0589 | 0.0116 | -0.0859 | 0.0070 | -0.0622 | 0.0054 |
| EXTNd | -0.2667 | -0.1096 | 0.0710 | -0.1537 | 0.0700 | -0.1112 | 0.0620 | -0.0588 | 0.0537 | -0.0480 |
| EXTNn | -0.3138 | 0.0755 | -0.1089 | 0.0719 | -0.1062 | 0.0710 | -0.0906 | 0.0426 | -0.0687 | 0.0330 |

Table C.3: (continued)

| Signal | CCn5 | CCd6 | CCn6 | CCd7 | CCn7 | CCd8 | CCn8 | CCd9 | CCn9 | CCd10 |
|--------|------|------|------|------|------|------|------|------|------|-------|
| NC | -0.1564 | -0.0590 | -0.1171 | -0.0416 | -0.0767 | -0.0222 | -0.0403 | -0.0102 | -0.0234 | -0.0042 |
| CCd1 | 0.0376 | 0.0267 | 0.0282 | 0.0159 | 0.0185 | 0.0075 | 0.0097 | 0.0033 | 0.0056 | 0.0019 |
| CCn1 | 0.0664 | 0.0157 | 0.0439 | 0.0111 | 0.0324 | 0.0059 | 0.0156 | 0.0027 | 0.0096 | 0.0011 |
| CCd2 | 0.0359 | 0.0290 | 0.0268 | 0.0168 | 0.0176 | 0.0078 | 0.0092 | 0.0034 | 0.0054 | 0.0021 |
| CCn2 | 0.0653 | 0.0155 | 0.0432 | 0.0109 | 0.0319 | 0.0058 | 0.0154 | 0.0027 | 0.0094 | 0.0011 |
| CCd3 | 0.0354 | 0.0257 | 0.0265 | 0.0152 | 0.0174 | 0.0071 | 0.0091 | 0.0032 | 0.0053 | 0.0018 |
| CCn3 | 0.0574 | 0.0137 | 0.0380 | 0.0097 | 0.0280 | 0.0052 | 0.0135 | 0.0024 | 0.0083 | 0.0010 |
| CCd4 | 0.0212 | 0.0149 | 0.0159 | 0.0089 | 0.0104 | 0.0042 | 0.0055 | 0.0019 | 0.0032 | 0.0011 |
| CCn4 | 0.0485 | 0.0119 | 0.0323 | 0.0084 | 0.0237 | 0.0045 | 0.0115 | 0.0021 | 0.0070 | 0.0009 |
| CCd5 | 0.0164 | 0.0117 | 0.0123 | 0.0069 | 0.0081 | 0.0033 | 0.0042 | 0.0014 | 0.0025 | 0.0008 |
| CCn5 | 1.0000 | 0.0092 | 0.0260 | 0.0065 | 0.0192 | 0.0035 | 0.0092 | 0.0016 | 0.0057 | 0.0007 |
| CCd6 | 0.0092 | 1.0000 | 0.0069 | 0.0047 | 0.0045 | 0.0021 | 0.0024 | 0.0009 | 0.0014 | 0.0006 |
| CCn6 | 0.0260 | 0.0069 | 1.0000 | 0.0049 | 0.0127 | 0.0026 | 0.0062 | 0.0012 | 0.0038 | 0.0005 |
| CCd7 | 0.0065 | 0.0047 | 0.0049 | 1.0000 | 0.0032 | 0.0013 | 0.0017 | 0.0006 | 0.0010 | 0.0003 |
| CCn7 | 0.0192 | 0.0045 | 0.0127 | 0.0032 | 1.0000 | 0.0017 | 0.0045 | 0.0008 | 0.0028 | 0.0003 |
| CCd8 | 0.0035 | 0.0021 | 0.0026 | 0.0013 | 0.0017 | 1.0000 | 0.0009 | 0.0003 | 0.0005 | 0.0002 |
| CCn8 | 0.0092 | 0.0024 | 0.0062 | 0.0017 | 0.0045 | 0.0009 | 1.0000 | 0.0004 | 0.0013 | 0.0002 |
| CCd9 | 0.0016 | 0.0009 | 0.0012 | 0.0006 | 0.0008 | 0.0003 | 0.0004 | 1.0000 | 0.0002 | 0.0001 |
| CCn9 | 0.0057 | 0.0014 | 0.0038 | 0.0010 | 0.0028 | 0.0005 | 0.0013 | 0.0002 | 1.0000 | 0.0001 |
| CCd10 | 0.0007 | 0.0006 | 0.0005 | 0.0003 | 0.0003 | 0.0002 | 0.0002 | 0.0001 | 0.0001 | 1.0000 |
| CCn10 | 0.0039 | 0.0006 | 0.0024 | 0.0004 | 0.0019 | 0.0002 | 0.0009 | 0.0001 | 0.0005 | 0.0000 |
| CCd11 | 0.0003 | 0.0002 | 0.0002 | 0.0001 | 0.0001 | 0.0001 | 0.0001 | 0.0000 | 0.0000 | 0.0000 |
| CCn11 | 0.0010 | 0.0003 | 0.0007 | 0.0002 | 0.0005 | 0.0001 | 0.0002 | 0.0001 | 0.0001 | 0.0000 |
| CCd12 | -0.0000 | 0.0001 | -0.0000 | 0.0000 | -0.0000 | 0.0000 | -0.0000 | 0.0000 | -0.0000 | 0.0000 |
| CCn12 | 0.0009 | 0.0000 | 0.0005 | 0.0000 | 0.0005 | 0.0000 | 0.0002 | 0.0000 | 0.0001 | 0.0000 |
| CCd13 | -0.0000 | 0.0000 | 0.0000 | 0.0000 | -0.0000 | -0.0000 | -0.0000 | -0.0000 | -0.0000 | -0.0000 |
| CCn13 | 0.0001 | 0.0000 | 0.0001 | 0.0000 | 0.0000 | 0.0000 | 0.0000 | 0.0000 | 0.0000 | -0.0000 |
| CCd14 | 0.0000 | 0.0000 | 0.0000 | -0.0000 | -0.0000 | 0.0000 | 0.0000 | -0.0000 | 0.0000 | -0.0000 |
| CCn14 | 0.0000 | -0.0000 | 0.0000 | -0.0000 | 0.0000 | -0.0000 | 0.0000 | -0.0000 | 0.0000 | -0.0000 |
| CCd15 | 0.0000 | 0.0000 | -0.0000 | -0.0000 | 0.0000 | -0.0000 | -0.0000 | -0.0000 | 0.0000 | 0.0000 |
| CCn15 | 0.0000 | 0.0000 | 0.0000 | -0.0000 | 0.0000 | 0.0000 | 0.0000 | 0.0000 | 0.0000 | 0.0000 |
| CCd16 | -0.0000 | 0.0000 | 0.0000 | -0.0000 | -0.0000 | -0.0000 | -0.0000 | -0.0000 | -0.0000 | -0.0000 |
| CCn16 | 0.0000 | 0.0000 | 0.0000 | -0.0000 | -0.0000 | 0.0000 | 0.0000 | -0.0000 | 0.0000 | 0.0000 |
| CCd17 | 0.0039 | 0.0046 | 0.0029 | 0.0025 | 0.0019 | 0.0011 | 0.0010 | 0.0005 | 0.0006 | 0.0003 |
| CCn17 | -0.0000 | 0.0000 | 0.0000 | 0.0000 | -0.0000 | 0.0000 | -0.0000 | 0.0000 | -0.0000 | -0.0000 |
| ESd | 0.0065 | -0.0625 | 0.0048 | -0.0452 | 0.0032 | -0.0507 | 0.0017 | -0.0472 | 0.0010 | -0.0490 |
| ESn | -0.0555 | 0.0030 | -0.0541 | 0.0021 | -0.0452 | 0.0011 | -0.0710 | 0.0005 | -0.0420 | 0.0002 |
| EXTNd | 0.0417 | -0.0514 | 0.0312 | -0.0204 | 0.0205 | -0.0056 | 0.0108 | -0.0018 | 0.0062 | -0.0036 |
| EXTNn | -0.0667 | 0.0185 | -0.0228 | 0.0131 | -0.0320 | 0.0070 | -0.0102 | 0.0032 | -0.0083 | 0.0013 |

Table C.3: (continued)

| Signal | CCn10 | CCd11 | CCn11 | CCd12 | CCn12 | CCd13 | CCn13 | CCd14 | CCn14 | CCd15 |
|---|---|---|---|---|---|---|---|---|---|---|
| NC | -0.0102 | -0.0017 | -0.0050 | 0.0002 | -0.0007 | 0.0000 | -0.0006 | -0.0000 | 0.0001 | -0.0000 |
| CCd1 | 0.0024 | 0.0006 | 0.0012 | 0.0001 | 0.0002 | -0.0000 | 0.0001 | 0.0000 | -0.0000 | -0.0000 |
| CCn1 | 0.0065 | 0.0005 | 0.0017 | -0.0000 | 0.0016 | -0.0000 | 0.0002 | 0.0000 | 0.0000 | 0.0000 |
| CCd2 | 0.0023 | 0.0007 | 0.0011 | 0.0002 | 0.0002 | 0.0000 | 0.0001 | 0.0000 | -0.0000 | -0.0000 |
| CCn2 | 0.0064 | 0.0005 | 0.0017 | -0.0000 | 0.0015 | -0.0000 | 0.0002 | 0.0000 | 0.0000 | 0.0000 |
| CCd3 | 0.0023 | 0.0006 | 0.0011 | 0.0001 | 0.0002 | -0.0000 | 0.0001 | 0.0000 | -0.0000 | 0.0000 |
| CCn3 | 0.0056 | 0.0004 | 0.0015 | -0.0000 | 0.0013 | -0.0000 | 0.0001 | -0.0000 | 0.0000 | -0.0000 |
| CCd4 | 0.0014 | 0.0003 | 0.0007 | 0.0001 | 0.0001 | -0.0000 | 0.0001 | 0.0000 | -0.0000 | -0.0000 |
| CCn4 | 0.0046 | 0.0004 | 0.0013 | -0.0000 | 0.0011 | -0.0000 | 0.0001 | 0.0000 | 0.0000 | 0.0000 |
| CCd5 | 0.0011 | 0.0003 | 0.0005 | 0.0001 | 0.0001 | -0.0000 | 0.0001 | 0.0000 | -0.0000 | 0.0000 |
| CCn5 | 0.0039 | 0.0003 | 0.0010 | -0.0000 | 0.0009 | -0.0000 | 0.0001 | 0.0000 | 0.0000 | 0.0000 |
| CCd6 | 0.0006 | 0.0002 | 0.0003 | 0.0001 | 0.0000 | 0.0000 | 0.0000 | 0.0000 | -0.0000 | 0.0000 |
| CCn6 | 0.0024 | 0.0002 | 0.0007 | -0.0000 | 0.0005 | 0.0000 | 0.0001 | 0.0000 | 0.0000 | -0.0000 |
| CCd7 | 0.0004 | 0.0001 | 0.0002 | 0.0000 | 0.0000 | 0.0000 | 0.0000 | -0.0000 | -0.0000 | -0.0000 |
| CCn7 | 0.0019 | 0.0001 | 0.0005 | -0.0000 | 0.0005 | -0.0000 | 0.0000 | -0.0000 | 0.0000 | 0.0000 |
| CCd8 | 0.0002 | 0.0001 | 0.0001 | 0.0000 | 0.0000 | -0.0000 | 0.0000 | 0.0000 | -0.0000 | -0.0000 |
| CCn8 | 0.0009 | 0.0001 | 0.0002 | -0.0000 | 0.0002 | -0.0000 | 0.0000 | 0.0000 | 0.0000 | -0.0000 |
| CCd9 | 0.0001 | 0.0000 | 0.0001 | 0.0000 | 0.0000 | -0.0000 | 0.0000 | -0.0000 | -0.0000 | -0.0000 |
| CCn9 | 0.0005 | 0.0000 | 0.0001 | -0.0000 | 0.0001 | -0.0000 | 0.0000 | 0.0000 | 0.0000 | 0.0000 |
| CCd10 | 0.0000 | 0.0000 | 0.0000 | 0.0000 | 0.0000 | -0.0000 | -0.0000 | -0.0000 | -0.0000 | 0.0000 |
| CCn10 | 1.0000 | 0.0000 | 0.0001 | -0.0000 | 0.0001 | -0.0000 | 0.0000 | -0.0000 | 0.0000 | -0.0000 |
| CCd11 | 0.0000 | 1.0000 | 0.0000 | 0.0000 | 0.0000 | 0.0000 | 0.0000 | 0.0000 | 0.0000 | -0.0000 |
| CCn11 | 0.0001 | 0.0000 | 1.0000 | -0.0000 | 0.0000 | -0.0000 | 0.0000 | -0.0000 | -0.0000 | 0.0000 |
| CCd12 | -0.0000 | 0.0000 | -0.0000 | 1.0000 | -0.0000 | -0.0000 | -0.0000 | 0.0000 | -0.0000 | 0.0000 |
| CCn12 | 0.0001 | 0.0000 | 0.0000 | -0.0000 | 1.0000 | -0.0000 | 0.0000 | 0.0000 | 0.0000 | -0.0000 |
| CCd13 | -0.0000 | 0.0000 | -0.0000 | -0.0000 | -0.0000 | 1.0000 | -0.0000 | -0.0000 | -0.0000 | -0.0000 |
| CCn13 | 0.0000 | 0.0000 | 0.0000 | -0.0000 | 0.0000 | -0.0000 | 1.0000 | -0.0000 | -0.0000 | -0.0000 |
| CCd14 | -0.0000 | 0.0000 | -0.0000 | 0.0000 | 0.0000 | -0.0000 | -0.0000 | 1.0000 | -0.0000 | 0.0000 |
| CCn14 | 0.0000 | 0.0000 | -0.0000 | -0.0000 | 0.0000 | -0.0000 | -0.0000 | -0.0000 | 1.0000 | -0.0000 |
| CCd15 | -0.0000 | -0.0000 | 0.0000 | 0.0000 | -0.0000 | -0.0000 | -0.0000 | 0.0000 | -0.0000 | 1.0000 |
| CCn15 | 0.0000 | 0.0000 | 0.0000 | 0.0000 | 0.0000 | 0.0000 | 0.0000 | 0.0000 | -0.0000 | 0.0000 |
| CCd16 | -0.0000 | 0.0000 | -0.0000 | -0.0000 | -0.0000 | -0.0000 | -0.0000 | -0.0000 | -0.0000 | 0.0000 |
| CCn16 | 0.0000 | 0.0000 | 0.0000 | 0.0000 | 0.0000 | -0.0000 | -0.0000 | 0.0000 | -0.0000 | 0.0000 |
| CCd17 | 0.0003 | 0.0001 | 0.0001 | 0.0000 | 0.0000 | -0.0000 | 0.0000 | -0.0000 | -0.0000 | -0.0000 |
| CCn17 | -0.0000 | 0.0000 | -0.0000 | -0.0000 | 0.0000 | 0.0000 | 0.0000 | -0.0000 | 0.0000 | 0.0000 |
| ESd | 0.0004 | -0.0572 | 0.0002 | 0.0000 | 0.0000 | -0.0000 | 0.0000 | -0.0163 | -0.0000 | -0.0383 |
| ESn | 0.0012 | 0.0001 | -0.0361 | -0.0000 | 0.0003 | -0.0000 | -0.0229 | 0.0000 | -0.0139 | 0.0000 |
| EXTNd | 0.0027 | -0.0007 | 0.0013 | -0.0010 | 0.0002 | -0.0000 | 0.0002 | -0.0000 | -0.0000 | 0.0000 |
| EXTNn | -0.0145 | 0.0005 | -0.0001 | -0.0001 | -0.0061 | -0.0000 | 0.0002 | -0.0000 | -0.0002 | 0.0000 |

Table C.3: (continued)

| Signal | CCn15 | CCd16 | CCn16 | CCd17 | CCn17 | ESd | ESn | EXTNd | EXTNn |
|---|---|---|---|---|---|---|---|---|---|
| NC | -0.0000 | 0.0000 | -0.0000 | -0.0248 | 0.0000 | -0.0413 | -0.0514 | -0.2667 | -0.3138 |
| CCd1 | 0.0000 | -0.0000 | 0.0000 | -0.2233 | -0.0000 | -0.0838 | 0.0124 | -0.1096 | 0.0755 |
| CCn1 | 0.0000 | -0.0000 | 0.0000 | 0.0066 | -0.0000 | 0.0110 | -0.0818 | 0.0710 | -0.1089 |
| CCd2 | 0.0000 | 0.0000 | 0.0000 | 0.0157 | -0.0000 | -0.0636 | 0.0118 | -0.1537 | 0.0719 |
| CCn2 | 0.0000 | -0.0000 | 0.0000 | 0.0065 | -0.0000 | 0.0108 | -0.0589 | 0.0700 | -0.1062 |
| CCd3 | 0.0000 | -0.0000 | 0.0000 | 0.0136 | -0.0000 | -0.0653 | 0.0116 | -0.1112 | 0.0710 |
| CCn3 | 0.0000 | -0.0000 | -0.0000 | 0.0058 | -0.0000 | 0.0096 | -0.0859 | 0.0620 | -0.0906 |
| CCd4 | 0.0000 | 0.0000 | 0.0000 | 0.0078 | 0.0000 | -0.0712 | 0.0070 | -0.0588 | 0.0426 |
| CCn4 | 0.0000 | -0.0000 | 0.0000 | 0.0050 | -0.0000 | 0.0083 | -0.0622 | 0.0537 | -0.0687 |
| CCd5 | 0.0000 | -0.0000 | 0.0000 | 0.0061 | -0.0000 | -0.0705 | 0.0054 | -0.0480 | 0.0330 |
| CCn5 | 0.0000 | -0.0000 | 0.0000 | 0.0039 | -0.0000 | 0.0065 | -0.0555 | 0.0417 | -0.0667 |
| CCd6 | 0.0000 | 0.0000 | 0.0000 | 0.0046 | 0.0000 | -0.0625 | 0.0030 | -0.0514 | 0.0185 |
| CCn6 | 0.0000 | 0.0000 | 0.0000 | 0.0029 | 0.0000 | 0.0048 | -0.0541 | 0.0312 | -0.0228 |
| CCd7 | -0.0000 | -0.0000 | -0.0000 | 0.0025 | 0.0000 | -0.0452 | 0.0021 | -0.0204 | 0.0131 |
| CCn7 | 0.0000 | -0.0000 | -0.0000 | 0.0019 | -0.0000 | 0.0032 | -0.0452 | 0.0205 | -0.0320 |
| CCd8 | 0.0000 | -0.0000 | 0.0000 | 0.0011 | 0.0000 | -0.0507 | 0.0011 | -0.0056 | 0.0070 |
| CCn8 | 0.0000 | -0.0000 | 0.0000 | 0.0010 | -0.0000 | 0.0017 | -0.0710 | 0.0108 | -0.0102 |
| CCd9 | 0.0000 | -0.0000 | -0.0000 | 0.0005 | 0.0000 | -0.0472 | 0.0005 | -0.0018 | 0.0032 |
| CCn9 | 0.0000 | -0.0000 | 0.0000 | 0.0006 | -0.0000 | 0.0010 | -0.0420 | 0.0062 | -0.0083 |
| CCd10 | 0.0000 | -0.0000 | 0.0000 | 0.0003 | -0.0000 | -0.0490 | 0.0002 | -0.0036 | 0.0013 |
| CCn10 | 0.0000 | -0.0000 | 0.0000 | 0.0003 | -0.0000 | 0.0004 | 0.0012 | 0.0027 | -0.0145 |
| CCd11 | 0.0000 | 0.0000 | 0.0000 | 0.0001 | 0.0000 | -0.0572 | 0.0001 | -0.0007 | 0.0005 |
| CCn11 | 0.0000 | -0.0000 | 0.0000 | 0.0001 | -0.0000 | 0.0002 | -0.0361 | 0.0013 | -0.0001 |
| CCd12 | 0.0000 | -0.0000 | 0.0000 | 0.0000 | -0.0000 | 0.0000 | -0.0000 | -0.0010 | -0.0001 |
| CCn12 | 0.0000 | -0.0000 | 0.0000 | 0.0000 | 0.0000 | 0.0000 | 0.0003 | 0.0002 | -0.0061 |
| CCd13 | 0.0000 | -0.0000 | -0.0000 | -0.0000 | 0.0000 | -0.0000 | -0.0000 | -0.0000 | -0.0000 |
| CCn13 | 0.0000 | -0.0000 | -0.0000 | 0.0000 | 0.0000 | 0.0000 | -0.0229 | 0.0002 | 0.0002 |
| CCd14 | 0.0000 | -0.0000 | 0.0000 | -0.0000 | -0.0000 | -0.0163 | 0.0000 | -0.0000 | -0.0000 |
| CCn14 | -0.0000 | -0.0000 | -0.0000 | -0.0000 | 0.0000 | -0.0000 | -0.0139 | -0.0000 | -0.0002 |
| CCd15 | 0.0000 | 0.0000 | 0.0000 | -0.0000 | 0.0000 | -0.0383 | 0.0000 | 0.0000 | 0.0000 |
| CCn15 | 1.0000 | 0.0000 | 0.0000 | -0.0000 | -0.0000 | 0.0000 | -0.0188 | 0.0000 | -0.0000 |
| CCd16 | 0.0000 | 1.0000 | -0.0000 | -0.0000 | -0.0000 | -0.0000 | -0.0000 | -0.0000 | -0.0000 |
| CCn16 | 0.0000 | -0.0000 | 1.0000 | -0.0000 | -0.0000 | 0.0000 | -0.0085 | 0.0000 | 0.0000 |
| CCd17 | -0.0000 | -0.0000 | -0.0000 | 1.0000 | 0.0000 | 0.4280 | 0.0013 | -0.0366 | 0.0078 |
| CCn17 | -0.0000 | -0.0000 | -0.0000 | 0.0000 | 1.0000 | -0.0000 | -0.0183 | -0.0000 | -0.0000 |
| ESd | 0.0000 | -0.0000 | 0.0000 | 0.4280 | -0.0000 | 1.0000 | 0.0021 | -0.0286 | 0.0130 |
| ESn | -0.0188 | -0.0000 | -0.0085 | 0.0013 | -0.0183 | 0.0021 | 1.0000 | 0.0137 | -0.0185 |
| EXTNd | 0.0000 | -0.0000 | 0.0000 | -0.0366 | -0.0000 | -0.0286 | 0.0137 | 1.0000 | 0.0837 |
| EXTNn | -0.0000 | -0.0000 | 0.0000 | 0.0078 | -0.0000 | 0.0130 | -0.0185 | 0.0837 | 1.0000 |

# VITA

Kathryn K. Schaffer Miknaitis grew up in Athens, Ohio. In 1994 she began studies at Bard College in Annandale-on-Hudson, NY, under the Excellence and Equal Cost Scholarship program. She began studies in philosophy and religion, having never considered science as a possible direction. In her first year at Bard, she took a course in the History and Philosophy of Science from the charismatic and often incomprehensible Professor Peter Skiff. After she spent the year pestering him with questions, Professor Skiff convinced her to enroll the following semester in an advanced Modern Physics class. Despite the fact that she had not taken introductory physics or calculus, she survived that course and went on to complete a double major in Physics and the History and Philosophy of Science. For her senior theses, she studied Big Bang Nucleosynthesis and the Pre-Socratic foundations of certain central ideas in ancient Greek astronomy. She received several awards and scholarships while at Bard.

Dr. Miknaitis began graduate studies in the Department of Physics at the University of Washington in 1998. After a year teaching introductory physics, she joined the Electroweak Interactions Group at the University of Washington, where she worked on the construction of the Neutral Current Detector array for the Sudbury Neutrino Observatory (SNO). She earned her Masters in Science from the University of Washington in 2000. She participated in the analysis of data from the first phase of the SNO experiment before beginning work on the analysis of the day-night effect in the second phase of the experiment. In 2004, she was awarded a Huckabay Teaching Fellowship at the University of Washington, allowing her to teach an undergraduate course of her own design. Returning to her interests in the broader issues surrounding science, she created a course on radiation and nuclear technology for non-science students. After completing her Doctor of Philosophy in Physics at the University of Washington in 2005, she joined the Kavli Institute for Cosmological Physics at the University of Chicago.